DOCTOR OF PHILOSOPHY

Lithium Accelerated Corrosion of Zirconium Alloys

Stephens, Gareth Frank

Award date:
2024

Awarding institution:
Bangor University

Lithium Accelerated Corrosion of Zirconium Alloys

Gareth Frank Stephens

PRIFYSGOL
BANGOR
UNIVERSITY

School of Computer Science and Electronic Engineering

College of Environmental Sciences and Engineering

Submitted in partial satisfaction of the requirements for the

Degree of Doctor of Philosophy in Nuclear Engineering and Science.

October 2023

Declaration

I hereby declare that this thesis is the results of my own investigations, except where otherwise stated. All other sources are acknowledged by bibliographic references. This work has not previously been accepted in substance for any degree and is not being concurrently submitted in candidature for any degree unless, as agreed by the University, for approved dual awards.

Yr wyf drwy hyn yn datgan mai canlyniad fy ymchwil fy hun yw'r thesis hwn, ac eithrio lle nodir yn wahanol. Caiff ffynonellau eraill eu cydnabod gan droednodiadau yn rhoi cyfeiriadau eglur. Nid ywsylwedd y gwaith hwn wedi cael ei dderbyn o'r blaen ar gyfer unrhyw radd, ac nid yw'n cael ei gyflwyno ar yr un pryd mewn ymgeisiaeth am unrhyw radd oni bai ei fod, fel y cytunwyd gan y Brifysgol, am gymwysterau deuol cymeradwy.

Abstract

With a global push to reach net zero, the need to consider small modular reactors (SMRs) to reduce costs and accelerate delivery of nuclear power has become clear. SMRs would benefit greatly from simplifications in design which could also reduce engineering, operation and running costs. One particular simplification under consideration is a boron-free coolant chemistry whereby reactivity management could be maintained through control rod operations. Issues associated with boric acid within the coolant chemistry could be eliminated, which can increase efficiency, particularly at the end of cycle.

To elevate the pH of the coolant water, combatting the radiation hydrolysis effect, lithium is added to the coolant chemistry as lithium hydroxide. In the absence of boron, lithium has been found to accelerate the corrosion of the zirconium alloy fuel cladding in some circumstances. The mechanisms that underpin this phenomenon have not been identified and formed the basis for this thesis.

This work was divided into two areas of investigation where, first, a simulation route was undertaken to explore potential predictions which might provide an indication of the mechanisms that could cause the accelerated corrosion of the zirconium alloys. These simulations were focused on the likely location that Li would reside within the bulk or grain boundary ZrO_2 structures and how the Lithium might affect the oxide layer. From this, the impact of Li on defect chemistry could be assessed. Once the simulations provided sufficient data and focus, experimentation could then take place with the aim of validating the simulated results.

Literature provided a number of hypotheses:

1. Lithium forms solution into the bulk zirconium oxide reducing the crystal volume, promoting pore growth which might allow oxygen to pass through the oxide layer and reach the metal surface [1,2].

    The work carried out within this document used a combination of density functional theory, Brouwer diagram and solution energy calculations to produce a number of predictions. The solution energy of lithium into the bulk oxide structures, however, was high indicating that the solution of lithium would be unlikely. This result led to the second hypothesis where lithium might form solution along the grain boundaries.

2. Previous works have identified that grain boundaries can be complex in structure [3,4]. Investigations were carried out to compare solubilities of Li in these amorphous grain boundaries and compare these values to the bulk solubilities.

    In this work, it was found that lithium formed solution into the amorphous structure and the Brouwer diagrams suggested that an increase of lithium within the grain boundaries would also increase the oxygen vacancy concentrations, particularly at the water oxide interface. This provided an indication that oxygen could be transported through the oxide layer via oxygen vacancy sites along the grain boundaries.

    From the results of the simulations, amorphous ZrO_2 and lithium doped amorphous ZrO_2 were created and characterised. Through thermal analysis, it was found that lithium produced amorphous phase stability where an increase in lithium would increase the temperature required to crystallise the sample. It was also found that lithium segregates outside of the resulting crystallised bulk oxide and that the lithium phase was highly soluble in water. This did provide verification for the simulations that showed low solubility of lithium into the bulk material and good solubility into the amorphous structure.

The work within this thesis outlines the above hypotheses and highlights the route by which Li can accelerate corrosion of Zr-alloys by preferentially attacking grain boundaries in the protective oxide layer.

Acknowledgements

There are many people who have been amazing during the four years of this of this work who are well deserving of acknowledgment and thanks.

Of course, my supervisor Prof Simon Middleburgh who has shown, not only infinite patience, but real and consistent guidance through every stage and at every point whilst also having a spot of fun here and there too.

My industrial supervisor Dr Aidan Cole-Baker at Jacobs has always maintained a very keen interest in my work and provided me with some fantastic guidance at every stage. I believe I had the best luck when it came to supervisors for my PhD.

All of the academic staff, PDRAs and students at Bangor Universities Nuclear futures institute who have all been amazing throughout my time at Bangor.

My long-suffering family, friends and loved ones (including all dogs) who have always supported me and have pushed me to keep going. Obviously, mum and dad are both brilliant!

A.4. Contents

Table of figures

1. Introduction

The main focus of this work was to understand the mechanisms that underpin the accelerated corrosion of zirconium alloys when subject to lithiated coolant water within a fission nuclear reactor. Gaining an understanding of the basic principles of a fission reactor from the literature may grant insights into potential hypotheses that were drawn from previous works. There are, however, many physical interactions taking place within the core of a reactor which include thermal gradients, hydraulic flux and pressures, coolant chemistry, oxidation, hydriding, neutron flux, fission products, radiation damage, amongst many other interactions. Understanding the materials used could also provide an indication of possible mechanistic causes for lithium accelerated corrosion of zirconium alloys.

Before getting too far ahead with the specific problem, a general idea of nuclear fission power and the materials used can provide a foundation on which to build a hypothesis.

1.1. Nuclear Power

To an absolute basic level, in most forms of on grid electrical power plant, a heat source is used to heat water. The water may undergo a phase change to steam which can then be used to turn a turbine which generates electricity. At this level, a nuclear reactor is no different in this respect.

The basic principle of a fission nuclear reactor is a self-sustained chain reaction which was first achieved by Enrico Fermi in 1942 at the University of Chicago [5]. This used natural uranium, which contains low amounts of the desired uranium ^{235}U (0.7%) and mostly ^{238}U (99.3%), placed between graphite blocks which were used to slow an incoming neutron enough to increase the likelihood of fission with ^{235}U. Fission is the reduction of a larger "parent" atom to one or more "daughter" atoms with a release of energy. This fission reaction produces smaller elements along with an average of 2.5 neutrons which may then continue causing further fission events. The heat produced from this reaction is then used to heat the coolant water which may then turn a turbine to generate electricity.

1.1.1. Nuclear Fission

Through nuclear fission, the event can produce virtually all lighter elements than the "parent" atom with common reactions producing daughters from the parent uranium atom such as: ^{141}Ba + ^{92}Kr + 2n, ^{95}Sr + ^{138}Xe + 2n, ^{95}Y + ^{138}I + 2n, ^{98}Nb + ^{135}Sb + 2n. e.g.:

$$ {}^{1}_{0}n + {}^{235}_{92}U \rightarrow {}^{138}_{54}Xe + {}^{95}_{38}Sr + 2({}^{1}_{0}n) \qquad \text{Equation 1} $$

Equation *1* shows a neutron (n) combining with a uranium 235 atom which causes a fission event producing xenon 138, strontium 95 and two neutrons. Each fission reaction of U^{235} produces roughly 200 MeV [6] where the most probable products have roughly a 95 and 137 mass number in a probability distribution as shown in *Figure 1*.

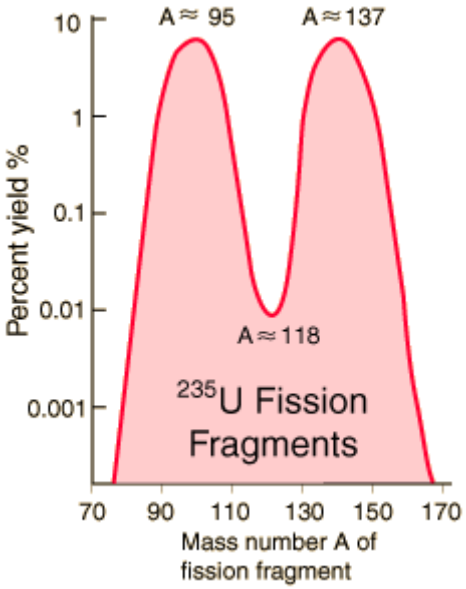

Figure 1 Probability distribution of fission fragment [7].

The examples provided produce 2 neutrons but often have fission events producing 3 neutrons or more hence the 2.5 neutron average. The average likelihood of one neutron from an event causing a fission event with another ^{235}U atom is denoted ***k*** as the reproduction constant. Criticality and a sustained, controlled reaction has a ***k*** value of 1. A value above 1 would indicate a runaway reaction and below 1 would be below self-sustained reaction or criticality [5].

In order to slow fast neutrons to thermal neutrons which have a higher likelihood of causing a fission event, a moderator material is used. In the case of the first reactor build, this was graphite blocks. Graphite is able to interact with fast neutrons either with elastic collision or absorption and emission. This slows the initially fast neutrons to thermal neutrons. Today in water cooled reactors, water is used which also doubles as coolant. There are two main types of water used depending on the type of reactor. Light Water Reactors (LWR), which is standard water and can absorb neutrons, or Heavy Water Reactors (HWR) which is deuterium oxide (D_2O or ^2H_2O). Deuterium oxide works as well as a moderator but is less likely to absorb neutrons. For this reason, heavy water is used within reactors that use natural uranium rather than enriched uranium as it increases the number of thermal neutrons available for reaction. Whilst enriching uranium is expensive, so too is creating deuterium oxide where most countries do not have their own production capability.

To control the level of fission events and maintain criticality with K=1 within the reactor core, control rods are used in order to absorb neutrons and to reduce the likelihood of fission events. Control rods are typically stainless-steel tubes filled with boron carbide, silver-indium-cadmium [8] or a cadmium-based variant [5]. The control rods are lowered between the uranium fuel rods to reduce or lower the reaction events where rods can be partially lowered or fully lowered in a particular sequence. In the event of an emergency, all rods can be lowered together causing a reactor shutdown known as SCRAM.

The fuel itself, typically UO_2 (Uranium dioxide), is often clad in a variation of zirconium alloy (Zircaloy) containing a typical mix of tin (Sn), iron (Fe), chromium (Cr), niobium (Nb) and nickel (Ni)[9]. These alloy additives hold desirable properties that are introduced to the metal with specific advantages.

Every component within the reactor core, primary circuit and (when used) secondary circuit needs to be meticulously tested to ensure that the materials can undertake their task with minimal corrosion or failure when subject to heat, pressure and, where needed, irradiation.

1.2.2. Pressurised Water Reactors

Because the work focused on the zirconium cladding used in the current, most popular reactors in the world, the pressurised water reactor, the general components are given in Figure 2.

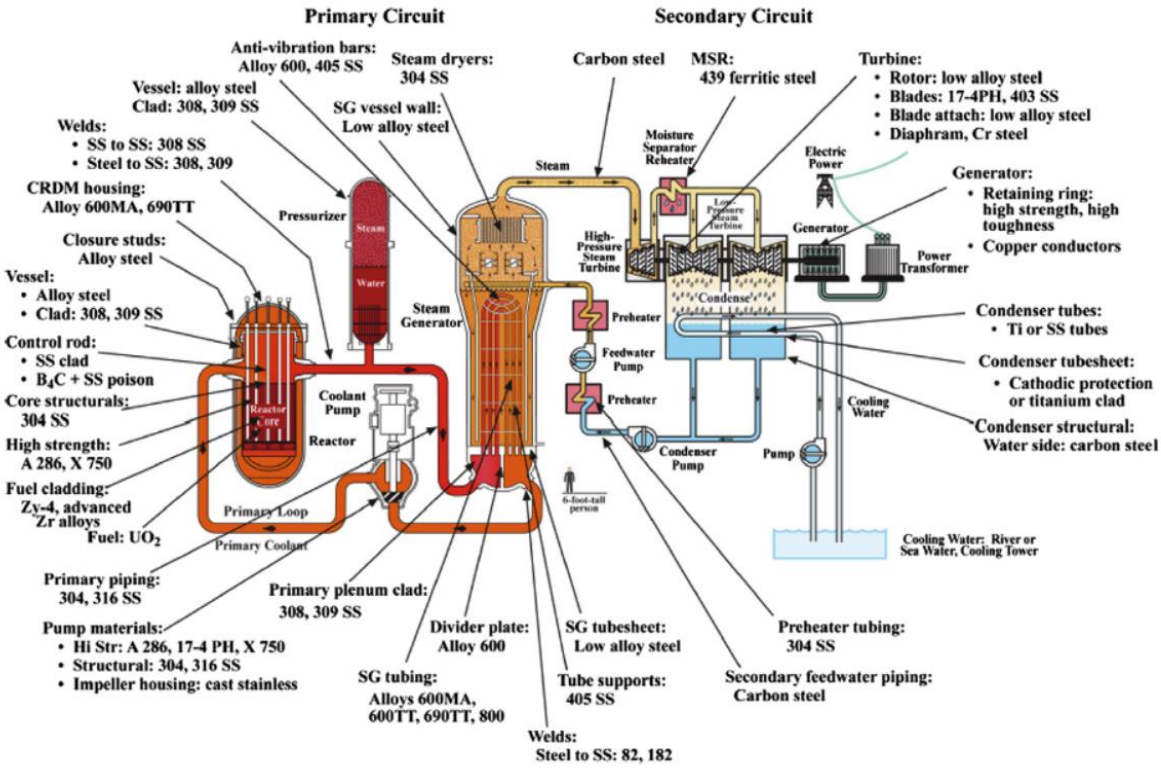

Figure 2 PWR Primary and Secondary Circuit typical materials [8].

The materials that are within a reactor core must be expected to withstand a high level of neutron, thermal and aqueous flux. In the case of the cladding, neutrons need to be able to pass through as freely as possible with minimal hindrance or interaction whilst maintaining a reliable heat transfer. Zirconium alloy has been identified as a suitable option due to a low neutron cross-section and corrosion resistive properties [10,11].

This document has briefly outlined the basic aspects and history of a nuclear reactor but will now focus on the interactions between the water-based coolant/moderator, the fuel and fuel cladding.

1.2.3. The Future of Reactor Designs (Coolant chemistry reduction)

With the current drive to produce small modular reactors (SMRs), developing methods to reduce complexity and, hence, reduce running, design and maintenance costs has become an area of interest within the industry. One particular method is to remove additives from the coolant chemistry such as boron [12]. Boric acid is added to the coolant water and is used as a chemical "shim" to control the reactivity of the core as a neutron poison due to boron having a large neutron cross section [13]. Removing boron has many beneficial outcomes, particularly with overall efficiency of the reactor. When combined with another coolant additive, lithium hydroxide (LiOH), boron and lithium can combine at high burnup regions with other CRUD materials (by many thought to be the acronym for Chalk River Unidentified Deposit but is also thought to derive from the Welsh

word *Cryd* meaning disease or plague, both definitions of which are used to describe undesirable deposits left on surfaces within the reactor [14]). Due to the high neutron cross section of boron, which acts as a neutron absorber, this can reduce local reaction rates which have been identified to reduce the electric generation efficiency up to as much as 70% over several months. This is due to a reduction of capacity through shortened fuel cycles and shutdown margins [15,16]. This phenomenon is known as axial offset anomalies which could be prevented in the absence of boron from the coolant water. The chemical shim could be replaced by a shim rod, which is, essentially, additional control rods to manage the level of reactivity [12].

Although boron is added as an acid which requires a pH balancing additive to prevent additional corrosion, a base additive is still required to elevate the pH up to 10 at room temperature [17]. This is due to the acidic nature of radiolysis which, much like boric acid, can cause corrosion of internal components if not pH balanced by a base material [18].

There is a particularly large hurdle that needs to be crossed when considering a boron free coolant chemistry. In the absence of boron, lithium within the coolant chemistry has been found to accelerate the corrosion of the zirconium alloy fuel cladding material [19–26]. Whilst there was much evidence to support the case for lithium accelerated corrosion of zirconium alloy cladding, there was no strong evidence to underpin the mechanisms of this accelerated corrosion.

Identifying the mechanism by which lithium accelerates the corrosion of zirconium alloys was the basis of this work which will be reviewed in much more detail later in the chapter. Prior to this, gaining an understanding of surrounding aspects of the zirconium alloy fuel cladding might provide an indication of other potential sources that may combine with lithium to initiate the accelerated corrosion.

1.2. Fuels and Fuel Cladding

In conjunction with this work, Megan W. Owen et al. worked to identify oxidation effects of the cladding material from the zirconium alloying additions [27]. The simulation work focused undoped and highly doped zirconium oxide grain boundaries and compared these to crystalline equivalents. It was discovered that oxygen diffusivity was found to be much higher in amorphous ZrO_2 structures than bulk ZrO_2 structures, both doped and undoped. This did open an avenue for further investigation as a potential cause of accelerated corrosion due to lithium. If lithium were to increase the availability of oxygen pathways through the grain boundaries, it might have provided a mechanism by which lithium accelerated the corrosion of zirconium alloys. This will be discussed and investigated in subsequent chapters and partially provides the basis for hypothesis two which would look at lithium ingress along grain boundaries which might increase oxygen diffusion to the metal oxide interface.

1.2.1. Fuels In Use

Usually, the fuel used within a nuclear reactor are not associated with lithium accelerated corrosion. There are, however, a number of mechanisms which may explain corrosion through hydrogen pickup which is usually associated with hydrogen embrittlement of the zirconium alloy cladding material. This could also have a detrimental impact on corrosion rates. It has also been shown that hydrogen pickup increases when electron transport decreases [11]. This would indicate that an increase in bandgap for the oxide would reduce hydrogen intake and prevent hydrogen embrittlement. The most widely used fuel in PWRs, and heavy water reactors, is UO_2 and, as mentioned, this can produce a vast array of fission products which would require an in-depth analysis to identify how or if these fission products may accelerate the corrosion of the zirconium alloy internally [28]. What will be shown later in this chapter is that lithium has been found to accelerate the corrosion of zirconium

alloys without any assistance from fuels used, so this can largely be ruled out for further consideration.

1.2.2. Fuel Claddings in use

The first instance of Zirconium to be used as a cladding material was due to Admiral Rickover (1975) of the US Navy who needed a material within a small reactor that offered low corrosion in aqueous high temperature environments and minimal neutron interference [29]. A pressurised water nuclear reactor was chosen as a small power source that could fit within a submarine offering many benefits over conventional power sources. This resulted in the Mark I PWR in Idaho and the Mark II reactor being placed within the first nuclear submarine, the US Nautilus [29]. However, this used zirconium in a form as pure as possible. As zirconium was sourced from different purification manufacturers, it was noted that manufacturers provided the material slightly more or less pure than the others. But the purer zirconium was less corrosion resistant. Analysis of the less pure material found iron, chromium and nickel and also indicated that additives such as tin, tantalum and niobium may improve corrosion resistance. Tin was selected due to low effect on neutron economy [29] producing Zircaloy-1. Zircaloy-1 displayed a particular issue where, over time, the rate of corrosion would increase. An alternative would be needed which came by accidental means. At the Bettis fabrication shops, a melted Zircaloy-1 ingot was accidentally contaminated with stainless steel. This produced Zircaloy with 1.5% tin, 0.14% iron, 0.10% chromium and 0.06% nickel (Table 2) [11]. This produced Zircaloy-2 with, however, high hydrogen pickup issues that were evident and higher tin concentrations were considered to be of concern during longer lifetime uses [29,30]. For this reason, an attempt to make a new composition, Zircaloy-3, was made. For this, a reduction in tin was made from 1.5% to 0.25%. In testing, it was identified early that a network of exaggerated collections of intermetallic phases caused Fe-Cr corrosion known as “stringers” [29]. This required further alteration which brings us to Zircaloy-4. The high hydrogen pickup, which causes zirconium hydride embrittled regions, of Zircaloy-2 was still a problem but was found to be a result of nickel coating during fabrication which, in turn, suffered from higher hydrogen absorption [29]. Removing the nickel reduced the corrosion resistance so an increase of iron to substitute the nickel was made [11] producing Zircaloy-4. Table 1 contains typical cladding materials used in boiling water reactors (BWR) and pressurised water reactors (PWR).

Table 1 Typical commercial zirconium alloys used as cladding [8].

Reactor Type	**Zr alloy Composition**	**Thermomechanical Treatment**
BWR	Zircaloy-2 (1.5% Sn, 0.15% Fe, 0.1% Cr, 0.05% Ni)	Recrystallized
PWR	Zircaloy-4 (1.5% Sn, 0.2% Fe, 0.1% Cr)	Cold-worked and stress relief anneal
PWR	ZIRLO (1-2% Nb, 1% Sn, 0.1% Fe)	Quench and temper/stress relief anneal
PWR	M5 (1% Nb)	Recrystallized

Fuel cladding rods can vary in length but are usually an approximate diameter of 10 mm with a thickness of 0.6 mm [11]. The fuel cladding rods function is the first defence in preventing fission products from entering the primary circuit.

Table 2 Chemistry of zirconium alloys irradiated in pressurized water reactors to high burnup [29,31].

Alloy	Nominal alloy composition weight percent (wt%)							
	Sn	**Nb**	**Fe**	**Cr**	**Cu**	**V**	**Ni**	**O**
Zircaloy-1	2.5							
Zircaloy-2	1.5		0.12	0.10			0.05	
Zircaloy-3	0.25		0.25					
Zircaloy-4	1.30		0.20	0.10				
E110		1.00						
E635	1.20	1.00	0.35					
Zirlo	1.00	1.00	0.10					
M5		1.00						0.14
J-Alloys								
J1		1.80						
J2		1.60		0.10				
J3		2.50						
AXIOM alloys								
X1	0.30	0.7-1	0.05		0.12	0.20		
X2		1.00	0.06					
X4		1.00	0.06	0.25	0.08			
X5	0.30	0.70	0.35	0.25			0.05	
X5A	0.45	0.30	0.35	0.25				

In works obtained from literature, zirconium alloys (Zircaloys) containing no niobium, such as Zircaloy-4, in high lithium hydroxide environments were found to exhibit accelerated corrosion with higher relative hydrogen uptakes of approximately 50% in autoclave conditions. Zircaloys containing 1% or above of Nb took longer to exhibit accelerated corrosion with a lower hydrogen uptake [32].

1.2.3. Zircaloy-4 structure.

The composition of Zircaloy-4 needs to be within parameters set by ASTM (American Society for Testing Materials) document B353. Whilst the name indicates this would just be for the US, the ASTM is one of the international standards organisations that provides details on current safe operational and production specifications for materials and components across many industries and by many countries. This includes optimal use and compositions of materials within nuclear reactors.

Table 3 Typical Zircaloy-4 properties.[33][34].

Property	Value
Density	6.56 g/cc
Tensile Strength Ultimate	>= 413 Mpa
Tensile Strength Yield	>= 241 Mpa @Strain 0.200
Elongation at Break	20%
Modulus of Elasticity	99.3 Gpa
Poisson's Ratio	0.37
Shear Modulus	36.2 Gpa
Electrical Resistivity	0.0000740 ohm-cm
Coeff of Thermal Expansion, linear	6.00 µm/m- °C @Temperature 25.0 °C
Specific Heat Capacity	0285 J/g-°C
Thermal Conductivity	21.5 W/m-K
Melting Point	1850°C
Boiling Point	4375°C
Chromium, Cr	0.10%
Iron, Fe	0.20%
Oxygen, O	0.12%
Tin, Sn	1.40%
Zirconium, Zr	98.50%
Alpha Phase Crystal Structure	Hexagonal Closed Packed up to 810°C
Beta Phase Crystal Structure	Body Centred Cubic (Total Beta at 980°C)

As shown in Table 3, at room temperature and up to 810°C, the alpha phase Zircaloy-4 (α-phase) is a hexagonal closed packed structure (hcp). It is possible to have a metastable beta phase (β-phase) body centred cubic structure (bcc) below this temperature which may need to be taken into consideration [35]. The bulk of the material is usually α-phase up to 810°C where the structure will begin to change to the β-phase in order to maintain the lowest internal energy as a process of entropy [36]. This is a result of free energy with the entropy contribution becoming increasingly important at higher temperature. The β-phase will totally dominate the bulk material content at 980°C before melting at 1850°C [33].

The additives used to promote favourable properties in Zircaloy-4 are split between solid solution and second phase precipitates (SPPs). Tin usually forms a solid solution with zirconium between 50 and 170 ppm where the SSPs of iron, chromium and, in the case of Zircaloy-2, nickel forms in crystals between 1 µm and 100 nm [37].

Table 4 Lattice parameters of Zr phases and intermetallic phases [37].

Species	Space group	Lattice parameters		
		a (nm)	b (nm)	c (nm)
Pure αZr	$P6_3/mmc$	0.322	-	0.520
Pure βZr	$Im\bar{3}m$	0.359	-	-
Pure ωZr	P6/mmm	0.506	-	0.312
C15 Laves $ZrCr_2$	$Fd\bar{3}m$	0.712	-	-
C14 Laves $ZrCr_2$	$P6_3/mmc$	0.505	-	0.814
Zr_2Cr (Speculative)	I4mcm	0.625	-	0.537
Zr_3Fe	Cmcm	0.330	0.1086	0.885
Zr_2Fe	I4mcm	0.625	-	0.563
C15 Laves $ZrFe_2$	$Fd\bar{3}m$	0.702	-	-
C14 Laves $ZrNi_2$	$P6_3/mmc$	0.498	-	0.811
Zr_2Ni	I4mcm	0.625	-	0.563
ZrNi	Cmcm	0.332	0.984	0.407
C15 Laves $ZrNi_2$	$Fd\bar{3}m$	0.649	-	-
C14 Laves $ZrNi_2$	$P6_3/mmc$	0.492	-	0.804
Zr_3Sn	$Pm\bar{3}n$	0.564	-	-
Zr_5Sn_3	$P6_3/mmc$	0.848	-	0.588
Zr_5Sn_4	$P6_3/mmc$	0.883	-	0.599
$ZrSn_2$	Fddd	0.570	0.965	1.00
Zr_2V (Speculative)	I4mcm	0.746	-	0.568
C15 Laves ZrV_2	$Fd\bar{3}m$	0.738	-	-
C14 Laves ZrV_2	$P6_3/mmc$	0.523	-	0.847

Table 4 includes a new concept to this review of phases. These are representations of atomic size ratios which are between 1.05 and 1.67 and have a composition of AB_2 (laves). The three types of laves are the cubic (C15), hexagonal (C14) and hexagonal (C36). In all of these, the A atoms take the positions as diamond and hexagonal diamond, respectively, and the B atoms are in tetrahedral positions around the A atoms [38].

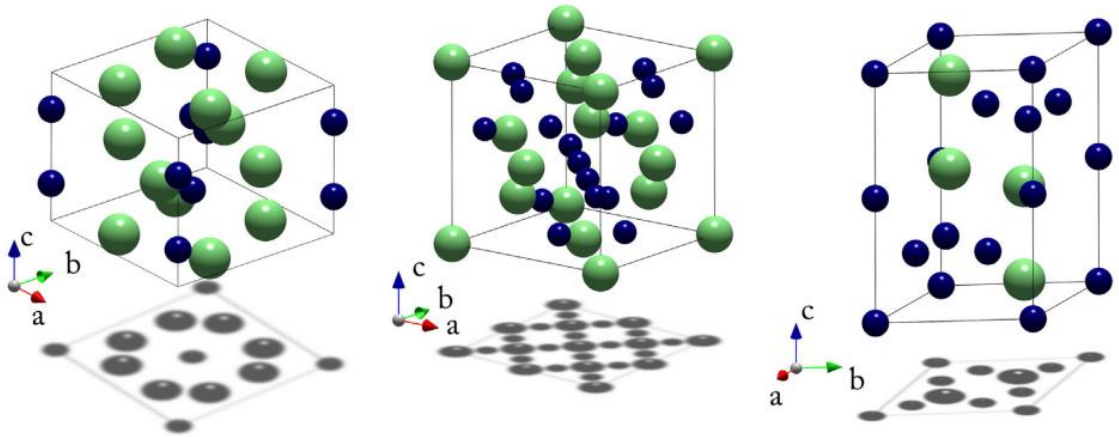

(a) The Zr-rich phase, with formula Zr_2M and structure archetype Al_2Cu.

(b) The cubic Laves phase (C-15), with formula ZrM_2 and structure archetype Cu_2Mg. This phase consists of a face-centred cubic lattice of Zr, with tetrahedral lattice sites alternately occupied with either another *Zr* atom or a sub-tetrahedron of M atoms.

(c) The hexagonal Laves phase (C-14), with formula ZrM_2 and structure archetype $MgZn_2$. The C-36 Laves phase is similar to the C-14 phase, except for being twice as long in the *c* axis, with the bottom half of the cell being a point reflection of the top half, through the centre of the cell.

Figure 3 Crystal structures of Zr alloys. Zr are green where alloy agents are blue [37].

There are also a number of rules that can determine whether metal A will form with metal B as an intermetallic solution or as a compound. These are known as the Hume-Rothery rules [37]. In order to create an intermetallic solution, metal A and B must have an atomic diameter within 15% of one another. They must also have the same crystal structures, similar electronegativity and the same valency [36]. In relation to Zircaloy in the α-phase, this is evident as Cr and Fe prefer to occupy interstitial sites due to their smaller atomic diameter where the other elements considered are in substitutional sites [37].

As mentioned, there are second phase precipitates within the material as alloying additives. The primary precipitate in Zircaloy-4 is the $Zr(Fe, Cr)_2$ hexagonal intermetallic C14 laves structure [39]. It was also suggested that the size, distribution and chemical composition of second phase precipitates have an effect on corrosion where smaller precipitates can reduce nodular corrosion. Precipitates, however, need to be larger than a particular size to ensure that, where corrosion does occur, that it is uniform [39–41].

1.2.4. Zirconium alloys and issues within a nuclear reactor

There are a number of notable issues that have been witnessed with zirconium alloys within nuclear reactors. For example, 13% of fuel failures are debris-induced failures for PWRs but 35 % for BWRs [42]. 40% of fuel failures are from grid-to-rod fretting [42,43]. There are other issues such as anisotropic irradiation growth [8]. Issues that have already been mentioned are hydriding [44] and

crud induced localized corrosion [45]. The main focus of this investigation, however, was waterside corrosion with an emphasis on the lithium accelerated corrosion, in particular, which we will look into in more detail.

1.2.5. Oxide Layer Formation of Zirconium Alloys

Zircaloy forms oxide layers that are formed in oxygen rich environments which can be considered corrosion in much the same way that iron rusts. Zirconium alloy holds similar properties to stainless steel where a thin oxide layer protects the main bulk of the material. Should the material be damaged or scratched, the oxide layer will quickly reform. In water, the reaction that takes place which forms the oxidised layer is:

$$Zr + 2H_2O = ZrO_2 + 2H_2 + Q \qquad \text{Equation 2}$$

Where Q is heat and equal to 6530 KJ/Kg [46]. When oxygen penetrates the metal, ZrO is created. This then becomes $ZrO_{saturated}$ before combining to another oxygen atom to become ZrO_2. This then pushes the oxide layers above it outward. During production, the primary tetragonal oxide layer is usually formed with a columnar crystal order which has a black appearance [47]. But within a reactor, crystal growth can be randomly orientated and equiaxed.

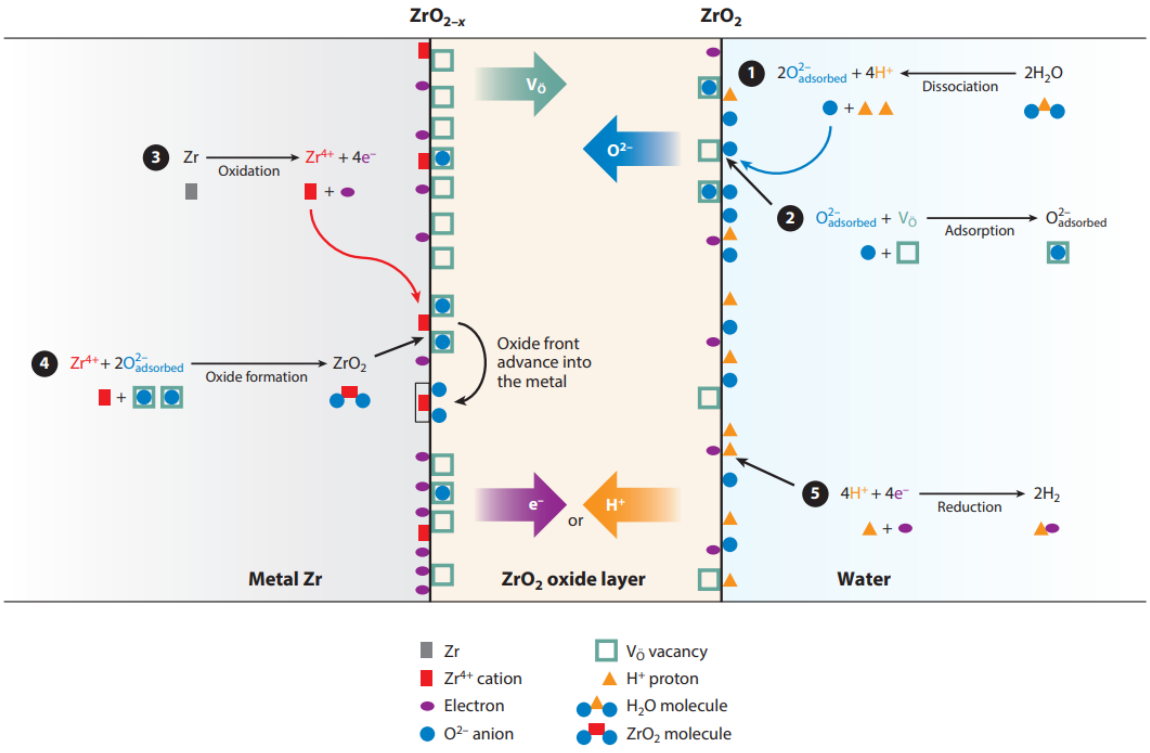

Figure 4 Corrosion process in zirconium alloys. Thick arrows indicate rate-limiting steps [48].

Figure 4 shows the current process of oxidisation and hydrogen pickup which form part of the corrosion mechanism of Zircaloy within water. In figure 4, a blue circle represents negative 2 charged oxygen atom, an orange triangle is a positively charged hydrogen atom, a green square is an oxygen vacancy with plus two charge, a red rectangle is a plus four charged zirconium atom, a grey rectangle is a neutral charged zirconium atom and a purple oval is an electron. Stage 1 (upper right), $2H_2O$, water dissociates to form $4H^+$ positively charged hydrogen cations and $2O^{2-}$ negatively charged oxygen anions. This dissociation can be caused by thermal energy enabling the bond to be broken

through vibration. Stage 2 (middle right), an oxygen vacancy on the oxide surface is able to absorb the negatively charged oxygen. At this stage, transport of the oxygen to the metal surface is at question so we move to stage 3 (upper left), during the oxidisation process, zirconium releases 4 electrons to become positive (Zr^{4+}) and, stage 4 (lower left), combines with 2 negatively charged oxygen atoms to become zirconium dioxide (ZrO_2). At stage 5 (lower right), the remaining electrons produced from zirconium oxidisation and the positive hydrogen protons may recombine to produce neutrally charged hydrogen. The hydrogen may form in the water, oxide layer or on the metal surface where the latter is termed hydrogen pickup. Again, the mechanism for transportation is not clear, however, the transport of the single proton hydrogen cation with relatively small volume will pass through the oxide layer with greater ease than the oxygen if only volume were to be taken into account. The charge may cause hindrance during its path, but this could also be said for the oxygen anion [48]. Much of the oxide weight gain through corrosion of zirconium alloys have been experimentally analysed showing a clear correlation between water exposure time and oxide weight gain [49].

The supposedly corrosion protective tetragonal zirconia layer at the metal oxide interface has caused some debate. This is due to the actual effectiveness of the protectiveness provided from corrosion. This is due to previous works identifying that ZIRLO has a much thinner oxide layer whilst also preventing lithium accelerated corrosion for longer periods than Zircaloy-4 which has a thicker tetragonal layer [50]. If the oxide is allowed to continue in growth stress relief allows the tetragonal polymorph to form monoclinic ZrO_2 [47]. This stress relief also enables cracks to form through the outer layers. Oxygen ions can also diffuse through the tetragonal layer to the oxide/metal (O/M) interface [51]. Though, it is worth noting that tetragonal and monoclinic layers, there-after, can also have a cyclic variation [52]. The rate of corrosion for zirconium alloy is as follows:

$$\omega = At^n \qquad \text{Equation 3}$$

Where ω is the weight gain in mg/dm^2, *t* is the exposure time (days), *A* and *n* are constants where *n* is the characteristic of the particular alloy [48]. Experimental works have also been conducted to identify the correlated hydrogen pickup with water-side corrosion of zirconium alloys [53].

It was unclear what the exact mechanism is for the initial transportation of oxygen to the metal through the tetragonal oxide layer though it has had some recent advancements that will be discussed later. Previous hypotheses included that it is possible that the oxygen may pass between grain boundaries [54]. However, evidence had been provided to suggest that lithium within coolant water can produce pores within the oxide layers allowing oxygen to penetrate the metal surface, accelerating corrosion rates [55]. Whilst this does provide a avenue of investigation that has a good potential to limit accelerated corrosion, it would not prevent the normal corrosion apparent in un-lithiated water. Understanding the formation energies of the intermetallic molecular structure can provide an insight into the corrosion process and what energies are required to allow corrosion to take place.

$$E_{\text{formation}} = \frac{1}{x+y}E\left(Zr_xM_y\right) - \left(\frac{y}{x+y}E(M) + \frac{x}{x+y}E(Zr)\right) \qquad \text{Equation 4}$$

Equation 4 [37] provides the formation energies of intermetallic phases where $E(Zr_xM_y)$ is the energy of a cell simulating the intermetallic and E(M) and E(Zr) being the single atom of the respective element.

It has been found that Fe, Ni and Sn intermetallics have negative enthalpies of formation which favour C15 $ZrFe_2$, ZrNi, and Zr_5Sn_4 through density functional theory simulations [37]. A similar method is hoped to be used in order to understand the potentials involved in the bulk material compared to that of the corrosion layers when different additives are added to the coolant.

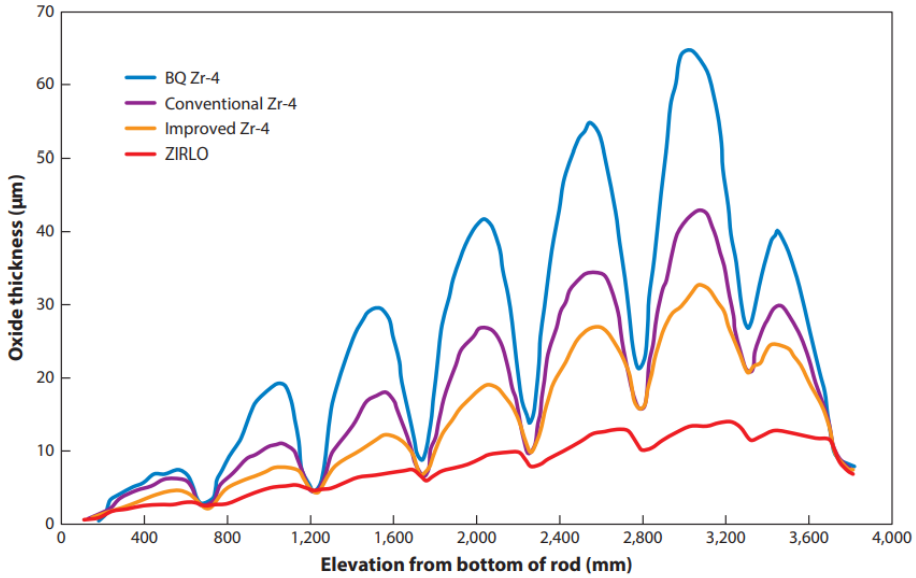

Figure 5 Axial variation of oxide thickness on zirconium alloy fuel rods. BQ Zr-4 is Zircaloy-4 that was processed with a beta quench near the final tube size, conventional Zr-4 is Zircaloy-4 with 1.5% Sn, and Improved Zr-4 is Zircaloy-4 with 1.3% Sn. Zero elevation is the lowest point in the fuel assembly, at which the colder cooling water first comes in [48].

Whilst normal oxide weight gain can be experimentally achieved in an autoclave, it is worth noting that a phenomenon occurs within reactor conditions that results in periodic oxide thickness differences along the fuel cladding. The periodic suppression of oxide thickness in Figure 5 are a result of cooler temperatures in these areas. This is due to an increase in turbulence as a result of spacers and lower reactivity due to parasitic thermal neutron absorption of the grid material [56].

The oxide that forms on Zircaloy at the metal oxide interface has also found body centre cubic (bcc), face centred cubic (fcc) and hexagonal closed packed (hcp) structures. Even ω-Zr sub-oxide phases have been found [51]. The oxide layer at the metal oxide interface, however, is the tetragonal phase zirconia and is usually several hundred nanometres thick. As mentioned, the growth continues with an increased distance from the metal-oxide layer, there is a reduction in compressive stress which allows the formation of the monoclinic phase [57]. This also allows crack formation from 3 µm thickness which reduces the ability of the oxide layer to protect and allow oxygen diffusion to the metal surface. There is evidence that suggests the partially protective oxide layer can prevent hydrogen pickup [58]. When hydrogen is able to diffuse into the material, it may collect, forming a pocket of hydrogen gas. This can pressurise and burst through the material weakening the local area. In addition to this, hydrogen can also cause embrittlement of the alloy reducing mechanical effectiveness.

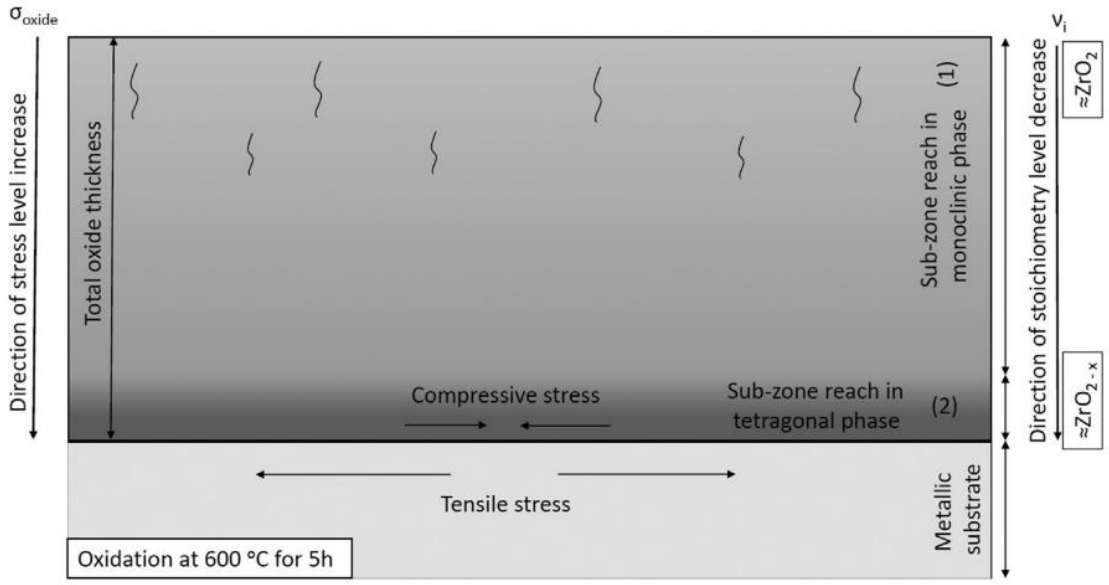

Figure 6 Metal Oxide layers with zone (1) representing monoclinic phase and (2) representing tetragonal phase. Visible cracks extend onto the oxide layer [57].

It is expected that there is a reduction in oxygen when approaching the metal oxide boundary and a higher oxygen content under an SEM would produce a brighter appearance [57]. This was also confirmed in literature as an energy dispersive x-ray spectroscopy scan (EDS). It was, however, noted from literature that EDS could only be used as an indication rather than quantifiable data. This was a result of the x-ray emissions increasing from the metal side as the current scan area approaches the boundary from the oxygen side.

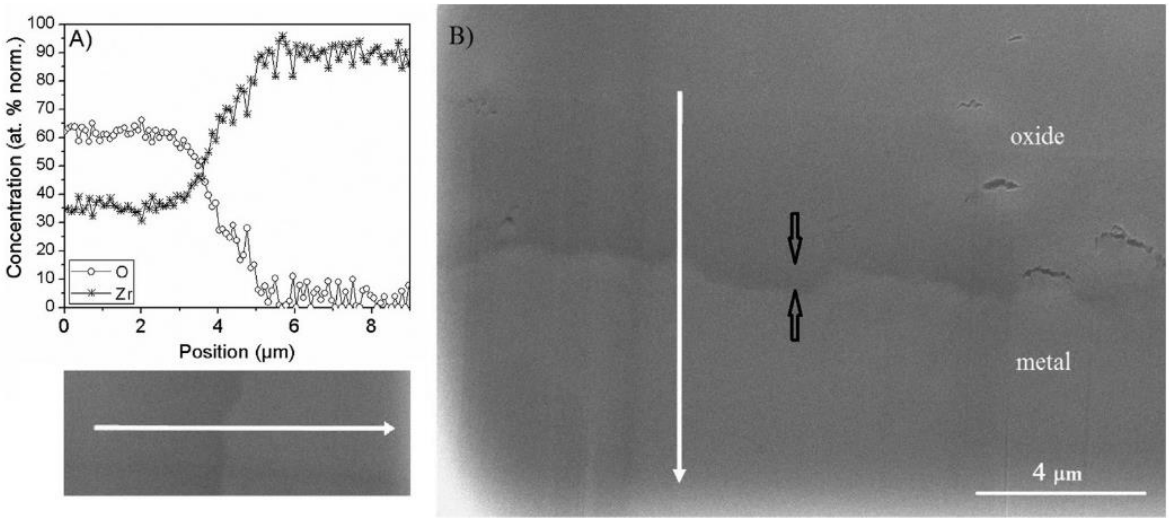

Figure 7 (A) EDS scan showing oxygen and zirconium concentrations at metal oxide boundary and (B) The same EDS scan across the metal oxide interface. The white arrows indicated the area scanned [57].

This was also confirmed using atom probe analysis with an indication of particular boundaries:

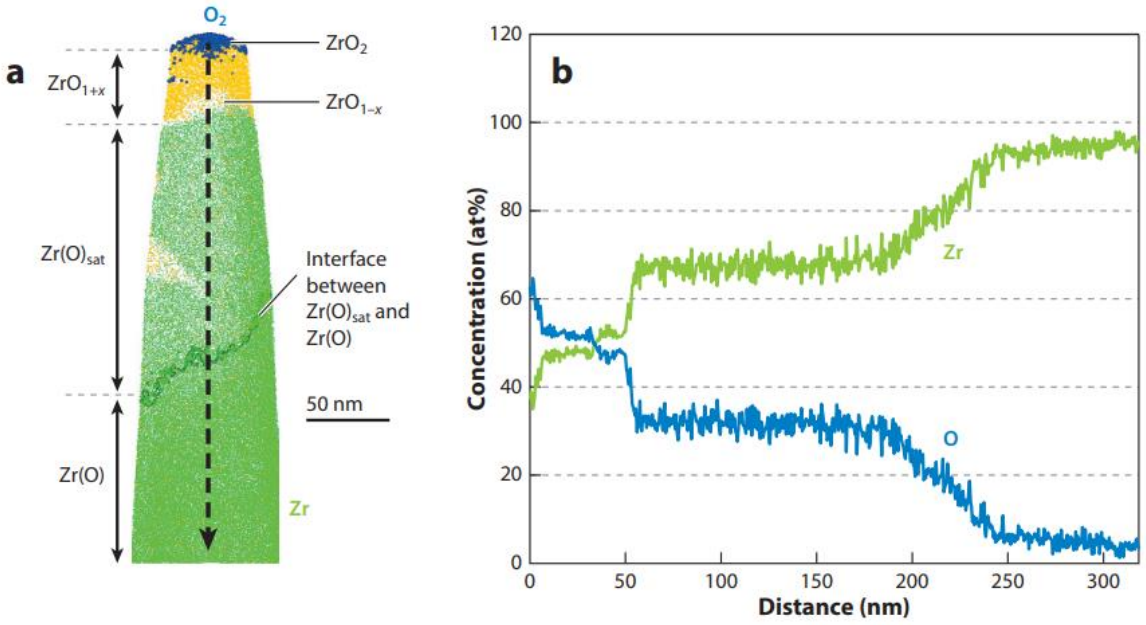

Figure 8 Atom probe analysis of the oxide/metal interface for Zircaloy-4 corrosion [48].

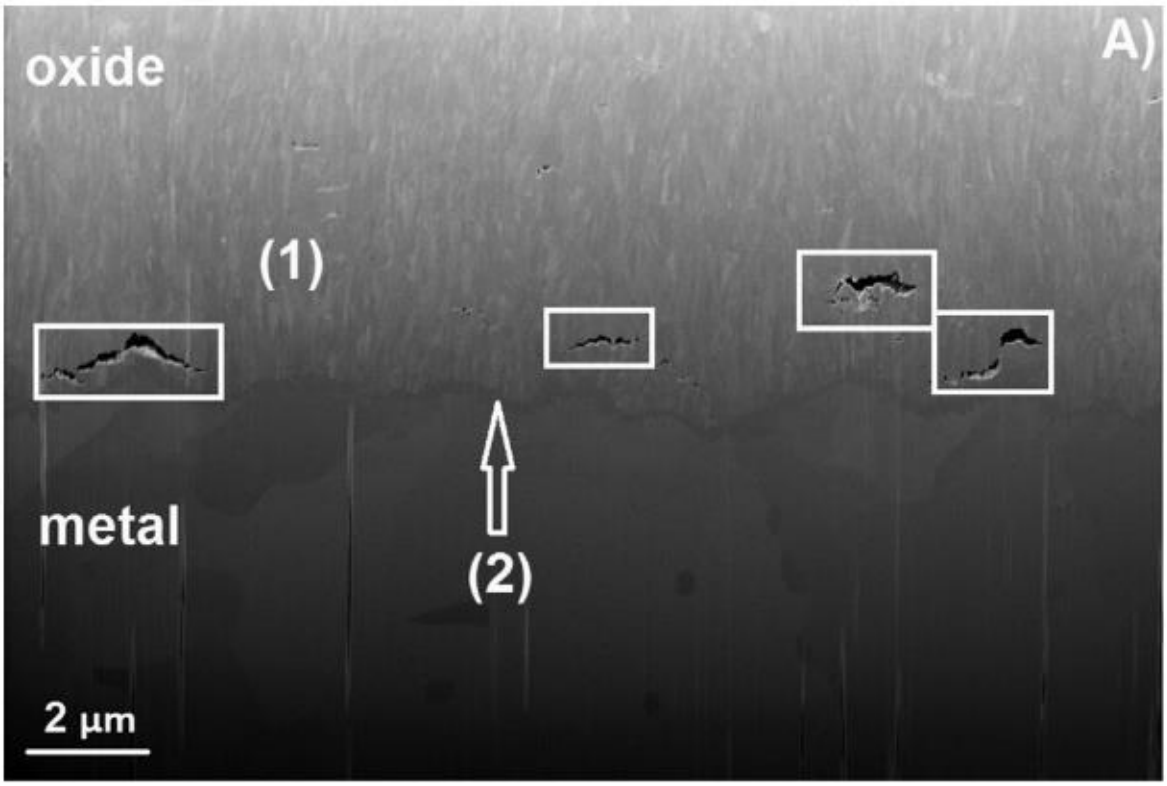

Figure 9 SEM of Zircaloy metal/oxide boundary. Darker tetragonal phase region (2) with monoclinic phase region (1) becoming brighter as a result of higher oxygen concentrations [57].

Where previous results showed that cracks would form perpendicular to the metal oxide layer, the above Figure 9shows cracks forming parallel to the metal oxide layer. The perpendicular cracks are thought to be a result of compressive stress at the tetragonal phase boundary which eventually gives way to cracks in higher layers in the monoclinic boundary during growth where the perpendicular

cracks have been attributed to equiaxed monoclinic zirconia grains [59]. It was also found, in reactor neutron irradiated samples of three cycles, the microstructures were also unstable where extra grain growth was observed as a result of electron beam microscopy [60]. In addition to this, samples taken where crystals were formed within a reactor show a larger proportion of nanocrystallised zones which do not hold a characteristic orientation, as shown in Figure 10.

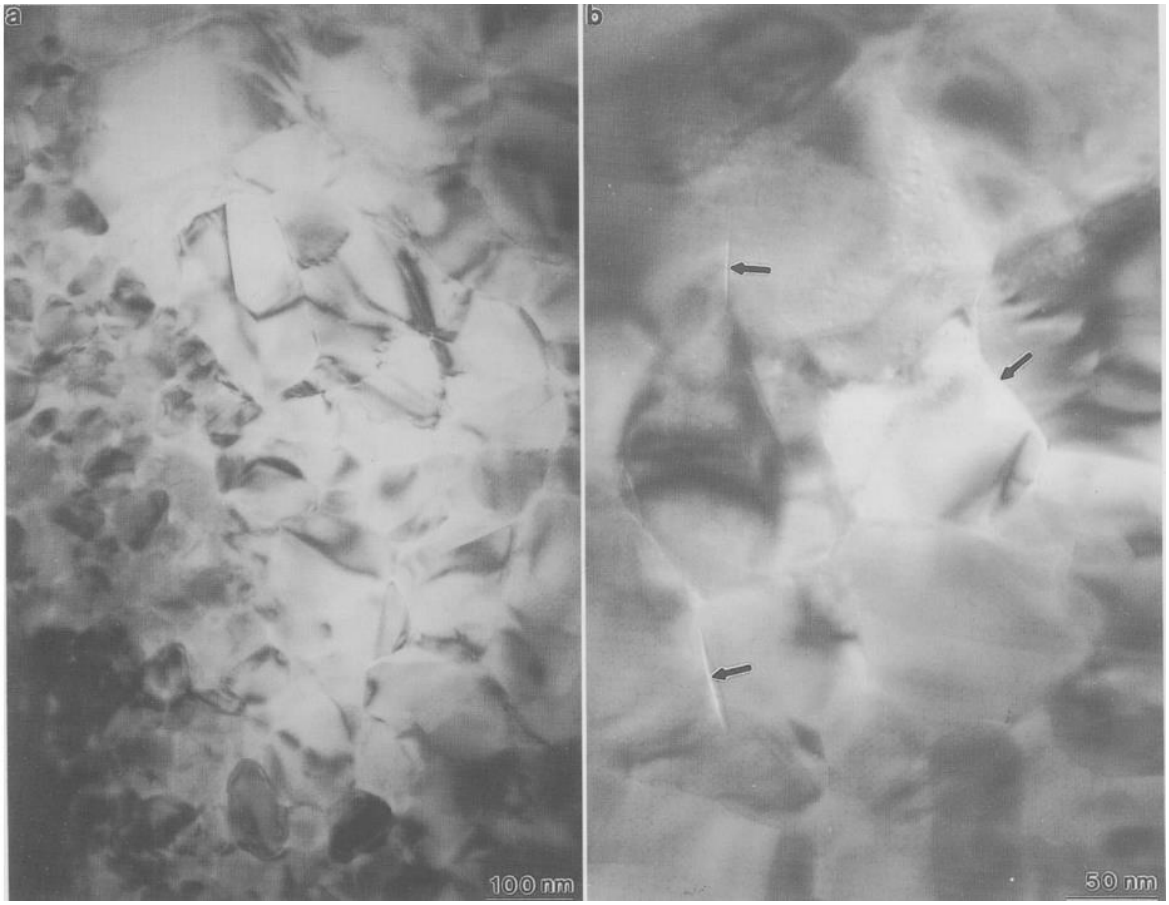

Figure 10 Equiaxed monoclinic oxide crystallisation microstructure a) General view, b) zoomed view showing intergranular decohesion (arrows) [60].

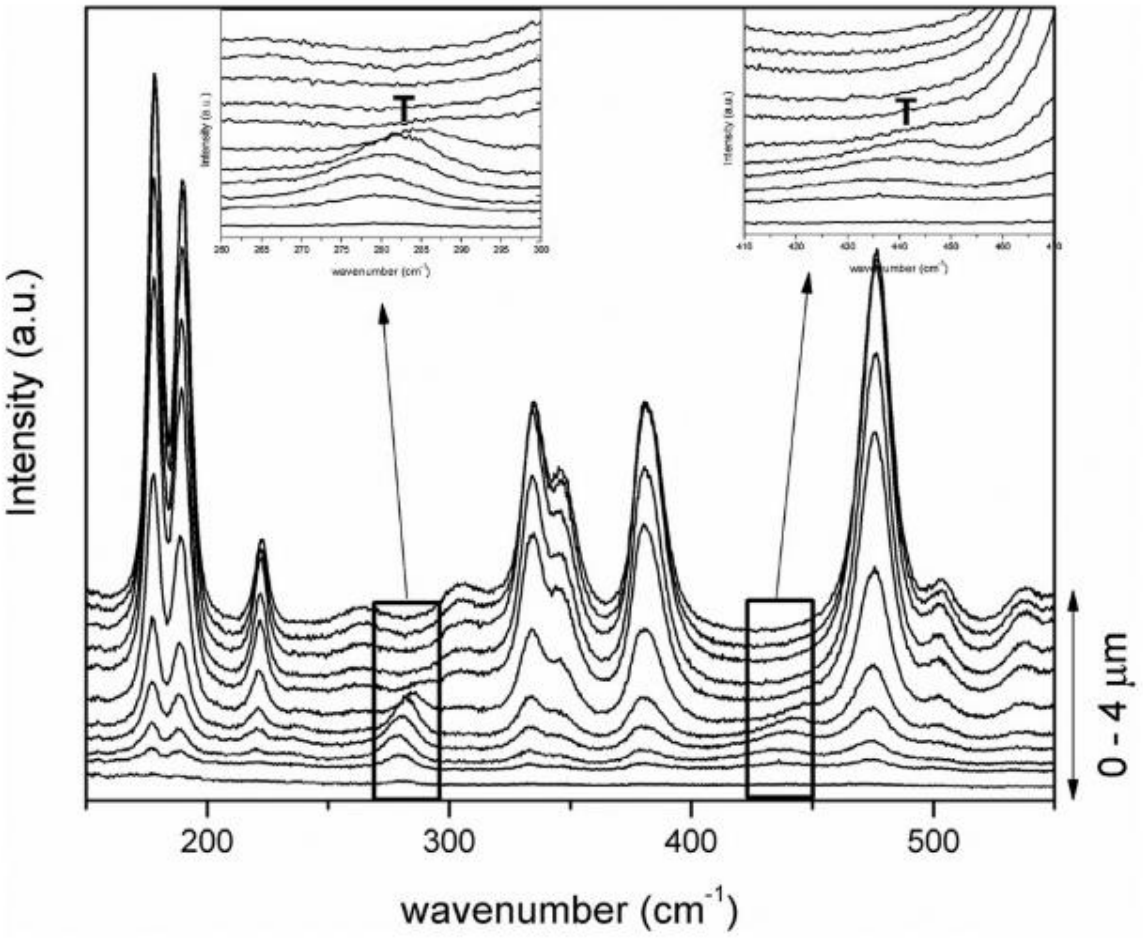

Figure 11 Raman spectroscopy of pure zirconium with zirconia cross section [57].

In the Raman spectroscopy from literature, Figure 11, tetragonal phases are evident at roughly 270 and 430 cm^{-1}. Rough confirmation of this can be found showing tetragonal phase peaks at 287 and 447 cm^{-1} and monoclinic peaks at 177 and 190 cm^{-1} [61]. The 17 cm^{-1} slight shift in peak value is common to all values so can be attributed to specific instrumentation used, laser parameters or oxide crystal purity where peak width would broaden. It was more likely to be a result of higher compressive stress in the sample area creating a higher frequency.

Strong evidence suggests that there is an increase in corrosion resistance of zirconium alloys where the second-phase particles are greater in size than a tenth of a micron [62] with minimal tin as to perform its function within the alloy [63,64].

In addition to oxidisation of zirconium alloys, it has also been found that PWR reactor grown oxide layers contained up to 1% iron rich areas [59]. Given that, in this case, Zircaloy-4 used contained roughly 0.2% Iron, this would indicate that there was a redistribution of Iron into specific areas, iron was obtained from another source through the coolant or that the distribution of iron through the original material was not uniform.

The initial partially protective tetragonal oxide layer has been found to grow in an orientation that favours a (001) orientation. This produces a minimal footprint on the metal interface and is likely driven by the compressive stress at the initial oxide/metal interface [54]. However, during higher

temperatures, the crystal growth of the monoclinic phase with less compressive stress produces a softening of the metal matrix [54].

Experimental data from literature was in agreement that oxidisation happens in all aqueous environments at medium to high temperatures (260 to 400 °C) [55,65]. Corrosion accelerants have been identified and higher temperatures are known to accelerate this further. However, the physical mechanics for the transport of oxygen to the metal surface have had many possible explanations which also conflict. D. J Park et al [47] provided three such proposed models. It was first thought that areas of lower intermetallic particle concentration enabled nodular oxide morphology. This allowed for greater proton migration and, hence, hydrogen pick-up. It was then thought that hydrogen build up occurred mostly at the metal oxide interface producing an eventual pressure that would break through the oxide layer allowing nodular corrosion at that site. The next proposed mechanism suggested that solute cations Fe^{2+}, Fe^{3+}, Cr^{3+} or Ni^{2+} could replace a Zr^{4+} site which could produce more oxygen vacancies in the ZrO_{2-x} lattice. This creates an area with a "nearly depleted solute element and a near-stoichiometric oxide layer" which is unstable in any kind of corrosive environment producing a porous oxide layer. This then allows the transport of hydrogen and also oxygen for further corrosion. This particular idea has further evidence where Zircaloy-4 was subjected to lithiated water acting as the alkaline, corrosive environment [55]. The final idea suggests that corrosion is the result of larger second-phase particles that are in contact with the metal surface. It may be possible that grain boundaries of the larger second-phase particles allow transport of hydrogen into the metal matrix. Again, this would allow for an accelerated oxide corrosion in the local area. However, there is also evidence that suggests corrosion is the cause of hydrogen pickup. A coupled current charge compensation model of corrosion kinetics has suggested that a reduction in electron transport causes hydrogen ingress in order to close the reaction [48]. This is a large area of debate between researchers as evidence can indicate particular kinetics of oxidation by interpretation but do not definitively cover all examples [66].

Another structure to consider is the grain boundaries which can be considered as complex structures of the amorphous polymorph [3,4]. Figure 12 shows possible complexions of polycrystalline Ni ranging from low complexion (A) to higher complexion (C).

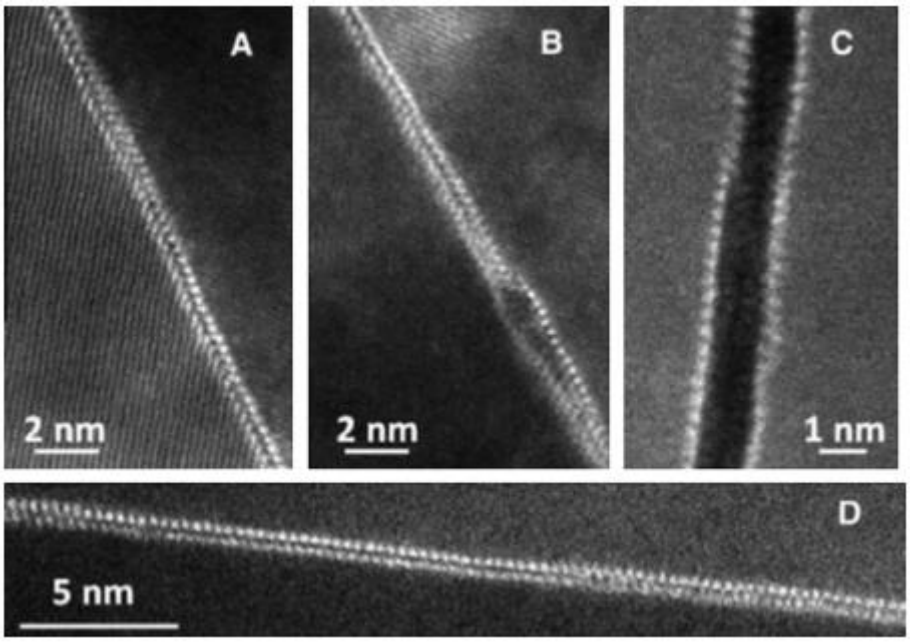

Figure 12 Bilayer complexion of general grain boundaries in polycrystalline Ni [3].

The amorphous grain boundary phase can produce under-coordinated and over-coordinated structures which represent an increase or decrease of intrinsic defects. They can also be regions in which extrinsic defects may segregate outside of the bulk material [67].

For the case of second phase precipitates, they are often crystals comprising of a number of elements as shown in Figure 13. The figure shows a particular precipitate which has been colourised to highlight the different phases. The precipitate is located at the metal/oxide interface with the primary dark blue background as the oxide layer and the lower pink shows the metal Zircaloy interface. The colours within the precipitate are red for Iron and green for chromium. It is also noteworthy that the precipitate itself oxidises which is highlighted in Figure 13 at the upper most tip where the chromium has high oxygen levels.

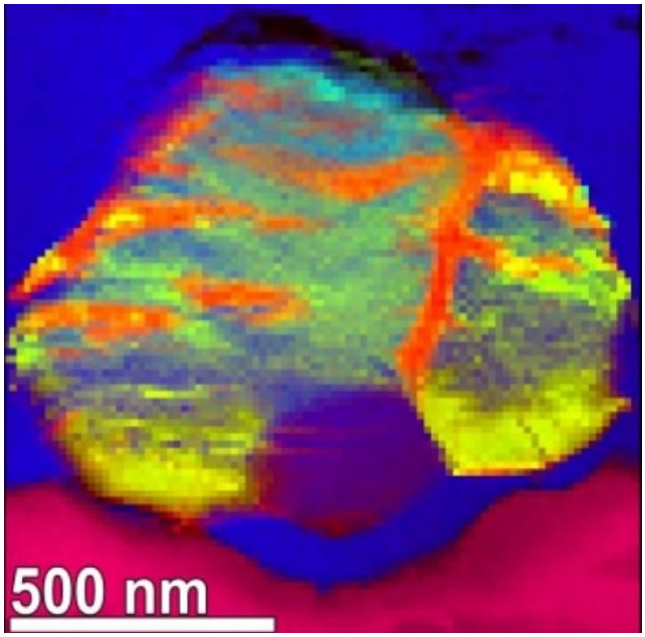

Figure 13 Scanning transmission electron microscope image with dual electron energy loss spectroscopy RGB composite of a second phase precipitate at Zircaloy metal/oxide interface. Pink = Zr, blue = O, red = Fe and green = Cr [39].

In Figure 13, K. Annand *et al* showed that diffraction patterns provide evidence for a possible pseudocubic structures that did not fit the known tetragonal ZrO_2 or Fe_2O_3 structures with a lattice parameter at roughly 4.7 Å. The work also does indicate that the second phase precipitates corrode in a manner where iron seems to be segregated into veins within regions that are yet to be oxidised where the rest of the precipitate is mixed chromium and zirconium oxides. Furthermore, it was found that around Zr_2Fe precipitates, cracking occurred perpendicular to the metal oxide interface to the sides of the precipitate but, in contrast, $Zr(Fe, Cr)_2$ precipitates showed cracks parallel to the metal/oxide to the above the precipitate and occasionally beneath [39]. This may be the result of the Pilling Bedworth ratio which can be seen as pressure as a result of lattice volume differences between phases. We will touch upon the Pilling Bedworth ratio in more detail in the next section.

1.2.6. The Pilling Bedworth Ratio

The Pilling Bedworth ratio is generally used for oxide layers at the metal/oxide interface and is used to describe the volume difference of unit cell between the metal crystal and the oxide crystal. As well as weight gained by the addition of oxygen, the unit cell also changes in volume resulting in reduced volume or increased volume. Where the volume is reduced, the ratio is below 1 which would form gaps between crystal boundaries. This offers poor protection and an increased rate of oxidisation. Where the ratio is between 1 and 2, the oxide layer volume is slightly greater than the

metal which results in compressive stress of the oxide and tensile stress to the metal. However, providing the higher ratio of 2 is not passed, this produces a partially protective layer preventing oxygen or hydrogen transportation to the metal surface as seen with stainless steel and Zircaloy. Should the volume ratio be greater than 2, the compressive stress becomes too much for the oxide to remain uniformly on the metal surface producing dislocations and overlapping which offers little protection as shown on Figure 14.

Figure 14 Visualisation of the Pilling Bedworth ratio. To the left, a ratio less than one. The middle is between 1 and 2 and the right has a ratio greater than 2 [2].

The pilling Bedworth ratio of Zr to ZrO_2 is 1.56 which is adequate to hold continuous coverage but would cause some compressive stress [68]. It has been found that 1 µm of zirconium alloy produces 1.56 µm thickness of zirconia (Zirconium dioxide)[48] but has also been found to be as low as 1.48 with a value of 1.51 based on lattice parameters [39]. In contrast, Zr_2Fe fully oxidised has a value of 1.67 which could be the mechanism for crack formation. The difference between the ZrO_2 and fully oxidised Zr_2Fe produces a compressive stress of the Zr_2Fe and tensile stress of the ZrO_2. This strain is along the growth direction of the crystal which results in cracks parallel to the metal oxide interface as mentioned before. For a fully oxidised mixture of monoclinic ZrO_2, Cr_2O_3 and α-Fe_2O_3, these have a Pilling-Bedworth ratio of 1.89 [39]. However, as noted and shown in Figure 13 the iron is often oxidised in veins within the precipitates which reduces the ratio. This is further reduced by the addition of $ZrCr_2$ which has a ratio of 1.78. A combination of these reductions provides an actual ratio of about 1.53 [39] which can be comparable to the surrounding oxide matrix of 1.51. This does not account for un-oxidised chromium within the precipitate which could lead to a lower ratio producing smaller cracks parallel to the metal/oxide interface above the precipitate and occasionally below. This could explain why a higher iron ratio to chromium results in increased crack formation. It is worth noting that the tetragonal ZrO_2 has been categorised as “partially protective” throughout this document. This is, predominantly due to the pilling Bedworth ratio of the oxide layer to the metal. There are, however, reasons to believe that this is not the case. The main reason for this is that the Zircaloy product ZIRLO produces a distinctively thin tetragonal zirconium oxide layer and exhibits prolonged resistance to corrosion over other Zircaloys [50]. This indicates that lattice matching between the metal and oxide layers may not be as pivotal in corrosion prevention as previously thought. Understandably, the oxide development of zirconium alloys has been of high interest for many years and has been extensively investigated [69–83]. But little is known about the mechanisms behind lithium accelerated corrosion.

1.2.7. Lithium Accelerated Corrosion

In the case of stainless steels, experimental evidence supports that oxide corrosion can be reduced when subject to lithiated water [52]. It is thought, in stainless steels, that lithium has a higher potential to form a bond with oxygen resulting in a lack of oxygen available to form oxide layers at the metal oxide interface[24].

Tests have been conducted using borated (H_3BO_3) and lithiated ($LiOH{\cdot}H_20$) water at high temperatures to find the levels of corrosion by oxidisation on stainless steel [84]. These showed that a higher level (ppm) of lithium within solution at 300°C (573.15 K) produced a higher pH level by calculation, which is to be expected. In PWR reactors, current levels of H_3BO_3 are 900 – 1800 ppm (by weight) with LiOH being 2 – 5 ppm lithium to bring the pH range between 6.9 and 7.4 at high

temperatures [85]. Whilst this solves an acidic corrosion problem, it also brings an additional problem of higher radiation dose rates and crud. To address this, zinc is added to the coolant [85]. These previous works focus mainly on the stainless-steel corrosion levels but do investigate the possible oxide solubility levels that could prevent the corrosion and oxide build up on the fuel cladding materials. The results from both papers showed some promise on pH levels by varying just the lithium levels for the former or both the boron and lithium levels with Zn included with the later shown in Table 5 Compositions of testing coolant solutions (ppm, by weight). Zinc NOT included [84][84] Table 5 and Table 6:

Table 5 Compositions of testing coolant solutions (ppm, by weight). Zinc NOT included [84].

B as H_3BO_3 (ppm in H_2O)	Li as $LiOH{\cdot}H_2O$ (ppm in H_2O)	pH at 573.15 k
1500	2.2	6.8
1500	23	7.7
1500	230	8.6
1500	690	9.1

Table 6 Compositions of testing coolant solutions (ppm, by weight). Zinc included as ZnO at 10 ppb [85].

B as H_3BO_3 (ppm in H_2O)	Li as $LiOH{\cdot}H_2O$ (ppm in H_2O)	pH at 573.15 k
1500	2.3	6.9
1200	3.6	7.1
900	5.0	7.4

In comparison, a large increase in lithium is required in order to make small changes in pH where the boron level is kept constant where zinc is not used, but small changes in lithium where boron levels are reduced have a similar trend where zinc is included. Though, because the presented results do not include the data of solutions without zinc in the later paper (Table 6), it is difficult to make an absolute comparison. It was later remarked that zinc should be tested in actual PWR reactors indicating a particular success [85]. In addition, an increased pH showed an increase in iron corrosion but a reduction in chromium corrosion. It was further noted that there was a distinct reduction of stainless-steel corrosion resulting from solutions where zinc was introduced. There are, however, potential issues that may become present when using lithium.

Turning the attention to Zircaloy cladding, as already discussed, lithium has been found to accelerate corrosion. There are a number of papers that have experimental data to confirm this, but the mechanisms were elusive with hypotheses including substitutional lithium in zirconia sites increased anion vacancies, formation of Li_2O in oxide films produced pores in the cubic ZrO_2 allowing further corrosion and, finally, LiOH alters the corrosion crystal growth producing crystals with a reduced volume [26,86,87]. Figure 15 provides some experimental data highlighting the level of lithium within a sample after a set time within an autoclave [24]. The recommended lithium content for 12-month cycles is 2.2 ppm and for 18 months 3.5 ppm according to the paper. For this experiment, the lithium content is set to 1.5 ppm for the lower scale and 70 ppm to highlight any difference at much higher levels of lithium. From Figure 15, it is easy to see that at lower lithium levels, after the suggested barrier layer, there is an almost uniform level of lithium within the oxide layer even after 360 days. However, with 70 ppm, there was a significant increase in lithium concentration after 50 days which remained consistent up to 150 days before another significant increase up to 204 days within the autoclave.

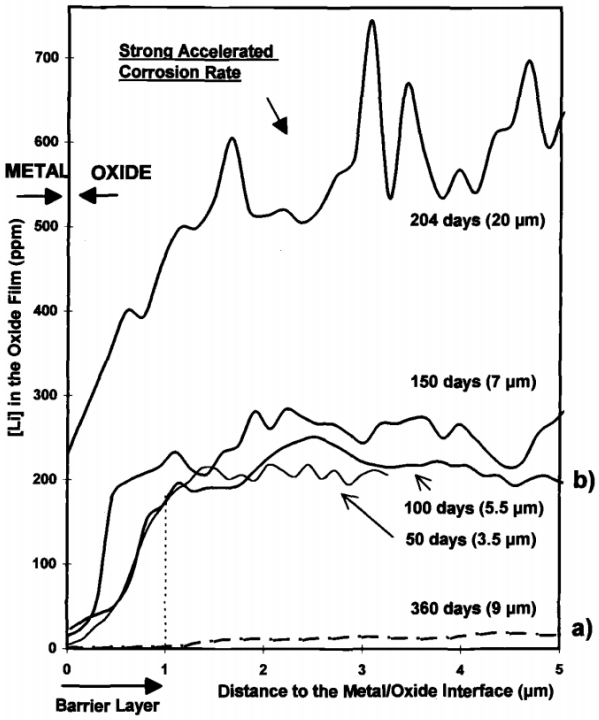

Figure 15 Lithium (ppm) in oxide layer from metal surface. a) (Bottom dashed line with no accelerated corrosion after 360 days in the autoclave.) is 1.5 ppm Li and 650 ppm B. b) (Solid lines with a range of days in autoclave with strong accelerated corrosion at 204 days) is 70 ppm Li and 0 B using secondary ion mass spectrometry [24].

A continuation of the same experiment at 70 ppm lithium [88], it was found that the oxide grains that formed prior to strong lithiated accelerated corrosion were columnar oxide grains. After accelerated corrosion, smaller equiaxed grains were produced with open grain boundaries which had the potential to create porous pathways to further accelerate corrosion as seen in Figure 16.

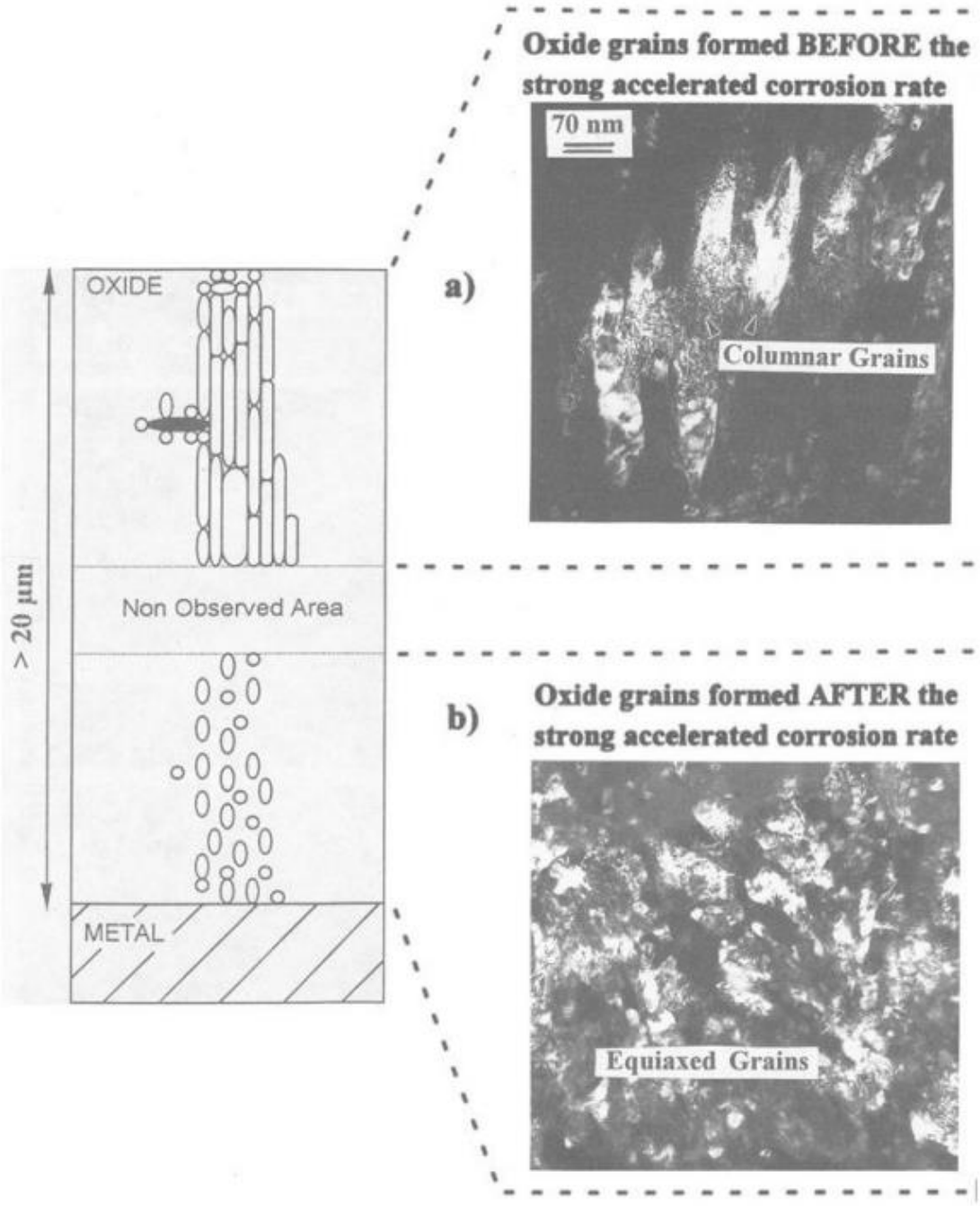

Figure 16 Zirconium oxide before and after strong lithiated accelerated corrosion [88].

It was also noted that there was evidence to suggest that where potassium was used, in place of lithium, there was no evidence of accelerated corrosion [88]. The summary suggests that the partially protective oxide layer had a reduction in depth, even in areas where lithium has not penetrated. It was thought that this may be a result of enhanced oxide production due to lithiated accelerated corrosion at higher oxide layers which allow this increased production but required further investigation. Subsequent experimentation has shown that an increase in boron within the water reduces the effect of lithiated corrosion and, more to the current subject, that the accelerated oxidisation as a result of lithiated corrosion does reduce the depth of partially protective oxide layer [26]. In relation to the reduced effect of lithiated accelerated corrosion, the evidence shows that 10 ppm and 70 ppm lithium within the coolant chemistry has a similar oxide growth rate as that with no lithium introduced to the system at all where 650 ppm B is added as shown in Figure 17. However,

this would come at a cost where an increase in boron within the coolant will reduce the number of reaction events within the reactor and, in turn, reduce the overall efficiency and output. However, with levels experimented being only 650 ppm and current guidelines suggest 1000 ppm, this is well within guidelines.

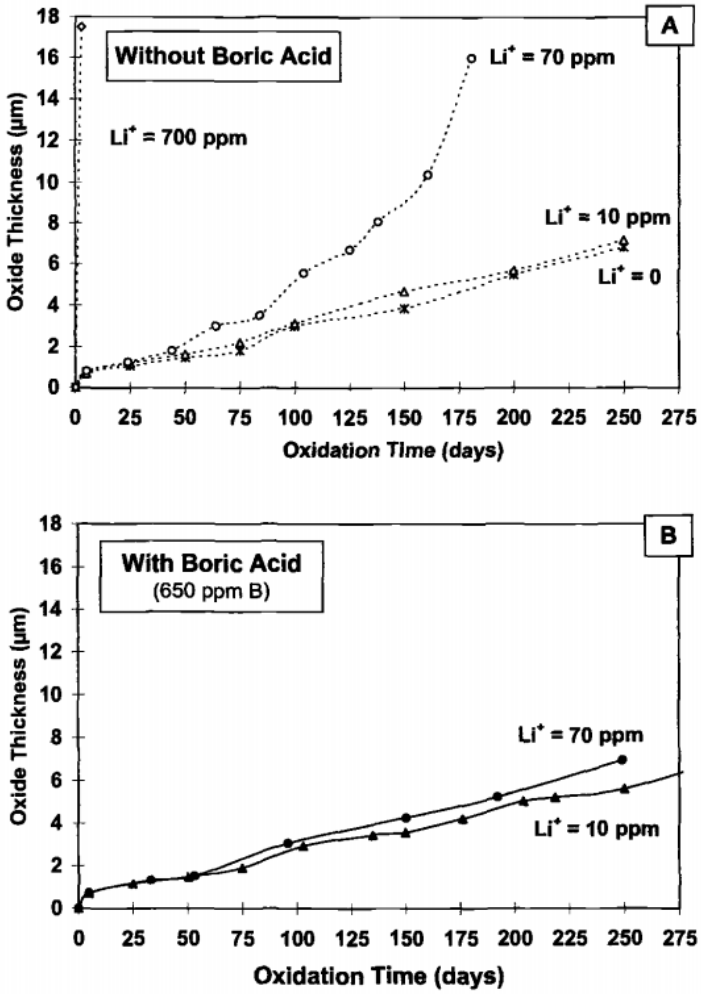

Figure 17 Corrosion oxide depth with A) no boron additive and B) 650 ppm boron within the water chemistry [26].

In addition to the experimental data obtained in relation to lithiated accelerated corrosion, LiOH can produce axial offset anomalies (AOA). Boron within the water accumulates in parts of the reactor with higher boiling areas (sub-cooled nucleate boiling) which can then combine to form Lithium Borate ($LiBO_2$) within the crud layer [89]. Lithium borate absorbs neutrons generating a loss in fission events at the top of the reactor, reducing power. In 2001, 20 US reactors were known to have issues that were related to AOAs. One of which even reduced power output to 70% for several months [90]. Previous work investigated potassium in favour of lithium for, apparently, this very reason [89]. However, it is important to note that should boron still be used within the reactor, it can still produce lithium as a neutron reaction [91]:

$$^{10}B\ (n) \rightarrow {}^{7}Li\ (\alpha) \qquad \text{Equation 5}$$

Alternative additives have also been the subject of experimentation such as ammonium hydroxide (NH_4OH) [55], sodium hydroxide (NaOH) [92] and, as mentioned, potassium hydroxide (KOH). However, where second phase precipitates are taken into account, it has been found that in high temperature lithiated water, the second phase precipitate does not begin to corrode until 300 nm

from the metal surface along with the ZrO_2 where it was suggested that iron precipitates stabilise the tetragonal ZrO_2 [39]. Whilst the evidence suggests that the tetragonal structure is partially protective, at best, if the tetragonal structure is protective, a change in alkaline additive whilst maintaining boron within the coolant chemistry might aid corrosion rather than prevent it.

Simulations for the oxidisation process in lithiated water have been conducted and show that a higher lithium concentration does increase the rate of corrosion of Zircaloy and is known as lithium-accelerated corrosion [1]. This has also been confirmed experimentally [55]. Through simulation, within the oxide layer, lithium becomes a positively charged interstitial defect which increases the level of free electrons, negatively charged oxygen interstitials and zirconium vacancies [2]. The lithium interstitials and zirconium vacancies reduce the volume of tetragonal ZrO_2 which reduces compression stress and, so too, the Pilling Bedworth ratio which promotes the tetragonal oxides transformation to monoclinic [2]. Through simulation, the mechanism of volume reduction is that the positive lithium interstitial resides within the O-O bonds sharing the surrounding electrons of the oxygen. This reduced the ionicity and, in doing so, reduced the repulsion between the oxygen. This had been suggested to produces a 3.2% volume reduction in monoclinic ZrO_2 and a 4.8% volume reduction in tetragonal ZrO_2 [1].

The energy volume (E-V) profile can be fitted using the Birch-Murnaghan equation of state [1]:

$$E(V) = E_0 + \frac{9V_0B_0}{16}\left\{\left[\left(\frac{V_0}{V}\right)^{\frac{2}{3}} - 1\right]^3 B_0' + \left[\left(\frac{V_0}{V}\right)^{\frac{2}{3}} - 1\right]^2 \left[6 - 4\left(\frac{V_0}{V}\right)^{\frac{2}{3}}\right]\right\} \quad \text{Equation 6}$$

Where V_0 = the equilibrium volume, E_0 = equilibrium energy, B_0 = the bulk modulus and B_0' = the isothermal derivative with respect to pressure. And in addition to this, the stress-volume (P-V) relationship:

$$P(V) = \frac{3B_0}{2}\left[\left(\frac{V_0}{V}\right)^{\frac{7}{3}} - \left(\frac{V_0}{V}\right)^{\frac{5}{3}}\right]\left\{1 + \frac{3}{4}(B_0' - 4)\left[\left(\frac{V_0}{V}\right)^{\frac{2}{3}} - 1\right]\right\} \quad \text{Equation 7}$$

This gives the enthalpy-stress relationship by calculating $H = E + PV$ (where H is the enthalpy and E is the internal energy) at constant pressure (P) [1]. This paper and an additional follow up paper have used the electron shell structure $2s^2 2p^4$ for oxygen and $4s^2 4p^6 4d^2 5s^2$ for zirconium [1,93] and have made the zirconium vacancy quadruple negative charged: V_{Zr}'''' and the oxygen interstitial double negative charged: O_i''. The Lithium is a positively charged interstitial: $Li_i^{\bullet}$

Other metals were used as a pH buffer moving down group 1 of the periodic table. Over a 300-day time period, the corrosion weight gain for lithium was found to be 2500 mg/dm^2 where the other metals were all less than 200 mg/dm^2 [2]. The materials considered were LiOH (Lithium hydroxide), NaOH (Sodium hydroxide), KOH (Potassium hydroxide), RbOH (Rubidium hydroxide), and CsOH (Caesium hydroxide). Yang et al. considered this to be the result of the ionic radius of the element as an interstitial defect within the ZrO_2. The ionic radius of Zr^{4+} is 72 pm and in order of size, Li^+ = 76 pm, Na^+ = 102 pm, K^+ = 151 pm, Rb^+ = 161 pm and Cs^+ = 174 pm. This made the other alkaline metals less likely to be situated in an interstitial site and, in addition, the other metals increased the volume of the tetragonal ZrO_2 which prevents pores from forming as they do with lithium.

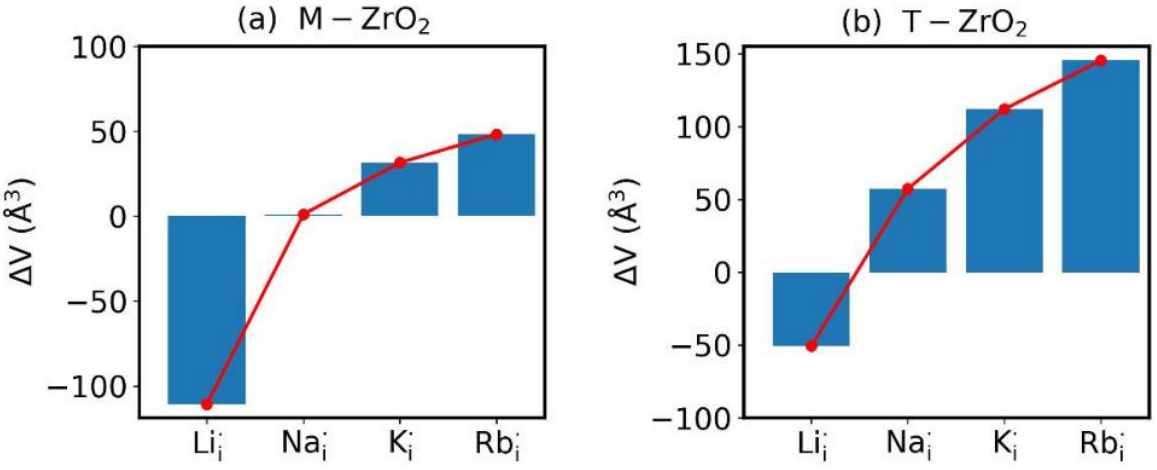

Figure 18 Volume change in ZrO_2 with interstitial alkaline material in a) monoclinic and b) tetragonal ZrO_2 [1].

There is also a possible mechanism that may aid the lithiated accelerated corrosion within a nuclear reactor. Under high energy radiation, it has been found that atomic displacements are quite common in zirconium [94]. Namely, Frenkel pairs, where an atom is forced out of its normal lattice location and placed elsewhere as an interstitial. This produces a vacant site that may allow substitution. For example, should a zirconium atom become displaced, this opens a vacant site for a lithium atom. The reduction in repulsion of the surrounding oxygen atoms will reduce the volume of the lattice at the site. The volumetric simulations produced by Yang et al., however, have not identified the plausibility through solution energies that would need to be calculated in order for such an interstitial or substitution to be a viable prospect in the bulk ZrO_2 structures. Though, it is an area where further investigation would need to take place and forms the basis for the first hypothesis. Could the accommodation of lithium into the bulk oxide produce a volume change that would reduce the volume of the crystals and promote pore growth allowing oxygen to ingress into the metal?

To investigate the solution of lithium into the bulk oxide further, the phase diagrams for LiZrO do follow similar trends in publications where physical experimentation and calculation are used:

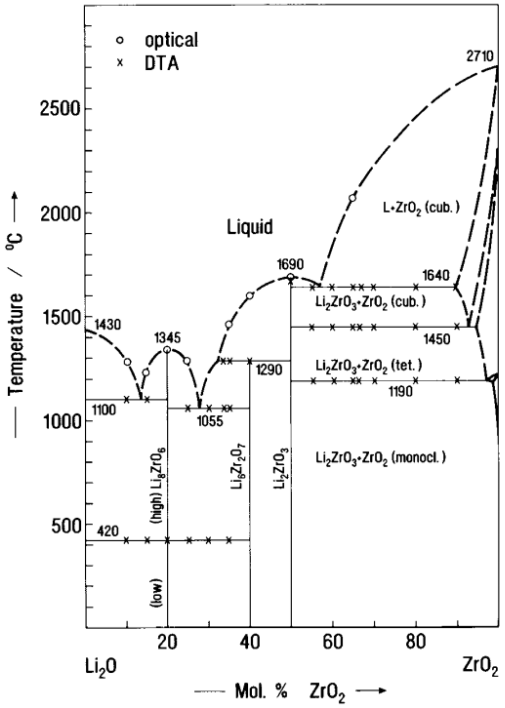

Figure 19 Li_2O-ZrO_2 Phase diagram from 1991 [95].

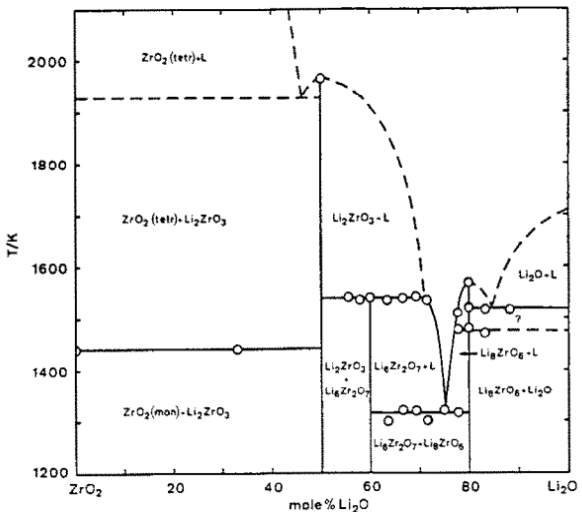

Figure 20 Li_2O-ZrO_2 Phase diagram from 1989 [96].

As seen in Figure 19 and Figure 20, most phase diagrams do not show a solid solution of lithium into the bulk ZrO_2. There are, however, exceptions.

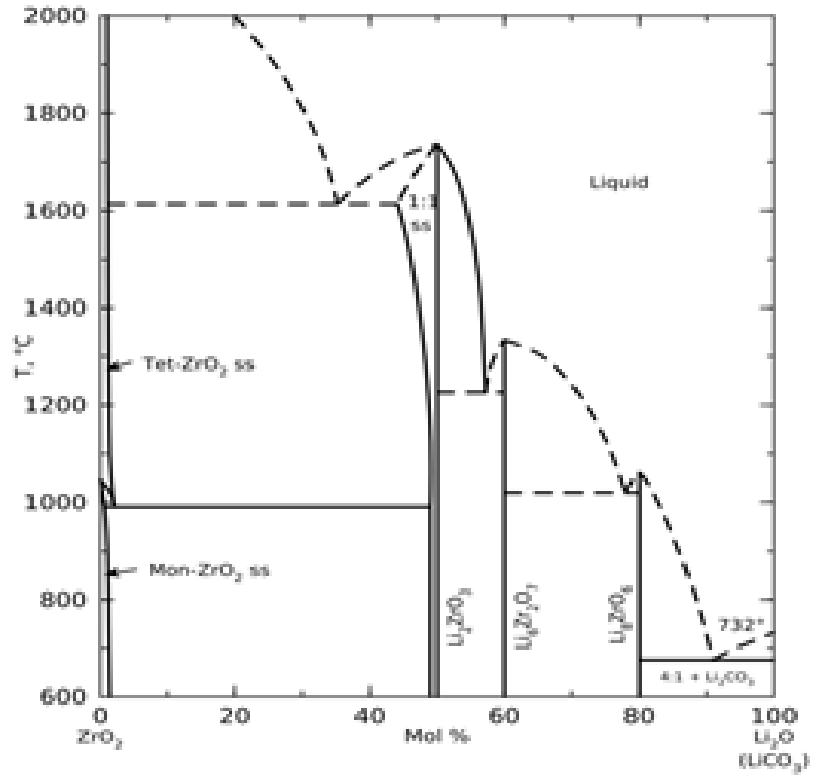

Figure 21 Phase diagram of ZrO_2 and Li_2O (with Li_2CO_3) showing a small amount of Li solid solution to the far left from 1981 [97].

Figure 21 shows a possibility for lithium to form solid solution into both monoclinic and tetragonal ZrO_2. This marked a position in which to begin the investigation.

1.2.8. Literature hypotheses for Lithium Accelerated Corrosion to Guide a Plan

Through the literature review, there were two main areas in which to investigate. The most basic start would be to look at the bulk material. This is because it had the most historically well-defined structures for simulation and would be the most productive start to the investigation. It could answer the question, does lithium accommodation in the bulk material reduce the volume of the oxide crystal and promote pores along grain boundaries as a result?

The second hypothesis would require additional steps to produce a close to true amorphous structure through simulation and enable that structure to be calculated through density functional theory simulations. This hypothesis would investigate the possibility of lithium forming solution along complex grain boundaries causing a change in oxygen diffusion which could provide a highway for oxygen to the metal oxide interface that was identified by Megan Owen *et al.* [27]. As mentioned, grain boundaries can range between little thickness and disorder to disordered amorphous structures that may provide a location for defect segregation.

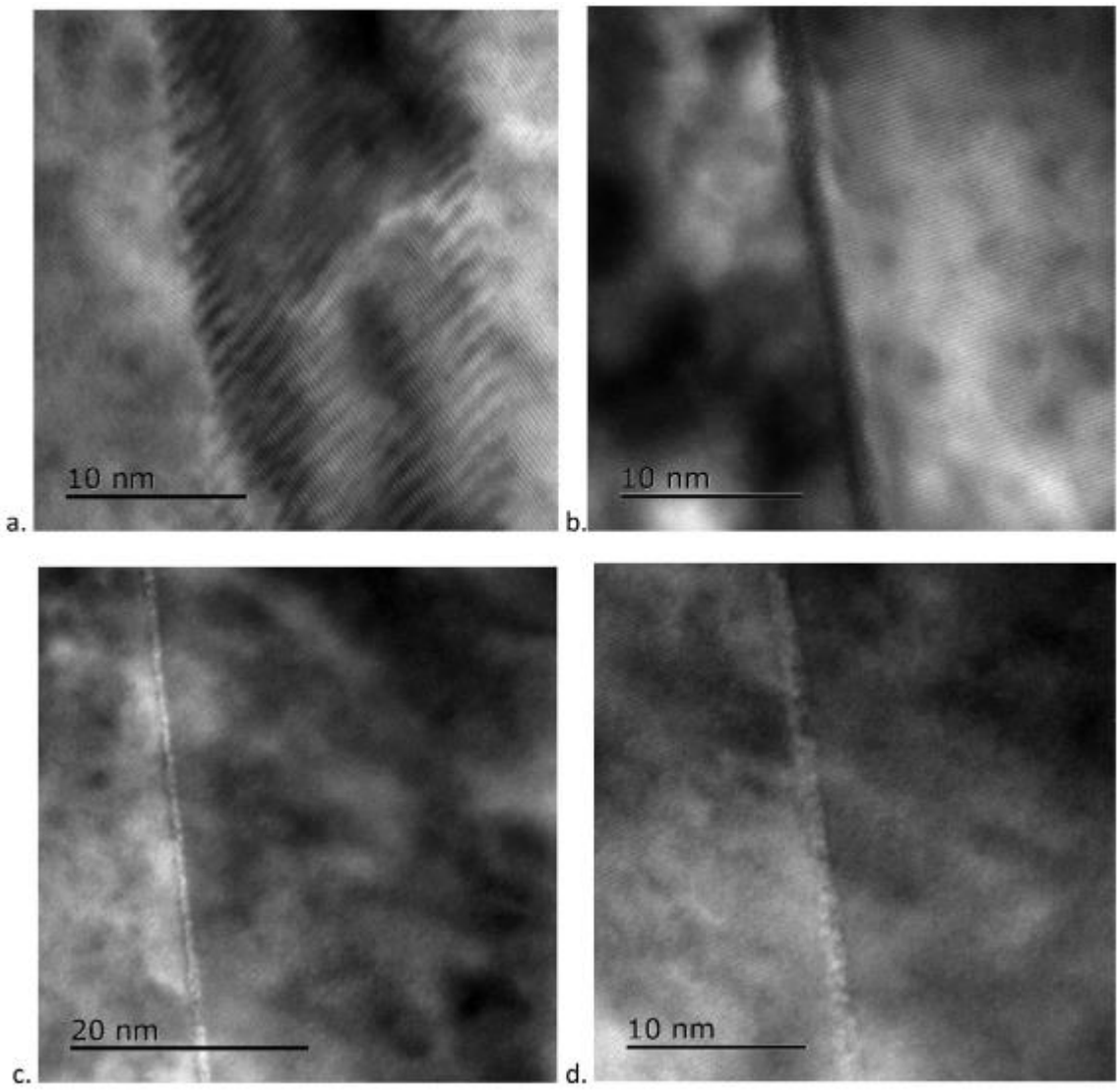

Figure 22 High resolution microscopy of undoped UO_2 (a and b) with thin and ordered grain boundaries and (c and d) at the bottom which show disordered grain boundaries with greater thickness [98].

In Figure 22, a and b show well defined grain boundaries with little disorder or thickness and more complex grain boundaries with greater thickness in c and d.

Once the possible solution of lithium, either within the grains themselves or the grain boundaries could be identified, this could then be used to experimentally verify the results for validation.

2. Methodology

When attempting to identify potential routes to investigate a particular problem, it is often quicker and cheaper to conduct simulations to gain an idea of plausibility for a hypothesis before moving on to experimental verification of the results. The simulation method selected is dependent on the scale in which the investigation is to take place. At the very small atomistic scale, first principal calculations may be conducted in the Å scale. This would be used to identify possible point defects that may be found within a structure. From there, molecular dynamics can be used which operates in the nm scale. As the name suggests, molecular dynamics identifies the molecular and atomic positions over time with a particular input criterion. Moving further up the scale, there are many methods which can be utilised such as kinetic Monte-Carlo or cluster dynamics. Given that our main objective is to identify the solubility of lithium into zirconia, first principle (Ab-initio) and molecular dynamics should be sufficient to identify the point defects and small defect clusters that may be expected.

2.1. Atomistic Crystal and Amorphous Structure Modelling of Li doped ZrO_2

The crystal structures under investigation are the monoclinic and tetragonal phases of zirconia. Both of these structures are readily available in the Physical Sciences Data Science Service Inorganic Crystal Structure Database (ICSD) [99–102]. From this database, the monoclinic [103] and tetragonal [104] structures were used. From here, defects could be added to both structures and analysed using ab-initio simulation software.

The amorphous structure, however, was not readily available and needed to be produced using molecular dynamics. By melting a larger structure and rapidly quenching it, this could produce a good amorphous representation. The resulting structure, however, was much too large to analyse point defects through ab-initio software and needed to be reduced. For this, reverse Monte-Carlo was used to maintain radial distributions of the amorphous structure atoms whilst minimising the structure size to one that could then be used in the ab-initio software, much as was the case with the crystal, bulk, structures. Due to more steps being involved in creating the amorphous structure, and that the methods both eventually converged, the order in methodology will be of the amorphous structure simulations.

2.1.1. Molecular Dynamics

LAMMPS is the Large-scale atomic/molecular massively parallel simulator which uses potentials to gain a large-scale simulation of molecular dynamics [105]. LAMMPS has the ability to model solid, liquid and gaseous materials and the transitions for metals, ceramics and oxides, amongst many others. LAMMPS uses the Newtonian equations for motion and can use pairwise potentials to obtain the optimal atomic separation.

$$F = ma \qquad \text{Equation 8}$$

Equation 8 shows Newton's second law of motion which states that the force of on object, *F*, is equal to the mass, *m*, times by acceleration, *a*.

$$\vec{F} = -\vec{\nabla}U \qquad \text{Equation 9}$$

Equation 9 shows the vector for Newton's second law where *U* is the potential of the object and $\vec{\nabla}$ is the gradient, with respect to the vector, [109]

When the pairwise potentials are applied to the objects, whether atomic or molecular, with the relative coordinates, the objects are relaxed into favourable locations with respect to each other in the surrounding area. By increasing pressure/temperature on the structure, this can result in altered separation between objects. This is a very simplified representation of how LAMMPS works, as the potentials used require a great deal of derivation from electron density to many-body effects including angular terms and screening effects between atoms. The used potentials usually have an empirical basis and are specific to the atoms/molecules being calculated. For example, in the structure calculated in this work, the potentials were developed for fluorite structured actinide oxides [106,107].

To create the amorphous structure a method previously used in the literature by Megan Owen et al. was followed [27]. A 6144 atom supercell was used containing 2048 formula units of cubic ZrO_2. This was heated at 10 K/ps to 5000 K from 300 K to allow the structure to become entirely molten and amorphous using the NPT isothermal-isobaric thermodynamic ensemble which used the Nosé-Hoover thermostat and barostat [108]. This was then rapidly cooled back to 300 K at 2.35 K/ps and then further relaxed for 1000 ps at 300 K. This ensured that the amorphous structure would be maintained. The atomic interaction potential model used was the Cooper-Rushton-Grimes (CRG) multi-body pair potentials [106,107].

2.1.2. Reverse Monte-Carlo

Reverse Monte-Carlo is a method used to reduce a molecular dynamics supercell, (8 x 8 x 8 unit cells) down to a supercell that can be used efficiently in ab initio calculations (around 100 atoms with 2 x 2 x 2 unit cells) without losing the main structural properties. This method was developed and tested by Michael Rushton et al. [109]. The details of the molecular dynamics cell were provided for the calculation including the total number of atoms, including species, and atom positions. The partial radial distribution, atomic density, atomic species concentration, separation distances, and total structure factor were calculated. These values are the “measured” values.

The structure was reduced in size from 6144 atoms down to 96 atoms by Fourier transform of the partial radial distribution function. From this, the partial structure factor was calculated and then the total structure factor was calculated. The root mean squared (RMS) difference between the measured total structure factor and the calculated total structure factor were compared. A random atom was selected and moved within a stipulated maximum distance. If the move resulted in atomic distances becoming too close, the move was rejected, otherwise, the move was accepted. After the move, the partial radial distribution function, partial structure factor and total structure factor were recalculated. If the RMS difference between the new calculation was less than that of the previous calculation and the measured value, the move was accepted. If the move produced a greater value difference, this could still be accepted if within the Metropolis Hastings algorithm [110]. This was repeated until the difference oscillated in equilibrium.

2.1.3. Density Functional Theory

The ab initio simulation used was VASP (Vienna Ab initio Simulation Package) which uses Density Functional Theory (DFT) to identify the ground state energy of a given structure. Energy calculations analyse ground state energies and electronic properties resulting from atomic position variations within a structure. The motion of electrons resulting from atomic nuclei position forms the basis of the calculation of the structures ground state energy [111–114].

The Schrödinger equation is used to calculate the ground state energy for electrons moving in a field of nuclei. For simplification, the problem can be broken into two parts. The Born-Oppenheimer approximation is used to calculate the electron and nuclei problems separately [115]. For the nuclei

calculation, the adiabatic potential energy surface function is used [115]. This is given as the ground state energy, E, as a function of nuclei, M, at position, R; $E(R_1,\ldots,R_M)$. This can then be applied to solve the problem including electrons with the time-independent, nonrelativistic Schrödinger equation $\hat{\mathrm{H}}\psi = \mathrm{E}\psi$ where $\hat{\mathrm{H}}$ is the Hamiltonian operator and ψ are the eigenstates (set of solutions) [115]. Each Eigenstate solution, ψ_n, has an eigenvalue, E_n. Expanding the Schrödinger equation for interacting multiple j electrons and nuclei gives the following equation [115].

$$\left[\frac{\hbar^2}{2m}\sum_{i=1}^{N}\nabla_i^2 + \sum_{i=1}^{N}V(r_i) + \sum_{i=1}^{N}\sum_{j<i}U(r_i,r_j)\right]\psi = E\psi \qquad \text{Equation 10}$$

Where ħ is the Plank constant and m is the mass of the electron. The bracketed three terms from left to right are the kinetic energy of each electron, the interaction energy between all atomic nuclei and each electron, and the interaction between each electron. E is the ground state energy of the electrons and ψ is the electron wave function containing the spatial coordinates of each electron: $\psi = \psi(r_1,\ldots,r_N)$ [115].

Hohenberg and Kohn proved a theorem stating that "the ground-state energy from the Schrödinger equation is a unique functional of the electron density." [115]. This was followed by the second theorem "The electron density that minimizes the energy of the overall functional is the true electron density corresponding to the full solution of the Schrödinger equation." [115]. These are extremely useful tools that are utilized to simplify the Schrödinger equation down to three dimensions in total, rather than three dimensions per electron. It also states that the electron density could be altered until the energy from the functional is minimized.

Another proved simplification which makes DFT a viable computational option is that of Kohn and Sham [115]. This involved solving the Schrödinger equation for a single electron at a time to create a set of equations. These equations are similar to the Schrödinger equation already presented with some alterations. The summations are removed and there is an addition of the Hartree potential. This is the Coulomb repulsion between the currently calculated electron and the combined electron density of all other electrons [115].

The self-consistency of the Kohn and Sham simplification can be solved by a series of steps. First, a trial electron density could be applied. Solve the Kohn and Sham equations with trial electron density to produce single particle wavefunctions. Calculate the electron density from the Kohn and Sham single particle wavefunctions. Compare the calculated electron density with the Kohn and Sham equations electron density. If the densities are the same, the electron density is at the ground state. If the values are different, the trial density should be altered and repeat the steps again.

The exchange-correlation function is required to identify the electron density at each point in space. This is, however, an unknown value and requires approximations. The simplest approximation is that of a homogeneous uniform electron gas [115]. Because this is used to calculate each exchange-correlation at each point in space, this is called the local density approximation (LDA). With locally calculated approximations, a generalized gradient approximation (GGA) can be applied to the local electron density. Further refinements to the GGA have been made where the most widely used approximation is the Perdew-Burke-Ernzerhof (PBE) [116] which have been used for all calculations within this work.

Electrons which are closest to the core of an atom are not usually of any interest where the outer valence electrons are more likely to provide interactions or information of a materials characteristics. To further simplify the simulations, the electron potentials for each atom species can be split between simple approximations for fixed core electrons whilst maintaining reliable properties of the outer valence electrons. This splitting of electron potentials is known as pseudopotentials. The most widely used pseudopotentials are the project augmented wave (PAW) potentials and have been used throughout this work.

When conducting calculations on periodic structures, it is more convenient to solve the equations in reciprocal space on primitive cells. The reciprocal space primitive cell is known as the Brillouin zone. The convenience associated with this is that Bloch's theorem which states that the periodic potential for the wavefunction of an electron can be solved in reciprocal space [115]. The sampling points of the Brillouin zone are known as the Bloch vectors or k-points. The central point of the Brillouin zone is the gamma (Γ) and when used, as part of the calculations, a gamma k-point mesh is centred around the gamma point. The more popular k-point mesh used is the Monkhorst-Pack [115]. This samples the Brillouin zone with a homogeneously spaced mesh. The Monkhorst-Pack k-point mesh was used throughout this work.

In general, a higher number of k-points would logically indicate a higher degree of accuracy, but this is at the expense of computational cost. Convergence testing, however, can be used to identify sufficiently accurate calculations with minimal computational cost. A 4x4x4 k-point mesh proved to be more than sufficient and was used throughout this work. Additional convergence testing was also used to identify the stopping criteria. The electronic relaxation stopping criteria was set to 1 x 10^{-4} eV with an atomic relaxation stopping criterion of 1 x 10^{-3} eV. The cut-off energy was set to 500 eV for the plane-wave-basis set.

Calculated defects were placed in multiple positions, including Wykoff positions for the bulk crystal oxides and random positions within the amorphous structures to identify the most suitable location.

2.1.4. [121]Defect Solution Energies

The defect solution energies were straight forward to calculate and simply identified the difference between the ground state energy of the initial combined reactants and the energy of the combined products produced. The solution energy can give an indication of plausibility for defects to form within the subject structures. Solution energy equations use Kröger-Vink notation which will be used for the remainder of this document [117,118]. Defect interstitials are represented as a subscript "i" of the particular element. For example, a lithium interstitial would be given as Li_i. A vacancy is given as a "V" with a subscript element such as a oxygen vacancy V_O. A substitution is given by the substituting element with the element being replaced as a subscript. For example, lithium on a zirconium site would be presented as Li_{Zr}. Defects can have a charge associated with them and with Kröger-Vink, this is represented as ' for a negative charge, $^{\bullet}$ for a positive charge and ^{x} for a neutral charge. The number of each is representative of the charge such as $^{\bullet\bullet}$ is a +2 charge. A plus two charged oxygen vacancy would be given as $V_O^{\bullet\bullet}$. These can also be combined for cluster defects such as two lithium interstitials around a zirconium vacancy site with an overall negative two charge $\{Li_i^{\bullet\bullet}: V_{Zr}''''\}''$. Both sides of the equation should conserve atoms, charge and atomic sites. An example of a chemical equation is as follows.

$$Li_2ZrO_3 + O_O^{\times} + Zr_{Zr}^{\times} \rightarrow \{Li_i^{\bullet\bullet}: V_{Zr}''''\}'' + V_O^{\bullet\bullet} + 2ZrO_2 \qquad \text{Equation 10}$$

Both the $O_O^\times$ and $Zr_{Zr}^\times$ occupy positions within the supercell solid structure and Li_2ZrO_3 is introduced as a reactant.

2.1.5. Formation Energy against Fermi Level

The formation energy vs Fermi energy plots produce an indication of the formation energies associated with the Fermi level across the bandgap energy. To calculate this, VASP can be used to provide the bandgap energy and the ground state energy difference between the defect structure and the structure containing no defects which can be plotted vs Fermi level. In this work, the software DefAp 2.7 was used [119].

The calculation is made with the following equation.

$$\Delta H_{D,q}(E_F, \mu) = \left[E_{D,q} - E_H\right] + \sum_i n_i \mu_i + qE_F + E_{corr} \quad \text{Equation 12}$$

$\Delta H_{D,q}(E_F, \mu)$ is the calculated ground state defect formation energy at the given Fermi level.

$\left[E_{D,q} - E_H\right]$ is the difference in ground state energy where $E_{D,q}$ is the defect structure energy with charge q, E_H is the energy of the host structure without defects.

$\sum_i n_i \mu_i$ is the chemical potential where n_i is the number of atoms added or removed (+1 for atom removed, -1 for atom added), μ_i is the chemical potential and i is the atomic species.

qE_F is the charge of the defect, q, multiplied by the given Fermi level across the Bandgap.

E_{corr} is defect-defect charge interaction with periodic images. This is calculated using the following.

$$E_{corr} = \frac{q^2 v_M^{scr}}{2} = \frac{q^2 \alpha}{2\epsilon L} \quad \text{Equation 13}$$

The screened Madelung potential, v_M^{scr}, is used for a point charge general dielectric within a 3-D box and is generally used for cubic supercells (other options available for non-cubic supercells [120]) where $v_M^{scr} = \frac{\alpha}{\epsilon L}$ and α is the coefficient 2.837, ϵ is the dielectric constant of the host material and *L* is the length of the host supercell.

2.1.6. Brouwer Diagrams

Brouwer diagram calculations can provide an indication of possible defect concentration through a material measured as the partial pressure of oxygen. Producing the Brouwer diagrams utilised the same software that was used to produce the formation energy vs Fermi energy diagrams [119]. The DFT energy values were required with constant volume calculations to provide a defect dilution limit, which is convention [119,121].

Historically, Brouwer diagrams used simple calculations where the partial pressure of oxygen was split to three areas (low, medium and high).

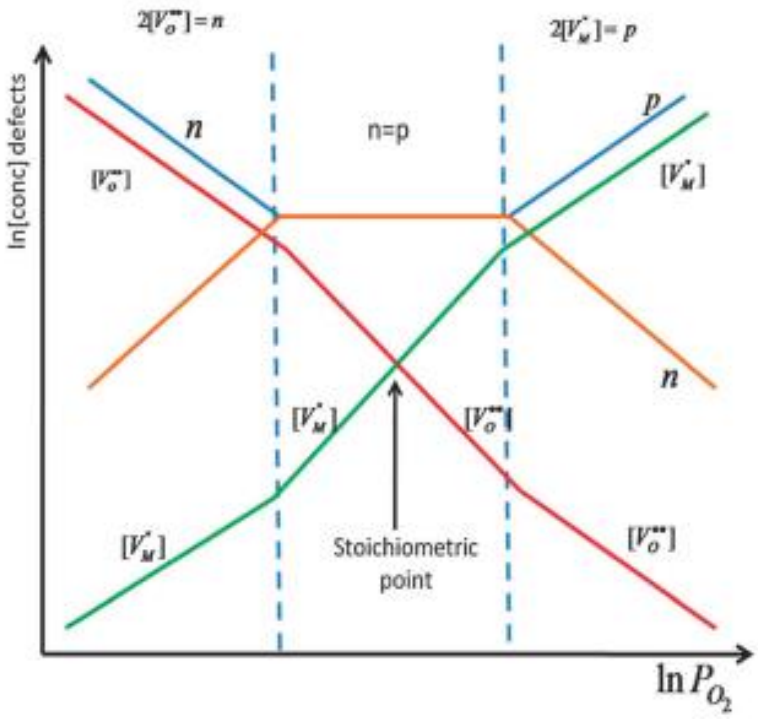

Figure 23 Basic Brouwer diagram with three sections of high (right) medium (middle) and low (left) partial pressure of oxygen [122].

The Brouwer diagram above (Figure 23) shows defect concentrations of defects on the y-axis at changes in partial pressure of oxygen on the x-axis. In general, the partial pressure of oxygen is analogous to the depth within the material. At high partial pressures to the right, this can be considered as the water/oxide interface, in our case. To the left, this can be considered working towards the metal oxide interface.

The sum of charge multiplied by defect energies should sum to zero throughout the partial pressures. First, the chemical potentials are calculated and then the defect concentrations are calculated. The equations used to calculate Brouwer diagrams are as follows [123].

$$\mu_{ZrO_2(solid)} = \mu_{Zr}(T, P_{O_2}) + \mu_{O_2}(T, P_{O_2}) \qquad \text{Equation 14}$$

In Equation 145, the chemical potentials for each constituent, per formula unit, is given by μ with the partial pressure of oxygen given as P_{O_2} at temperature T. To calculate the concentrations of each defect to form the Brouwer diagram, the charge of each defect multiplied by the sum of all defects must be equal to zero with the following [123].

$$\sum_i q_i c_i - N_c \exp\left(-\frac{E_g - \mu_e}{k_B T}\right) + N_v \exp\left(-\frac{\mu_e}{k_B T}\right) = 0 \qquad \text{Equation 15}$$

In Equation 15, from left to right, the first term is the sum of defect charges. The next term is the concentration of electrons, and the last term is hole concentration where q_i is the charge of the defect. c_i is the concentration of the defect. E_g is the band gap. μ_e is the electron chemical potential (also the Fermi Level at zero Kelvin). k_B is the Boltzmann constant. T is the temperature. N_c is the density of the conduction band. N_v is the density of states of the valence band. The temperature used within this work was set to 635 K as the general operating temperature of PWR reactors.

2.2. Experimental Techniques

Once the simulations provided a solid indication for an area of further investigation, synthesis and characterisation of the samples could begin.

2.2.1. Synthesis of undoped and Doped ZrO_2

To create amorphous ZrO_2, a plan was made loosely based on previous works [124] where, in place of zirconium nitrate, lithium hydroxide and ammonium hydroxide, zirconium butoxide, lithium tert-butoxide and butanol was used.

A solution of $LiOC(CH_3)_3$ in n-butanol (12.5 mM, 100 mL) was prepared using the following procedure: Lithium tert-butoxide (0.1 g, 12.5 mmol) was weighed using a glovebox analytical balance. The powder was then removed from the glovebox and transferred to a glass beaker. A small amount of n-butanol was added, and the beaker swirled to dissolve the contents. The solution was then poured into a volumetric flask (100 mL) and made up with n-butanol.

To create amorphous ZrO_2, Zirconium n-butoxide $Zr(OC_4H_9)_4$ solution (7 mL, 2.19 M, 80 wt % in n-butanol) was added to a round bottom flask (100 mL) and stirred whilst mixing in (not for pure ZrO_2 but Li doped ZrO_2) lithium to create Li - ZrO_2 in a butanol solution. This was then stirred for 1 hr at 70 °C under reflux. Deionized water (equivalents listed below) was added dropwise, and the resulting mixture stirred under reflux at 70 °C for 2 hrs. The reflux apparatus was removed, and the solution added to a flat bottom flask, and the mixture stirred overnight at 90 °C on a magnetic mixing hotplate until the solvent evaporated completely. The completed experiment resulted in a fine powdered Li doped amorphous ZrO_2.

Table 7 shows the sample masses required to gain the desired lithium defect concentration.

Table 7 Lithium tert-butoxide mass used to produce required lithium concentrations.

Li concentration (% mol)	Li *tert*-butoxide mass (g)	Deionized water (mL)
0	-	1.13
0.1	0.0013	1.13
1	0.013	1.13
5	0.0658	1.13
10	0.13	1.4
20	0.246	2
30	0.39	3
40	0.52	4
50	0.615	5
60	0.738	5

Using slightly higher volumes of deionised water ensured hydrolysis of Li tert-butoxide and zirconium n-butoxide where any additional water would evaporate.

2.2.2. Raman Spectroscopy

Raman spectroscopy is a method to identify molecular characteristics of a sample. It can be used to analyse the structure of ZrO_2 up to the metal oxide interface [26,125]. A sample is subject to an incident laser and is inelastically scattered. The molecular bonds vibrate and absorb specific wavelengths resulting in a reduced energy light to be emitted from the sample. The Raman spectrometer filters out any reflected light of the same wavelength of the initial laser. This results in a spectrum of light with higher intensities associated with the specific wavelengths resulting from energy loss through molecular phonons. For extremely pure monoatomic samples, such as diamond, this would result in one narrow and high intensity peak associated with the carbon molecule. For more complex structures, multiple lines may be present. Defects can cause peak broadening as well as peak shifts.

The Raman spectrometer used in this work was the Bruker SENTERRA II with a 532 nm laser at 25 mW of power. The aperture was set to 15 µm and the optical lens used a combination of 20 and 50 times optical zoom. Five coadditions (repeated measurement at the same location) were used to reduce noise with an integration time of 1 second.

2.2.3. X-ray Diffraction

X-ray diffraction is a powerful method to identify crystal structures through changes in constructive interference produced when x-ray diffraction occurs. An x-ray source is aligned with a sample with an angle θ and a detector at the same, apposing, angle producing 2θ as shown in Figure 24.

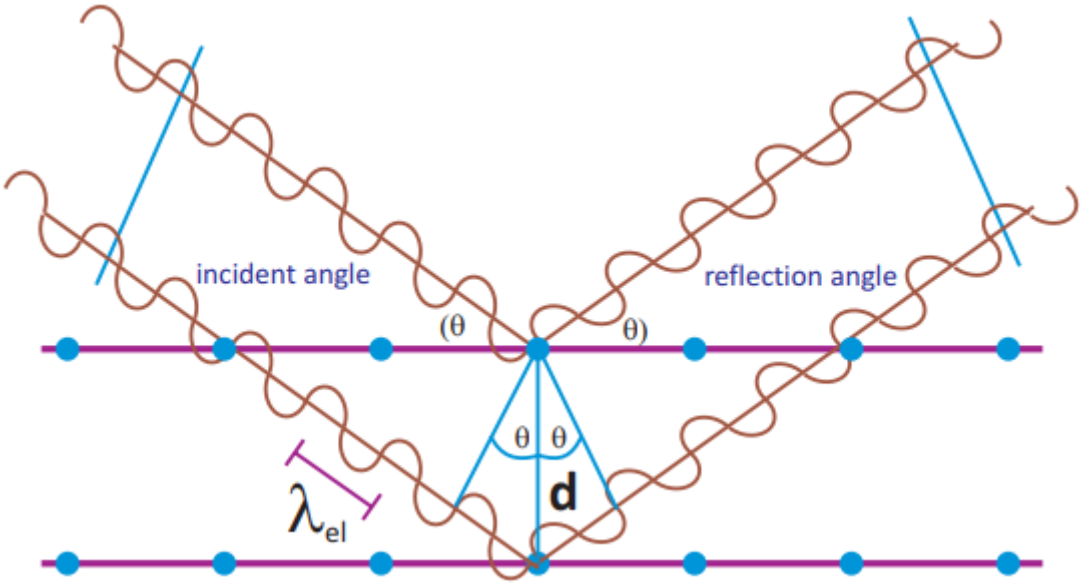

Figure 24 X-ray diffraction incident and reflection angle [126].

From the obtained XRD peaks, the Bragg's equation can be used to identify the distance between the atomic layers.

$$n\lambda = 2d \sin\theta \qquad \text{Equation 11}$$

Where n is the peak number, λ is the x-ray wavelength, d is the distance between atomic layers and θ is the incident angle.

Bragg-Brentano reflection for powder diffraction was performed with the Malvern Panalytical Aeris XRD with an Empyrean Cu LFF HR X-ray tube. Limitations of XRD include no depth profiling and inability to identify amorphous structures.

2.2.4. Scanning Electron Microscopy

Scanning electron microscopy (SEM) uses a focused beam of electrons which results in back-scattered and secondary electrons that are excited from the surface. The secondary electrons are detected producing a topographical visualisation of the sample surface as shown in Figure 25. Backscattered electrons, on the other hand, are electrons that originate from the electron source and are elastically scattered back out of the sample. The larger the atoms (higher atomic number) within the sample, the brighter the material region appears.

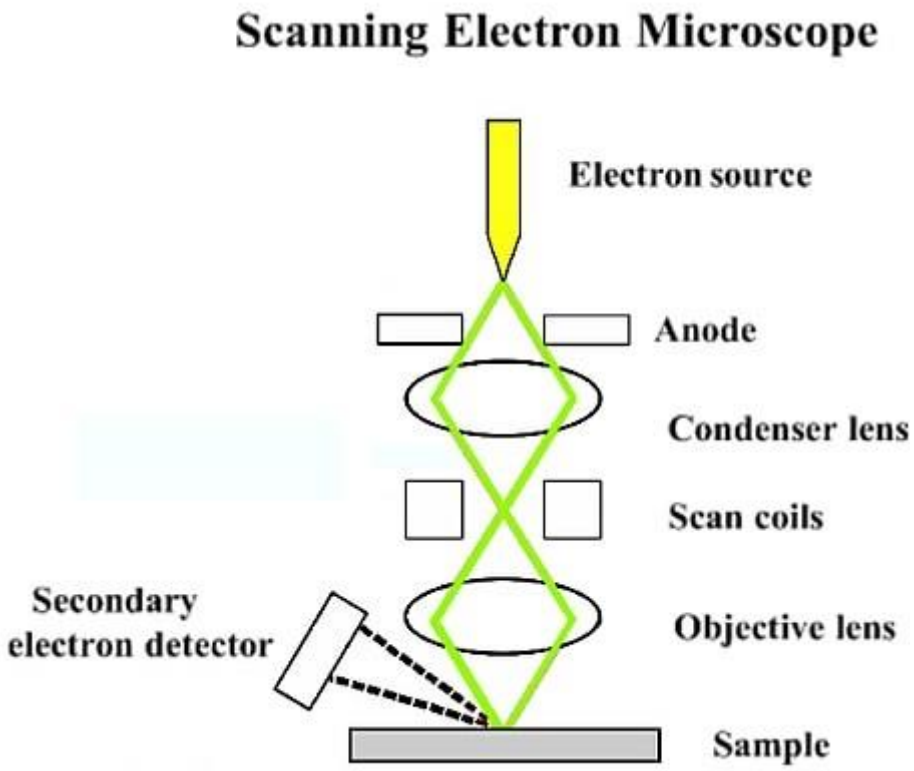

Figure 25 Basic components of an SEM [127].

The SEM can also be coupled with an energy dispersive x-ray detector (EDS) to identify the chemical composition of the sample. The electron beam used during SEM imaging can also cause x-rays to be immitted from the sample which provide a signature energy level associated with the specific elements present along with relative concentration. There is, however, a limitation where the dispersed x-rays have a very low energy from lithium, placing it in the noise range.

2.2.5. Simultaneous Thermal Analysis with Mass spectroscopy and thermogravimetric analysis

As the name suggests, the simultaneous thermal analyser (STA) can accomplish multiple tasks simultaneously providing thermogravimetric (TG), differential scanning calorimetry (DSC) and mass spectroscopy data whilst heating a sample. A sample can be placed within the furnace and the STA can be programmed to conduct specified heat, dwell and cool rates under different environments. TG can provide an indication of mass changes such as weight gain through oxidation and hydrogen uptake as well as weight loss during events such as changes in polymorph changes through, for

example, evaporation. The environmental and mass loss gas could be monitored through mass spectroscopy during the process. The DSC can monitor heat transfer between the internal furnace and the sample which could provide evidence of polymorph changes, melting and solidification.

The STA with mass spectroscopy equipment used in this work was the Netzsch STA 449 F with the Netzsch QMS 403 Aëolos Quadro mass spectrometer, Figure 26.

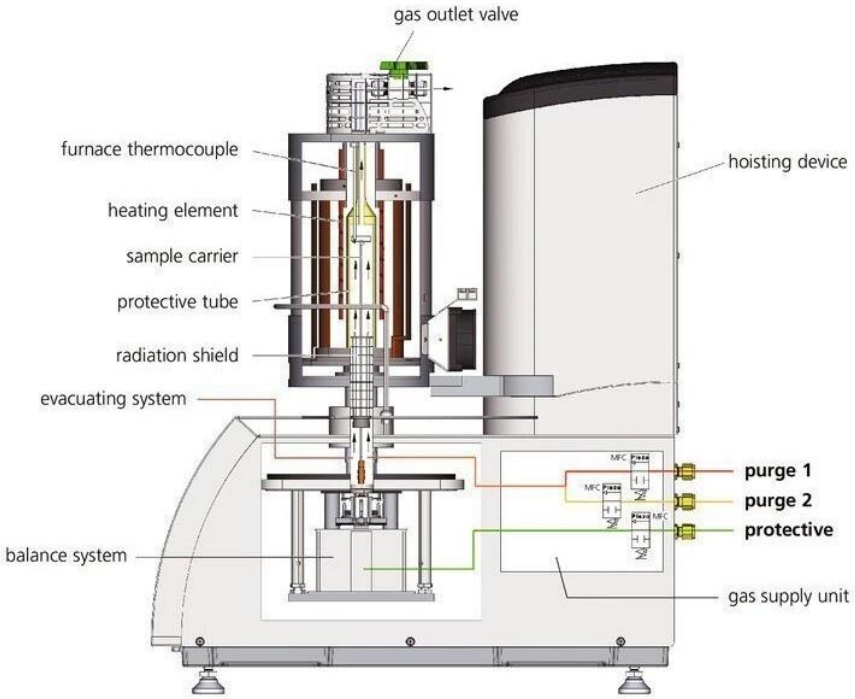

Figure 26 Schematic of simultaneous thermal analyser [128].

2.2.6. Scanning Transmission Electron Microscopes with Electron Energy Loss Spectroscopy

Much like an SEM, a scanning transmission electron microscope (STEM) uses a focused electron beam focused on a sample. Where this differs from the SEM is that the samples are required to be 100 nm or less in thickness as the electrons are required to pass through the sample. High resolution transmission electron microscopy can detect oxide grain morphologies as a result [125]. Each element reduces some of the energy of electrons through inelastic scattering at varying levels depending on the particular atom in question. As a result, Electron Energy Loss Spectroscopy (EELS) can produce a chemical map of the sample.

The equipment used during this investigation was the JEOL ARM 200F (S)TEM operating at 200 kV equipped with a Gatan GIF Quantum 965 ER with EELS capabilities.

2.2.7. Inductively Coupled Plasma Optical Emission Spectroscopy

Inductively coupled plasma optical emission spectroscopy (ICP-OES) can provide the elemental concentration within a sample. ICP-OES excites orbital electrons to a higher energy level using a very high temperature plasma (~8000 K). When the electron returns to a lower energy level, light is emitted with a specific wavelength which can be attributed to a specific element. The atomic concentration can be identified through the intensity gained of the particular wavelength. In this work, the Agilent 5800 spectrometer was used.

3. Atomistic Modelling of Lithium and Alloying Additions in Bulk ZrO_2

*The work in this chapter pertaining to lithium defects within the bulk oxide along with solution energies was published in the paper*s.

"The accommodation of lithium in bulk ZrO_2" in the Solid State Ionics Journal [129] **(1st author)**

The contribution of the author to this work was all simulations and first draft manuscript creation.

and in the Top Fuel conference proceedings "Lithium accommodation in ZrO_2" [130]**. (1st author)**

The contribution of the author to this work was all simulations and first draft manuscript creation.

Previous work had hypothesised that lithium ingress into the bulk material may alter the volume of the structure [1]. This went on further to suggest that a lithium induced reduction in volume may open pores within the oxide which would explain the evident accelerated corrosion caused by lithium which was demonstrated under thermal gradient in autoclaves [55]. This chapter investigated the accumulation of potential intrinsic and extrinsic defects within the bulk zirconia structures to identify potential routes for lithium to accelerate the corrosion of the zirconium alloy Zircaloy-4.

As discussed in chapter 1.2.5, there are two main polymorphs of bulk ZrO_2 that are formed on zirconium alloys as a result of oxidation in water. Primarily, the tetragonal polymorph is observed to form at the metal oxide interface which is under compressive stress, and this gives way to the monoclinic polymorph through stress relief [47,51,131] as the thickness of the oxide layer grows and is less restrained by the metal substrate. The mechanism for this, typically between room temperature and 400 °C, is through the diffusion kinetics of moisture in-diffusion on oxygen vacancies [132].

This chapter looks at the predicted intrinsic defect concentrations expected in each of these polymorphs of ZrO_2 and then the change of intrinsic defects (defects occurring from the native material) concentrations that may be expected with the introduction of extrinsic defects (defects produced from a foreign element) by the alloying elements in the metal or from the reactor coolant. Any lithium defects that may be found within the oxide layer originate from the coolant water. The chromium, iron and tin defects have the potential to originate from the coolant water through corrosion of other primary loop components. But can also be found at the metal oxide interface because of alloying additions within the zirconium alloy itself. Defects included were interstitials, vacancies, and substitutions.

Brouwer diagrams were utilised to produce an indication of defect concentration throughout the tetragonal and monoclinic oxide layer. Each defect or element may have an impact on other defect concentrations which will be assessed with the combined dopant Brouwer diagrams. The expected volume change of the oxide associated with the ingress of dopants will be reviewed and, finally, the solution energies will also be addressed to assess if the defects are soluble within the bulk oxide.

To accomplish this, density functional theory (DFT) was first used to calculate the lowest energy configuration for each structure (perfect and defect structures) as described in chapter 2.1.3. Then, formation energy values across the bandgap were produced, as outlined in chapter 2.1.5. Brouwer diagrams were produced to provide an indication of defect concentrations, described in chapter

2.1.6, which also provided a base for expected volumetric changes associated with the concentration of combined defects. Finally, the solution energies were calculated from DFT reactant and product energy differences as given in chapter 2.1.4.

By evaluating the lithium solubility into bulk ZrO_2 along with possible concentrations, the overall change in bulk volume was simulated to address the hypothesis of volumetric reduction producing potential porosity in the oxide layers [133].

It is worth mentioning that, due to the two polymorphs, this chapter is quite long. In addition to this, the number of lithium, chromium, iron and tin defects that have been found in the two bulk polymorphs produced complexities requiring a lengthy breakdown. An unfortunate conclusion to this chapter is that the solution of lithium was calculated and found to be unlikely in the bulk ZrO_2 oxide. For this reason, the chromium, iron and tin results for this chapter have been moved to the Appendix section. Whilst the results for this chapter are disappointing, the chapter provides a foundation of techniques used for further investigation and produced evidence that discounts the hypothesis that lithium will change the volume of the bulk oxide.

3.1. Tetragonal ZrO_2 (Undoped)

The initial zirconium oxide layer that forms at the metal/oxide interface is tetragonal ZrO_2. At equilibrium without extrinsic defects, intrinsic defects are still expected to form and can be assessed [175]. These defects include oxygen vacancies, zirconium vacancies, oxygen interstitials and interstitial zirconium. Each of these defects may also be associated with a charge (e.g., the +2 charged oxygen vacancy [176]. The formation energy of each intrinsic defect could be plotted as a function of the Fermi level across the bandgap which was found to be 3.8 eV through DFT calculations, which confirms previously calculated values [177]. Zirconium interstitials are calculated with a Fermi level outside of the bandgap range, so are omitted from the final calculations. Zirconium vacancy defects, including ionic charges of -1 to -4, produce a calculated plot of formation energy versus Fermi energy (the change of Fermi level across the bandgap). The general principle of formation energy diagrams is that a negative charged defect has a higher formation energy at the top of the valence band at $E_F = 0$ and lower formation energy at the bottom of the conduction band at the top of the bandgap energy and vice-versa for positive charged defects. In simple terms, this is due to the “cost” of transferring electrons to and from a pseudo electron reservoir and the material. An increase in Fermi level is accompanied with an increase in electron energy level. For a positively charged defect, donating an electron at such high energies becomes increasingly difficult producing a higher formation energy. Because the formation energies are calculated using 0 K temperature DFT calculation values, there are no finite-temperature effects on the Fermi energy to consider.

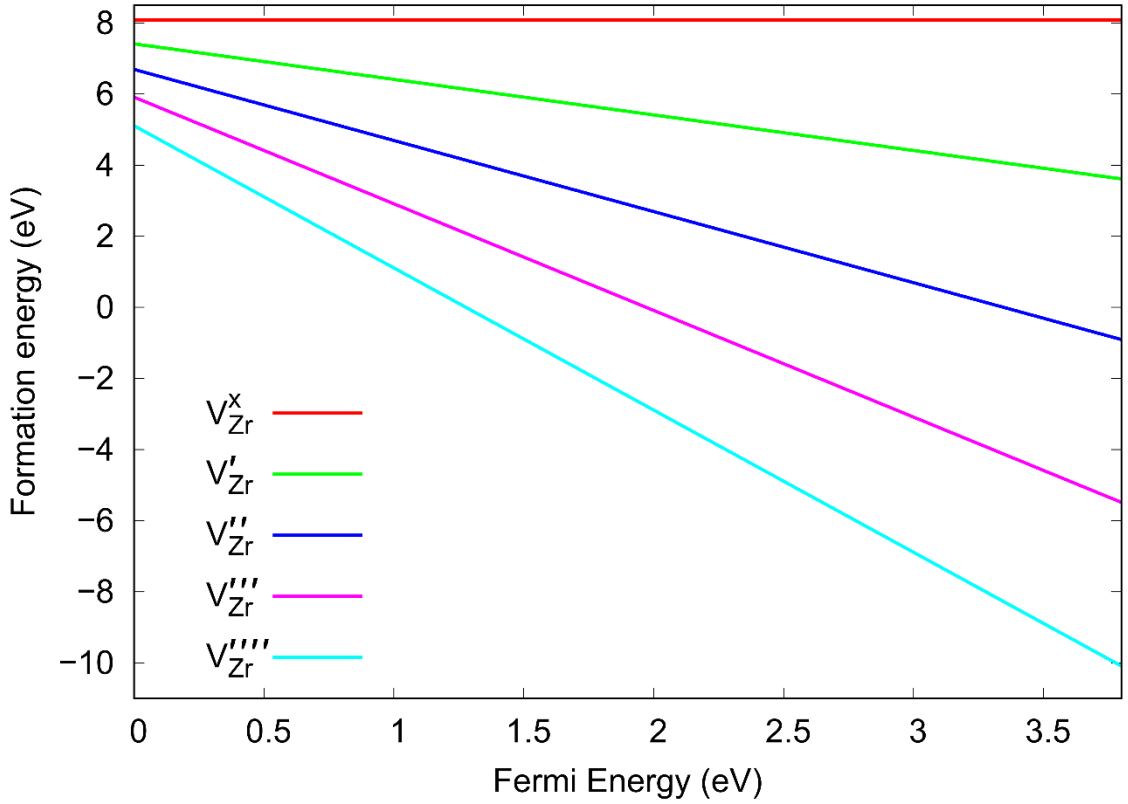

Figure 27 Formation energy of zirconium vacancy with a range of charges across the Fermi energy of the bandgap of tetragonal ZrO_2.

The lowest formation energy defect is more likely to be the prevalent defect within the structure when competing with other defects of the same type, Figure 27. In the case of zirconium vacancies, the negative four charged defect, (V_{Zr}''''), is prevalent across the entire bandgap, so is likely to dominate. However, this does have a negative four charge and will require charge balancing from a positively charged defect, for example holes or positively charged point defects.

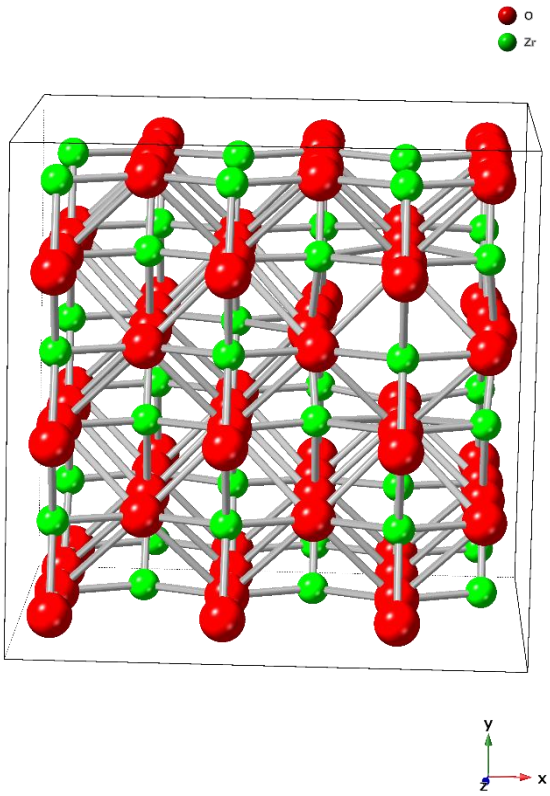

Figure 28 Tetragonal ZrO_2 with zirconium vacancy (green) position middle right.

In the relaxed structure, the oxygen defects move away from the zirconium vacancy site in the x direction as seen in Figure 28. The atomic radii used for all structural figures in this document are based on experimental results outlined in literature known as the “Crystal” radii [134].

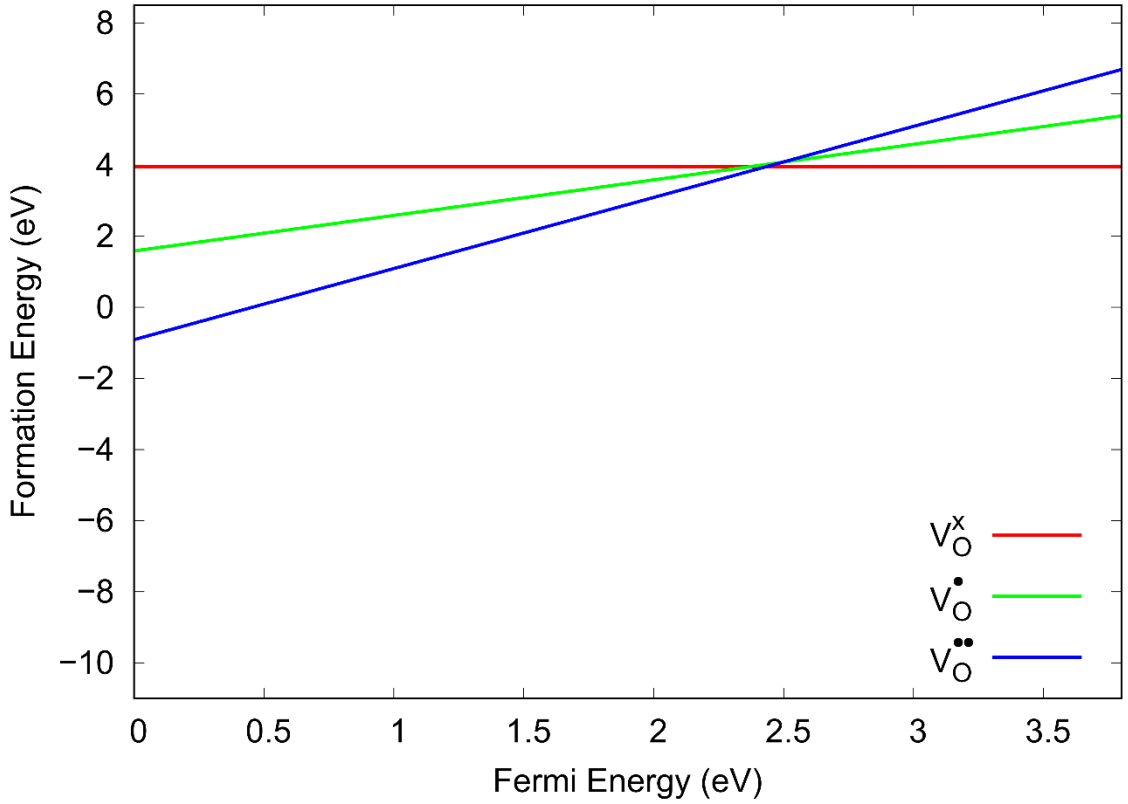

Figure 29 Formation energy of oxygen vacancy with a range of charges across the Fermi energy of the bandgap of tetragonal ZrO_2.

For oxygen vacancy defects, the bandgap is shared, with respect to Fermi level, between the +2 charged ($V_O^{\bullet\bullet}$) and the neutral charged oxygen vacancy defect ($V_O^{\times}$), Figure 29. The lowest part of the bandgap is given as zero on the plot and represents the valence band and to the right is the conduction band at the top of the bandgap at 3.8 eV. Where the Fermi level is close to the top of the valence band to the left, the oxide would be negatively charged favouring the plus two oxygen vacancy defect ($V_O^{\bullet\bullet}$). It would be expected that the plus two charged oxygen vacancy would follow electron concentrations.

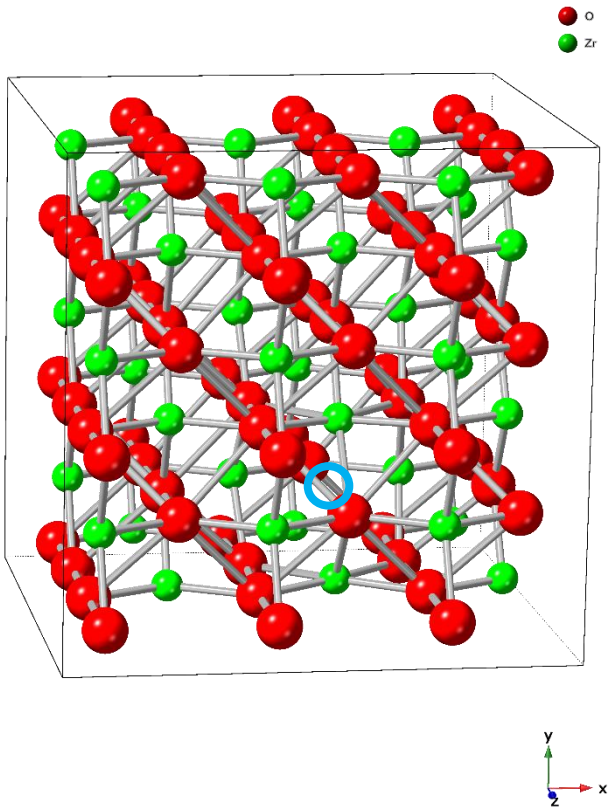

Figure 30 Tetragonal ZrO_2 with oxygen vacancy (Marked in blue) position middle.

In the oxygen vacancy structure (Figure 30), the remaining oxygen defects spread on the z-plane but did not affect the other surrounding atoms to any visually remarkable degree.

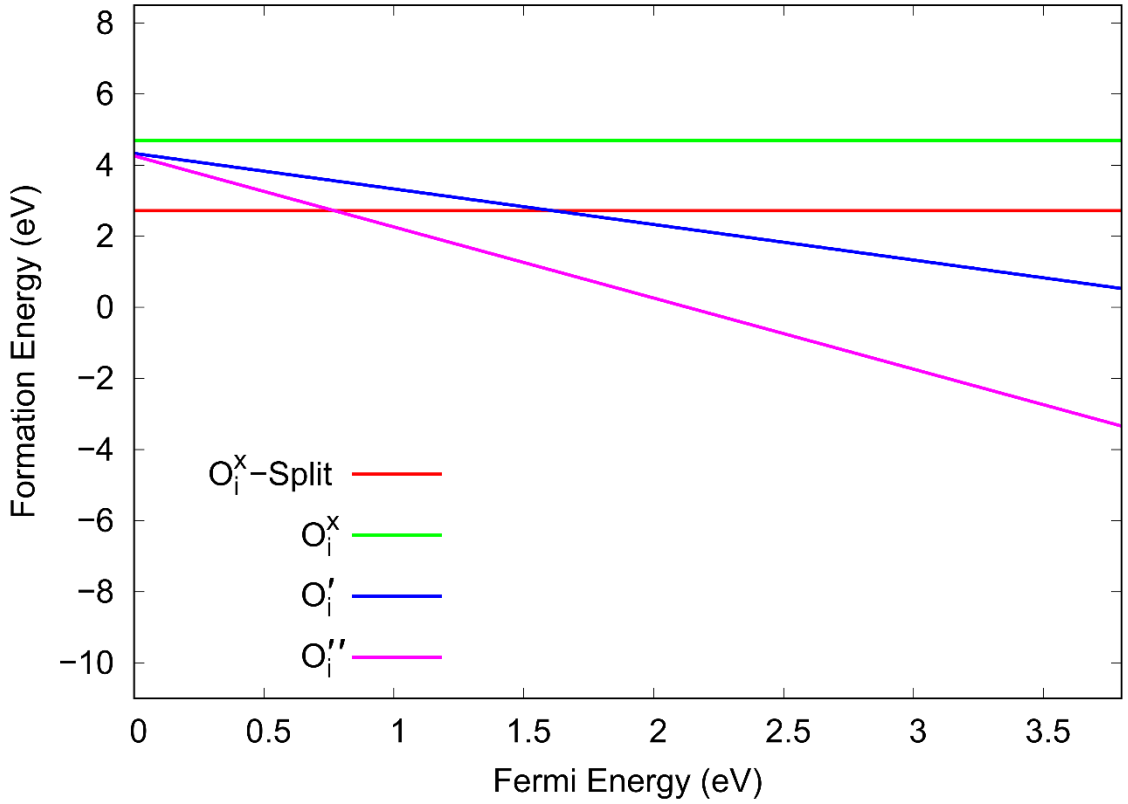

Figure 31 Formation energy of oxygen interstitials with a range of charges across the Fermi energy of the bandgap of tetragonal ZrO_2.

For oxygen interstitials, Figure 31, we have introduced a "split" interstitial. This is where one oxygen atom is displaced, and an additional oxygen interstitial atom share a region around the original oxygen site. This split interstitial is found closer to the valence band (0 eV) to the left of the plot, where the negative two charged oxygen interstitial, (O_i''), is more favourable towards the conduction band on the right.

Brouwer diagrams may be produced using the data from the formation energy vs Fermi energy calculations.

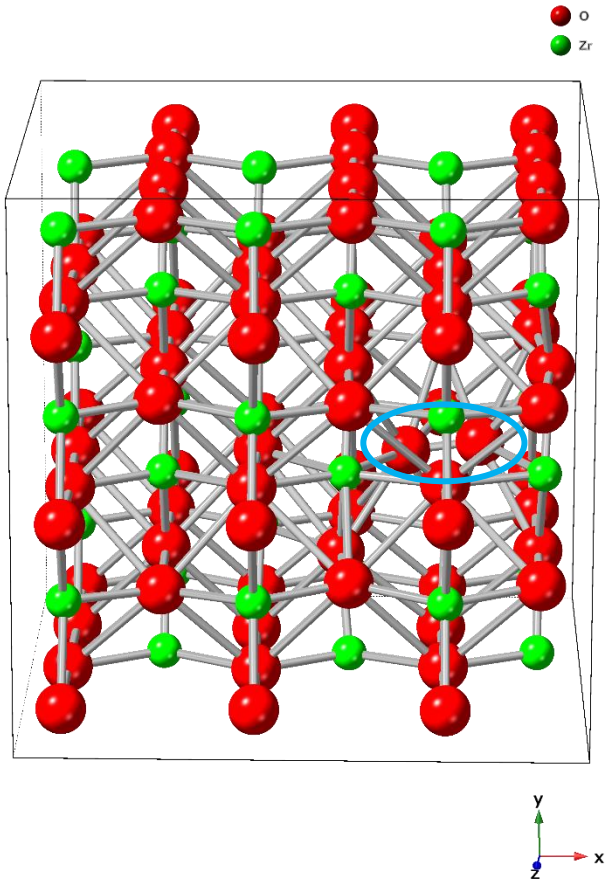

Figure 32 Tetragonal ZrO_2 with split oxygen interstitial (Circled blue) position middle right.

When viewing the structure of a split oxygen interstitial (Figure 32), the two oxygen atoms offset in the x-direction around the initial oxygen site but remain on the general z-plane without altering the surrounding atomic locations.

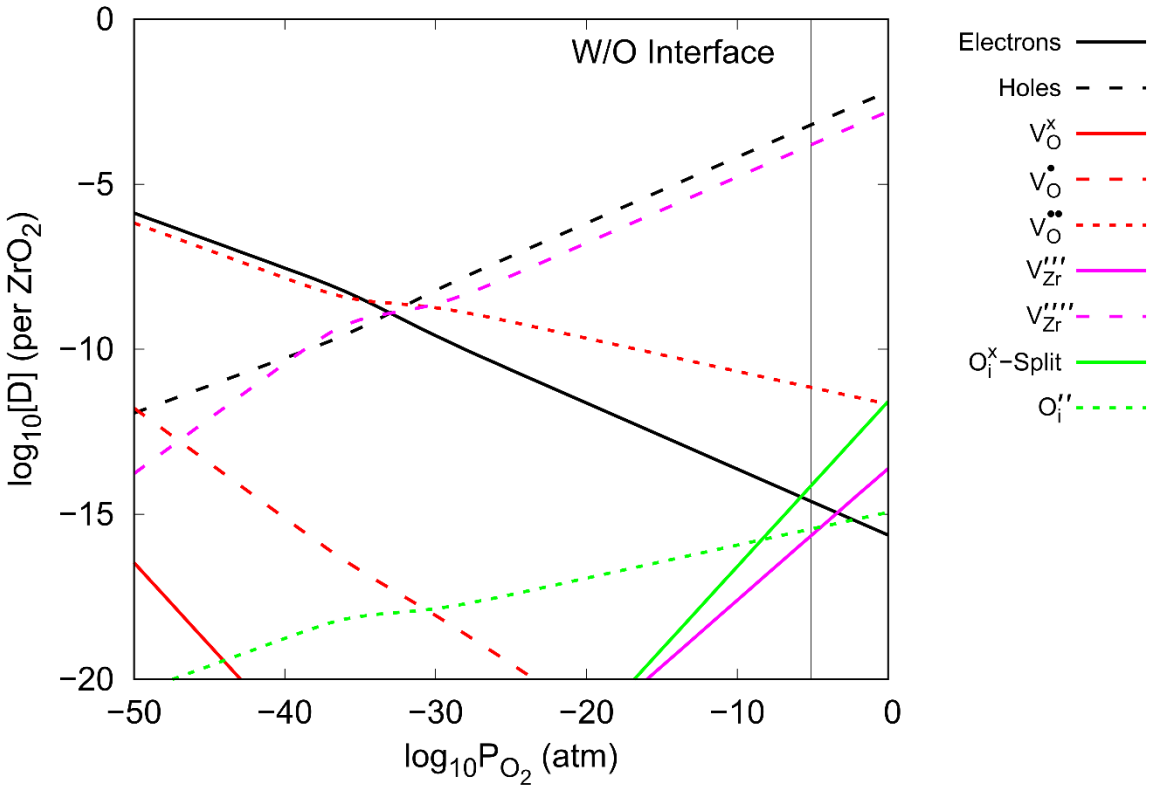

Figure 33 Brouwer diagram at 635 K of intrinsic defects in tetragonal ZrO_2. The vertical black line shows the water oxide interface.

The Brouwer diagram of intrinsic defects in tetragonal ZrO_2 shows two main defects that follow the electron and hole defect concentrations, Figure 33. The $(V_O^{\bullet\bullet})$ defect concentration follows the electrons (red dashed) where the (V_{Zr}'''') follows the hole concentration (purple dashed). The lower concentration of $(V_O^{\bullet})$ causes a reduction of (V_{Zr}'''') towards lower partial pressures of oxygen and, conversely, (V_{Zr}''') and (O_i'') causes an increase in $(V_O^{\bullet\bullet})$ at higher partial pressures towards the water oxide interface. Establishing the expected intrinsic defects offers an indication of changes that may take place as a result of extrinsic defects, such as Li, Cr, Fe and Sn.

3.2. Li Doped Tetragonal ZrO_2

Several defects were considered when applying lithium defects in tetragonal ZrO_2 including interstitials, substitutions and small clusters. These included (Li_i), $(2Li_i)$, (Li_O), $(2Li_O)$, (Li_{Zr}), $(2Li{:}\,V_{Zr})$, and $(2Li_{Zr})$ with various charges. Only the lithium interstitials, (Li_i), and the small defect cluster of two lithium interstitials around a zirconium vacancy site, $(2Li{:}\,V_{Zr})$, were identified as potentially stable and of consequence to defect populations in tetragonal ZrO_2. All other defects were found outside of the bandgap when calculating formation energy vs Fermi energy.

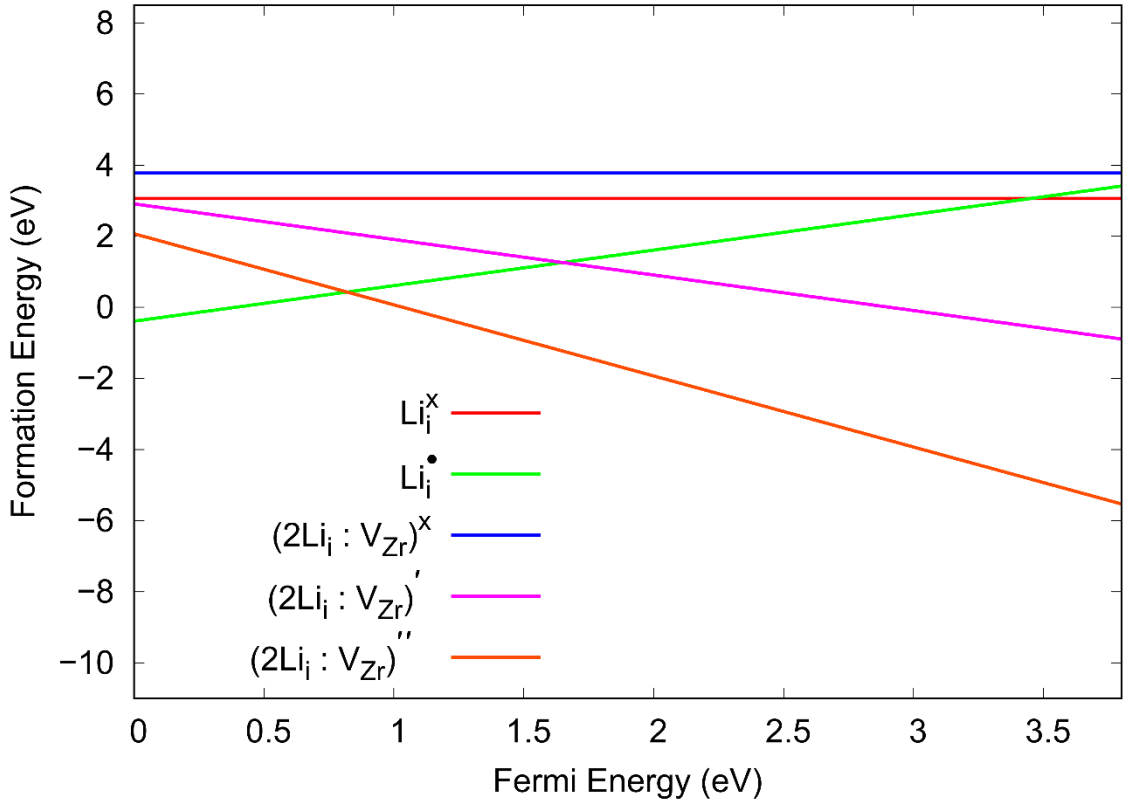

Figure 34 Formation energy of lithium defects with a range of charges across the Fermi energy of the bandgap of tetragonal ZrO_2.

From the formation energy vs Fermi energy plot, the most stable defects are the +1 charged lithium interstitial, Figure 34, $(Li_i^\bullet)$ and the -2 charged defect cluster $(2Li_i^\bullet : V_{Zr}'''')''$. The $(Li_i^\bullet)$, green, is more likely to form close to the top of the valence band to the left of the plot, where the $(2Li_i^\bullet : V_{Zr}'''')''$, orange, cluster has a lower formation energy towards the top of the bandgap and bottom of the conduction band. However, when calculating the Brouwer diagrams, the extrinsic defect concentration is provided as a stipulated concentration where all other intrinsic defects are calculated around it. These means that the lithium concentration will be 10^{-3} overall, if stipulated as such. There is the ability to add an allowable deviation of extrinsic defect concentration, which becomes important when adding multiple different elements for extrinsic defects. The Li doped ZrO_2 Brouwer diagram provides an indication of defect concentrations based on the concentration of Li within the system. It does not, however, provide evidence of the solubility of Li into the system and this will be reviewed later in the chapter. The intrinsic defect Brouwer diagram is added to the figure to provide comparison with lithium doped ZrO_2 at various concentrations.

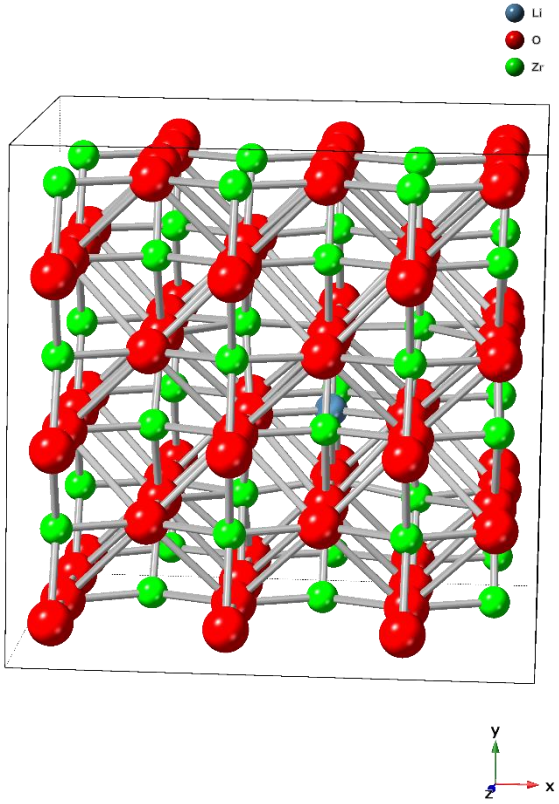

Figure 35 Tetragonal ZrO_2 with lithium interstitial (blue) middle.

The lithium interstitial has very little effect on surrounding atoms when considering local positions (Figure 35). There is, however, a slight change in location of oxygen atoms which move inward towards to the lithium interstitial.

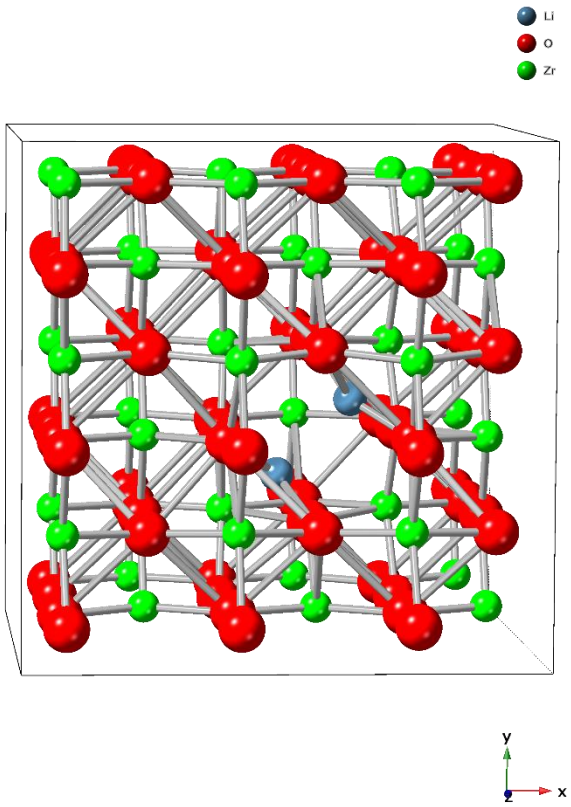

Figure 36 Tetragonal ZrO_2 structure with the small cluster of two lithium interstitials around a zirconium vacancy site.

The two lithium interstitials around a zirconium vacancy site along with an oxygen vacancy (Figure 36) show that the lithium interstitial defects are found in areas between oxygen sites. There is a little deviation, visually, in oxygen atom locations surrounding the cluster of defects.

From this, the tetragonal zirconia Brouwer diagram containing lithium and intrinsic defects could be calculated to highlight defect concentrations throughout the tetragonal oxide layer.

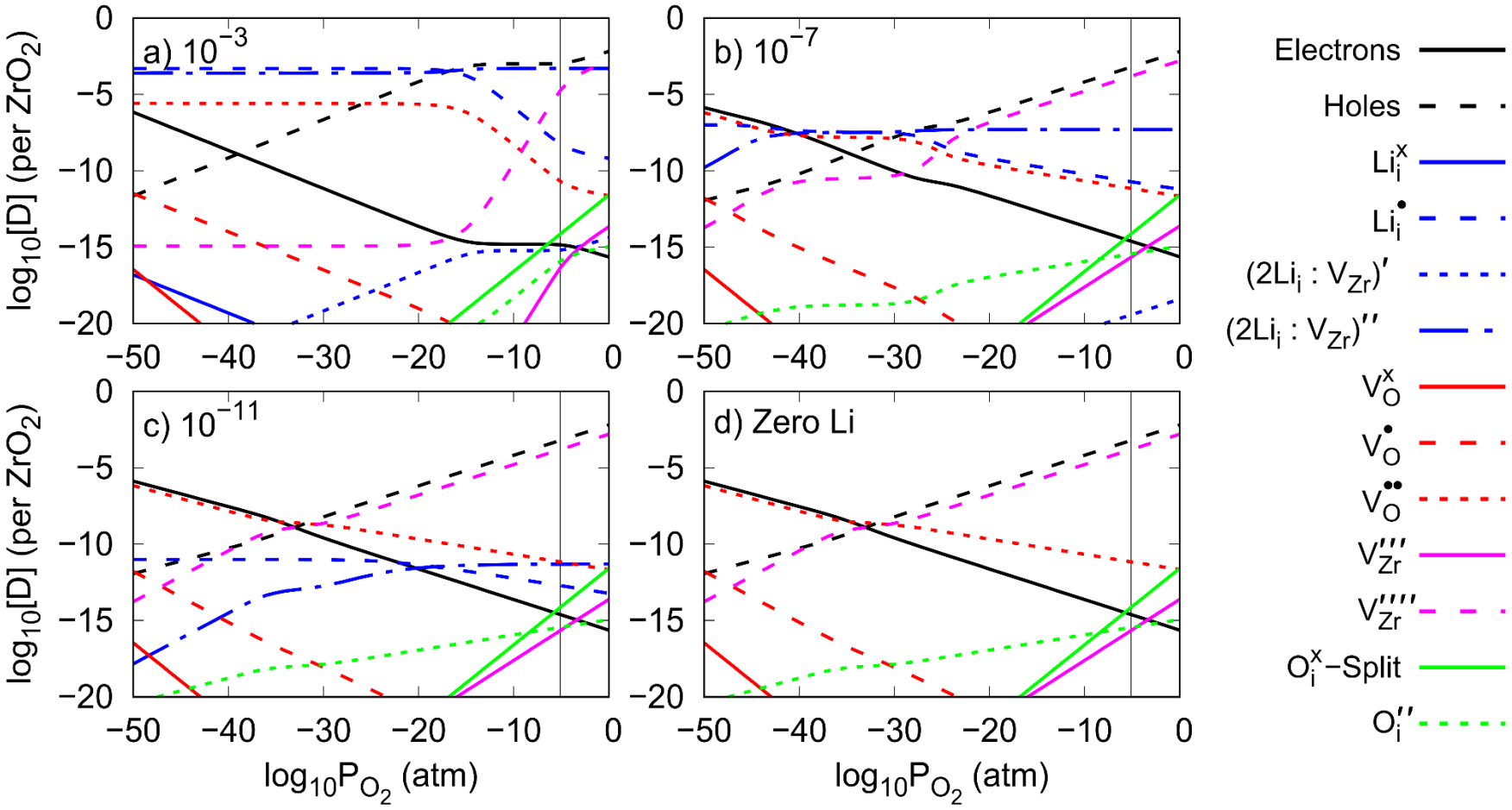

Figure 37 Li doped tetragonal ZrO_2 Brouwer diagrams with the Li concentrations of a) 10^{-3} b) 10^{-7} c) 10^{-11} and d) with intrinsic defects only.

The lithium doped tetragonal ZrO_2 Brouwer diagram, *Figure 37*, is given in lithium concentrations between 10^{-3} and10^{-11} and compared with the Brouwer diagram only considering intrinsic defects. The vertical black line to the right of the plots shows an estimation of the water oxide interface. Blue represents defects containing Li, red are oxygen vacancies, purple are zirconium vacancies and green represents oxygen interstitial defects.

The most evident intrinsic defect concentration changes that can be seen is at the highest concentration of extrinsic defects 10^{-3} Li in Figure X(a), as expected. All intrinsic defects are affected by lithium apart from $(V_O^{\times})$ and $(V_{Zr}^{''''})$ which remain unchanged, with the exception of a small change in $(V_{Zr}^{''''})$ at 10^{-3} Li concentration. The largest change is that of $(V_O^{\bullet\bullet})$ and $(V_{Zr}^{''''})$. At 10^{-3} Li, $(V_O^{\bullet\bullet})$ is shown to have a higher concentration through most of the partial pressure range. However, this is reduced to intrinsic levels around the water oxide interface. Conversely, $(V_{Zr}^{''''})$ is shown to be repressed through most of the oxide with the exception of the water oxide interface, where it resumes intrinsic levels. The dominant lithium defects are the $(Li_i^{\bullet})$ and $(2Li_i^{\bullet}:V_{Zr}^{''''})''$ which combine to meet the stipulated concentration with $(Li_i^{\bullet})$ dominating at lower partial pressures and $(2Li_i^{\bullet}:V_{Zr}^{''''})''$ at the higher partial pressures. As the lithium concentration is reduced to 10^{-7}, Figure X (b), a smaller deviation is observed when compared to the system only considering intrinsic defects, as is expected. Finally, with a lithium concentration at 10^{-11}, c), the intrinsic defects are largely unchanged from zero lithium concentration Figure 37(d).

3.3. Monoclinic ZrO_2 (Undoped)

After the tetragonal zirconium oxide layer at the metal oxide interface, the monoclinic oxide layer is found and extends to the water oxide interface. As with the tetragonal, this oxide layer may have intrinsic defects including oxygen vacancy (V_O), zirconium vacancy (V_{Zr}), oxygen interstitials (O_i) and zirconium interstitials (Zr_i). It was also found with the monoclinic oxide that the zirconium interstitial was found outside of the bandgap so was omitted from further calculations. The bandgap in the monoclinic structure was found to be 3.5 eV which confirms previous work in the literature [177]. The defect formation energies were plotted starting with the zirconium vacancy having a negative two, three and four charge. The neutral and negative one charge defects were omitted, as these were found to be outside of the bandgap during calculations.

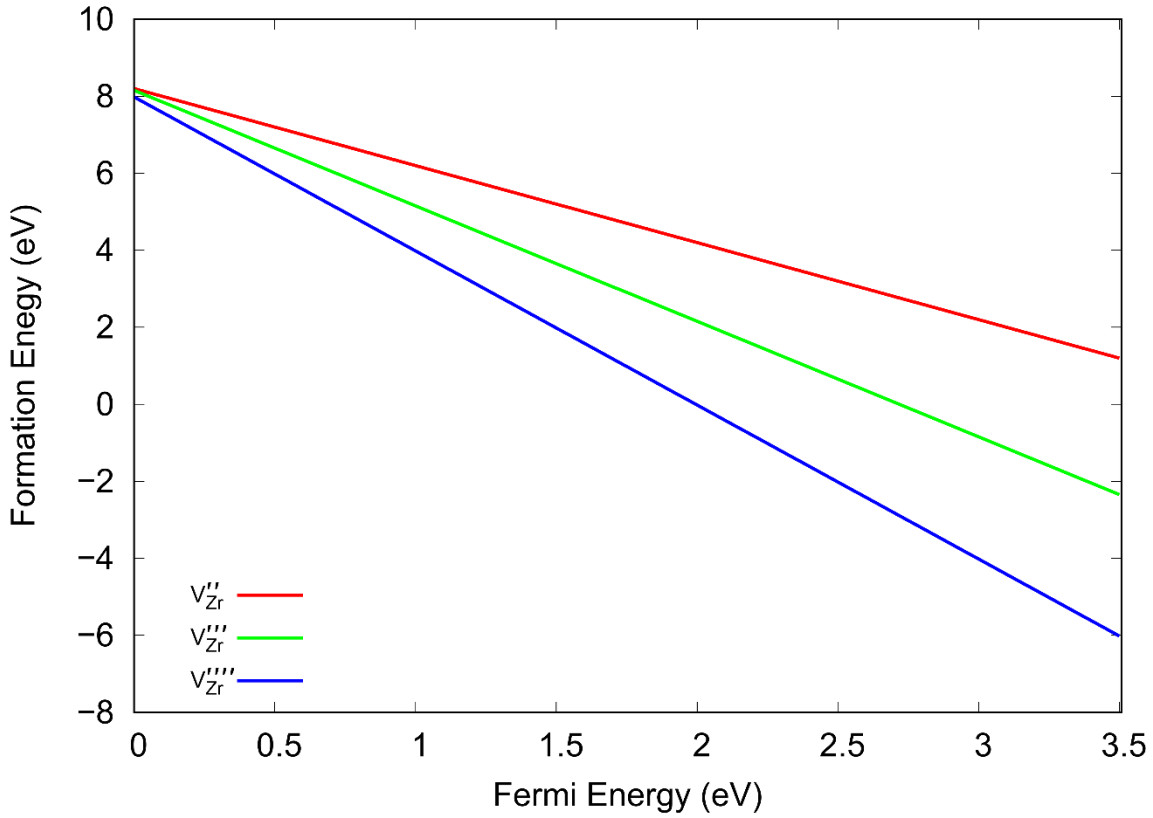

Figure 38 Formation energy of zirconium vacancy with a range of charges across the Fermi energy of the bandgap of monoclinic ZrO_2.

For the zirconium vacancy defects in the monoclinic structure, Figure 38, there is one clear defect that has the lowest formation energy across the bandgap and that is the negative four charged zirconium vacancy. This defect, however, does have a positive formation energy towards the valence band to the right but then has a negative formation energy from roughly 2 eV through to the bottom of the conduction band to the right. The negative three zirconium vacancy defect has a negative formation energy from roughly 2.7 eV through to the bottom of the conduction band. The negative two charged zirconium vacancy defect has a positive formation charge throughout the bandgap.

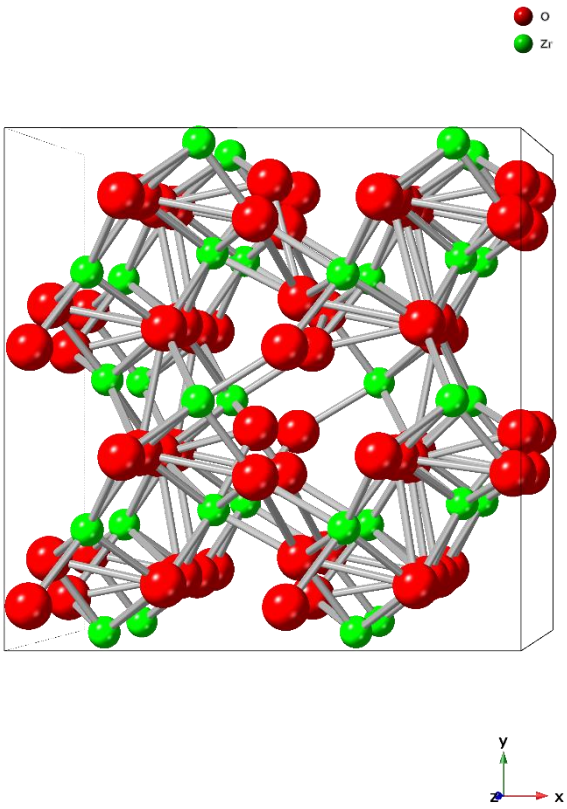

Figure 39 Monoclinic ZrO_2 structure with a zirconium vacancy defect (green) centre.

The monoclinic structure, by definition, looks less uniform than the tetragonal structure. But changes in atomic positions are still apparent. The zirconium vacancy structure (Figure 39) shows no big change in zirconium or oxygen positions over a perfect, relaxed, structure.

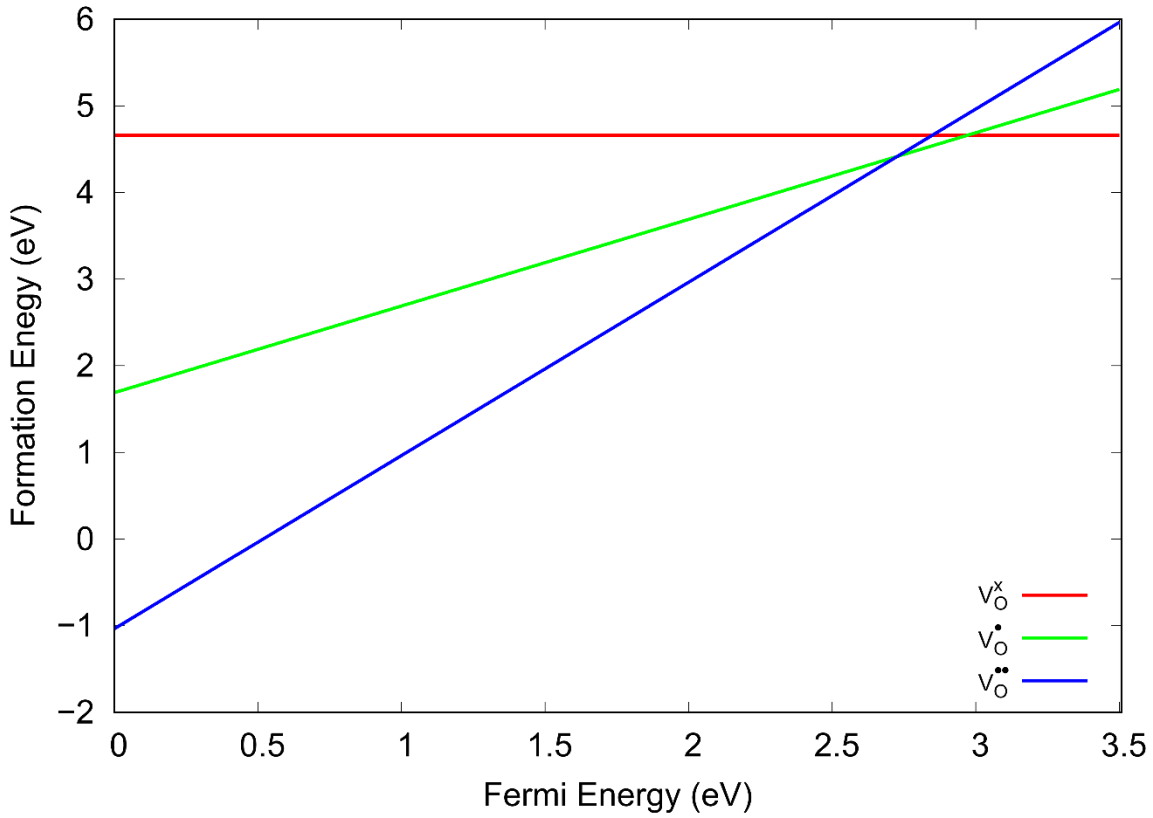

Figure 40 Formation energy of oxygen vacancy with a range of charges across the Fermi energy of the bandgap of monoclinic ZrO_2.

In the case of oxygen vacancy defects, the plus two charged defect shows the lowest formation energy towards the top of the valence band to the left, Figure 40. This defect is the only oxygen vacancy defect to have a negative formation energy which extend from the valence band to approximately 0.5 eV into the bandgap. It remains the lowest formation energy defect up to approximately 2.7 eV. This is followed by a small Fermi energy of plus one oxygen vacancy which is replaced by the neutral charged oxygen vacancy defect which has the lowest formation energy for the remainder of the band gap to the bottom of the conduction band.

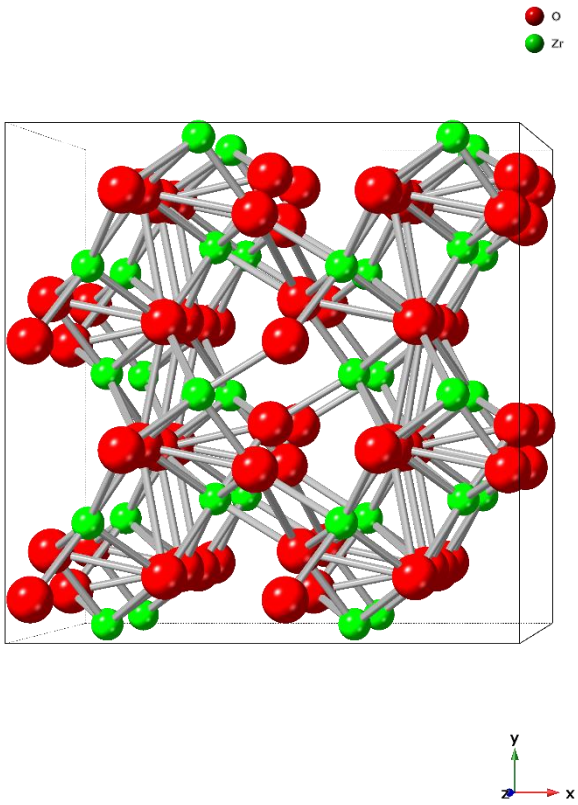

Figure 41 Monoclinic ZrO_2 structure with a oxygen vacancy (red) defect.

In the monoclinic ZrO_2 structure with an oxygen vacancy defect (Figure 41), the zirconium atom positions remain largely unchanged. The oxygen atoms also change slightly in position around the defect.

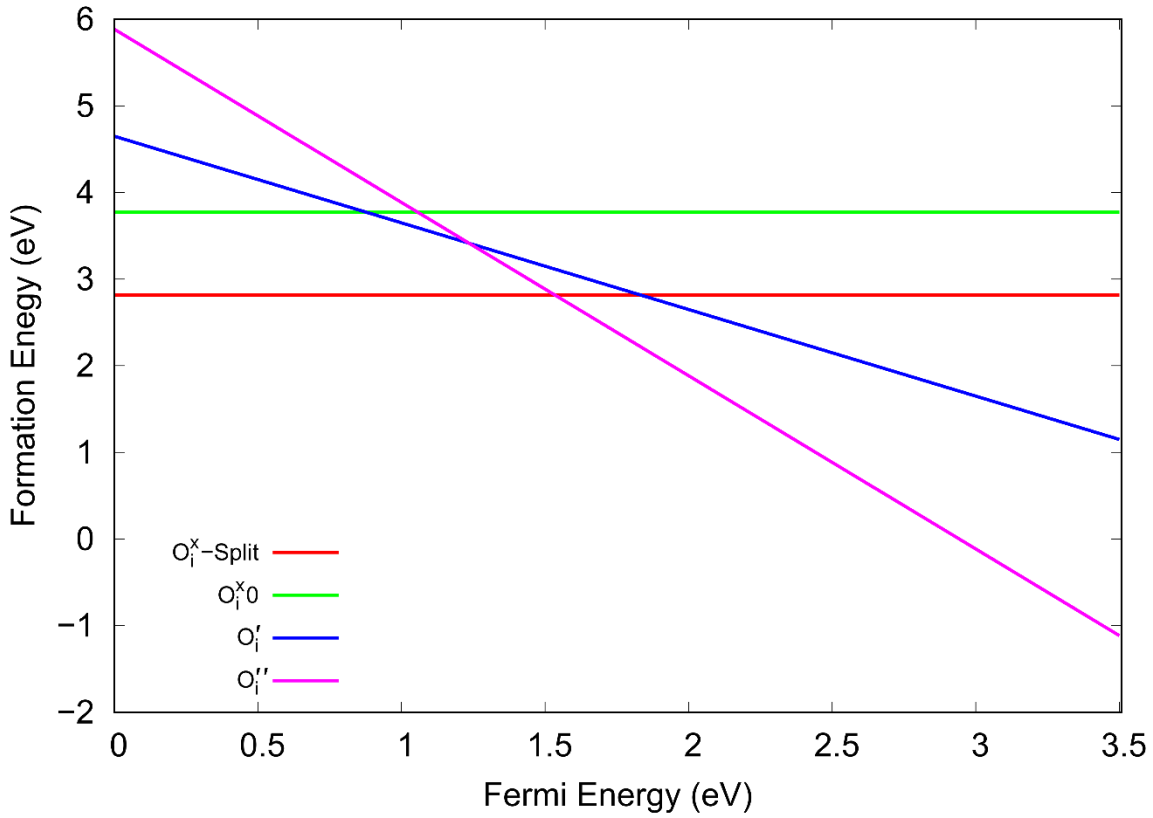

Figure 42 Formation energy of oxygen interstitials with a range of charges across the Fermi energy of the bandgap of monoclinic ZrO_2.

Finally, the oxygen interstitial shows two defects that share the lowest formation energies through the bandgap, Figure 42. From the top of the valence band, the neutral charged split interstitial has the lowest formation energy up to, roughly, 1.5 eV. From there, the negative 2 charged oxygen interstitial has the lowest formation energy to the bottom of the conduction band to the right. Only the negative 2 charged oxygen defect shows a negative formation from around 3 eV up to the bottom of the conduction band to the right. The neutral charged and the negative one defects do not have a lowest or negative formation energy across the band gap.

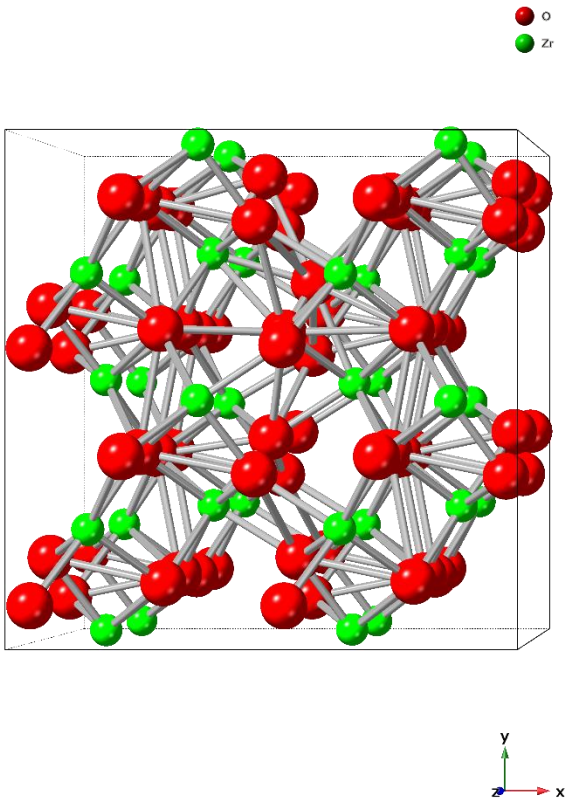

Figure 43 Monoclinic ZrO_2 structure with a split oxygen interstitial.

Much like the zirconium vacancy and oxygen vacancy monoclinic structures, the split oxygen interstitial structure, Figure 43, shows little change in zirconium and oxygen atom positions. The split oxygen defect is found slightly above the central point within the structure which slightly changes the surrounding oxygen atom positions.

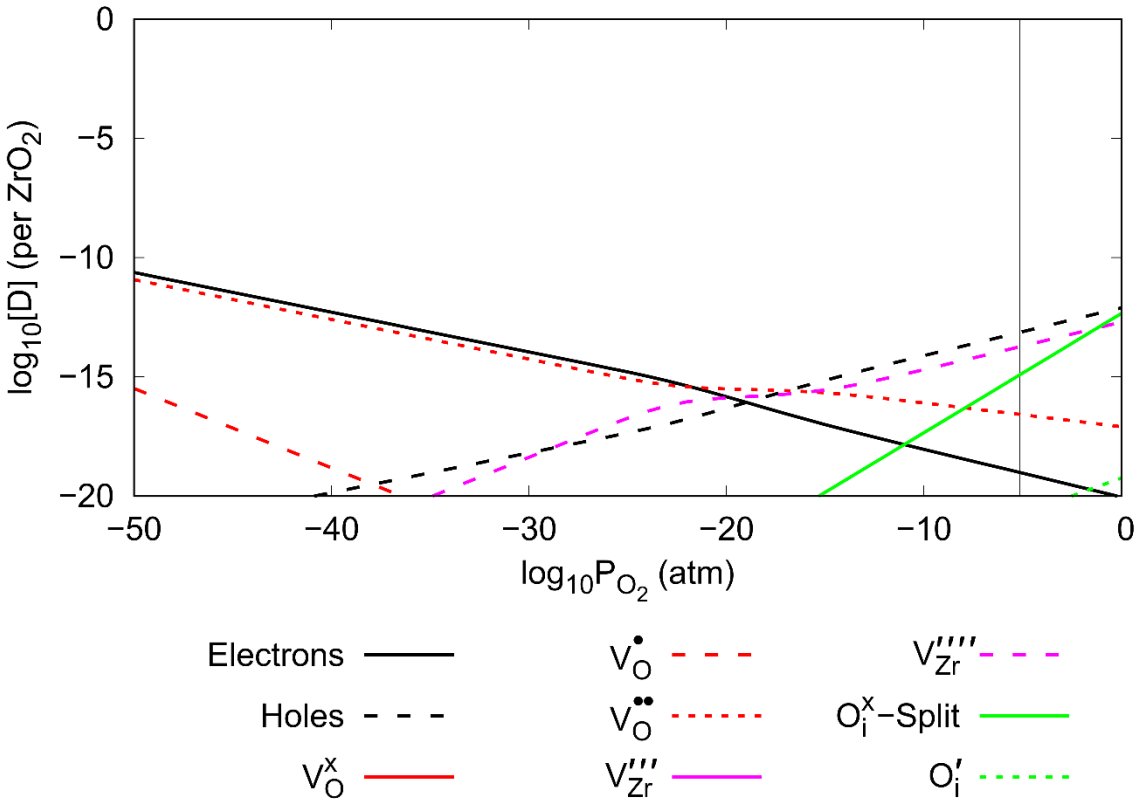

Figure 44 Brouwer diagram at 635 K of intrinsic defects in monoclinic ZrO_2.

The intrinsic defect Brouwer diagram for monoclinic ZrO_2, Figure 44, is not too dissimilar to that of the tetragonal. All defects, whilst maintaining the same trends, are at a reduced concentration when compared to the tetragonal Brouwer diagram. Where electrons and the plus two charged oxygen vacancy ($V_O^{\bullet\bullet}$) defects reach almost 10^{-5} concentrations at lower partial pressures, for the monoclinic, they reach almost 10^{-10}. Because of the overall reduction in all defect concentrations, the neutral charged oxygen vacancy ($V_O^{\times}$) is bellow the 10^{-20} concentration cut-off and cannot be seen in the monoclinic Brouwer diagram. This is also the case for the negative three zirconium vacancy (V_{Zr}''') and the negative two oxygen interstitial (O_i''). This does make for a more simplistic Brouwer diagram. A noteworthy difference in trends between the tetragonal and monoclinic Brouwer diagrams is that the split neutral charge oxygen interstitial ($O_i^{\times} - \text{split}$) maintains the same concentration in both, which results in this defect sharing similar concentrations to the negative four zirconium vacancy defect (V_{Zr}'''') at the highest partial pressure to the right. The ($V_O^{\bullet\bullet}$) defects closely follow the electron defect concentrations from the low partial pressure to the left of the diagram up to the roughly 10^{-20} atm partial pressure. Likewise, the (V_{Zr}'''') closely follows the hole concentration at higher partial pressures to the right. Where both defects meet at roughly 10^{-20} atm, the oxygen vacancy defect ($V_O^{\bullet\bullet}$) deviates with an increase in concentration over the electron concentration towards higher partial pressures and the zirconium vacancy (V_{Zr}'''') fluctuates from the hole concentration towards lower partial pressures. First, this shows an increase in concentration moving to the left, followed by a decrease. All other intrinsic defect concentrations seem unaffected by any other defect.

3.4. Li Doped Monoclinic ZrO_2

The first of the defects to be reviewed in the monoclinic structure is lithium. As with the tetragonal structure, the defects included were $(\mathrm{Li_i})$, $(2\mathrm{Li_i})$, $(\mathrm{Li_O})$, $(2\mathrm{Li_O})$, $(\mathrm{Li_{Zr}})$, $(2\mathrm{Li}{:}\,\mathrm{V_{Zr}})$, $(2\mathrm{Li_{Zr}})$, $(\mathrm{Li_{Zr}}{:}\,\mathrm{V_O})$, and $(2\mathrm{Li}{:}\,\mathrm{V_{Zr}}{:}\,\mathrm{V_O})$ with various charges. And again, only the lithium interstitials, $(\mathrm{Li_i})$, and the small defect cluster of two lithium interstitials around a zirconium vacancy site, $(2\mathrm{Li}{:}\,\mathrm{V_{Zr}})$, were found to be within the bandgap during the calculations which resulted in all other defects being omitted. Due to the low number of possible lithium defects, these could be plotted on one formation energy figure.

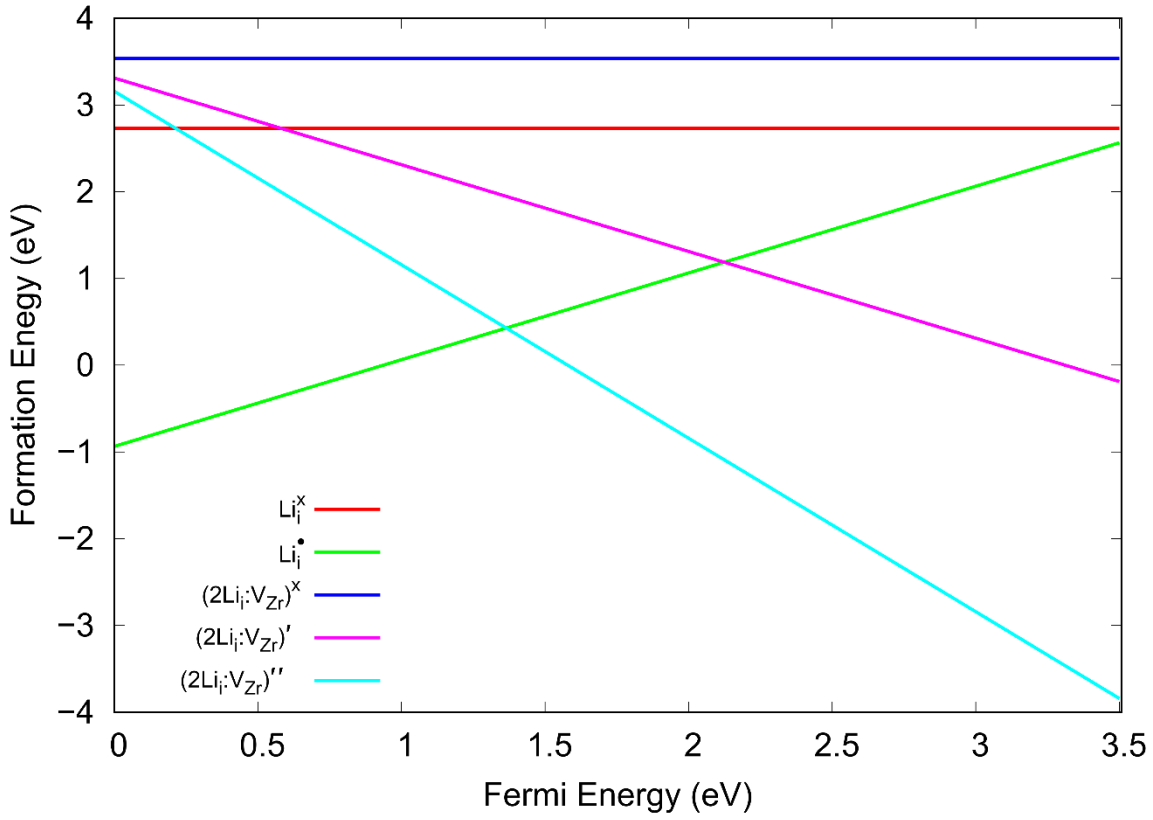

Figure 45 Formation energy of lithium defects with a range of charges across the Fermi energy of the bandgap in monoclinic ZrO_2.

For the lithium defect formation energy plot, Figure 45, the plus one charged lithium interstitial $(Li_i^\bullet)$ has the lowest formation energy towards the top of the valence band to the left. And the small negative two charged cluster $(2\mathrm{Li_i}{:}\,\mathrm{V_{Zr}})''$ has the lowest formation energy towards the bottom of the conduction band to the right. Both defects show a negative formation energy with the exception of the region between 1 and 1.5 eV Fermi energy which has a positive formation energy which coincides with the transition from $(\mathrm{Li_i^\bullet})$ to $(2\mathrm{Li_i}{:}\,\mathrm{V_{Zr}})''$ of lowest formation energy. All other defects remain in positive formation energy, however, the negative one charged cluster $(2\mathrm{Li_i}{:}\,\mathrm{V_{Zr}})'$ has a small negative formation energy at the very bottom of the conduction band to the far right. The neutral charged lithium interstitial and small cluster maintain a consistent, positive, formation energy.

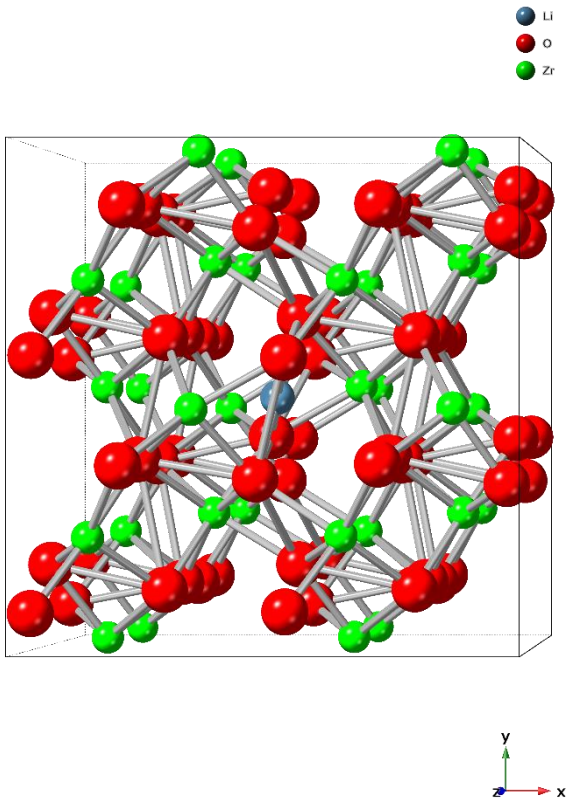

Figure 46 Monoclinic ZrO_2 structure with a lithium interstitial (blue) centre.

The lithium interstitial in the monoclinic ZrO_2 structure (Figure 46) shows only one subtle change in intrinsic atom position and that is with the two zirconium atoms either side of the lithium interstitial in the x direction which show separation of the zirconium atoms. But this does not affect any other atomic position.

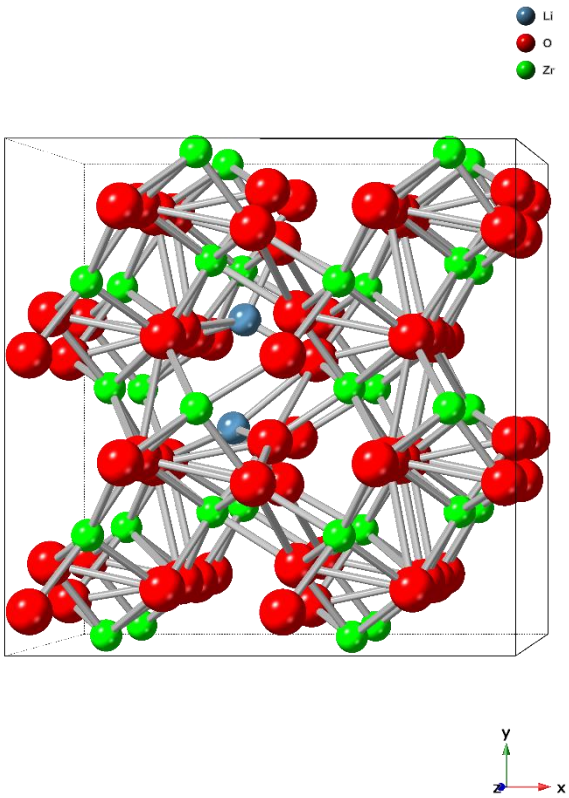

Figure 47 Monoclinic ZrO_2 structure with two lithium interstitials around a zirconium vacancy site with a oxygen vacancy.

For the cluster of two lithium interstitials around a zirconium vacancy site and an oxygen vacancy, Figure 47), there are very small changes in position of oxygen neighbouring defects which may be associated with the oxygen vacancy part of the cluster.

With the collection of lithium defect formation energy calculations, the monoclinic Brouwer diagram could be produced.

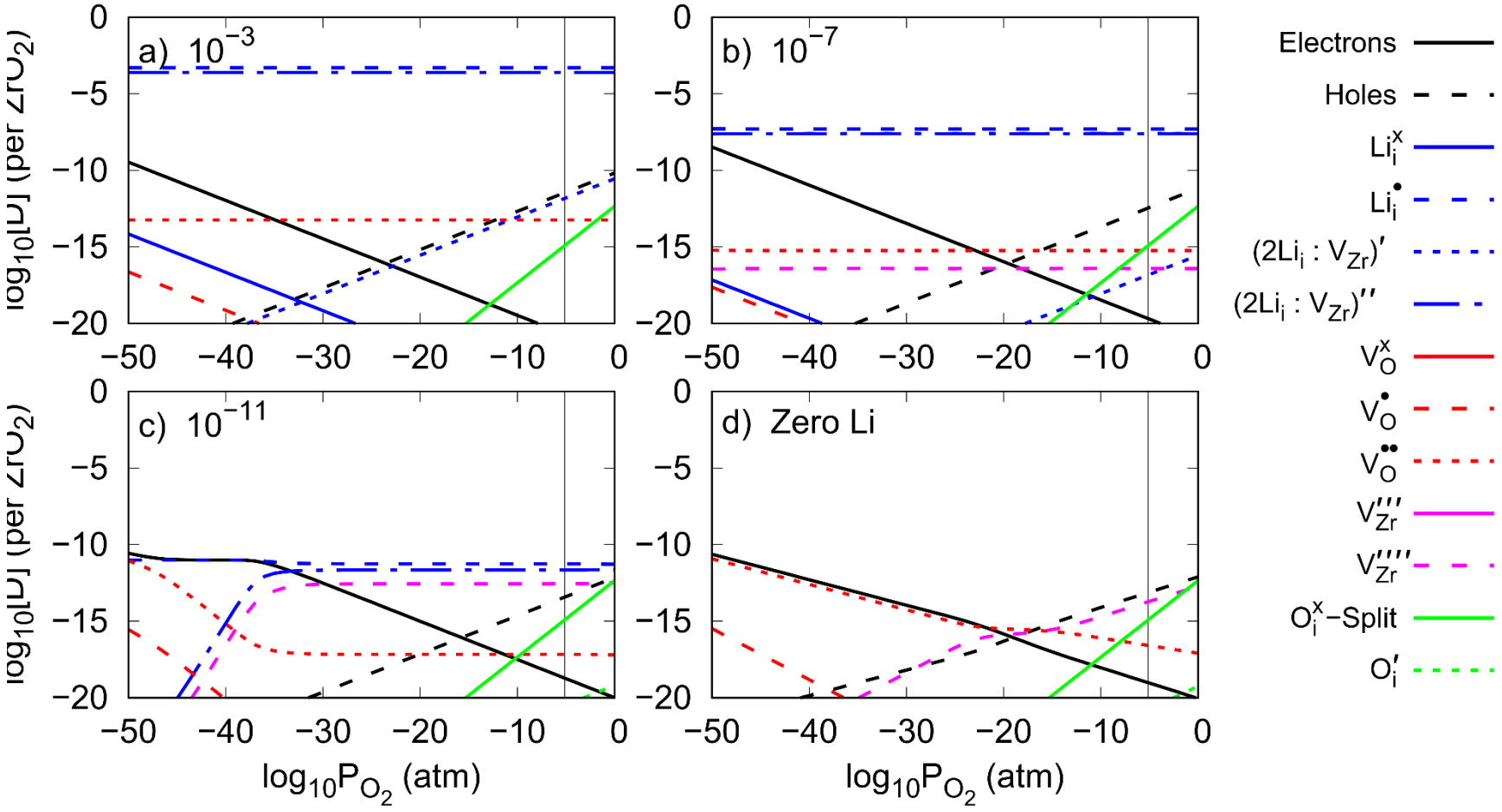

Figure 48 Li doped monoclinic ZrO2 Brouwer diagrams with the Li concentrations of a) 10^{-3} b) 10^{-7} c) 10^{-11} and d) with intrinsic defects only.

When viewing the highest lithium concentration of 10^{-3} per ZrO_2, Figure 48, (a), both the plus one lithium interstitial ($Li_i^{\bullet}$) and the small cluster of negative two charged two lithium interstitials around a zirconium vacancy site ($2Li_i : V_{Zr}''$) dominate as the highest concentration defects across the partial pressure range. When reviewing the tetragonal defects earlier, the intrinsic defects held a much higher concentration in the absence of lithium, so were not affected quite so much as the monoclinic. The negative four zirconium vacancy defect (V_{Zr}'''') is completely absent from the Brouwer diagram where the concentration is suppressed below the concentration range. The (V_{Zr}'''') is replaced with the small negative one cluster ($2Li_i : V_{Zr}'$) which follows the hole defect concentrations. There is a small concentration of neutral charged lithium interstitial defects ($Li_i^{\times}$) towards the lowest partial pressures to the right, but this defect does not appear to have any effect on the intrinsic defects. The most striking change is that of the plus two charged oxygen vacancy ($V_O^{\bullet\bullet}$) which has uncoupled from the electron concentrations and produces a linear concentration across all partial pressures. This results in a reduction in concentration at lower partial pressures to the left and an increase in concentration at higher partial pressures to the right towards the water oxide interface. The linear nature of this change looks to be a coupling with the lithium defect concentration of the negative two charged cluster ($2Li_i : V_{Zr}''$). It is likely that the plus one lithium interstitial ($Li_i^{\bullet}$) is charged balanced by the slightly lower concentration of the negative two charged cluster ($2Li_i : V_{Zr}''$). When the lithium concentration is reduced to 10^{-7} (b), we see a consistent reduction in the oxygen vacancy ($V_O^{\bullet\bullet}$), which remains linear, and the introduction of the zirconium vacancy defect (V_{Zr}''''). This also coincides with the reduction in concentration of the ($2Li_i : V_{Zr}'$) and the neutral charged lithium interstitial ($Li_i^{\times}$). When the overall lithium concentration is reduced to 10^{-11}, we begin to see more interactions between the defects as the lithium concentration becomes comparable to that of the intrinsic defects. The plus one charged lithium interstitial ($Li_i^{\bullet}$) reduces the electron concentration towards lower partial pressures to the left which coincides with a reduction in the negative two charged cluster ($2Li_i : V_{Zr}''$). Whilst the overall concentration of plus two oxygen vacancy ($V_O^{\bullet\bullet}$) decreases and the negative four zirconium vacancy (V_{Zr}'''') decreases, this drop in electron concentration removes the linearity of both, causing an increase of ($V_O^{\bullet\bullet}$) and a decrease in (V_{Zr}'''') at the lower partial pressures. Both the negative one small cluster ($2Li_i : V_{Zr}'$) and the neutral lithium interstitial ($Li_i^{\times}$) have concentrations below the range given. Finally, (d) shows a return to the intrinsic defects only without any lithium.

3.5. Volume Changes Due to Defects

Previous simulation work in the literature has identified larger than expected changes in volume in structures when allowing volumetric relaxation using DFT on charged defects over neutral charged defects [179]. Whilst there are methods to mitigate this, for the purpose of this investigation, we attempted to identify overall changes in volume when all defects are combined in their respective concentrations. This is not to provide a specific value of volume change, but to identify trends associated with these changes.

An increase in external pressure is expected to reduce the volume of the structure in all cases when applied. However, understanding the extent of compression, and its dependence on defects, may provide a method of pore growth or an increase in relative pressure resulting in mechanical/compressive failure. By reviewing a selection of defects for the tetragonal and monoclinic structures at pressures ranging from zero to three GPa, we can gain a general understanding of structural volume change under compression. Simply applying the volume change per defect multiplied by the defect concentration per ZrO_2 was used to calculate relative volumetric changes.

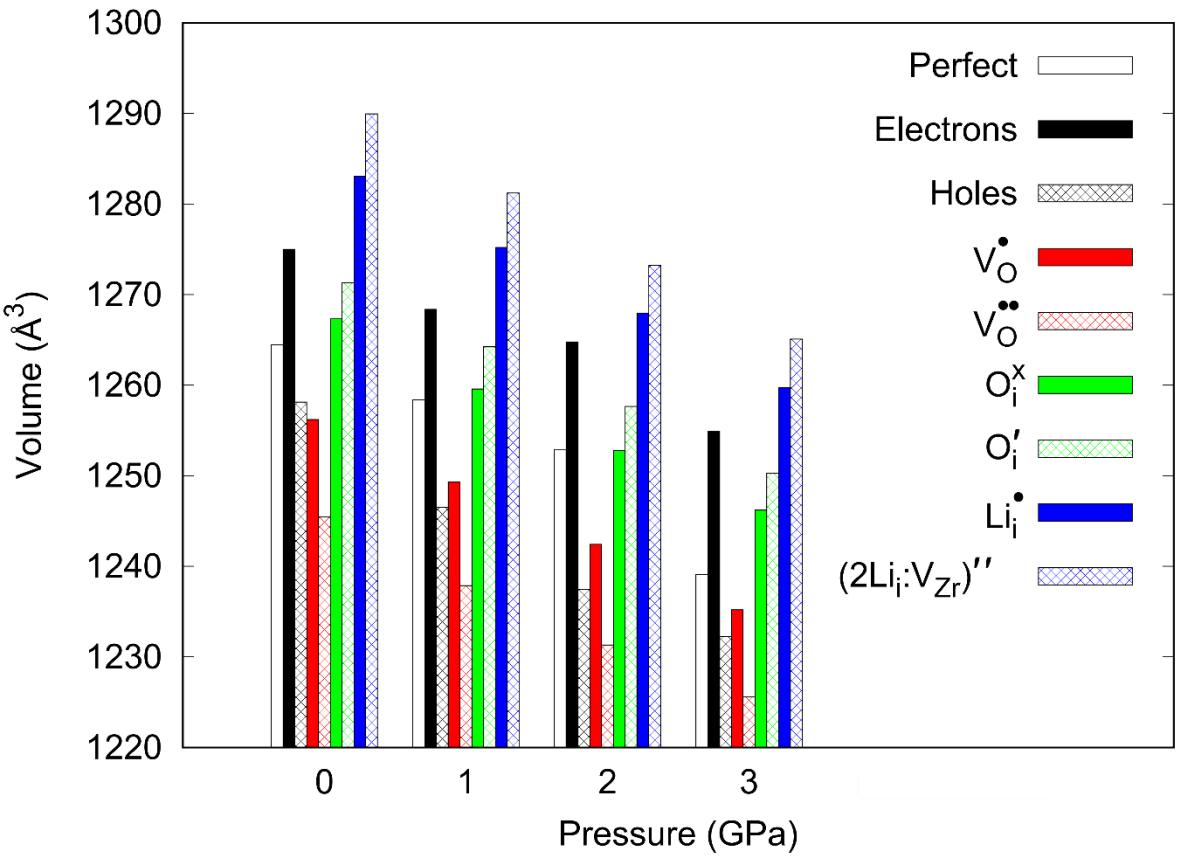

Figure 49 External pressure from zero to three GPa in tetragonal ZrO_2 neutral charge for a perfect (defect free) supercell (White), electrons (black), holes (black shaded), oxygen vacancy (red and red shaded), oxygen interstitial (green and green shaded), lithium interstitial (blue), and two lithium interstitials around a single zirconium vacancy (blue shaded).

For the tetragonal structure, *Figure 49*, we can see a general trend of reduced volume associated with increased pressure for all defects. Whilst this was expected, it was helpful to confirm this and to find a fairly linear volume reduction due to pressure. Whilst the defect structures oxygen vacancy, oxygen interstitial, lithium interstitial and the small cluster of two lithium interstitials around a zirconium vacancy site all show a linear volume reduction associated with increased pressure, they all reduce at different rates. The plus one charged oxygen vacancy, neutral charged oxygen interstitial and plus one charged lithium interstitial all had the same gradient of volume change (28° or 1:2.246). The plus two charged oxygen vacancy had a reduced gradient (23° or 1:2.356), the negative one charged oxygen interstitial had a greater gradient (26° or 1:2.050) and the plus one charged lithium interstitial had a greater gradient still (28° or 1:1.881). The perfect structure, however, maintained a 20° gradient from zero to two GPa, at three GPa, the volume dropped substantially. The electrons, however, showed no consistent gradient through the change in pressure. The hole defect showed a rapid reduction in volume from zero to two GPa but levelled off at three GPa. Other than an expected reduction in volume due to volume change, there appeared to be no other trends that could be associated with the defect gradient differences.

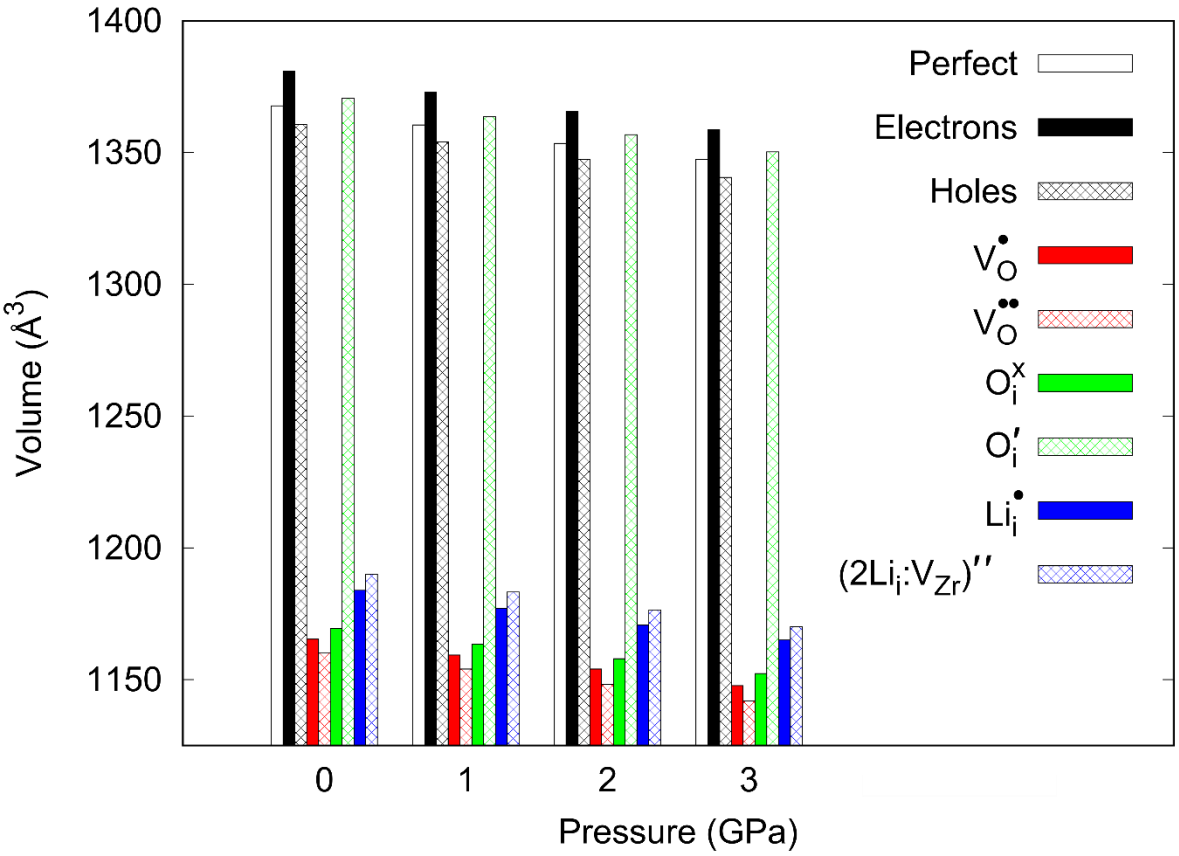

Figure 50 External pressure from zero to three GPa in monoclinic ZrO_2 neutral charge for a perfect (defect free) supercell (White), electrons (black), holes (black shaded), oxygen vacancy (red and red shaded), oxygen interstitial (green and green shaded), lithium interstitial (blue), and two lithium interstitials around a single zirconium vacancy (blue shaded).

In the case of the monoclinic structure, there was a much greater volume change associated with the defects, *Figure 50*, and this will be reviewed later. All the structures had a linear volume reduction associated with pressure increase in the monoclinic structure. The volume change associated with pressure was much less than what was observed in the tetragonal structure. The perfect structure, holes, plus two charged oxygen vacancy, neutral charged oxygen interstitial, negative one oxygen interstitial, and the cluster of two lithium interstitials around a zirconium vacancy site all had a relative gradient of 7°. electrons had an 8° gradient and the plus one charged oxygen vacancy and plus one lithium interstitial had a 6° relative gradient.

The tetragonal structure showed less volumetric difference between defects at a single pressure than what we see in the monoclinic structure. When pressure was applied, however, the tetragonal structure showed greater volumetric changes with increasing pressure. It was likely that the more uniform tetragonal structure withstood defects by subtle local atomic movements to the defect where the overall volume change is much lower when compared to the perfect structure. The monoclinic structure was a little less uniform where small local changes of atomic location had a knock-on effect on next nearest neighbours resulting in greater volumetric differences between defects overall. The monoclinic 2x2x2 supercell structure had 32 units of ZrO_2 where the tetragonal structure has 36. Even so, the perfect tetragonal structure had a smaller volume than the monoclinic due to efficient atomic ordering. All defects found on the Brouwer diagram will, however, need to be reviewed to confirm this.

Whilst the volume change associated with pressure produced fairly predictable results, finding the overall volume change associated with all defects combined could provide a clearer picture to

address hypothesis one (volume change could produce pores and accelerate corrosion). Using the defect concentration data gained from the Brouwer diagrams combined with volumetric data from constant pressure DFT calculations, the overall change in bulk ZrO_2 structure volume could be calculated providing an indication of an increase in pressure or an increase in oxygen pathways.

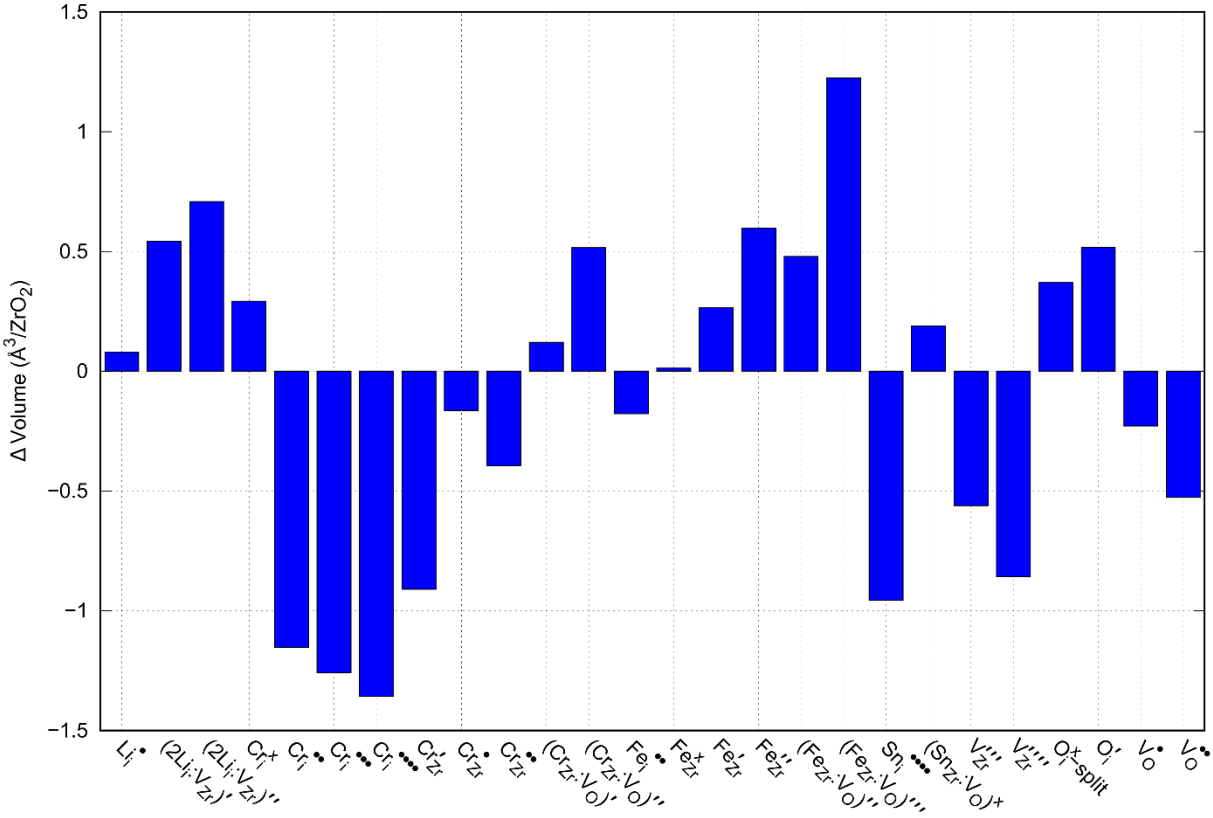

Figure 51 Defect volume change per ZrO_2 in the tetragonal structure.

When viewing all of the defects calculated within the tetragonal ZrO_2 Brouwer diagram and the volume changes per ZrO_2, *Figure 51*, many defects reduce the volume. There are, however, equal defects that increased the volume as there are that reduced the volume. The volume change ranged from -1.36 to 1.22 $Å^3$ per ZrO_2 with the greatest increase of volume from the iron substitution on a zirconium site with an oxygen vacancy and a negative three charge. The defect that reduced the volume the most was the chromium interstitial with a positive four charge. In the tetragonal structure, all lithium defects caused an increase in volume. The plus one charged lithium interstitial showed a small increase in volume, particularly when compared to the small cluster lithium defects. The volume of the perfect tetragonal structure was found to be 1267 $Å^3$ with 36 ZrO_2 units producing 25.2 $Å^3$ per ZrO_2.

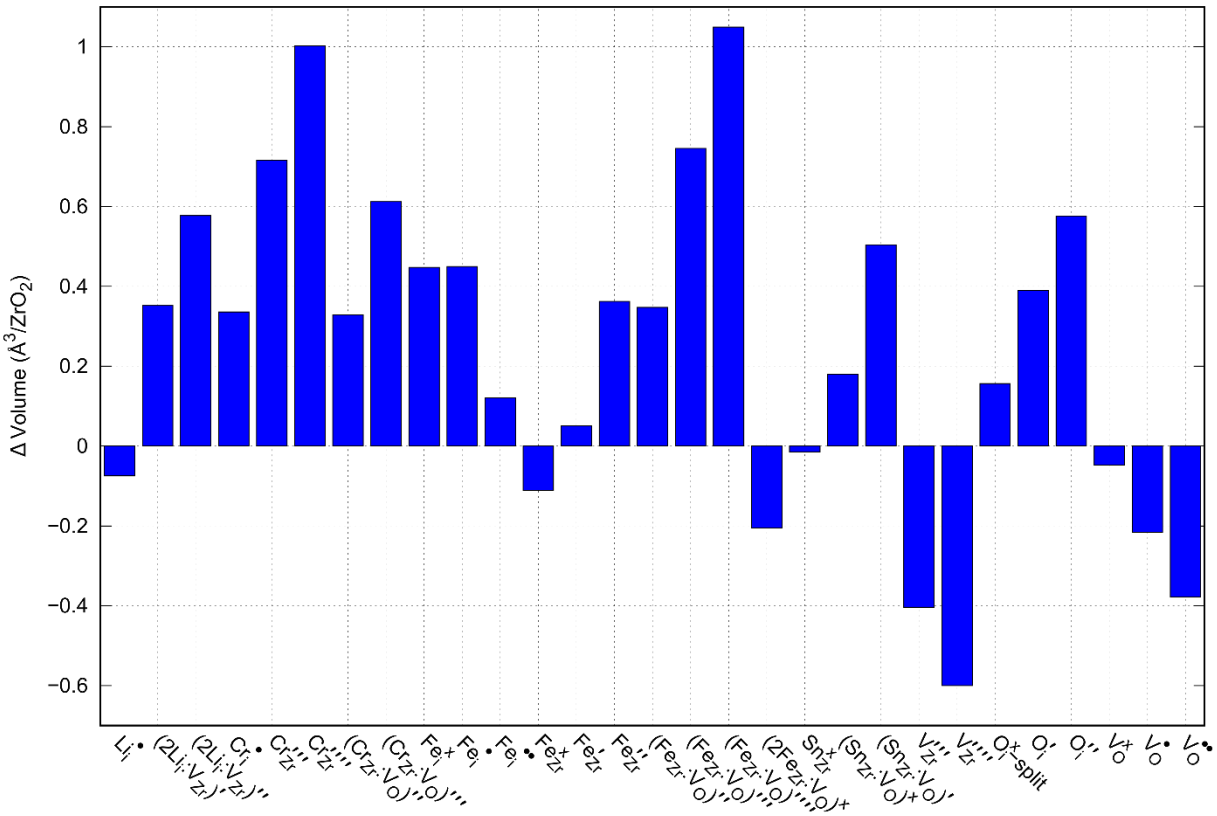

Figure 52 Defect volume change per ZrO2 in the monoclinic structure.

In the monoclinic structure, most defects caused an increase in volume where 20 defects caused an increase in volume and only 8 caused a decrease, *Figure 52*. The greatest increase in volume at 1.05 $Å^3$ per ZrO_2 was caused by the small cluster of an iron substation on a zirconium site with an oxygen vacancy and a negative four charge, which is similar to that of the tetragonal structure. The defect that caused the greatest reduction in volume was the zirconium vacancy defect with a negative four charge. The small lithium clusters, again, caused an increase in volume. The lithium interstitial with a plus one charge, however, caused a reduction in volume. Previous work in the literature has shown a decrease in volume for the plus one charged lithium interstitial in both the tetragonal and monoclinic structures [180]. More so for the monoclinic structure than the tetragonal structure but understanding how this might affect overall volume change will provide a more complete picture.

The volume change per ZrO_2 could not be an accurate representation unless it was combined with the concentration of defects per ZrO_2 which was provided by the Brouwer diagrams. Combining the data from both could produce an overall volume change through the oxide layer.

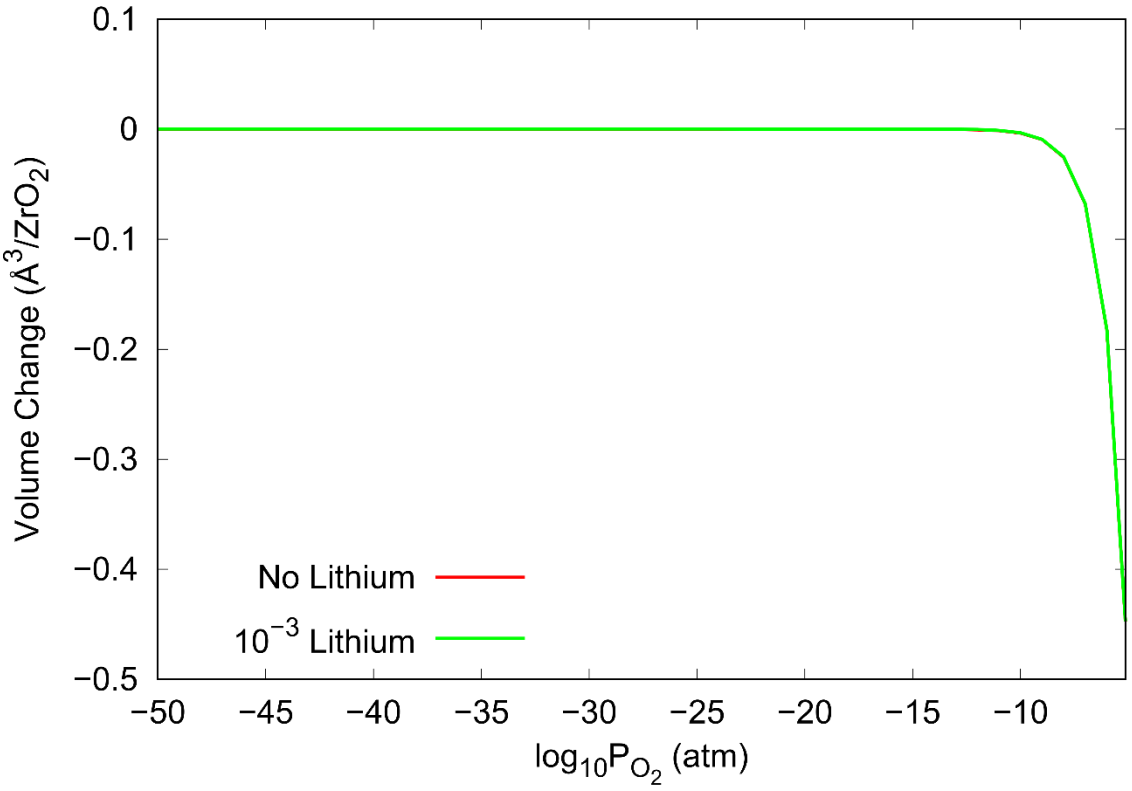

Figure 53 Combined volume change from the perfect (No lithium) tetragonal ZrO_2 structure and all defects found in the Brouwer diagram showing the sum of all defects and concentrations per ZrO_2 with lithium doped and undoped.

When all defect volume changes were multiplied by the defect concentration found within the Brouwer diagram and summed, the overall volume change could be calculated from the water oxide interface ($10^{-5.14}\ P_{O_2}\ atm$) and through the oxide layer, *Figure 53*. For the tetragonal structure, the volume changed between the structures containing Li, Cr, Fe, Sn and the structure containing Cr, Fe, Sn (No Li) were virtually the same at first glance. *Figure 53***Error! Reference source not found.** shows the change in volume from the perfect ZrO_2 structure. Both the 10^{-3} per ZrO_2 lithium concentration and no lithium structures showed very little change in volume from the perfect structure and remained at zero for most of the partial pressure range. However, at higher partial pressures, towards the water/oxide interface to the right, the volume dropped by -0.45 Å^3 per ZrO_2. This drop began at roughly $10^{-10}\ P_{O_2}$ atm all the way up to the water/oxide interface. Though, it is important to point out that the tetragonal structure is unlikely to be in contact with the water/oxide interface, as it predominantly resides towards the metal oxide interface as a thin layer before stress relief gives way to the monoclinic structure.

Because the cladding material is an alloy, measuring the net volume change difference between the combined intrinsic and alloying additive defects and the forementioned including lithium defects in the tetragonal structure provided a more accurate depiction.

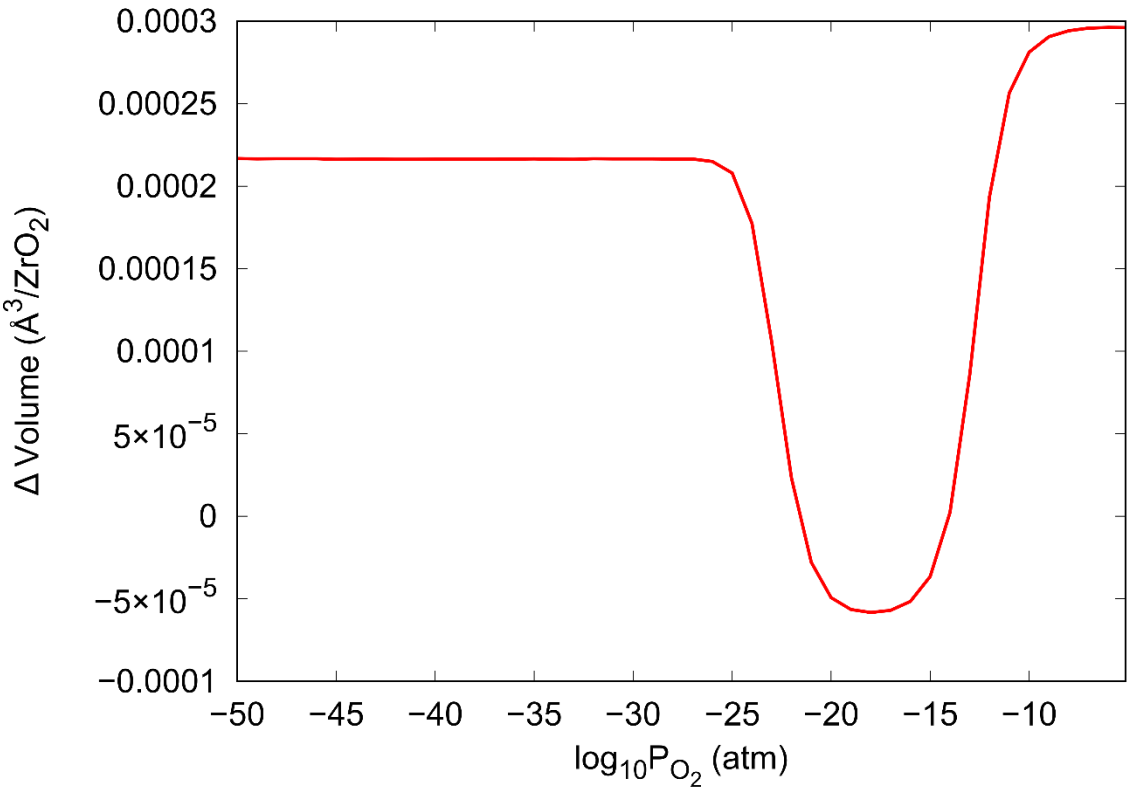

Figure 54 Volume difference (ΔV) between tetragonal ZrO_2 containing Cr, Fe, Sn and tetragonal ZrO_2 containing 10^{-3} Li, Cr, Fe and Sn across a partial pressure of oxygen range.

The comparison in volume change between the tetragonal ZrO_2 structure containing the alloying addition defects and the lithium doped with alloying addition defects could be considered as a much more representative indication of expected volume change due to lithium ingress, *Figure 54*. In general, lithium increased the volume of the structure overall with the highest volume increase at the water/oxide interface (0.0003 $Å^3$ per ZrO_2). Moving into the oxide layer, at around $10^{-10}\ P_{O_2}\ atm$, the volume difference drops where lithium reduced the volume of the alloyed structure down around -0.00005 $Å^3$ per ZrO_2. From the lowest partial pressure up to $10^{-25}\ P_{O_2}\ atm$, lithium increases the volume consistently at 0.00023 $Å^3$ per ZrO_2. Overall, the change in volume between the alloyed structure and the lithium doped alloyed structure was very small when the defects were all given concentrations predicted in the Brouwer diagrams. With the lithium concentration being stipulated and constant across the partial pressure range, the dip in volume was a result of lithium affecting the concentration of other defects. In the 10^{-3} per ZrO_2 lithium concentration Brouwer diagram containing all defects, the 10^{-3} per ZrO_2 lithium increased the plus two charged oxygen vacancy whilst also reducing the negative four zirconium vacancy defects. Both of which produced a reduced volume in the tetragonal ZrO_2 structure. The zirconium vacancy defect produced a larger volume reduction than the oxygen vacancy defect. The oxygen vacancy concentrations between 10^{-25} and $10^{-10}\ P_{O_2}$ atm, however, exceeded all other intrinsic defect concentrations when compared to the no lithium Brouwer diagram.

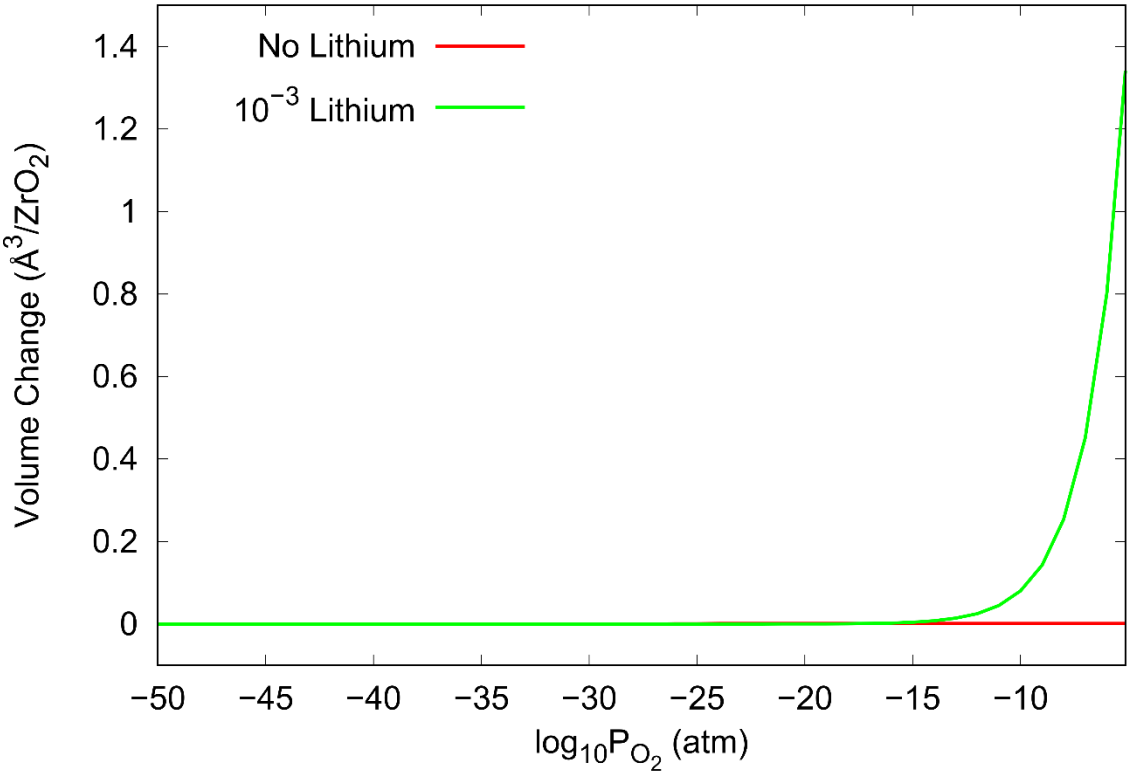

Figure 55 Combined volume change from the perfect monoclinic ZrO_2 structure and all defects found in the Brouwer diagram showing the sum of all defects and concentrations per ZrO_2 with lithium doped and undoped.

When comparing the volume difference between the perfect monoclinic structure against the alloying defects and the combined alloying and lithium defects there was more disparity than what was given in the tetragonal structure, *Figure 55*. The monoclinic structures containing the alloying additions maintained no apparent change to the perfect structure with alloying defect concentrations provided in the monoclinic Brouwer diagram. With the addition of 10^{-3} per ZrO_2 lithium per ZrO_2 showed an increase in volume from 10^{-15} P_{O_2} atm up to the water/oxide interface. This reached an increased volume up to 1.4 $Å^3$ per ZrO_2 at the water/oxide interface.

Given that the volume change in the alloying defects without lithium appear to maintain a consistent volume similar to that of the perfect structure, it was no surprise that the change in volume between the alloy addition defects structure and the lithium doped alloying addition defects produced very similar results.

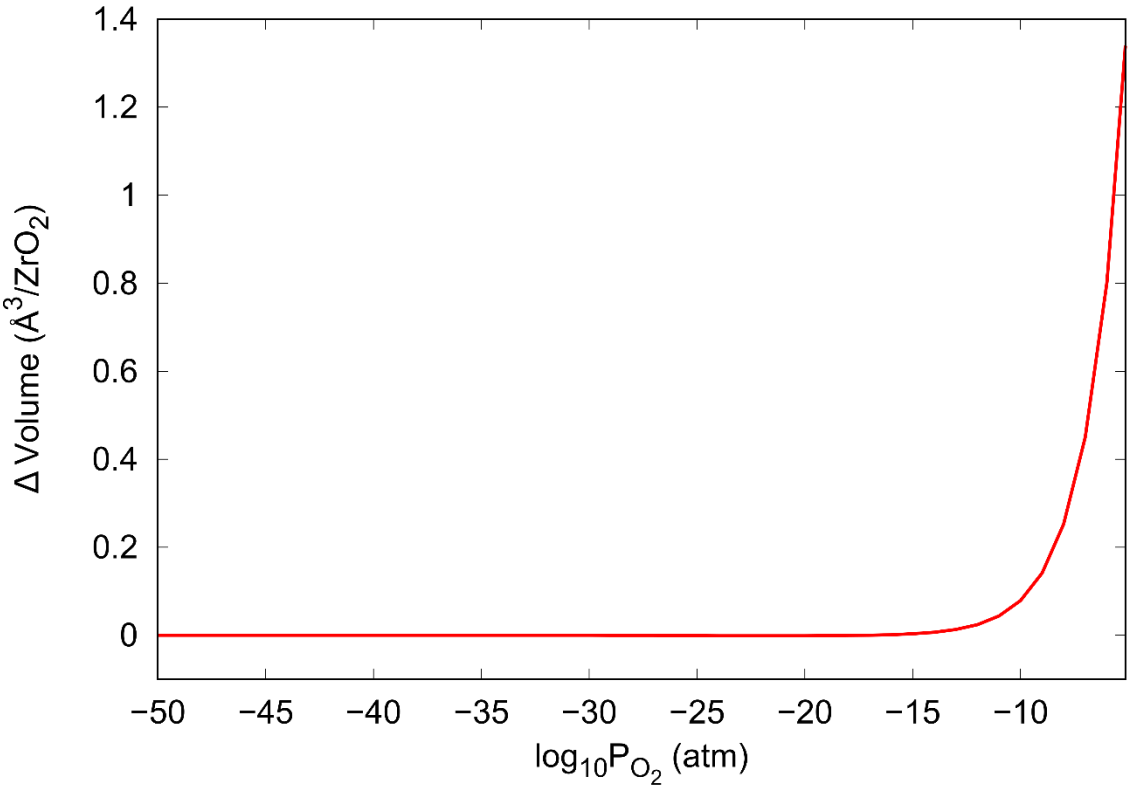

Figure 56 Volume difference between monoclinic ZrO2 containing Cr, Fe, Sn and monoclinic ZrO2 containing 10-3 Li, Cr, Fe and Sn across a partial pressure of oxygen range.

When reviewing the monoclinic ZrO_2 Brouwer diagram containing all defects, including lithium, it was apparent that the plus two charged oxygen vacancy defect concentration was increased greatly over the non-lithiated diagram, particularly towards the water/oxide interface. Should lithium form solution into the alloyed monoclinic structure, an increase in volume, predominantly at the water/oxide interface, has the potential to cause the outer oxide layers to form a compressed region and may even cause the outermost layers to break away, *Figure 56*. But this would require further investigation.

3.6. Solution Energies

Whilst calculations could be made to predict the formation energy of defects, the defect concentration and the volume change that may result from the defects within the structures, should a defect require external energy to form solution into the structure, it would make it unlikely to physically occur.

Because Sn did not affect any other defect concentration, according to the Brouwer diagram, creating solution energy reactions became tricky as the inclusion of other defects to balance the equation were not apparent.

The highest Sn defect concentration in the tetragonal structure was that of the small cluster $(Sn_{Zr}{:}V_O)^{\times}$, most reactions calculated produced a solution energy between 2.8 to 13.0 eV which were very high indicating a low likelihood of solution forming. There was, however, one reaction that produced a low solution energy.

$$SnO_2 + 3V_O^{\bullet\bullet} + V_{Zr}^{''''} + 2e' \rightarrow (Sn_{Zr}{:}V_O)^{\times} + 4O_O^{\times} \qquad \text{Equation 17}$$

Equation 17 produced a solution energy of -1.8 eV in the tetragonal structure indicating high solubility.

For the monoclinic structure, the interstitial ($Sn_i^{\bullet\bullet\bullet\bullet}$) showed the highest defect concentration in the Brouwer diagrams and produced solution energies that indicated a high likelihood for tin solution. The highest solution energy found was 3.3 eV which was found across three reactions. Five other reactions produced very negative solution energies with the most plausible value being obtained from equation 18 which produced a -0.87 eV solution energy.

$$Sn_3Zr_5 + 10O_i^{\times} \rightarrow 3Sn_i^{\bullet\bullet\bullet\bullet} + 5ZrO_2 + 12e' \qquad \text{Equation 18}$$

The tin defects all showed plausible solution energies but required intrinsic defects to balance the reaction equations. As mentioned earlier, evidence of tin being found throughout the bulk material has been found which indicates that further investigations might be needed to identify the species of tin and intrinsic defects that may be found to produce a reliable reaction.

For iron defects, the $(Fe_{Zr}: V_O)''$ defect showed the highest concentration in the tetragonal structure. Most reactions calculated produced a solution energy between 0.5 to 1.8 eV. The solution energy from equation 19 produced a very low solution energy of -3.6 eV, which indicates very high solubility.

$$FeZrO_3 + 2e' + Zr_{Zr}^{\times} + O_O^{\times} \rightarrow (Fe_{Zr}: V_O)'' + 2ZrO_2 \qquad \text{Equation 19}$$

The next highest iron concentration defect in tetragonal structure was the iron substitution on a zirconium site with a negative one charge (Fe'_{Zr}). The highest solution energy found through the reaction calculations was 2.3 eV with all others being below 0.2 eV indicating a favourable reaction. Equation 20 produced a solution energy of -1.3 eV indicating high solubility.

$$Fe_2Zr + 3V_{Zr}'''' + 5h^{\bullet} \rightarrow 2Fe'_{Zr} + Zr_{Zr}^{\times} \qquad \text{Equation 20}$$

For the monoclinic structure, the highest iron concentration defect was the positive one charged interstitial ($Fe_i^{\bullet}$). This produced mixed results with positive values between 3.5 to 3.6 eV and negative values between -0.02 and -5.9 eV. The most plausible reaction showing -0.02 eV is given in equation 21.

$$Fe_3O_4 + 4V_O^{\bullet\bullet} + 5e' \rightarrow 3Fe_i^{\bullet} + 4O_O^{\times} \qquad \text{Equation 21}$$

The iron defect with the second highest concentration in the Brouwer diagram is the small positive one charged cluster $(2Fe_{Zr}: V_O)^{\bullet}$. The reaction solution energies produced mixed results with positive values from 0.5 to 6.9 eV. The negative solution energies were, however, relatively low from -1.75 to -6.4 eV. The most plausible of these being the -1.75 eV given in equation 22.

$$Fe_2O_3 + 2V_O^{\bullet\bullet} + V_{Zr}'''' + h^{\bullet} + Zr_{Zr}^{\times} \rightarrow (2Fe_{Zr}: V_O)^{\bullet} + ZrO_2 + O_O^{\times} \qquad \text{Equation 22}$$

It was identified when calculating the Brouwer diagrams that iron defects had the potential to reduce the oxygen vacancy defect concentration. The two later equations for the monoclinic structure showed oxygen vacancy defects in the reactant which would result in reduced oxygen vacancy concentrations. In the tetragonal structure, however, there were no reactions that could be found with a negative solution energy which would result in a reduction in oxygen vacancy defect concentration. The most favourable reaction resulting in reduced oxygen vacancy defect concentration was calculated to -2.84 eV and given in equation 23.

$$2FeZrO_3 + 3V_O^{\bullet\bullet} + 2V_{Zr}^{''''} + 3h^{\bullet} + Zr_{Zr}^{\times} + O_O^{\times} \rightarrow (2Fe_{Zr}: V_O)^{\bullet} + 2ZrO_2 \qquad \text{Equation 23}$$

The two highest chromium defect concentrations in the tetragonal structure were the plus three charged interstitial ($Cr_i^{\bullet\bullet\bullet}$) and the negative one charged cluster $(Cr_{Zr}: V_O)'$. Both of which produced only positive solution energies from 2.27 to 6.2 eV for the interstitial and 6.04 to 9.79 eV for the small cluster. Other chromium defects, however, produced more promising results such as the substitution on a zirconium site with a negative three charge ($Cr_{Zr}^{'''}$) in equation 24 which produced a solution energy of -1.11 eV.

$$Cr_2Zr + 3V_{Zr}^{''''} + 6h^{\bullet} \rightarrow 2Cr_{Zr}^{'''} + Zr_{Zr}^{\times} \qquad \text{Equation 24}$$

The highest concentration defect found in the monoclinic structure was the chromium substitution on a zirconium site and a negative three charge. All calculated reactions produced negative energy results between -0.41 and -7.27 eV. The most plausible being the former with the reaction found in equation 25.

$$Cr_2Zr + O_2 + 2V_{Zr}^{''''} + 2h^{\bullet} \rightarrow 2Cr_{Zr}^{'''} + ZrO_2 \qquad \text{Equation 25}$$

The chromium defect with the second highest concentration found in the monoclinic Brouwer diagram was the negative two charged small cluster $(Cr_{Zr}: V_O)''$. The calculations were found to produce only negative values between -2.55 and -6.15 eV indicating a high likelihood of solubility. The former is given in equation 26.

$$Cr_2O_3 + V_O^{\bullet\bullet} + 2Zr_{Zr}^{\times} + O_O^{\times} + 6e' \rightarrow 2(Cr_{Zr}: V_O)'' + 2ZrO_2 \qquad \text{Equation 26}$$

The solubility of chromium is found to be plausible and can also explain variations in intrinsic defects that were found in the Brouwer diagrams. These are related to a decrease in oxygen vacancy and defects that have been shown, but these do not account for oxygen vacancy and increases in concentration which were also identified in the Brouwer diagrams.

Finally, the lithium defects have shown a large increase in oxygen vacancy defects on the Brouwer diagrams, particularly towards the water oxide interface and these are predominantly associated with the negative two charged small cluster $(2Li_i: V_O)''$. All attempted calculation for solution energies in the tetragonal and monoclinic structures were positive suggesting that the solution was unlikely. The energies were found between 2.80 to as high as 23.96 eV.

$$Li_2ZrO_3 + O_O^{\times} + Zr_{Zr}^{\times} \rightarrow \{2Li_i^{\bullet}: V_{Zr}^{''''}\}'' + V_O^{\bullet\bullet} + 2ZrO_2$$ Equation 27

This produced a solution energy of 2.29 eV in the tetragonal structure and 2.80 eV in the monoclinic structure. This has been confirmed with experimental data that shows the segregation of lithium along the grain boundaries [181].

3.7. Summary and Discussion

This chapter aimed to address the first hypothesis to find if lithium incorporation into the bulk oxide would alter the volume of the structures or if lithium might alter intrinsic defect concentrations that might aid the transport of oxygen from the water oxide interface to the metal oxide interface. This was the first stage in identifying a route in which lithium accelerates the corrosion of zirconium oxides.

The methods used in this chapter first identified the possible defects that may be found within the structure including the intrinsic defects, the potential alloying defects that may be found within the zirconium alloy (Zircaloy-4) and the introduced lithium defects. The formation energy of these defects were reviewed across the bandgap of both the tetragonal and monoclinic defects to find how charge might alter the concentrations of these defects. These defects were then calculated into Brouwer diagrams to assess the defect concentrations that may be found across the oxide layer. Volumetric changes were reviewed when all defect concentrations were combined and the solution energy for the highest concentration defects were evaluated to identify the plausibility of these defects to form solution into the tetragonal and monoclinic oxides.

The formation energy diagrams presented the possible formation energy of each defect that could be calculated within the Fermi level across the bandgap for both the tetragonal and monoclinic oxides. The formation energy of a defect within the structure is the required energy needed to form. Higher formation energies would require more energy to form and, thus, would be less likely to occur. The lower formation energy defects indicated a higher likelihood of these defects featuring in the Brouwer diagrams where positive charged defects held a lower formation energy at the top of the valence band which is indicative of a low Fermi level and a negatively charged structure. The opposite was found with negatively charged defects that held lower formation energies towards the bottom of the conduction band with a high Fermi level indicating a positively charged structure. The results were as expected where higher charged defects held a lower formation energy towards the respective Fermi level change. The more negative charged defects held a lower formation energy at higher Fermi energies and vice-versa for the positively charged defects. Neutral charge defects held a constant formation energy across the bandgap.

Whilst the formation energy across the bandgap diagrams provided a good indication of defects that may form with a preference to defects with a lower formation energy, this did not guarantee their appearance on the Brouwer diagrams themselves. The defects needed to produce charge neutrality across the oxide layer and required available opposite charged defects to achieve this. In general, this might give the indication that the neutral charged defects could fill the Brouwer diagrams but the formation energy was required to be sufficiently low against competing charged species to appear on the diagrams.

Brouwer diagrams containing lithium with intrinsic defects showed that lithium would increase the oxygen vacancy defects, particularly towards the water oxide interface at higher partial pressures. Should lithium form solution into the bulk oxide structures, this would provide a route for oxygen to

pass through the oxide by “hopping” from vacant site to vacant site forming a highway for oxidation at the metal oxide interface. This would only occur, however, when the lithium concentration was greater than that of the oxygen vacancy defect concentration (approximately 10^{-11} per ZrO_2 for tetragonal and 10^{-17} in monoclinic).

Chromium was found to slightly increase the oxygen interstitials in the tetragonal structure and also increase the zirconium vacancy concentration towards the water oxide interface. This also coincided with a slight decrease in oxygen vacancy defects. In the monoclinic structure, the opposite was found. Chromium increased the oxygen vacancy defect concentration significantly and reduced the zirconium vacancy defects below the evaluated range.

In the tetragonal structure, iron changed the intrinsic defect concentrations above the water oxide interface at high partial pressures but show very little changes into the oxide. In the monoclinic structure, on the other hand, the iron greatly reduced the oxygen vacancy defect concentration and increase the zirconium vacancy concentrations.

In both the tetragonal and monoclinic structures, the tin defects showed no apparent bearing on the intrinsic defect concentrations. This is due to tin having a similar oxidation state, atomic radii and occupy the same lattice site as zirconium [123].

Whilst each extrinsic defect elements had been reviewed individually with the zirconia intrinsic defects, bringing all of these defects together could provide a greater indication of possible defect concentrations when all defects compete. This also had the undesirable effect of producing Brouwer diagrams with such a large number of defects that it became difficult to identify changes associated with individual defects. By hiding the chromium, iron and tin defects and leaving only the lithium and intrinsic defects, the effect that lithium may have on the structures could become more apparent. At higher lithium concentrations (10^{-3} per ZrO_2), the oxygen vacancy was no longer increased at the water oxide interface in the tetragonal structure. This was due to the iron suppressing the oxygen vacancy defects in this region. There was, however, an increase of oxygen vacancy in a small region midway through the oxide layer (10^{-15} to 10^{-30} P_{O_2}). This resulted in lithium only affecting the concentration of oxygen vacancy with lithium concentrations of approximately 10^{-7} per ZrO_2 upward. At the same time, the zirconium vacancy defects were reduced in concentration over the same partial pressure region. In the monoclinic structure, lithium still increased the oxygen vacancy concentration at the water oxide interface but reduced the concentration deeper into the oxide. Again, this was the result of iron mitigating the effects of lithium within the structure. The zirconium vacancy concentrations in the monoclinic structure was very low when all Cr, Fe and Sn defects were present which makes it difficult to determine which elemental defect was the cause. Given that chromium was identified as a zirconium vacancy suppressant earlier, this was the likely cause.

By identifying the expected defect concentrations through Brouwer diagram calculations, these values could then be combined with volumetric relaxed DFT structure calculations to produce an overall indication of volume change. Volumetric changes through density functional theory, however, have shown to exaggerate volume changes associated with charged defects when compared to the neutral charged defect structures [135]. That is not to say that an indication of volume change could not be evaluated in a general form to confirm or to form an argument to the literature hypothesis that lithium could reduce the bulk volume and create pores in the oxide [1].

For both the tetragonal and monoclinic structures where all defect concentrations and associated volume changes were combined, the overall volume change between lithiated and non-lithiated structures was found to be extremely small where lithium increased the volume at the water oxide

interface by approximately 3×10^{-4} and reduced the volume by as little as -5×10^{-5} $Å^3/ZrO_2$ in the moving into the oxide. For the monoclinic structure, on the other hand, there was an increase in volume at the water oxide interface of approximately 1.3 $Å^3/ZrO_2$, but this did not extend into the oxide to any real depth where the remaining oxide shows very little change in volume due to lithium.

Whilst the previously acknowledged literature work has identified a route to mitigate the exaggerated volume changes in charged defects [135], this would likely fall under the bracket of future work to gain a more accurate representation of volume change. For the purposes of this work, an indication of volumetric change was sufficient to form an argument against the hypothesis that lithium causes volumetric changes in the bulk oxide which may accelerate corrosion through the formation of pores.

A small amount of work aimed to find how pressure within the material might affect the volume of the structures containing defects. This work applied external pressure to the structures from 1 to 5 GPa. This was, however, fairly uneventful where the output produced no unexpected results where an increase in pressure produced a general reduction in volume.

The calculated solution energies of defects with the highest concentrations for each element provided a good indication that tin, iron and chromium would all form solution within the tetragonal and monoclinic bulk oxide. They did, however, show that lithium was unlikely to form solution in bulk ZrO_2 and this was confirmed experimentally in the literature where lithium was found to segregate along the grain boundaries [67]. This indicates that lithium would not increase the oxygen vacancy defects within the bulk oxide or cause changes in the volume through bulk ingress. Due to this, it stands to reason that lithium is unlikely to cause the accelerated corrosion of zirconium alloys via bulk ZrO_2 and other possible mechanisms would need to be investigated such as accommodation in complex grain boundaries.

4. Atomistic Modelling of Lithium and Alloying Additions in Amorphous ZrO_2

The lithium doped aspect of this investigation was published in the paper.

"Assessing Li accommodation at amorphous ZrO_2 grain boundaries" in the Journal of Nuclear Materials [136] **(1st Author)**

The iron aspects were briefly investigated in the paper

The contribution of the author to this work was all simulations and first draft manuscript creation.

"Mechanistically Understanding the Role of Lithium in Accelerated Corrosion of Zirconium Alloys Using Advanced Characterisation and Atomistic Simulation" ASTM International Symposium 2022 [67] **(3rd Author)**

The contribution of the author to this work was all simulations and first draft of simulation sections.

The previous chapter set out to address volumetric changes that may have occurred due to lithium accommodation in the bulk material set out by hypothesis one. It was, however, found that lithium was unlikely to form solution in the bulk material. This led the investigation to the grain boundaries where many of the previous techniques could be used to assess the solubility of lithium along the complex grain boundaries which could be considered amorphous. This could also address hypothesis two which could assess lithium accommodation along grain boundaries that could potentially form pores or grain boundary phases.

As mentioned in the methodology section, creating an amorphous structure of ZrO_2 required additional steps in order to produce a representative structure. In summary, this involved creating a large atomic structure (roughly 6000 atoms) and melting the structure to remove any long-range order using molecular dynamics. Reverse Monte-Carlo could then be used to reduce the structure down to around 100 atoms whilst maintaining a representative amorphous structure. From here, the DFT calculations could continue to gain the values needed to produce formation energy and Brouwer diagrams along with gaining volumetric changes and solution energies for the defects of interest found in the Brouwer diagrams. Whilst lithium was the main dopant under investigation, as with the bulk ZrO_2 calculations, the Zircaloy-4 alloying additions were reviewed to find the changes that may occur as a result of lithium ingress into the amorphous structure.

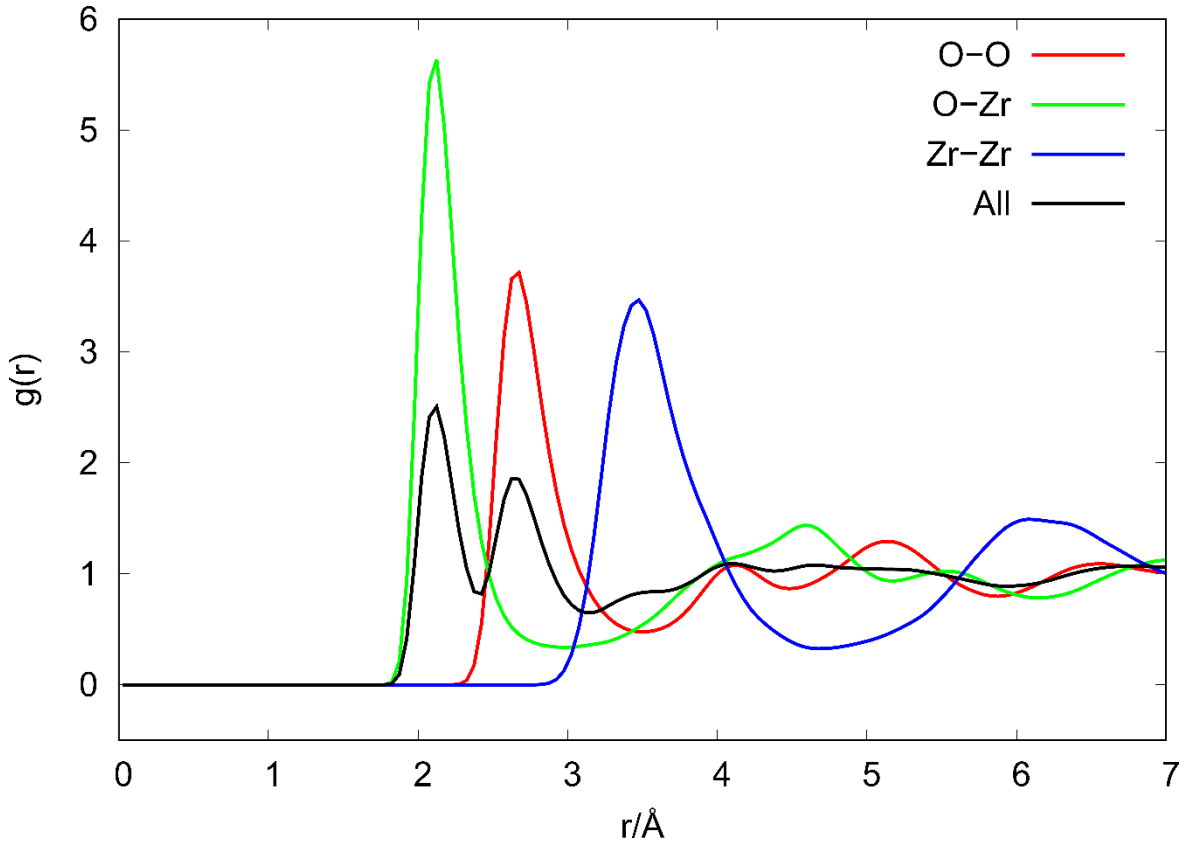

Figure 57 Typical partial radial distributions ((g(r)) vs radius (r/Å)) of O-O, O-Zr, Zr-Zr of amorphous structure after molecular dynamics [136].

The figure above, Figure 57, shows the radial distribution of atoms after molecular dynamics, of which, ten runs were conducted to ensure repeatability. A typical amorphous structure can be seen in Figure 58. The volume was not constrained during molecular dynamic calculations resulting in a non-cubic supercell shape. These showed very little changes and confirmed literature results [137]. This provided good evidence of an amorphous structure and could be used to monitor the radial distribution of atoms post reverse Monte-Carlo to ensure that the smaller structures for DFT calculations remained amorphous and representative producing the same radial distribution as seen in Figure 57. These were also in good agreement with the molecular dynamics radial distribution results. The radial distributions for both over-coordinated (oxygen interstitial) and under-coordinated (oxygen vacancy) structures were found to be almost identical with no noteworthy differences from the standard amorphous structure. Radial distributions were also checked after all DFT calculations to ensure there were no re-arrangements into an ordered structure. Once this was confirmed, the formation energy against Fermi energy plots could be made.

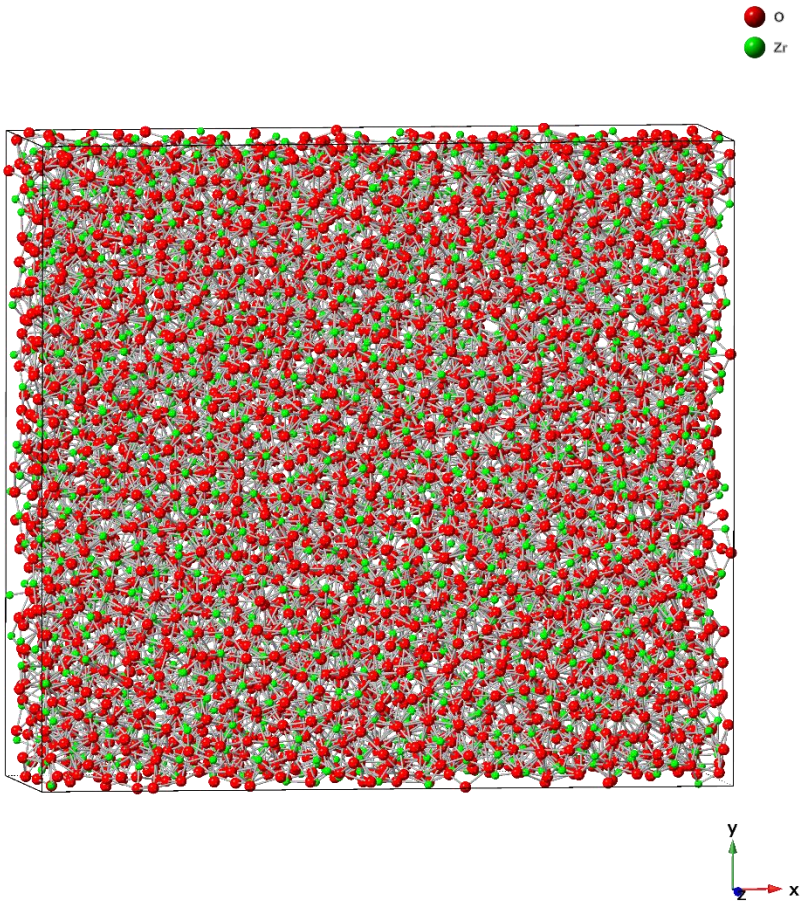

Figure 58 Amorphous ZrO_2 structure containing 6144 atoms post molecular dynamics melt and quench.

The molecular dynamics simulation used to create the amorphous structure allowed the cell dimensions freedom of movement. Whilst the input cell was cubic, as can be seen in Figure 58, the dimensions for that particular simulation resulted in a box of dimensions 13 × 10.5 × 2.1 µm.

4.1. Intrinsic Defects in Amorphous ZrO_2 (Undoped)

As with the bulk oxide section, starting with the intrinsic defects provides a good foundation to add extrinsic defects onto. Highlighting the formation energy against the changes in Fermi level, as before, can provide an indication of defects that may be favoured with lower formation energies, particularly those with a negative formation energy. This is not to say that defects with positive formation energies will not feature on a Brouwer diagram. But it requires favourable conditions to show with any meaningful concentration. As mentioned, a material which is n-type will have a lower Fermi energy level (towards the top of the valence band to the left of the formation energy diagram) and with a p-type material, the Fermi energy level will be higher (towards the bottom of the conduction band to the right). The first defect to look at is the zirconium vacancy. It is worth noting that, in the case of amorphous structures, there is some debate as to whether the terms vacancy or interstitial can be used. These can also be described as under-coordinated or over-coordinated, respectively. However, for simplicity and consistency with the bulk oxides, the terms vacancy and interstitial will be used for the remainder of this work. The bandgap was calculated to 2.78 eV ± 0.26 and experimental bandgap values in the literature range from 3.7 to 6.12 eV as a result in density fluctuations of the amorphous structure [138,139]. Photoluminescence has found a bandgap of 2.8 eV in amorphous ZrO_2 structures [138,140,141], which is representative of the values gained.

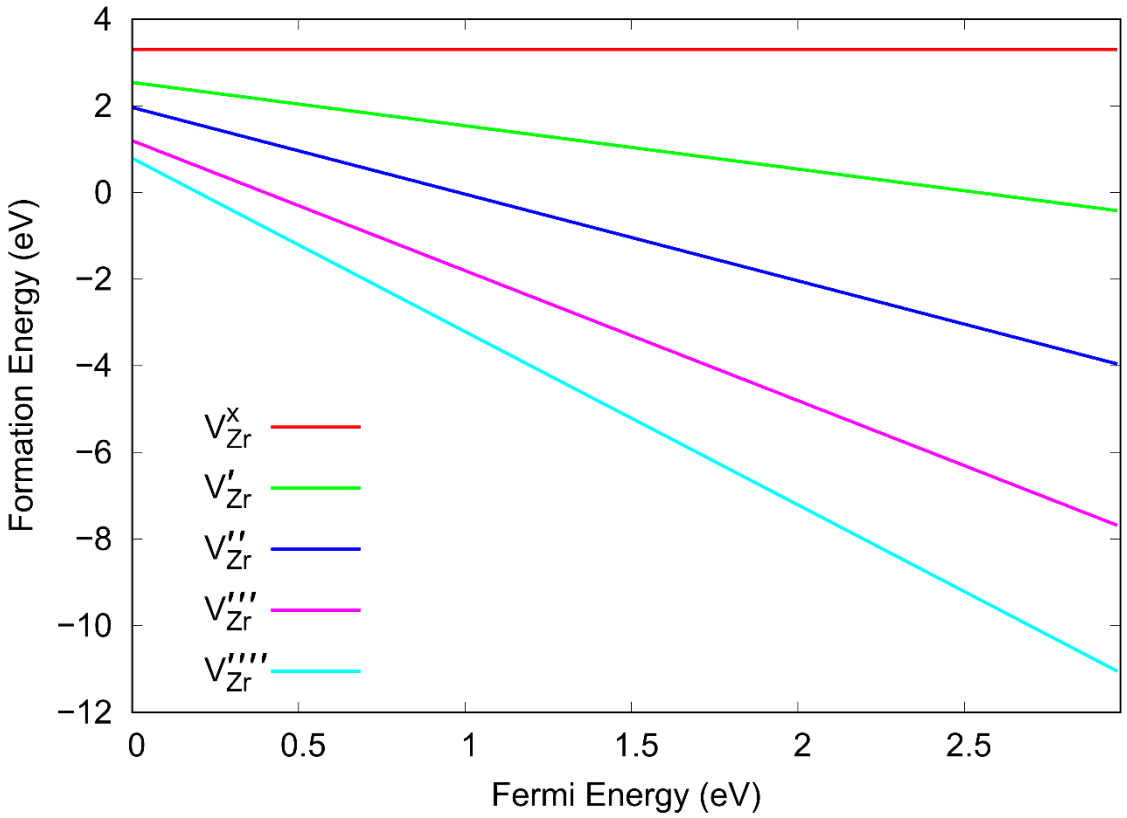

Figure 59 Formation energy of zirconium vacancy with a range of charges across the Fermi energy of the bandgap of amorphous ZrO_2 [142].

All defects show a positive formation energy at the top of the valence band to the left of the formation energy diagram which indicates that a negatively charged material will have a low concentration of zirconium vacancies, Figure 59. The neutral charged zirconium vacancy (V_{Zr}^{x}) maintains a positive formation energy across the Fermi energy which indicates that this will not likely feature on the Brouwer diagram. Towards the bottom of the conduction band to the right where the material has a positive charge overall, the negative charged zirconium vacancy defects are likely to have higher concentrations. An increasingly negative charge in zirconium vacancy defect results in a lower formation energy, particularly at the bottom of the conduction band. The negative four charged zirconium vacancy ($V_{Zr}^{\prime\prime\prime\prime}$) holds the lowest formation energy at all points through the Fermi level and will likely feature in the Brouwer diagram over all other zirconium vacancy defects.

Shifting the attention to the oxygen vacancy defects in the amorphous ZrO_2 structure, the formation energy diagram becomes a little more complex and less straight forward than that of the zirconium vacancy formation energy diagram.

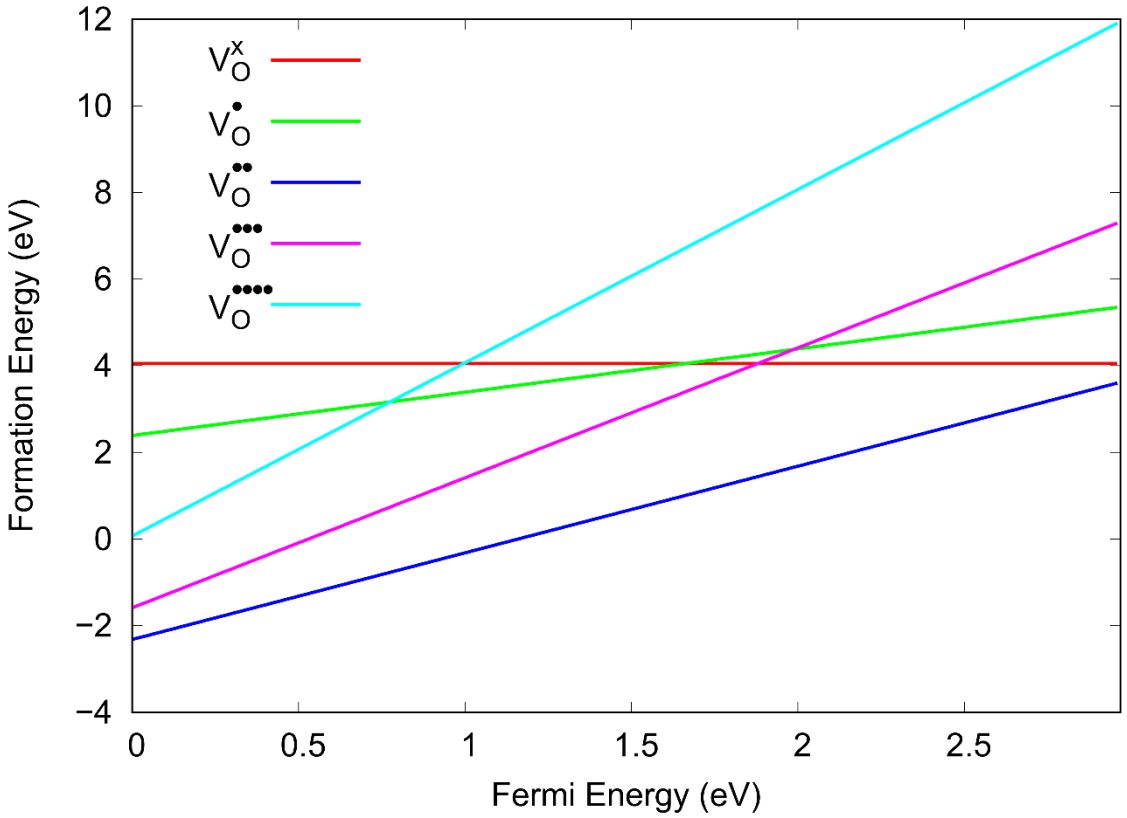

Figure 60 Formation energy of oxygen vacancy with a range of charges across the Fermi energy of the bandgap of amorphous ZrO_2 [142].

The neutral charged oxygen vacancy defect (V_O^x) holds a positive formation energy across the Fermi energy and is unlikely to appear in the Brower diagram, Figure 60. Towards the bottom of the conduction band, all oxygen vacancy defects have a positive formation energy indicating that the concentrations of these defects will be low where the material has an overall positive charge. Towards the top of the valence band to the left, two oxygen vacancy defects have a negative formation energy being the plus two and plus three charged oxygen vacancy defects (($V_O^{\bullet\bullet}$) and ($V_O^{\bullet\bullet\bullet}$) respectively). This indicates that these defects would have higher concentrations in a negatively charged material. As the positive two oxygen vacancy defect ($V_O^{\bullet\bullet}$) has the lowest formation energy across the Fermi energy range, it is likely to have a higher concentration over the other oxygen vacancy defects. Where this diagram differs to that of the zirconium vacancy formation energy diagram, is in the lack of uniform transition between charge and formation energy. Where zirconium vacancy defects have a lower formation energy with a more negative charge, the oxygen vacancy formation diagram shows the positive two defect with the lowest formation energy and both the more and less positive defects have higher formation energies. This is likely the result of the electron configuration of the structure where the oxygen vacancy defect with two electrons removed ($V_O^{\bullet\bullet}$) produces a more favourably relaxed structure to that of the other charges of oxygen vacancy. It is unfortunate that the plus three and plus four oxygen vacancy defects (($V_O^{\bullet\bullet\bullet}$) and ($V_O^{\bullet\bullet\bullet\bullet}$) respectively) for the bulk structures were calculated outside of the Fermi level so this could not be compared to the monoclinic and tetragonal structures.

The final intrinsic defect to be reviewed is that of the oxygen interstitial.

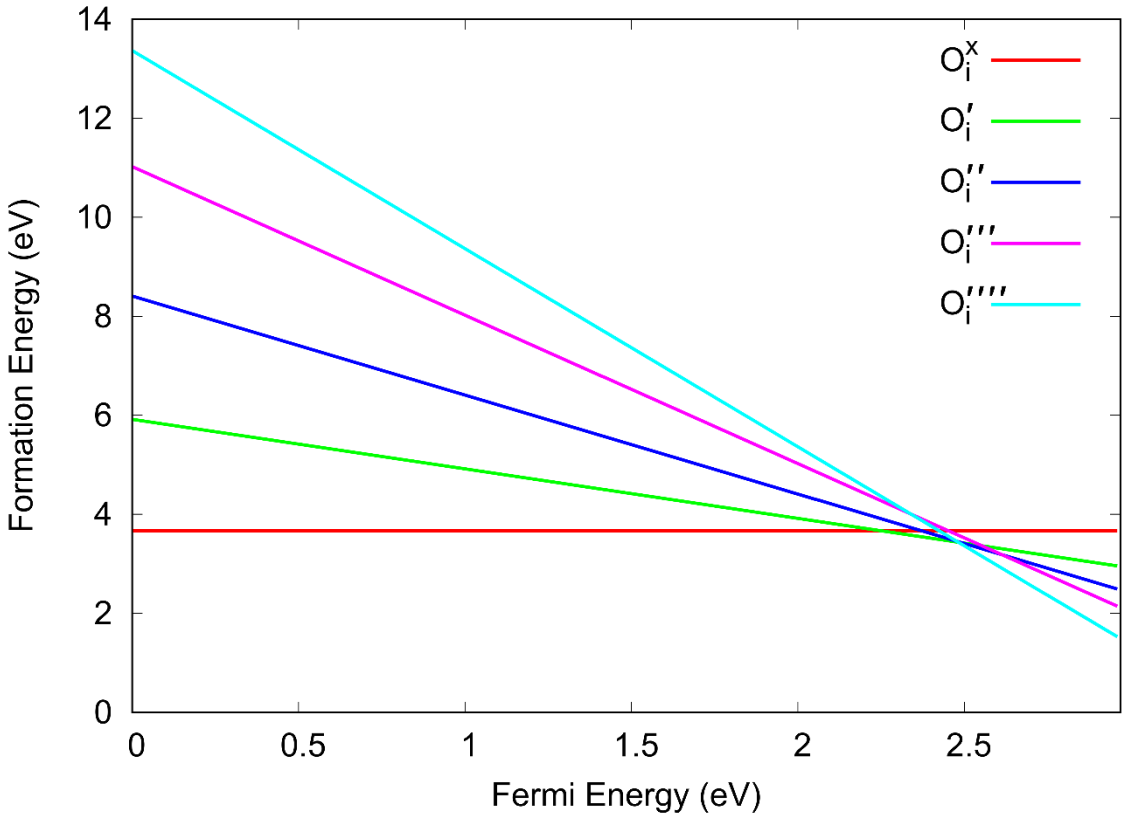

Figure 61 Formation energy of oxygen interstitials with a range of charges across the Fermi energy of the bandgap of amorphous ZrO_2 [142].

In the amorphous structure, the oxygen interstitial defects all have a positive formation energy across the entirety of the Fermi energy range, Figure 61. This is very different to that of the bulk oxides where both the monoclinic and tetragonal structures show a negative formation energy for the negative two charged oxygen interstitial (O_i''). The neutral charged oxygen interstitial formation energy is also found between 2 and 3 eV in the bulk oxides where, for the amorphous structure, it is just below 4 eV. Given that the oxygen interstitial defects are only found in low concentrations at higher partial pressures in the bulk material, if the amorphous Brouwer diagram follows similar trends, it is unlikely that the oxygen interstitial defects will be present for the amorphous structure Brouwer diagram with comparable concentrations. The neutral charged oxygen interstitial (O_i^x) has the lowest formation energy across much of the Fermi energy range from the top of the valence band to the left. The bottom of the conduction band to the right shows the lowest formation energy for all of the negatively charged defects indicating that a positively charged material would favour these defects over the neutral charge interstitial. The crossing point of the formation energies at ~2.5 eV means that the energy differences at $E_F = 0$ are proportional to charge.

Due to the potential differences that can be gained between amorphous structures, as mentioned, ten alternative structures were created for each defect. Whilst this made negligible differences in the formation energy vs Fermi energy diagrams, it did produce subtle variations for the Brouwer diagrams. As what became evident in the bulk structure Brouwer diagrams, a variation in one defect concentration can have an impact on other defect concentrations. For this reason, the amorphous Brouwer diagrams introduce a range of concentration for each defect within the concentration range. The range of concentration difference can be seen as a shaded area for each defect, Figure 62.

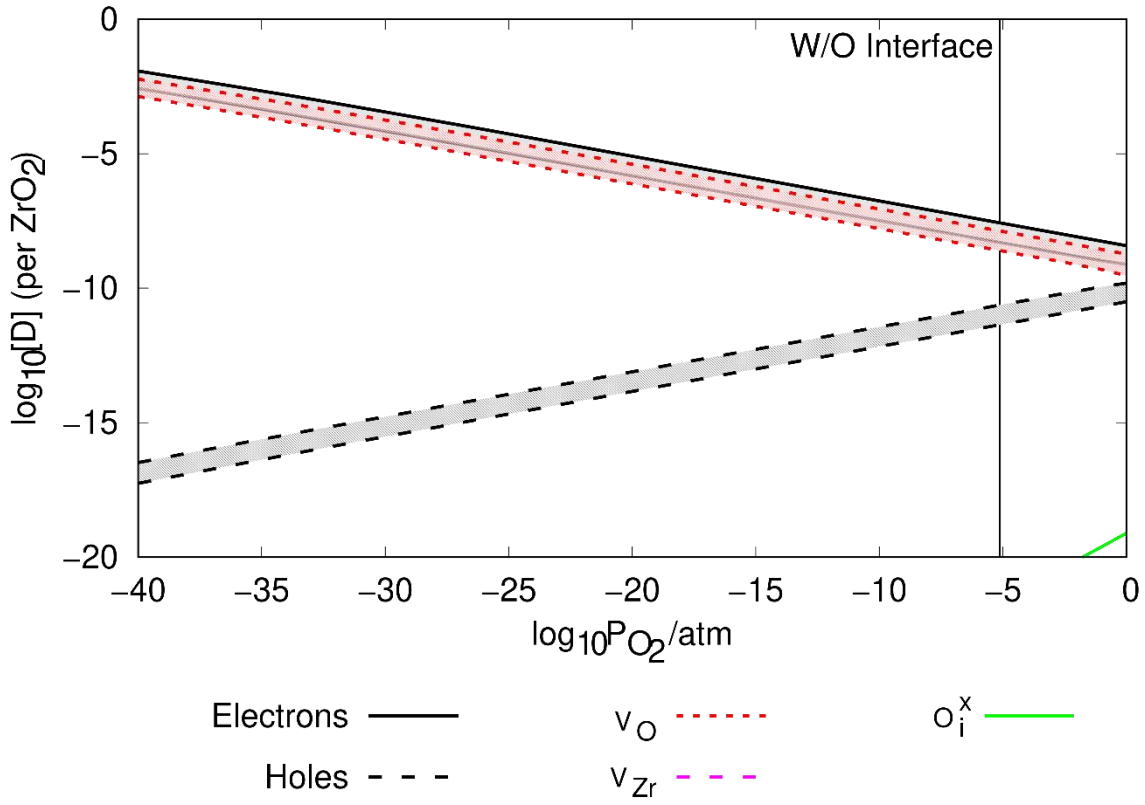

Figure 62 Brouwer diagram at 635 K of intrinsic defects in amorphous ZrO_2. The vertical black line shows the water oxide interface. D represents the defect concentration per ZrO_2. Zirconium vacancies are not present within the Brouwer diagram but are included in the legend to highlight the difference with the bulk oxide Brouwer diagrams.

The Brouwer diagram for the amorphous structure, Figure 62, is distinctly different from that of the bulk oxide Brouwer diagrams (Figure 63)The point at which electrons and holes converge is at very high partial pressures (>0) in the amorphous structure where bulk was in the region of 10^{-33} P_{O_2}/atm for tetragonal and 10^{-19} P_{O_2}/atm for the monoclinic structure.

This does make the amorphous oxide predominantly negatively charged throughout the oxide layer,

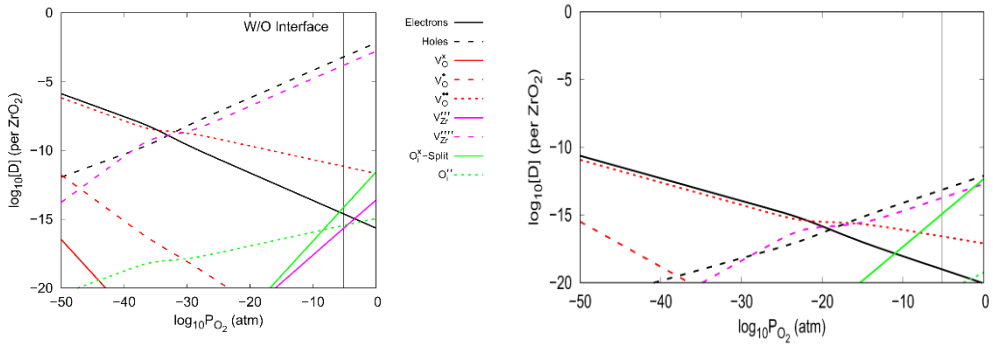

Figure 63 Intrinsic defects for tetragonal ZrO_2 Brouwer diagram from chapter 3.1 to the left and monoclinic Brouwer diagram from chapter 3.3 to the right.

where only intrinsic defects were present. This results in a lack of negatively charged defects such as the negative four charged zirconium vacancy (V_{Zr}'''') which shows high concentrations at higher partial pressures in the bulk structures. This also results in the relatively high concentration of the positive two charged oxygen vacancy defect ($V_O^{\bullet\bullet}$). The neutrally charged oxygen interstitial defect ($O_i^{\times}$), on the other hand, shows a negligible range of concentrations indicating a fairly indifferent

location preference when producing an over-coordinated amorphous structure. There are fewer intrinsic defects in the amorphous Brouwer diagram when compared to the bulk diagrams (Figure 63) and is due to the relatively high formation energies related to most defects for the amorphous structure along with a higher electron concentration throughout the oxide layer. This would favour a positively charged defect over a negative one. The relatively high plus two oxygen vacancy defect concentration, over that of the bulk oxide, can be seen as a possible pathway for normal corrosion along (amorphous) complex grain boundaries. This could be through a form of oxygen "hopping" between oxygen vacancy sites as found in the literature [137].

4.2. Lithium Doped Amorphous ZrO_2

The first extrinsic defect to be calculated in the amorphous structure is lithium. Very few lithium defects could be calculated within the Fermi level range.

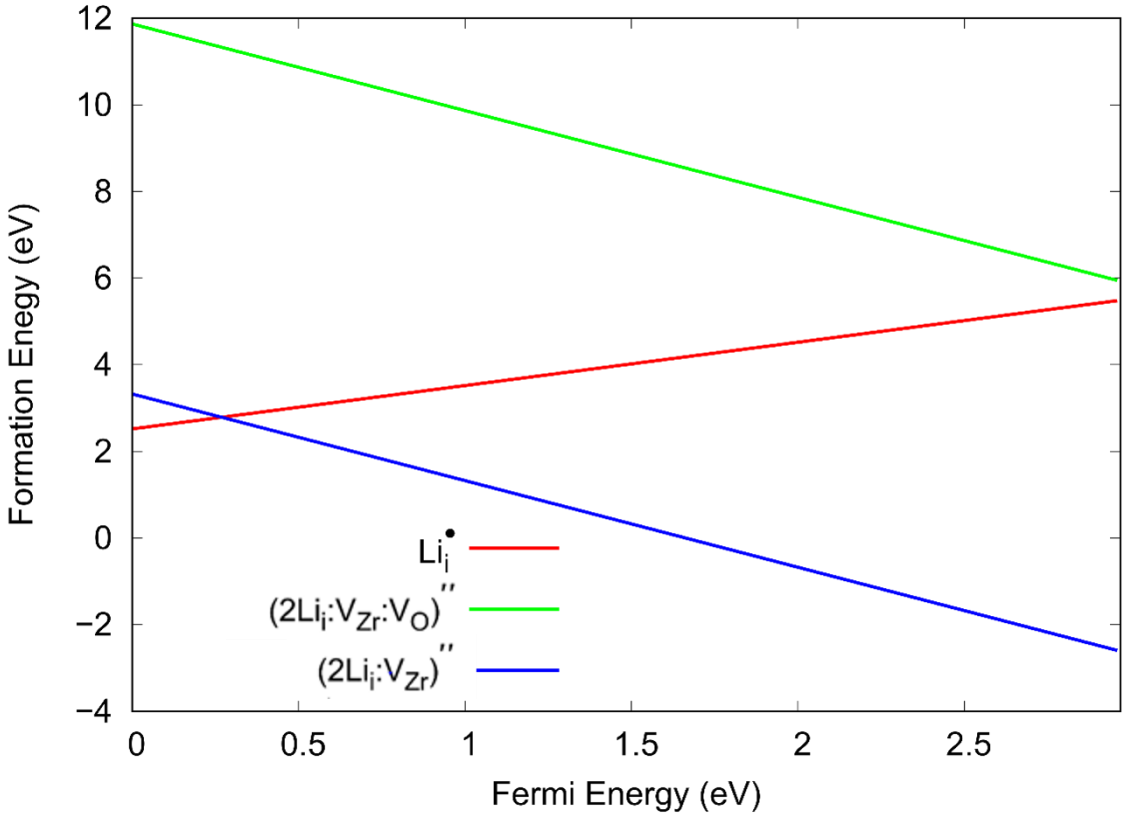

Figure 64 Average formation energy for lithium defects across the bandgap of amorphous ZrO_2 [142].

The general trends of the lithium defects follow what is expected, in that the positive lithium interstitial have a lower formation energy at lower Fermi energies and that negative defects have a higher formation energy at lower Fermi energies, Figure 64. The only defect to show a negative formation energy is the negative two charged small cluster of 2 lithium interstitials around a zirconium vacancy site $(2\mathrm{Li_i}:\mathrm{V_{Zr}})''$, Figure 65. Both cluster defects, $(2\mathrm{Li_i}:\mathrm{V_{Zr}})''$ and $(2\mathrm{Li_i}:\mathrm{V_{Zr}}:\mathrm{V_O})''$, show a lower formation energy towards the bottom of the conduction band to the right which indicates that a positive charged material will favour these defects. The positive one charged lithium interstitial $(\mathrm{Li_i^{\bullet}})$ has a lower formation towards the top of the valance band indicating that it would favour a negatively charged material.

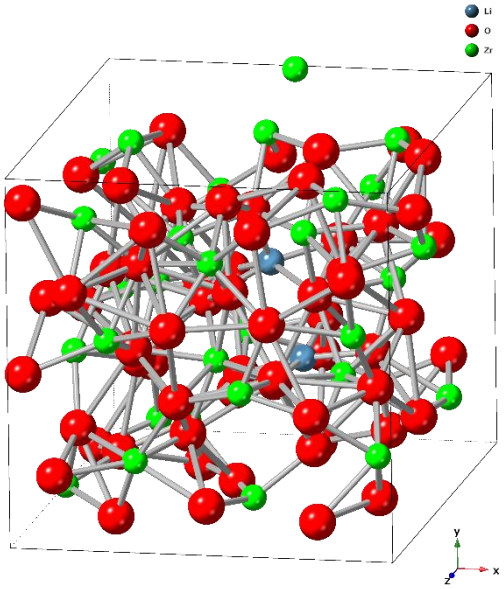

Figure 65 Small cluster of two lithium interstitials around a zirconium vacancy site in amorphous ZrO_2.

The actual concentration of lithium that may be found along the grain boundaries is likely to have a range depending on exposure time, amongst other potential factors. As stated earlier in chapter 3, lithium is unlikely to form a solution within the bulk material. This indicates that the concentration may be substantially higher along grain boundaries due to segregation. The literature has identified a general concentration of up to 0.013 ± 0.001 at. % lithium average across an atom probe ZrO_2 sample and between 0.2 to 0.6 at. % segregation along the grain boundaries [143]. This was with a maximum of 195 days exposure and up to 250 wt. ppm lithium concentration in autoclave water. For this reason, a higher value of 0.1 per ZrO_2 was given for the amorphous Brouwer diagram which is much higher than what was given to the bulk Brouwer diagrams (0.001 per ZrO_2 Li concentration). This is simply to provide a much greater range of concentrations to cover all bases. This was also included for all considered structures.

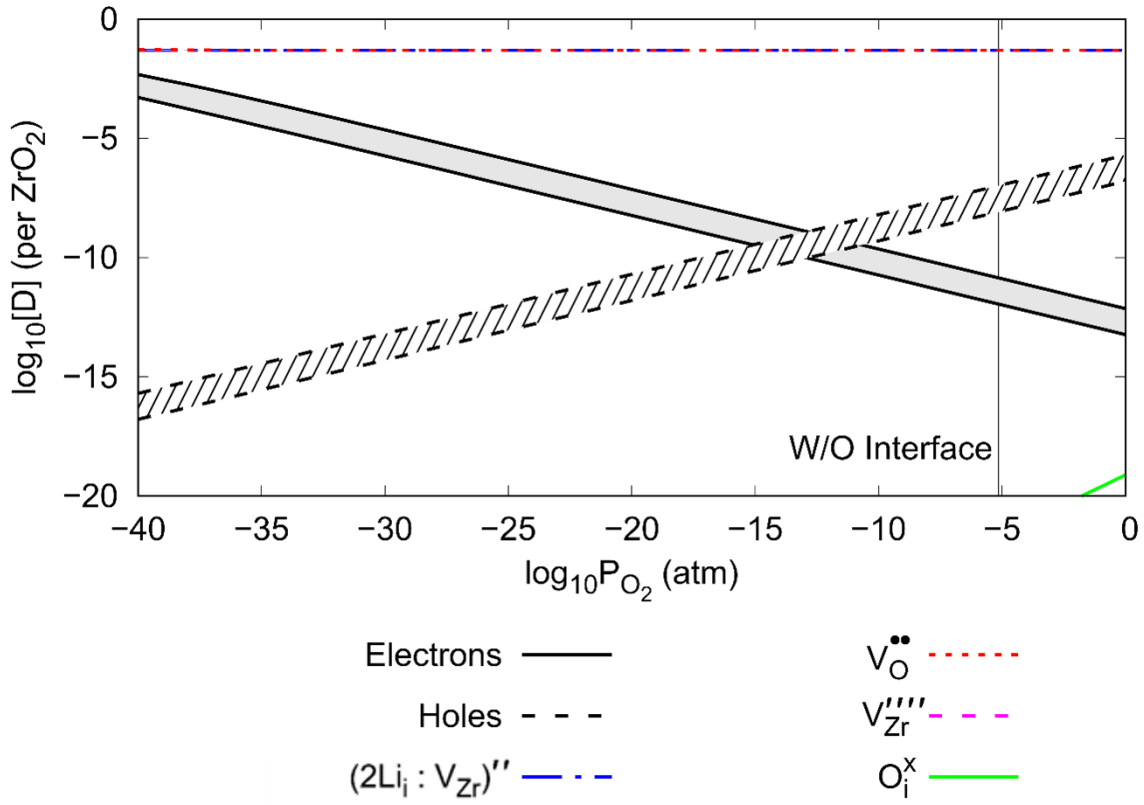

Figure 66 Brouwer diagram at 635 K of 0.1 Li per ZrO_2 and intrinsic defects in amorphous ZrO_2. The vertical black line shows the water oxide interface.

When viewing the Brouwer diagram containing 0.1 lithium per ZrO_2, Figure 66, it is immediately clear that the small cluster of two lithium interstitials around a zirconium vacancy site, $(2\mathrm{Li_i}{:}\,\mathrm{V_{Zr}})''$, not only matches the concentration of oxygen vacancy, $(\mathrm{V_O^{\bullet\bullet}})$, at equal concentrations, but also limits the oxygen vacancy range variation that was noted in the intrinsic defect Brouwer diagram. These two defects charge compensate one another throughout the partial pressure range. The electrons and holes converge at much lower partial pressures as a result of lithium also. The formation energy diagram showed that the small cluster $(2\mathrm{Li_i}{:}\,\mathrm{V_{Zr}})''$ would favour a positive charged material. This has been accomplished by increasing the plus two charged oxygen vacancy defect $(\mathrm{V_O^{\bullet\bullet}})$.

To understand how lithium might affect the intrinsic defects through a range of lithium concentrations, as with the bulk oxide chapter, placing 10^{-1}, 10^{-5} 10^{-11} and intrinsic defect diagrams side by side can highlight the changes that may be expected, Figure 67.

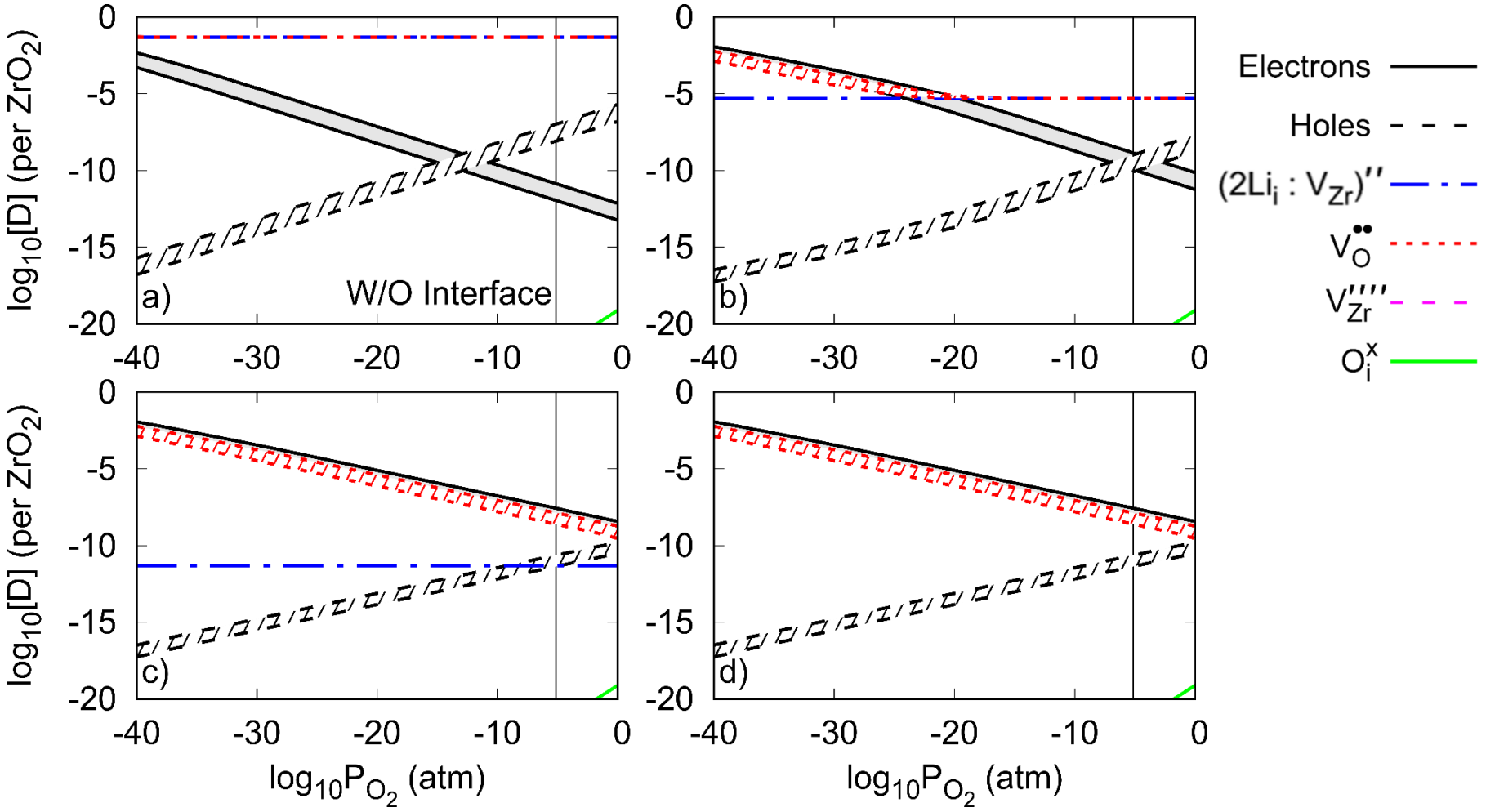

Figure 67 635 K Brouwer diagrams with defect concentrations [D] per unit amorphous ZrO_2 for (a) 10^{-1} Li (b) 10^{-5} Li (c) 10^{-11} Li (d) intrinsic defects [142].

The highest lithium concentration Brouwer diagram, Figure 67, 10^{-1} (a), has already been discussed, but as the concentration is reduced to 10^{-5} (b), the electron concentration at the lowest partial pressures to the left are higher than that of the lithium. Where this is the case, the plus two charged oxygen vacancy ($V_O^{\bullet\bullet}$) follows the electron concentration. Not only this, but the shaded range of oxygen vacancy defects returns. This shows a charge decoupling of the lithium and oxygen vacancy concentrations when electron concentrations are higher than lithium. The oxygen vacancy is then charge coupled with the electron concentration. At higher partial pressures to the right. The oxygen vacancy defects remain elevated in comparison to the undoped Brouwer diagram (d). The point at which the electrons and holes intersect at higher partial pressures is also shifted to higher partial pressures to the right compared to 10^{-1} Li concentrations (a). When the lithium concentration is below the minimum undoped oxygen vacancy concentration (10^{-11} (c)), lithium no longer has any effect on the intrinsic defects at all. This might provide an indication as to why lithium accelerated corrosion only occurs when LiOH in the coolant water is above a temperature dependant concentration [55].

4.3. Cr Doped Amorphous ZrO_2

The chromium defects within the amorphous structure has been identified in the literature, however, this has been found in the form of chromium nanoparticles rather than a solution within the amorphous ZrO_2 complex grain boundaries [144]. In the interest of completion, chromium was investigated to identify if there was potential for chromium to feature in the Brouwer diagrams with any defect species or charges. The defect species calculated with a Fermi level within the bandgap were few, only producing formation energies for the interstitials and the small cluster of two chromium interstitials around a zirconium vacancy site.

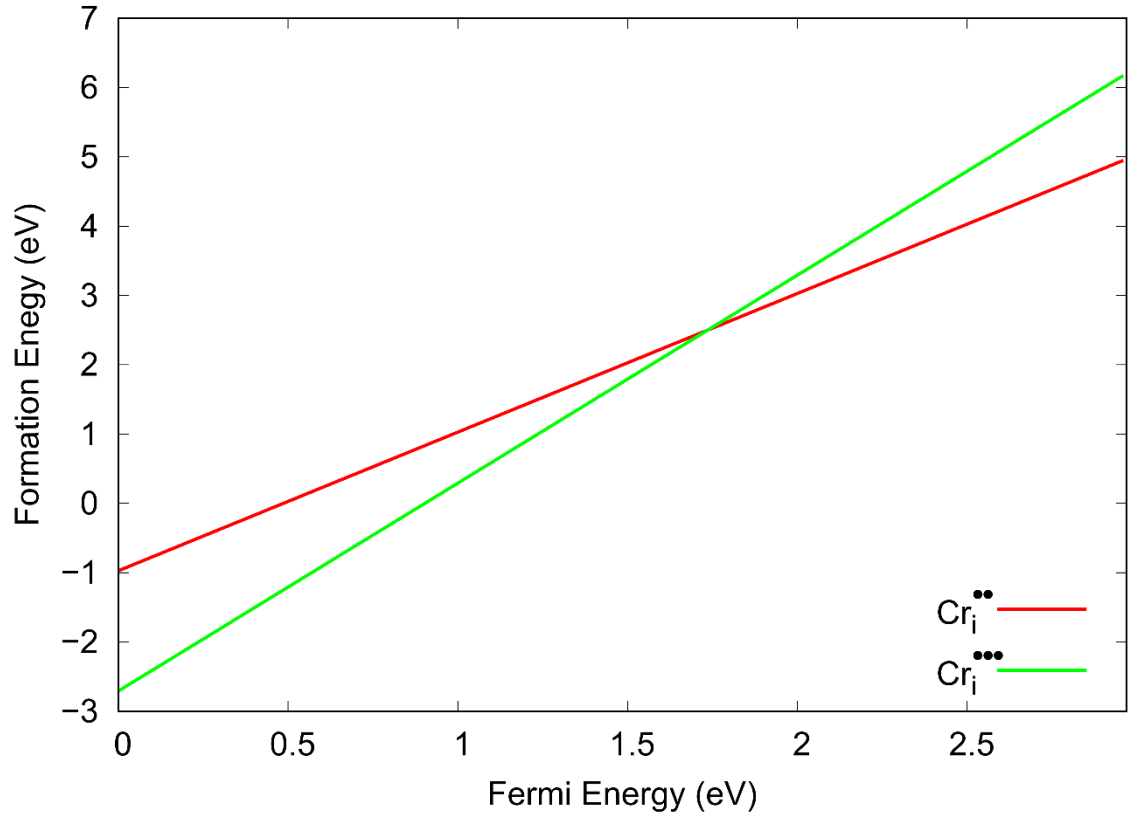

Figure 68 Formation energy of chromium interstitials with a range of charges across the Fermi energy of the bandgap of amorphous ZrO_2.

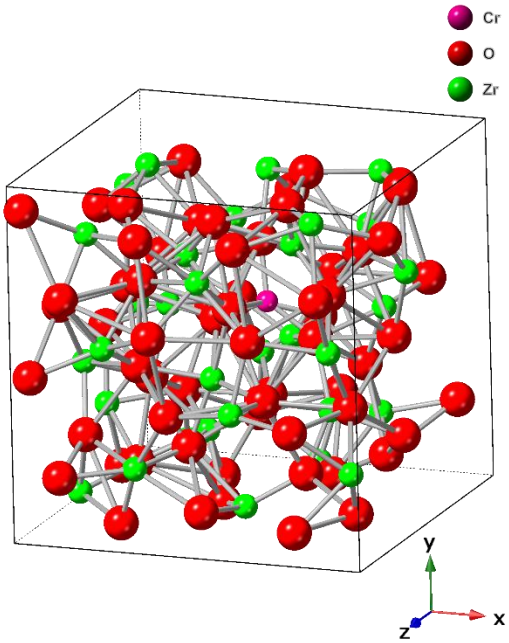

Figure 69 Chromium interstitial in amorphous ZrO_2.

The chromium interstitial defects, Figure 69, calculated with a Fermi level within the bandgap range were the positive two and positive three interstitial defects, Figure 68. Both have a negative formation energy towards the top of the valence band to the left indicating a favoured negatively charged material. Above a 1 eV Fermi level, both defects have a positive formation energy indicating that a positively charged oxide will not favour these defects. The lowest formation energy is found with the positive three interstitial ($Cr_i^{\bullet\bullet\bullet}$) at the top of the valence band.

Neither the chromium substitution defects are the cluster of two chromium interstitials around a zirconium vacancy coupled with an oxygen vacancy could be calculated with a Fermi level within the bandgap range. The cluster of two chromium interstitials around a zirconium vacancy site shows many of the charges reviewed in the formation plot.

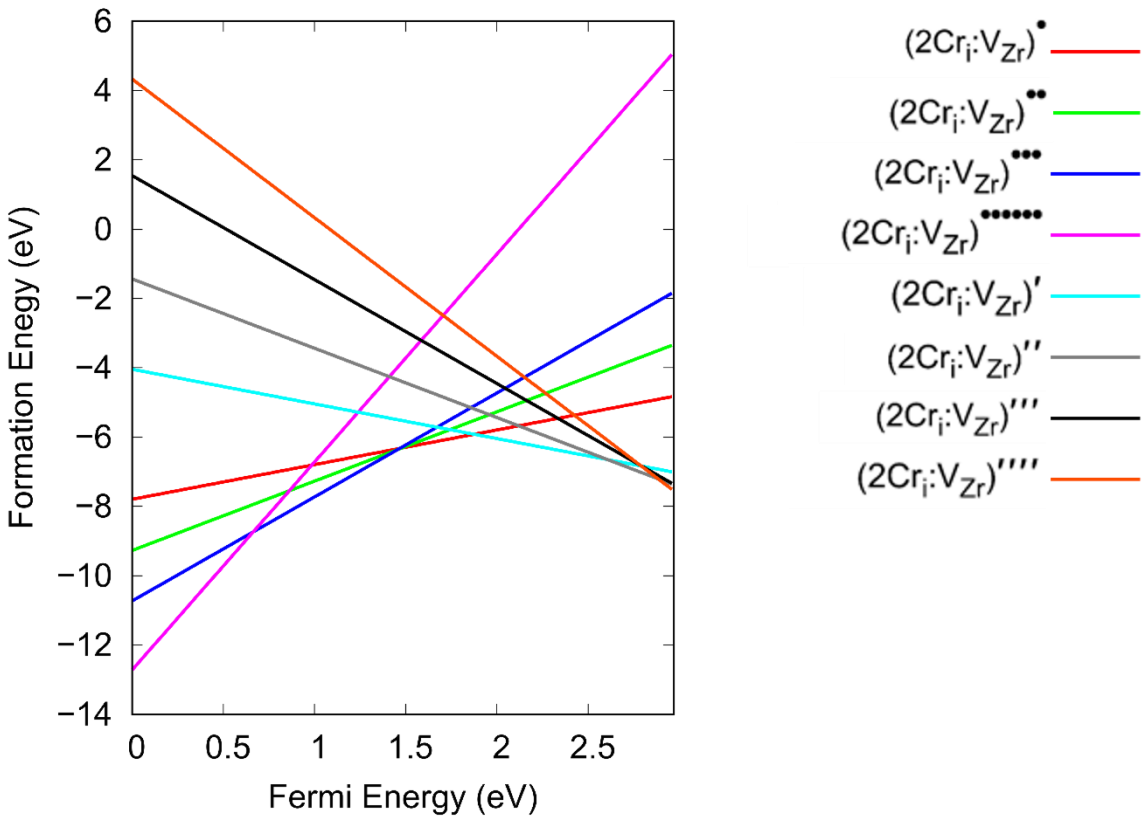

Figure 70 Formation energy of two chromium interstitials around a zirconium vacancy site with a range of charges across the Fermi energy of amorphous ZrO_2.

An interesting aspect of the formation diagram showing two chromium interstitials around a zirconium vacancy site (Figure 71) is that, despite many charge variations being present, the neutral charged defect was calculated with a Fermi level outside of the bandgap range, Figure 70. All of the chromium defects shown in the formation energy plot show negative formation energies. The positively charged defects all favour a negatively charged oxide with the lowest formation energies at the top of the valence band to the left. The negative charged defects have a lower formation energy at the bottom of the conduction band to the right, which would favour a positively charged oxide. Most of these defects, if not all, would be expected to be found with relatively high concentrations in the Brouwer diagrams. The defects are also fairly predictable in that the higher the charge, the steeper the gradient associated between the negative and positive charges of oxide across the bandgap.

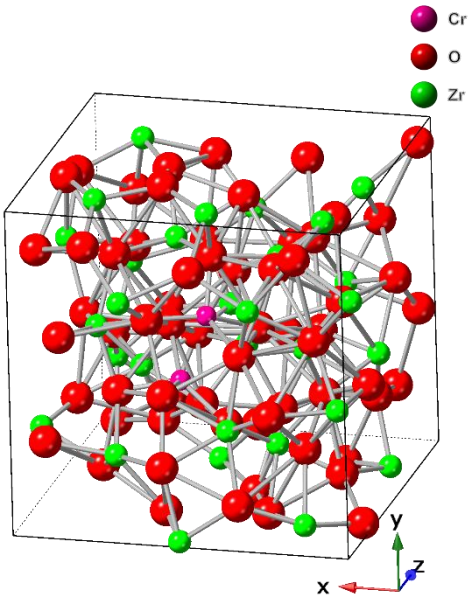

Figure 71 A small cluster of two chromium interstitials around a zirconium vacancy site in amorphous ZrO_2.

Chromium does not feature on an amorphous Brouwer diagram, but as mentioned, this does confirm previous experimental work that has identified Cr as segregating in nanoprecipitates rather than forming a solution into the ZrO_2 amorphous structure along grain boundaries [145]. This is due to the calculation of chromium defects being unable to determine a Fermi level that gave charge neutrality.

4.4. Fe Doped Amorphous ZrO_2

Much like the chromium defects, only the iron interstitials and two iron interstitials around a zirconium vacancy site were calculated within the Fermi range. The iron interstitials offered a few more charges of the defect species and the small cluster even presents a neutral charged defect.

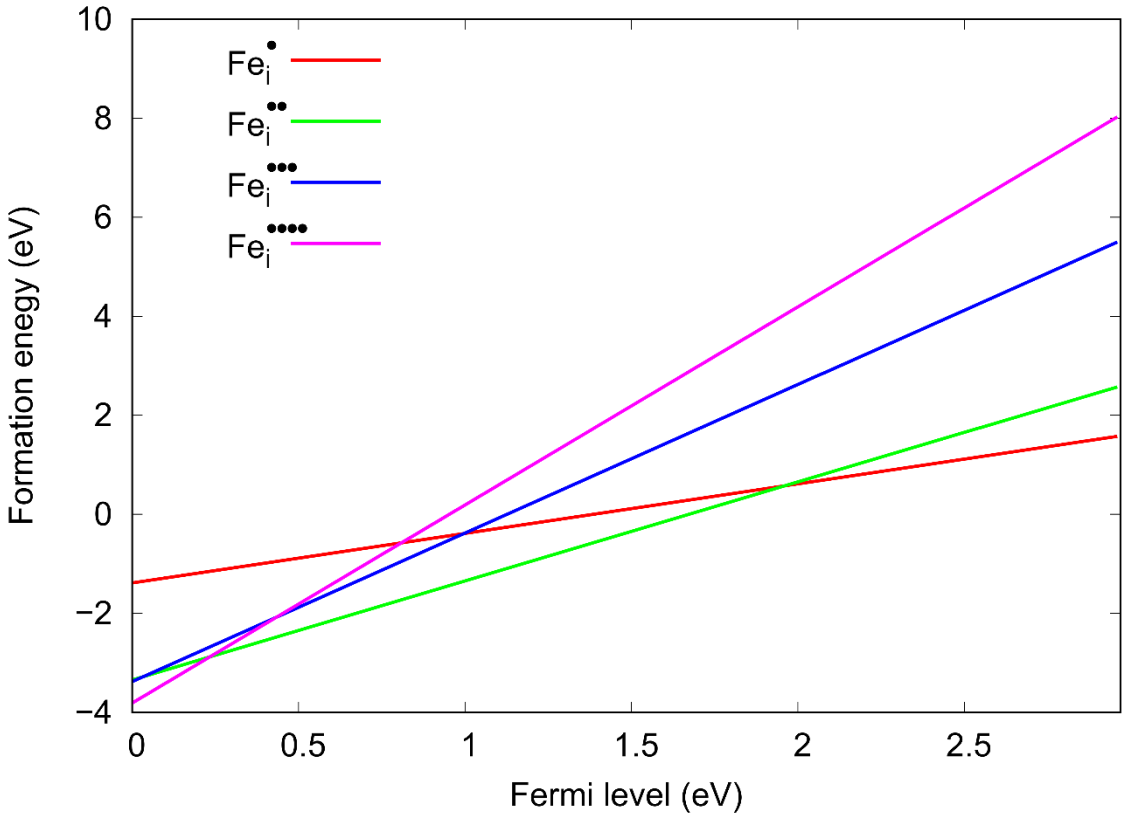

Figure 72 Formation energy of iron interstitials with a range of charges across the Fermi energy of the bandgap of amorphous ZrO_2.

The neutral charged iron interstitial held a Fermi level outside of the bandgap so was not included in the formation energy plot. All the interstitial defects, Figure 73, that were calculated within the Fermi range have a negative formation energy and have the lowest formation energy at the top of the valence band to the far left, Figure 72. Ionic iron interstitials have been found to stabilise the cubic, tetragonal and monoclinic zirconia structures in literature and form solid solution [146]. Once again, the highest charged defect has the lowest formation energy. At the bottom of the conduction band to the far right, all of the interstitial defects have a positive formation energy which indicates that the defects favour a negative charged oxide.

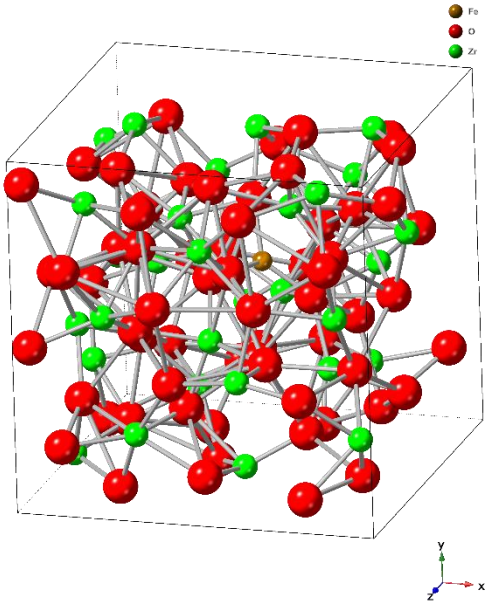

Figure 73 Iron interstitial in amorphous ZrO_2.

The small cluster of two iron interstitials around a zirconium vacancy site, Figure 75, had a range of charges that could be calculated within the Fermi range, both positive and negative in charge.

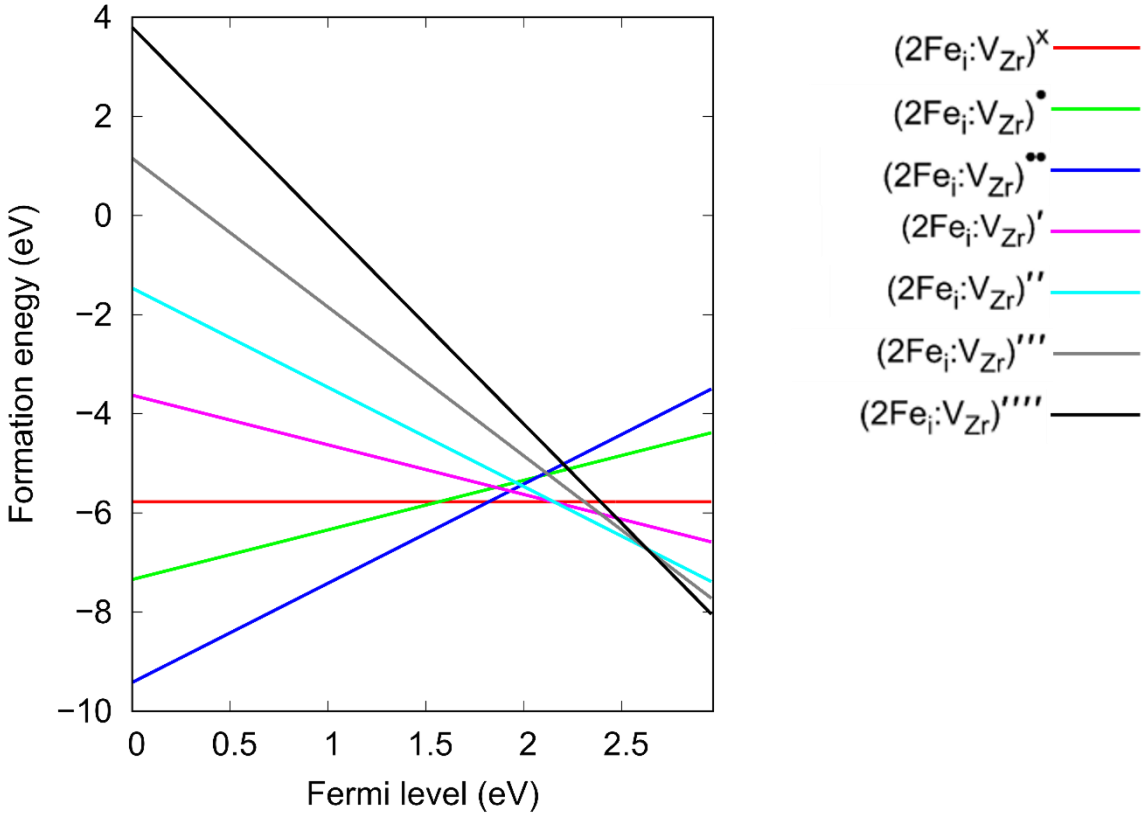

Figure 74 Formation energy of two iron interstitials around a zirconium vacancy site with a range of charges across the Fermi energy of the bandgap of amorphous ZrO_2.

The cluster defects are similar to that of the chromium cluster formation energy plot, Figure 70, in many ways. All the defects have a negative formation energy where positive charged defects have a lower formation energy at the top of the valence band to the far left and the negative charged defects have a lower formation energy at the bottom of the conduction band to the right, Figure 74. The higher the charge, the steeper the gradient between the negative charged oxide to the left and positive charged oxide to the right in relation to Fermi level. One defect which appeared in the iron cluster formation energy plot which is not on the chromium plot is the neutral charged cluster. As expected, this defect maintains a consistent formation energy across the bandgap and does show a very low formation energy.

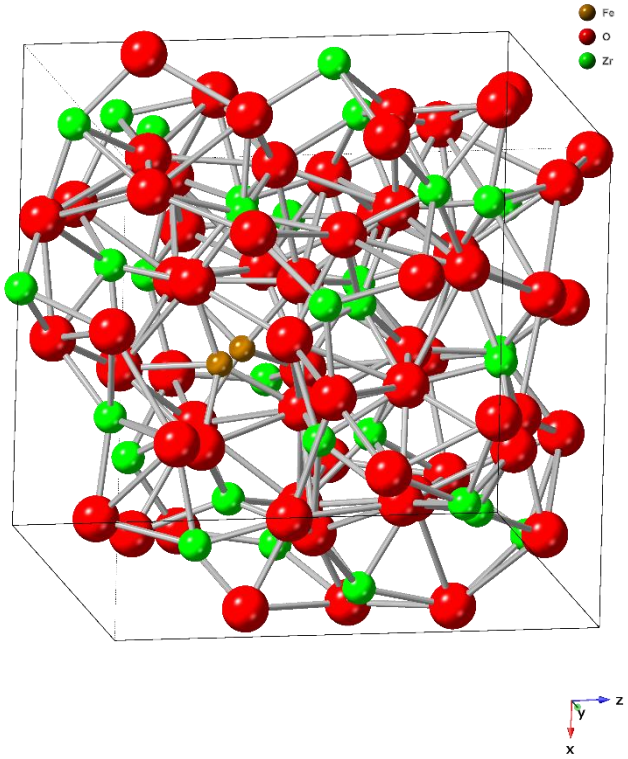

Figure 75 Two iron interstitials around a zirconium vacancy site in an amorphous ZrO_2 structure.

Figure 75 shows two iron interstitials around a zirconium vacancy site in an amorphous structure. The structure orientation was selected for clarity of defect position for presentation purposes.

Much like the lithium doped amorphous ZrO_2 Brouwer diagram, the iron doped amorphous ZrO_2 Brouwer diagram is interesting in how sparce the number of defects were.

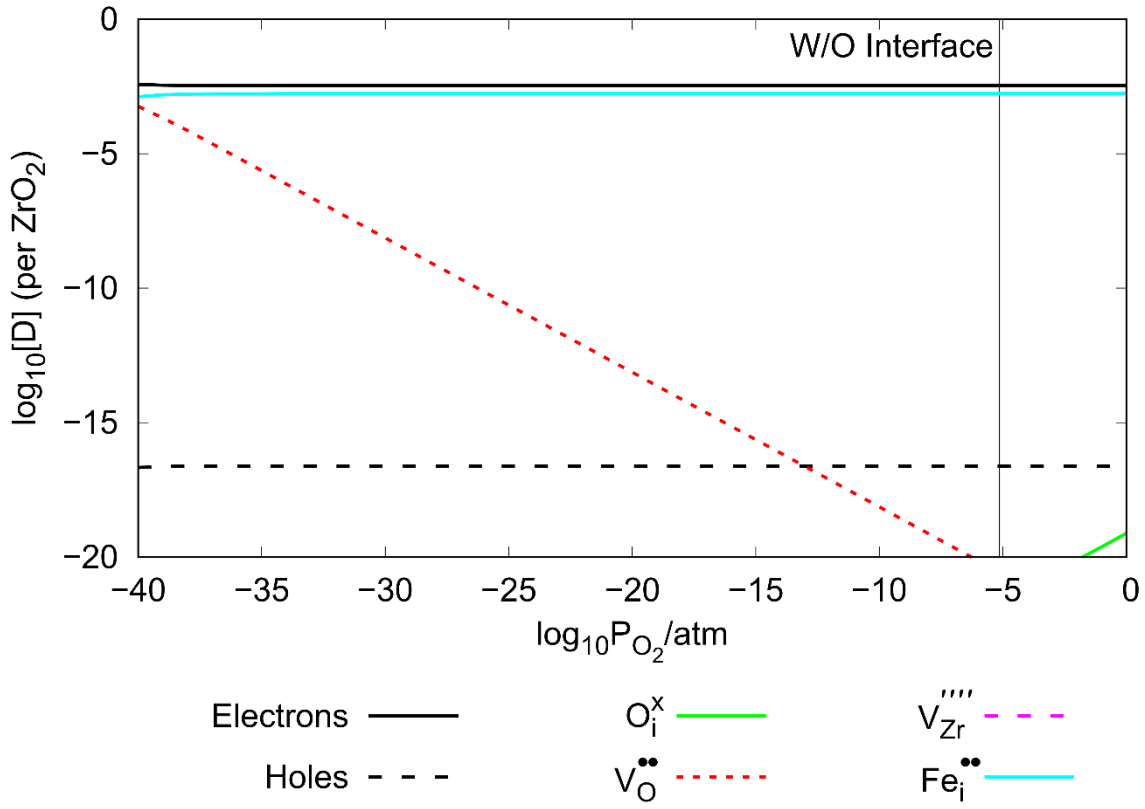

Figure 76 Brouwer diagram at 635 K of 0.0024 Fe per ZrO_2 and intrinsic defects in amorphous ZrO_2. The vertical black line shows the water oxide interface.

As mentioned, defects were placed in ten different locations providing a range of concentrations as a result. In the case of iron defects in an amorphous zirconium structure, the range of oxygen vacancy defect concentration from maximum to minimum was quite large making it difficult to present this in the Brouwer diagram results. The oxygen vacancy ranged from what can be seen in the Brouwer diagram above Figure 76, down to a value outside of the concentration range given (10^{-20} per ZrO_2). This obscured the results, so the decision was made to show only the maximum concentration for the oxygen vacancy defect. The other defects, however, were not altered. The only iron defect to feature on the Brouwer diagram is the plus two charged iron interstitial ($Fe_i^{\bullet\bullet}$). This was set to the alloying concentration of 0.0024 per ZrO_2, the iron interstitial elevates the electron concentration causing it to have high concentration across the oxide. This also caused the hole concentration to fall across the oxide layer also which maintains a low concentration (~10^{-17} per ZrO_2). The oxygen vacancy and oxygen interstitial defects remained unchanged as a result of this. However, at low partial pressures to the left, there is a small reduction in iron interstitial concentrations when the oxygen vacancy concentration is at the highest point. This was due to an increase of the plus two charged oxygen vacancy reducing the plus two charged iron interstitial to maintain charge neutrality. As mentioned, however, altering the location of the oxygen vacancy within the amorphous structures resulted in a large range of results which removed the oxygen vacancy defect from the Brouwer diagram when at the minimum. The oxygen vacancy defects, although difficult to see, are lower than what would be found in the intrinsic defect only Brouwer diagram. This will be evident in the multiple plots with varying iron concentration, side by side (Figure 77). Interestingly, when the stipulated concentration is removed during the calculation, the iron concentration seen in the 0.0024 per ZrO_2 is found to be exactly the same indicating that this is the preferred concentration of iron in the amorphous structure.

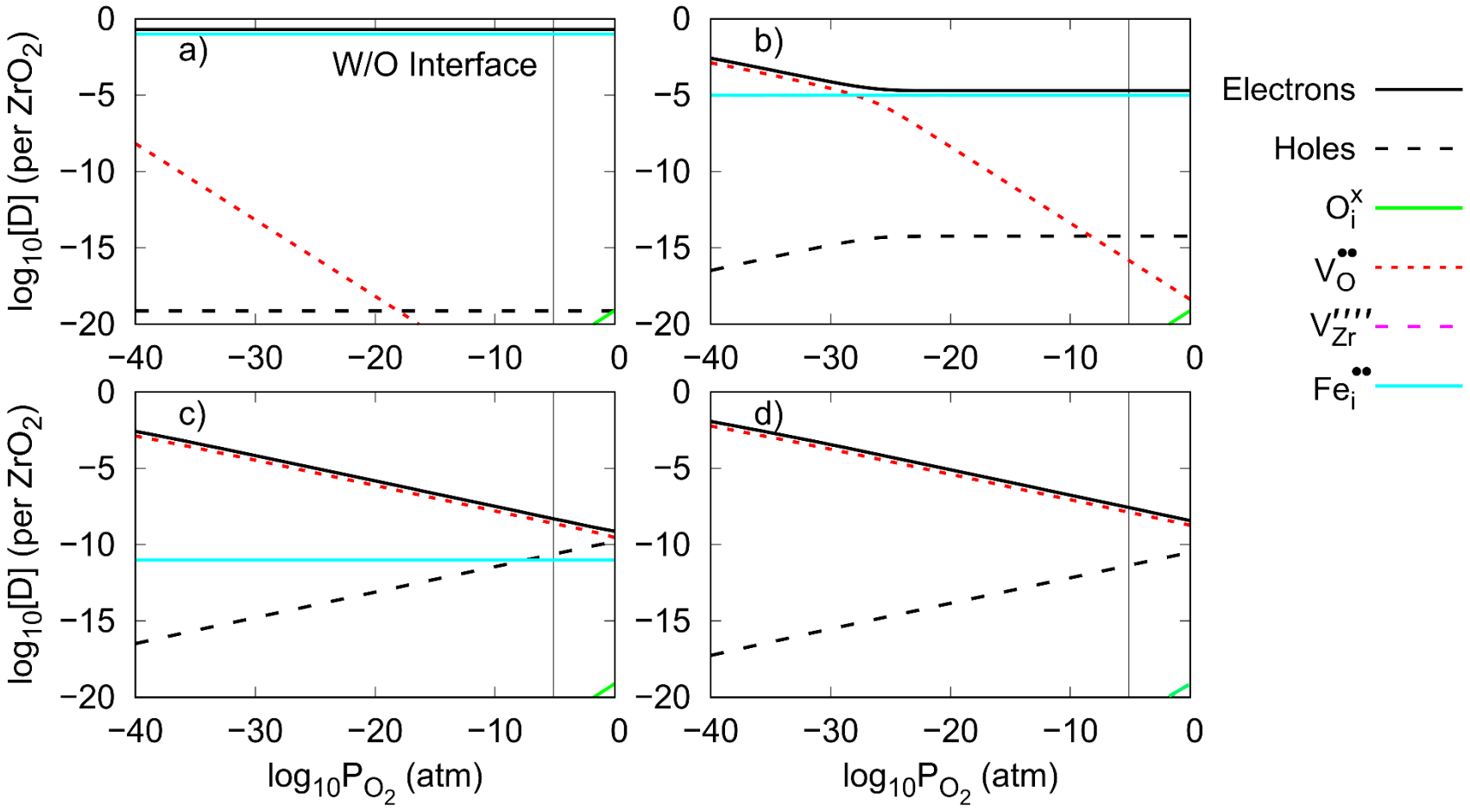

Figure 77 635 K Brouwer diagrams with defect concentrations [D] per unit amorphous ZrO_2 for (a) 10^{-1} Fe (b) 10^{-5} Fe (c) 10^{-11} Fe (d) intrinsic defects.

With the variations of iron defect concentration side by side, Figure 77, it is possible to see the changes in oxygen vacancy defects concentration as a result. It is clearly the opposite of what we find with the lithium defect Brouwer diagram. This is due to the iron charge coupling with electron concentrations, where lithium charge coupled with vacant oxygen concentrations. Here, the higher iron concentration (10^{-1} (a)) reduces the oxygen vacancy defects whilst also increasing the electron concentration to similar levels to that of the iron interstitial. The holes are reduced almost to a point of being below the concentration range of the Brouwer diagram (10^{-20} per ZrO_2). The oxygen interstitials, as is a common theme, was completely unchanged by iron concentration. As the iron concentration is reduced (10^{-5} (b)), at lowest partial pressures to the left shows that the electron concentration returns to interstitial only levels (d) which is also coupled with the oxygen vacancy defect concentrations. This, however, was only for a short partial pressure as at around 10^{-28} partial pressure of oxygen, where the iron interstitial crosses the electron and oxygen vacancy defect concentration, the electrons re-combine with the iron interstitial and the oxygen vacancy defect concentration is reduced from this point when compared to the intrinsic defect only Brouwer diagram. As with the lithium Brouwer diagram, Figure 67, when the extrinsic defect concentration drops beneath that of the electrons and oxygen vacancy defects, the intrinsic defects no longer seem to be affected by the iron within the structure. Upon closer inspection, however, electron and oxygen vacancy defects are slightly reduced whilst the hole concentration is slightly increased. The overall trends, however, are relatively unchanged. At 0 P_{O_2}, the electron, hole and oxygen vacancy defects intersect at a concentration of ~10^{-10} per ZrO_2 where iron has a concentration of 10^{-11} per ZrO_2 whereas there was an increase in electron and oxygen vacancy concentration of ~10^{-1} per ZrO_2 where no iron was present.

4.5. Sn Doped Amorphous ZrO_2

The number of tin defects that were calculated within the bandgap was quite high in comparison to other extrinsic defects reviewed in the amorphous structure.

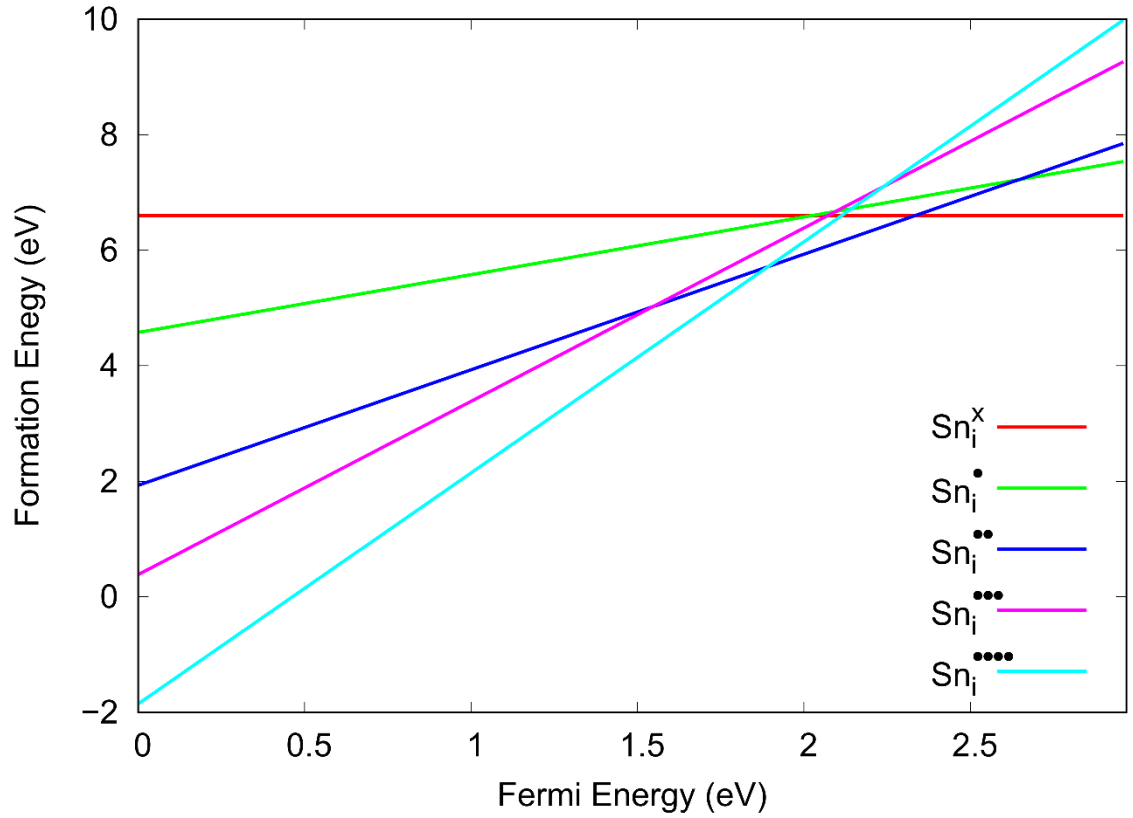

Figure 78 Formation energy of tin interstitials with a range of charges across the Fermi energy of the bandgap of amorphous ZrO_2.

For the tin interstitials, only one tin interstitial was calculated with a negative formation energy, the plus four charged interstitial ($Sn_i^{\bullet\bullet\bullet\bullet}$), Figure 78. This negative formation energy is at the top of the valence band to the far left but only remains negative up to, roughly, 0.5 eV. The trends found in the formation energy vs Fermi energy showed that the higher charged defect has the lowest formation energy and as the defect charge decreases, the formation energy increases at the valence band maximum to the left for positively charged defects. The gradient was also steeper for higher charged defects. The plus one interstitial ($Sn_i^{\bullet}$) and the plus three interstitial ($Sn_i^{\bullet\bullet\bullet}$) are the only defects which do not have a lowest formation energy across any of the bandgap. The neutral charged interstitial ($Sn_i^{\times}$) holds the lowest formation energy at the bottom of the conduction band to the far right.

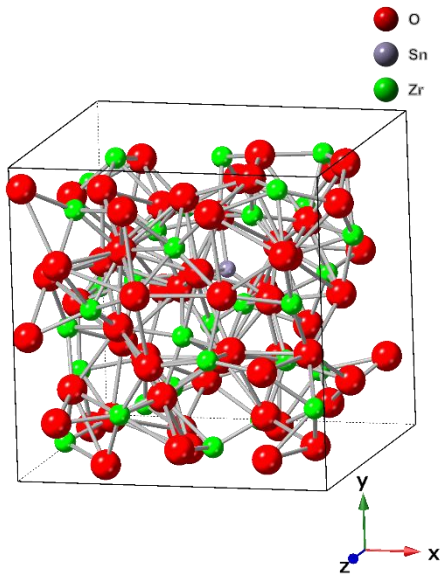

Figure 79 Tin interstitial in an amorphous ZrO_2 structure.

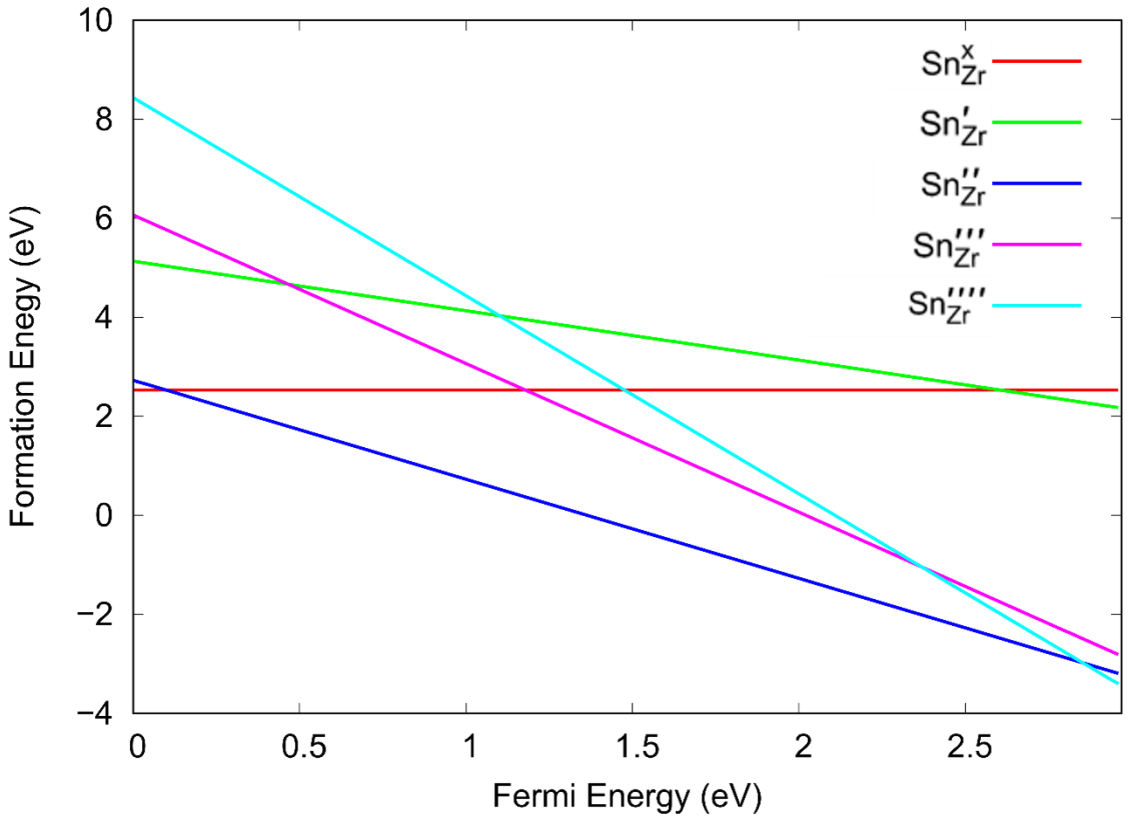

Figure 80 Formation energy of tin substitutions on zirconium sites with a range of charges across the Fermi energy of the bandgap of amorphous ZrO_2.

In the case of tin substitution defects, Figure 79, the formation energy results across the bandgap are less typical, Figure 80. Whilst the gradients are typical where an increase in charge results in a steeper gradient, the order in which the defects are presented does not follow the expected order. At the extremes, the negative four substitution holds the lowest formation energy at the bottom of the conduction band to the very far right and the neutral charged substitution at the top of the valence band to the far left, which is expected. It would normally be expected for the negative three

defect to have the lowest formation energy replacing the negative four moving away from the bottom of the conduction band, but this is not the case. There are a number of potential reasons for this. One route could be through larger than normal variations in DFT energy. This trend, however, was also identified in tetragonal ZrO_2 in the literature [147]. It was also stated that tin occupies the same lattice site, has the same oxidation state and has a similar ionic radius to Zr. For this reason, the tin has little effect on the intrinsic defect concentrations.

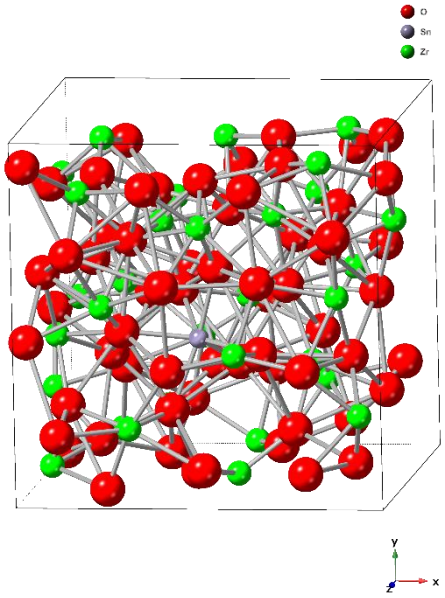

Figure 81 Tin substitution on a zirconium site in amorphous ZrO_2.

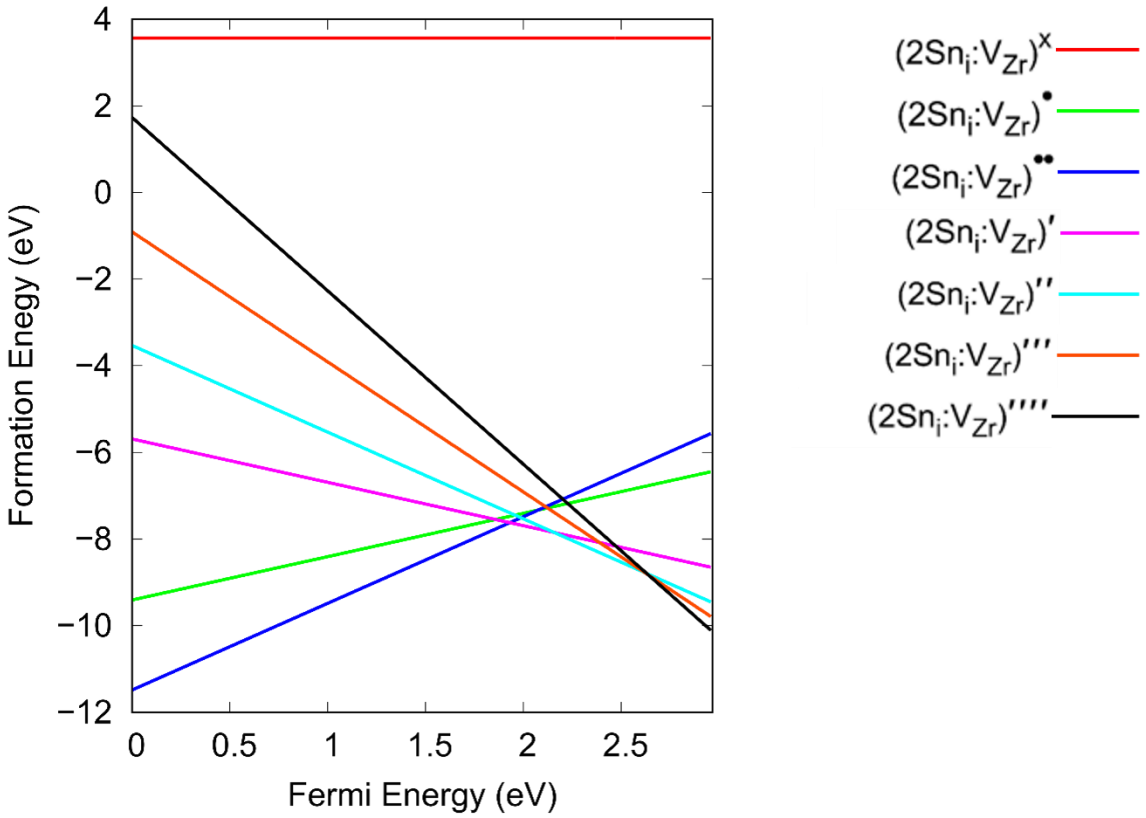

Figure 82 Formation energy of two tin interstitials around a zirconium vacancy site with a range of charges across the Fermi energy of the bandgap of amorphous ZrO_2.

In the case of the small cluster of two tin interstitials around a zirconium vacancy site, Figure 81, the formation energy vs Fermi energy diagram is much more typical, Figure 82, with the exception of the neutral charged cluster which shows a very high formation energy in comparison to the remaining defects. The formation energy for all of the charged defects, asides from the neutral charged defect, hold a negative formation energy with the exception of a small region of positive formation energy for the negative four cluster at the top of the valence band to the left. The lowest formation energy is also found at the top of the valence band to the far left with the plus two charged cluster $(2\mathrm{Sn_i}:\mathrm{V_{Zr}})^{••}$. This suggests a preference for a negatively charged oxide for the plus charged defect. For a positively charged oxide, the negative four charged cluster $(2\mathrm{Sn_i}:\mathrm{V_{zr}})''''$ has the lowest formation energy at the bottom of the conduction band to the far right.

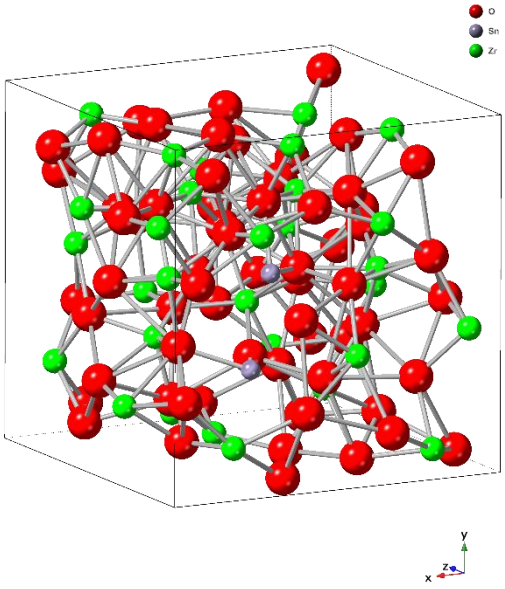

Figure 83 Two tin interstitials around a zirconium vacancy site in amorphous ZrO_2.

The tin defects could not be calculated within the Brouwer diagram concentration range, Figure 83. Given that tin defects seemed to show a good presence within the bulk of ZrO_2 whilst having little interactions with intrinsic defects, had the Sn defects of been present, it is likely that there would have been minimal interaction in the amorphous structure also. Atom probe results from literature have shown no tin segregation along grain boundaries, which may offer evidence to support this [144]. The literature also showed that tin can be found throughout the bulk of the material.

4.6. Combined Dopant Amorphous ZrO_2

Given the very few defects that were calculated and featured on the Brouwer diagrams, this offered more flexibility in presenting the diagrams. The only extrinsic defects being an iron interstitial $(\mathrm{Fe}_\mathrm{i}^{\bullet\bullet})$ and a small lithium cluster $(2\mathrm{Li}_\mathrm{i}\colon \mathrm{V}_\mathrm{Zr})''$.

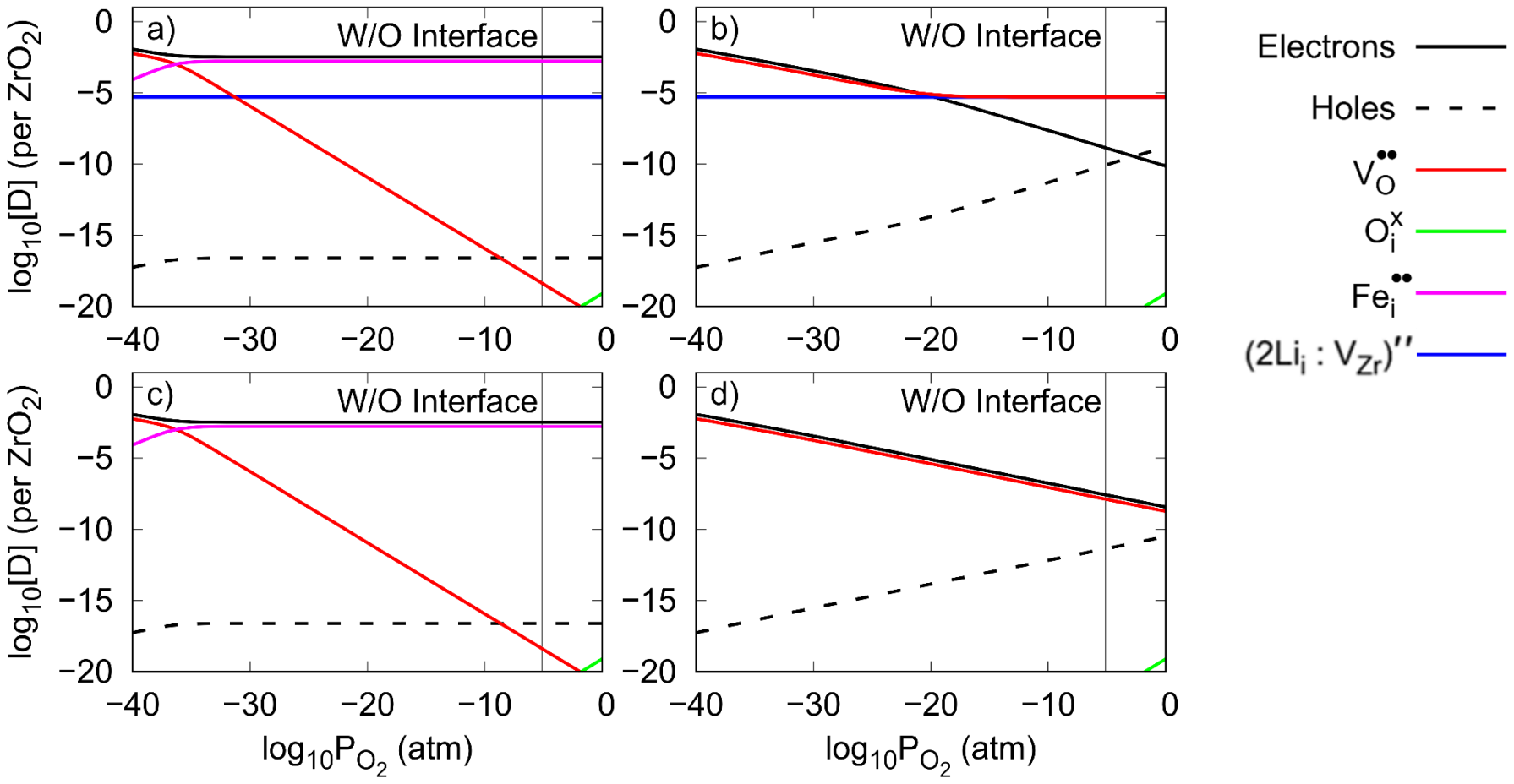

Figure 84 635 K Brouwer diagrams with defect concentrations [D] per unit amorphous ZrO_2 for (a) 10^{-5} Li and $24x10^{-3}$ Fe (b) 10^{-5} Li and no Fe (c) $2.4x10^{-3}$ Fe and no Li (d) intrinsic defects only [143].

The Brouwer diagrams containing lithium and iron defects presented an interesting set of results, Figure 84. In the diagram containing both lithium and iron (a), it can be seen that the iron interstitial ($\mathrm{Fe_i^{\bullet\bullet}}$) is couple with the electron concentration and that the electrons are elevated to a concentration of around 10^{-2} per ZrO_2. The lithium cluster $(2\mathrm{Li_i}\colon \mathrm{V_{Zr}})''$, however, did not have any effect on the intrinsic defects that had been previously observed in the lithium and intrinsic defects only Brouwer diagram, Figure 67. The oxygen vacancy defects ($\mathrm{V_O^{\bullet\bullet}}$) have a reduced concentration when compared to the level found in the intrinsic defects only diagram (d). The diagram showing only lithium defects along with intrinsic defects (b), shows that the lithium cluster $(2\mathrm{Li_i}\colon \mathrm{V_{Zr}})''$ does not affect the electron concentration, but it does couple with the oxygen vacancy defects ($\mathrm{V_O^{\bullet\bullet}}$) and increases the concentration of the oxygen vacancy defects, particularly towards the water oxide interface to the far right. It is apparent, however, that lithium only increases the concentration of oxygen vacancy defects when the lithium is at a higher concentration than what the oxygen vacancy defects are at intrinsic levels (d). Finally, the diagram showing the iron defects without lithium (c) produces the same intrinsic defect changes that we could see in the iron with lithium defect Brouwer diagram (a).

In summary, lithium will increase the level of oxygen vacancy defects if sufficiently high enough in concentration. Where iron is introduced, however, this subdues the effects of lithium on the intrinsic defects and also reduces the oxygen vacancy concentration as well as elevating the electron concentration. This is also coupled with a reduction in hole concentration. Iron can only subdue the effects of lithium on the oxygen vacancy concentrations when at a sufficiently high enough concentration (above 10^{-10} per ZrO_2).

4.7. Volume Changes Due to Defects

Previous work in literature has indicated a potential volumetric change associated with defects and that lithium, in particular, may reduce the volume and cause a more porous network within the oxide [1]. An advantage of producing Brouwer diagrams that provide an indication of defect concentration per ZrO_2 is that the constant pressure DFT calculations (degrees of freedom include ion positions, cell shape and cell volume) can produce volumetric variations due to defects and then be applied to the calculated concentration. This may provide a more accurate simulation for a change in volume. The first thing to view is the volume change calculated through DFT per ZrO_2. It is worth noting again that charged defects can show exaggerated volume changes through DFT [135]. Whilst this can be mitigated, this work aims to gain a general indication of volume change rather than a specific value.

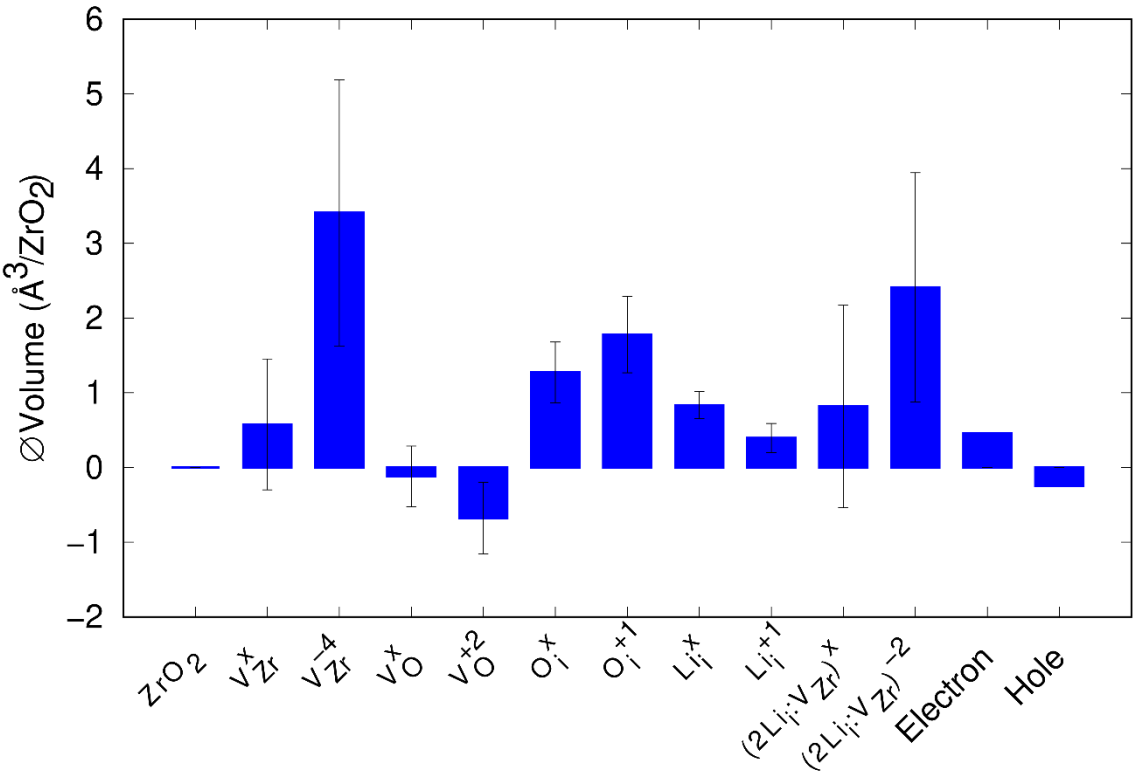

Figure 85 Volume change per ZrO_2 in amorphous ZrO_2 for a selection of defects at 0 K.

Figure 85 shows the volume change (Δ) for a selection of defects over the amorphous structure with no defects per ZrO_2. The volume changes related to defects in the amorphous structure was a little unexpected, Figure 85. It would be expected, in general, for an interstitial to increase volume and a vacancy to reduce volume as seen in the literature [148]. Electrons are expected to increase volume through columbic repulsion and holes are expected to reduce volume. In the bar graph above (**Error! Reference source not found.**), however, we see a neutral charged zirconium vacancy defect ($V_{Zr}^{\times}$) increases the volume and the plus two charged iron interstitial ($Fe_i^{\bullet\bullet}$) decreases the volume. There are large ranges of volume change, presented as error bars, due to the different locations of defects within the amorphous structures. On the most part, the range of volume difference between defect locations can account for this to a degree. However, it does indicate that the change in volume is not as predicted in the literature [1]. In particular, the positive one charged lithium interstitial was found to decrease the volume of bulk oxide in the literature, where in the amorphous structure, it is found to increase the volume.

Applying the defect volume change per ZrO_2 to the Brouwer diagram defect concentrations may present an overall indication of volume change when applied to the combined defects.

By combining the volume changes per ZrO_2 and the concentration per ZrO_2, the overall volume changes due to all the defects combined can be calculated. The lithium concentration was set to 10^{-1} (the highest calculated concentration) and iron to 2.4 x 10^{-3} per ZrO_2 which, when combined with all the other defects, produced a volume change between approximately 0.052 and -0.046 $Å^3$ per ZrO_2. At lower Li concentrations (10^{-3}), this value ranges between 0.0008 to -0.004 $Å^3$ per ZrO_2. This indicates that the change in volume is very small when considering all defects combined, even with the highest stipulated concentration of lithium.

4.8. Solution Energies

Many reactions were calculated to identify the likelihood of defect solution within the amorphous structure at 0 K. Some reactions were found to be very high with a positive solution energy and others very low. Whilst a negative value indicates solution is possible with an exothermic reaction (producing heat), an extremely negative solution energy would indicate a very explosive reaction. Therefore, the negative values needed to be within reason. A positive solution energy, on the other hand, would indicate that the reaction is unlikely and would require external energy and influences to occur.

Table 8 Reaction and solution energy for lithium and iron into zirconium oxide

Reaction	Solution energy eV
$2Li_2ZrO_3 + Zr_{Zr}^{\times} \rightarrow \{2Li_i^{\bullet}: V_{Zr}^{''''}\}'' + 2Li_i^{\bullet} + 3ZrO_2$	5.7
$2Li_2ZrO_3 + V_{Zr}^{''''} + Zr_{Zr}^{\times} \rightarrow 2\{2Li_i^{\bullet}: V_{Zr}^{''''}\}'' + V_O^{\bullet\bullet} + 3ZrO_2$	2.3
$Li_2ZrO_3 + \frac{1}{2}O_2 + Zr_{Zr}^{\times} \rightarrow \{2Li_i^{\bullet}: V_{Zr}^{''''}\} + 2h^{\bullet} + 2ZrO_2$	8.8
$Li_2ZrO_3 + \frac{1}{2}O_2 + Zr_{Zr}^{\times} \rightarrow \{2Li_i^{\bullet}: V_{Zr}^{''''}\} + 2Li_i^{\bullet} + 2ZrO_2$	5.3
$Li_2ZrO_3 \rightarrow 2Li_i^{\bullet} + V_O^{\bullet\bullet} + O_2 + ZrO_2 + 3e^{-}$	5.5
$Li_2ZrO_3 + V_{Zr}^{''''} + 2Li_i^{\bullet} \rightarrow 2\{2Li_i^{\bullet}: V_{Zr}^{''''}\}'' + V_O^{\bullet\bullet} + 2ZrO_2$	-0.01
$FeZrO_3 + V_O^{\bullet\bullet} \rightarrow Fe_i^{\bullet\bullet} + ZrO_2$	2.8
$Fe_3O_4 + 4V_O^{\bullet\bullet} \rightarrow 3Fe_i^{\bullet\bullet} + 2h^{\bullet}$	4.4
$Fe_2O_3 + 3V_O^{\bullet\bullet} \rightarrow 2Fe_i^{\bullet\bullet} + 2h^{\bullet}$	5.0
$FeZr_2 + 3O_i^{\times} + V_O^{\bullet\bullet} \rightarrow Fe_i^{\bullet\bullet} + ZrO_2$	1.7
$Fe_2O_3 + Fe_2Zr + V_O^{\bullet\bullet} + 6h^{\bullet\bullet\bullet\bullet\bullet\bullet} \rightarrow 4Fe_i^{\bullet\bullet} + ZrO_2$	-1.1

Negative solution energies were found for both lithium and iron, but not in all reactions, Table 8. In the case of lithium, the introduction of Li_2ZrO_3 along with a zirconium vacancy ($V_{Zr}^{''''}$) and two lithium interstitials ($Li_i^{\bullet}$) can result in the cluster $(2Li_i^{\bullet}: VZr'''')''$ and an increase in oxygen vacancy ($V_O^{\bullet\bullet}$) which is found in the Brouwer diagrams with high lithium concentrations (above 10^{-11} per ZrO_2). This defect, however, required the introduction of the lithium interstitial as part of the reactant.

To check if the lithium interstitial is more stable than the cluster, equation 28 can provide an indication.

$$2Li_i^{\bullet} + 2O_i^{\times} + Zr_{Zr}^{\times} + 2e'' \rightarrow \{2Li_i: V_{Zr}\}'' + ZrO_2 + 2h^{\bullet\bullet} \qquad \text{Equation 28}$$

This produces an energy of 3.0 eV indicating that the cluster is much more stable. Equation 29 provided a solution energy of -0.38 eV with a standard deviation of 1.27 eV which accounts for the average of each defect location change.

$$Li_2ZrO_3 + O_O^{\times} + Zr_{Zr}^{\times} \rightarrow \{2Li_i^{\bullet}: V_{Zr}^{''''}\}'' + V_O^{\bullet\bullet} + 2ZrO_2 \qquad \text{Equation29}$$

Whilst the standard deviation is greater than the negative solution energy, it allows for a large portion of lithium solution into the amorphous structure.

In the case of iron, a combination of the Fe_2O_3 and Fe_2Zr coupled with an oxygen vacancy ($V_O^{\bullet\bullet}$) and 6 holes can react to form four iron interstitials ($Fe_i^{\bullet\bullet}$). This highlights the reduction in oxygen vacancy and holes used in the reactant to form the product which confirms what was seen in the Brouwer diagrams also.

4.9. Summary and Discussion

This chapter aimed to answer the questions created by hypothesis in which lithium accommodation could be found along grain boundaries and potentially form pores or grain boundary phases. This required multiple steps to accomplish. Creating amorphous structures with sufficiently low number of atoms to use in density functional theory calculations could be attempted through two routes. The first method was to create amorphous structures through molecular dynamics multiple times and then to repeat this method with both over-coordinated and under-coordinated structures for both oxygen and zirconium to account for vacancies and interstitials, respectively. All of these calculations needed to have a fixed volume as that of the stochiometric zirconia structure and remain so throughout all calculations. The reason for this, as mentioned in the method section, is to provide a solution limit for defects and is a standard method when gaining values to calculate Brouwer diagrams [121]. The issue with this method is that lithium, in particular, does not currently have a robustly tested potential within zirconia to use during molecular dynamics calculations. This meant that the lithium defects needed to be added later when creating structures at the DFT stage. The alternative to this was to create a range of stoichiometric amorphous structures in molecular dynamics, simply to ensure consistency. The structures could then be reduced through reverse Monte-Carlo before being placed through DFT calculations. Through this method, the defects, including vacancies and interstitials, could be added to the constant volume structures. The first method is likely the preferred method, however, no substantial study has been carried out to confirm the differences to the knowledge of the author. For intrinsic defects, the two methods produced very similar results without any remarkable difference in the case of zirconia. Future work would likely be needed to review the differences of these two methods with different materials as changes in stoichiometry can, essentially, create a very different amorphous structure including the electrical properties. This could have the potential to produce vastly different formation energies, Brouwer diagrams, volume changes and solution energies.

For the formation energy diagrams, they provide a good indication of which defects may feature on the Brouwer diagrams and how the concentration may change due to the charge of the material or defects throughout the oxide. This was found to be the case for the intrinsic and lithium defects. However, for the chromium and tin defects, despite producing negative formation energies, these defects were not found on the Brouwer diagram. The formation calculations are a simple dissociation of the defect components in relation to material charge whilst the Brouwer diagram calculations use multiple variables such as temperature, deviation from stoichiometry, oxygen partial pressure, and charge to build an indication of charge balanced defects across the partial pressure range. Whilst all of the iron defects produced negative values on the formation energy plots, only one defect featured on the Brouwer diagram being the plus two charged iron interstitial ($Fe_i^{\bullet\bullet}$). This defect had neither the lowest formation energy or, even, the lowest formation energy at the valence band maximum or the conduction band minimum.

The amorphous zirconia intrinsic and extrinsic defect Brouwer diagrams produce very few defects when calculated. This is particularly evident when held in comparison with the bulk zirconia Brouwer diagrams which are almost illegible due to the huge number of defects presented. This is due to the large variations in calculated relaxed energies of the defect structures. For intrinsic defects, there is a small concentration of neutrally charged oxygen interstitials, but these defects show no interaction

with any other introduced defect at any concentration. The oxygen vacancy defects, on the other hand, show fairly high concentrations, particularly at greater depths into the oxide from the water oxide interface. When lithium is introduced, this causes the oxygen vacancy defects to increase, particularly at the water oxide interface. This, however, only occurs where the lithium concentration is higher than that of the intrinsic oxygen vacancy defect concentration. Iron, on the other hand, reduces the oxygen vacancy defect concentration overall but increases the electron concentration. The iron interstitial that causes this is plus two charged indicating that the oxide remains neutrally charged overall. The introduction of iron at sufficiently high concentrations prevents lithium from increasing the oxygen vacancy concentration. The chromium and tin defects were, unfortunately, unable to be calculated within the Brouwer diagram ranges of concentration and partial pressure. This is likely, again, due to the large variations in relaxed energies calculated due to no order in the amorphous structure.

Calculating volume changes with respect to defects predicted with the Brouwer diagrams has shown that the overall volume change is extremely small in the amorphous oxide. Whilst there is a small range to be found, the volume change is equally likely to be positive as it is negative depending on defect location within the structure. This would likely require experimental work for verification as volume changes may be associated with several external factors such as temperature and environment. This does answer one part of the second hypothesis where pore growth through volumetric changes may be identified. This investigation has found that this is unlikely, but it cannot rule out the possibility. This would require a more in-depth investigation into the amorphous structures and potential volume change associated with the defect accommodation.

By reviewing the potential defects presented on calculated Brouwer diagrams, the solution energies of possible reactions were also calculated to provide an indication of plausibility. Lithium and iron were both found to have a negative solution energy associated with both an increase in oxygen vacancy associated with lithium, and an oxygen vacancy reduction associated with iron. Again, future work would likely be needed to provide evidence for elevated iron concentrations in the amorphous structures preventing an increase of oxygen vacancy in high lithium environments. Whilst this would likely require an increase in iron as an alloying addition, it would require a host of investigations to assess this as a viable option to mitigate lithium accelerated corrosion. Alternative alkaline coolant additives is likely to be a more efficient area of investigation using the methods provided in this chapter to identify possible alternatives to prevent lithium accelerated corrosion.

The second part of the second hypothesis is regarding grain boundary phase formation along grain boundaries. Unfortunately, this has not been addressed in this chapter and will pass to the next chapter which will begin the experimental techniques.

5. Experimental Works – The Synthesis and Characterisation of Lithium doped ZrO_2 (From Amorphous to Bulk)

The work in this chapter was published.

"Lithium stabilization of amorphous ZrO_2" [149] **Progress in Nuclear Energy (1st Author)**

The contribution of the author to this work was to undertake synthesis, characterisation, SEM with EDX, Thermal analysis, mass spectroscopy and first draft manuscript creation. STEM with EELS and ICPOES were conducted by other authors.

The experimental work set out to answer the question, how lithium could affect the ZrO_2 oxide layer and how lithium would integrate into the structures, if at all. Given that the simulation work provided an indication of lithium solubility into the complex, amorphous, grain boundaries, producing lithium doped amorphous ZrO_2 made logical sense as a first step. From there, further experimentation could be conducted to find how lithium would behave when the amorphous structure would crystallise and what form would it take.

The steps utilised in this investigation were to first synthesise lithium doped ZrO_2 at various lithium concentrations. If lithium does segregate along grain boundaries as the simulation work indicated, the concentration of lithium could potentially be much greater than would be expected if it was soluble across the whole oxide layer. Conversely, when the Zircaloy is first placed into the lithium doped aqueous environment, the lithium concentration in the oxide layer would be expected to be zero. For that reason, the lithium concentration range was initially very large from 0.001 mol % to 50 mol %. From there, to confirm that the lithium doped and undoped structures were amorphous through Raman spectroscopy and x-ray diffraction (XRD). Scanning electron microscopy with energy dispersive x-ray (SEM/EDX) could provide information about the elemental distribution of the synthesised sample as well as evidence of atomic ratios of oxygen to zirconium to ensure that the ratio was correct. Simultaneously thermal analysis allowed for the samples to be heated up to the point where a change in morphology took place. By conducting thermal analysis with a range of lithium concentrations, this would provide an indication of stability or instability of the amorphous structure due to lithium concentration. In addition to this, the samples were simultaneously monitored through gravimetric changes and using mass spectroscopy (TG/MS), the gasses released from the sample could provide details of any losses such as lithium or steam. The resulting structure could then be again identified using Raman spectroscopy and x-ray diffraction. Scanning transmission electron microscope with electron energy loss spectroscopy (STEM/EELS) was used to identify the location of lithium within the crystallised samples to confirm if lithium had formed solution into the bulk material. Finally, inductive coupled plasma optical emission spectroscopy (ICP-OES) was used to identify lithium in aqueous solution where the crystallised ZrO_2 remained in solution.

5.1. Synthesis of Li Doped ZrO_2

The synthesis of undoped and lithium doped ZrO_2 was conducted without any apparent issues. The samples all produced a brilliant white, fine powder. The final structure, however, needed to be determined and confirmed to be amorphous. The lithium concentrations were 0.001, 0.01, 0.1, 1, 5, 10, 20, 30, 40 and 50 mol % in ZrO_2. The lower concentrations including 0.001, 0.01, 0.1, and 1 mol %

which showed no changes from that of the undoped structure through all processes including simultaneous thermal analysis and XRD, so were omitted from further investigation.

5.2. Raman Spectroscopy

Raman spectroscopy was conducted on the samples with higher lithium concentrations to confirm that the structures were amorphous, and then again after heat treatment through the simultaneous thermal analysis to confirm that the structures had crystallised.

5.2.1. Amorphous ZrO_2 and Li doped ZrO_2.

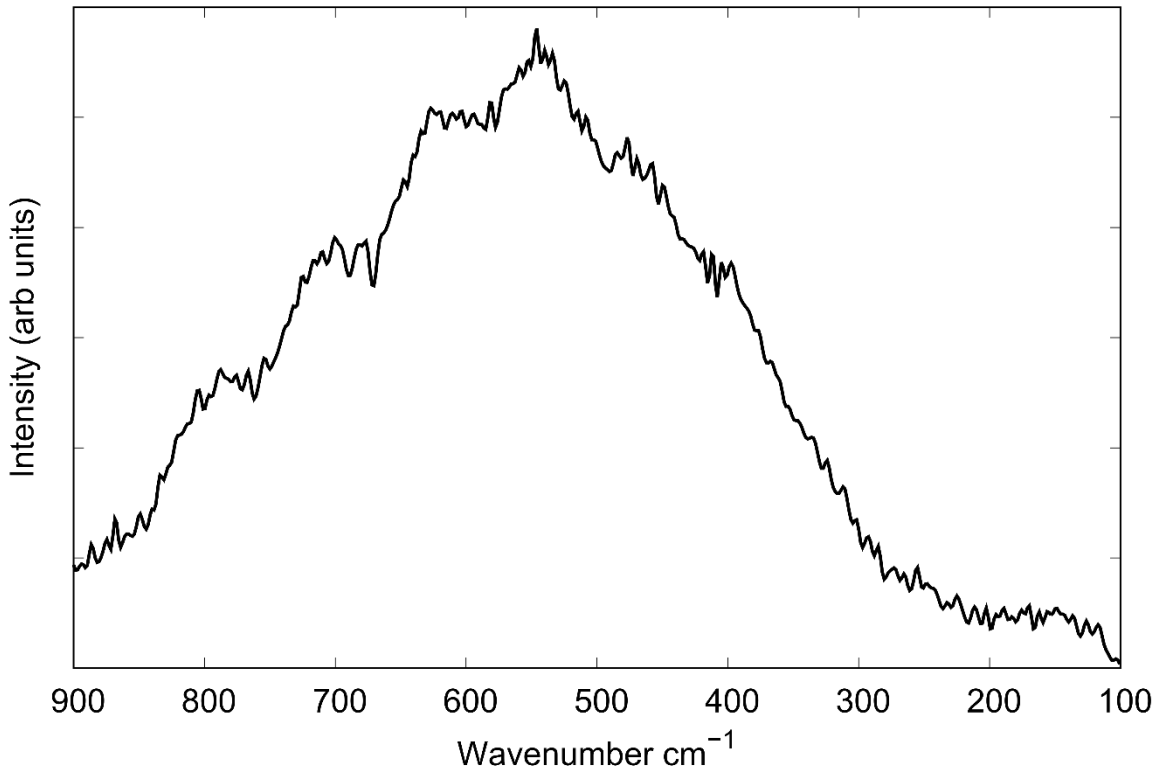

Figure 86 Typical Raman spectrum of amorphous ZrO_2.

As can be seen in the Raman spectrum of a typical sample (this was the 50 mol % sample), Figure 86, there is an absence of any order as no definitive peaks could be identified which indicates no long-range order within the sample. There were no notable differences between all samples which provided evidence that the samples were amorphous post synthesis. No change from the range of lithium concentrations could be observed between samples.

For all samples a 2-dimensional map was created using the Raman microscope in order to confirm that the regions were void of any long-range order. An average intensity could be gained that would also double to remove any noise that may have occurred during each individual measurement, also known as coadditions. Due to the fine powder produced during synthesis, a general focus across the entirety of the mapped area was virtually impossible to achieve. This resulted in changes in relative intensity between sample points within the mapped area. This, however, did not provide any evidence to suggest that any long-range order was within the sample.

5.2.2. Bulk ZrO_2

Once the samples had been heated in the simultaneous thermal analyser (STA) up to 600, 700 and 1000 °C, which will be described later, confirmation was required to ensure that the morphology of the structures had changed.

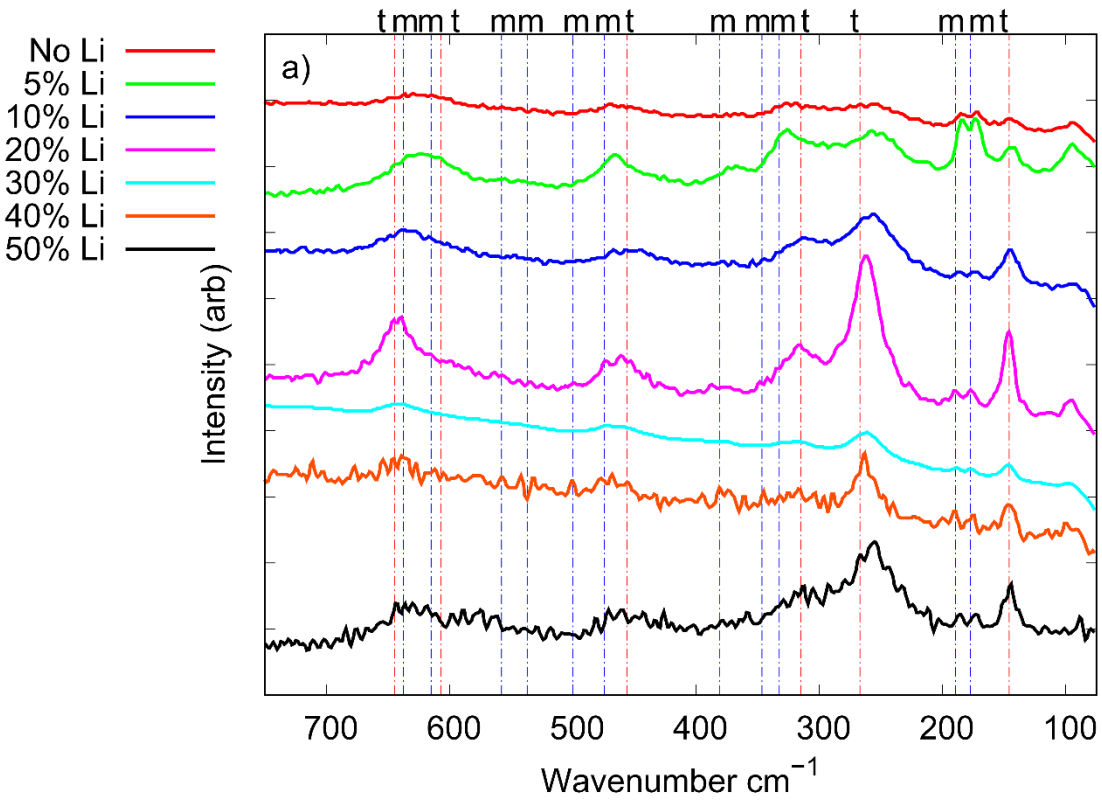

Figure 87 Averaged 2D map Raman of undoped and 5, 10, 20, 30, 40 and 50 mol % Li doped ZrO_2 post simultaneous thermal analysis to 700 °C. Vertical lines are given for expected peaks for monoclinic (blue) and tetragonal (red) structures.

When reviewing the post STA samples using Raman spectroscopy, evidence of long-range order could be seen, Figure 87. The peaks gained, however, were broad with low relative intensity when compared to the baseline for each sample which is indicative of short-range order and/or high intrinsic defect concentrations. It was later found, through STEM, that the crystal sizes were in the sub 100 nm range, which provides a small limitation for Raman spectral outputs for such cases. There are, however, small intensity peaks which can be seen to coincide with both tetragonal and monoclinic structures at low wavenumbers, particularly in the sub 300 cm^{-1} region, in all samples, These coincide with the tetragonal B_{1g} phonon at 155 cm^{-1} and the monoclinic pair B_g and A_g phonons at 177 and 189 cm^{-1}, respectively, confirming literature results [150] using the notation previously developed [151]. There does appear to be a small shift of the tetragonal peak at 260 cm^{-1} which may also be associated with defects or stresses present in all samples. This is likely due to defects within the sample, as mentioned earlier.

5.3. X-ray Diffraction

The more successful method in identifying both the amorphous and crystallised structures was gained using XRD analysis. This is due to the XRD equipment being specifically designed for powders and requiring only the smallest of samples to gain a positive pattern. XRD was first utilised to ensure that the synthesised samples were amorphous in all cases, and then again, post STA thermal treatment.

5.3.1. Amorphous ZrO_2 and Li doped ZrO_2

As with Raman spectroscopy on amorphous structures, the XRD is expected to produce no apparent peaks in the absence of any order with an unremarkable pattern of results.

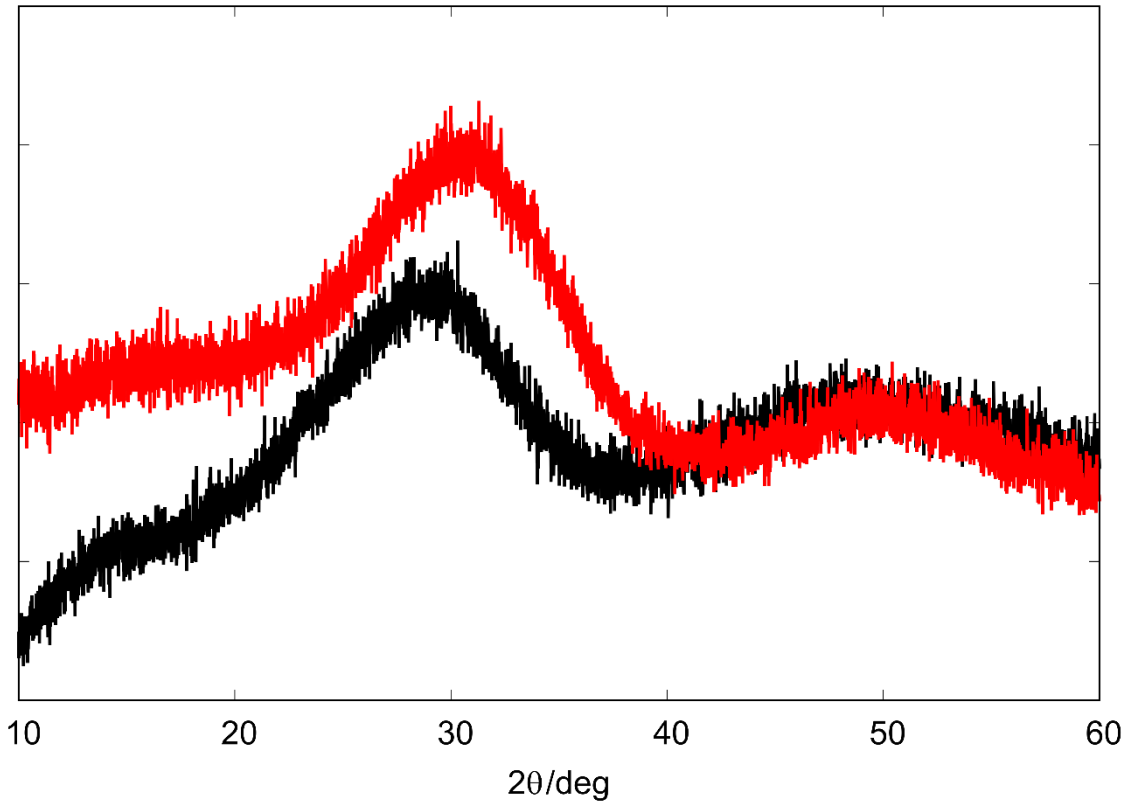

Figure 88 XRD of a typical ZrO_2 amorphous undoped structure (black) and 50 mol % doped (red).

The XRD patterns for all samples confirmed that the structures were amorphous which were comparable to both simulation [152] and experimental work [153] in the literature. The characteristic lack of prominent peaks and low relative peak intensity provided evidence of no order and an amorphous structure, Figure 88. Due to low intensity peaks, this also highlights noise. The very broad peaks are of very low relative intensity and are produced from irregular surfaces. This was the case for all samples including undoped and lithium doped ZrO_2 and corroborates with the Raman data obtained for the as-prepared samples.

5.3.2. Bulk ZrO_2

Whilst it was important to ensure the samples were amorphous once synthesised in the previous section, it did provide XRD patterns that were low in features to discuss. The patterns for the samples gained post STA, however, were much more interesting offering many more points for discussion. The peaks gained from the samples were representative of what can be found from literature for bulk ZrO_2 with the introduction of a number of interesting features.

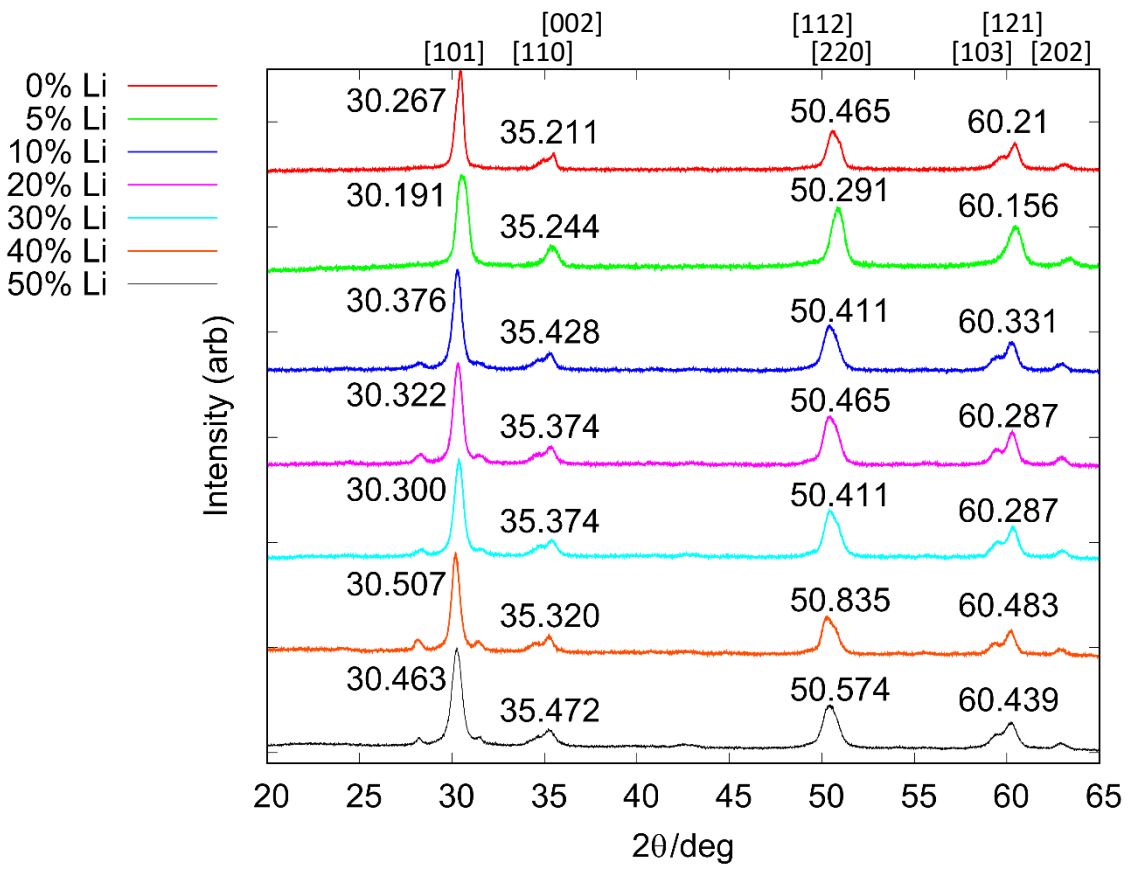

Figure 89 XRD patterns with a range of lithium concentrations from zero to 50 mol % in ZrO_2 samples post 700°C heat-treatment.

The range of lithium concentrations from zero to 50 mol % doped ZrO_2 heat treated to 700°C shows slight peak broadening for all patterns which is indicative of imperfections including defects such as vacancies or interstitials, Figure 89. More from this can be seen in the following plot which shows literature values. This is, however, consistent for all patterns so is not deemed as a result of lithium concentration. With lithium concentrations greater than 5 mol %, two small peaks either side of the first main peak ~30° 2θ gives an indication of some structural change due to lithium concentration. These small peaks are also reviewed in the following plot to identify the possible structure. There are subtle shifts in the vertex of the main peaks (± 0.2° 2θ), but these do not show a trend related to lithium concentration so cannot be attributed to lithium caused changes in lattice parameters. An interesting note to make is with that of the 5 mol % pattern which is missing the doublet in both the 35.3° and 60.4° 2θ regions. Prior to conducting the 700°C STA thermal treatment runs a few samples were heated up to 600°C. However, this will be discussed later, the crystallisation temperatures reached almost 600°C, so the decision was made to increase this temperature up to 700°C. When reviewing the XRD patterns for the few samples that were heated to 600°C, there is a surprising difference.

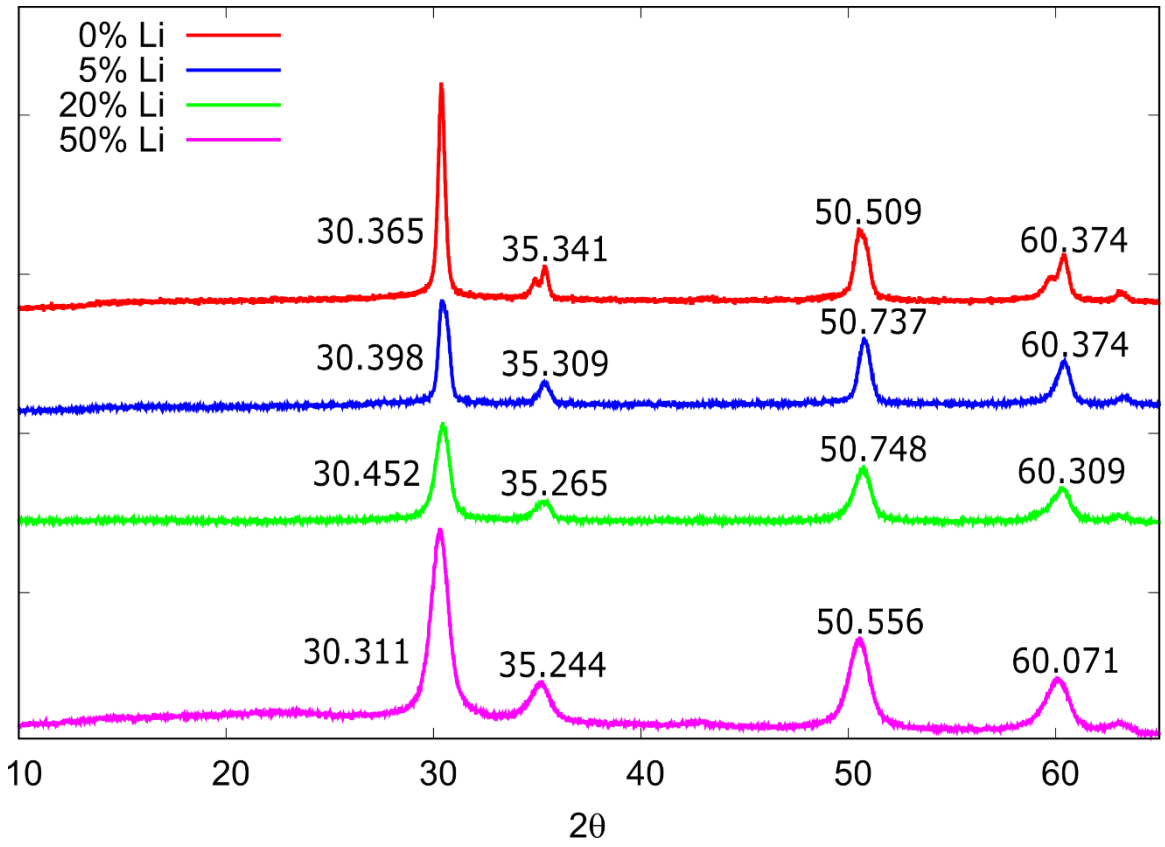

Figure 90 XRD patterns with a range of lithium concentrations from zero to 50 mol % in ZrO_2 samples post 600°C heat-treatment.

As with the 5 mol % XRD pattern for the 700°C heated sample, all samples with lithium included that were heated to 600°C are missing the doublets at ~30° and ~60° 2θ (monoclinic structure). The sample containing zero lithium maintains the doublet which gives an indication of some form of stability or pressure release through lithium dopants at the lower temperature, Figure 90. When increasing the temperature further to 1000°C, a different pattern is apparent.

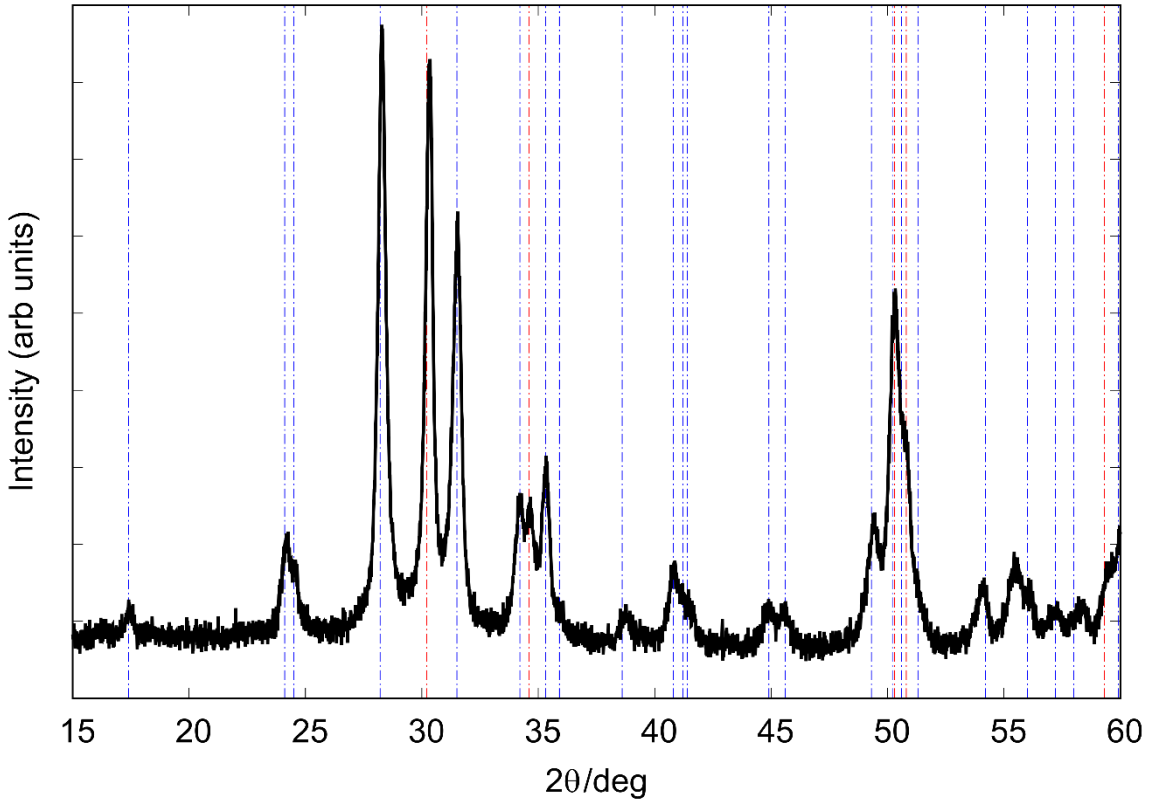

Figure 91 XRD pattern of undoped ZrO_2 pre-heated up to 1000° C. Literature monoclinic ZrO_2 is shown in blue [154] *and tetragonal in red* [155] *vertical dashed lines.*

The XRD pattern for the undoped ZrO_2 pre-heated to 1000°C pattern does look very different from that of the pre-heated patterns up to 600 and 700°C, Figure 91. The resulting pattern, however, shows only a change in ratio between peaks. The main peak seen at ~30° 2θ in the 600°C and 700°C XRD patterns is found in the 1000°C pattern but is overshadowed by the increase in ratio of the peaks either side of the 30° 2θ peak at 28° and 31° 2θ. These two peaks are also found in the lithiated samples that were heated up to 700 °C at much smaller ratios. There are also a number of peaks that are new to the 1000°C pattern including a doublet at 24° 2θ, and an additional cluster of small peaks between 54° and 58° 2θ.

To identify the changes in structure as a result of lithium and from higher temperatures, comparing these values with possible literature structures was required.

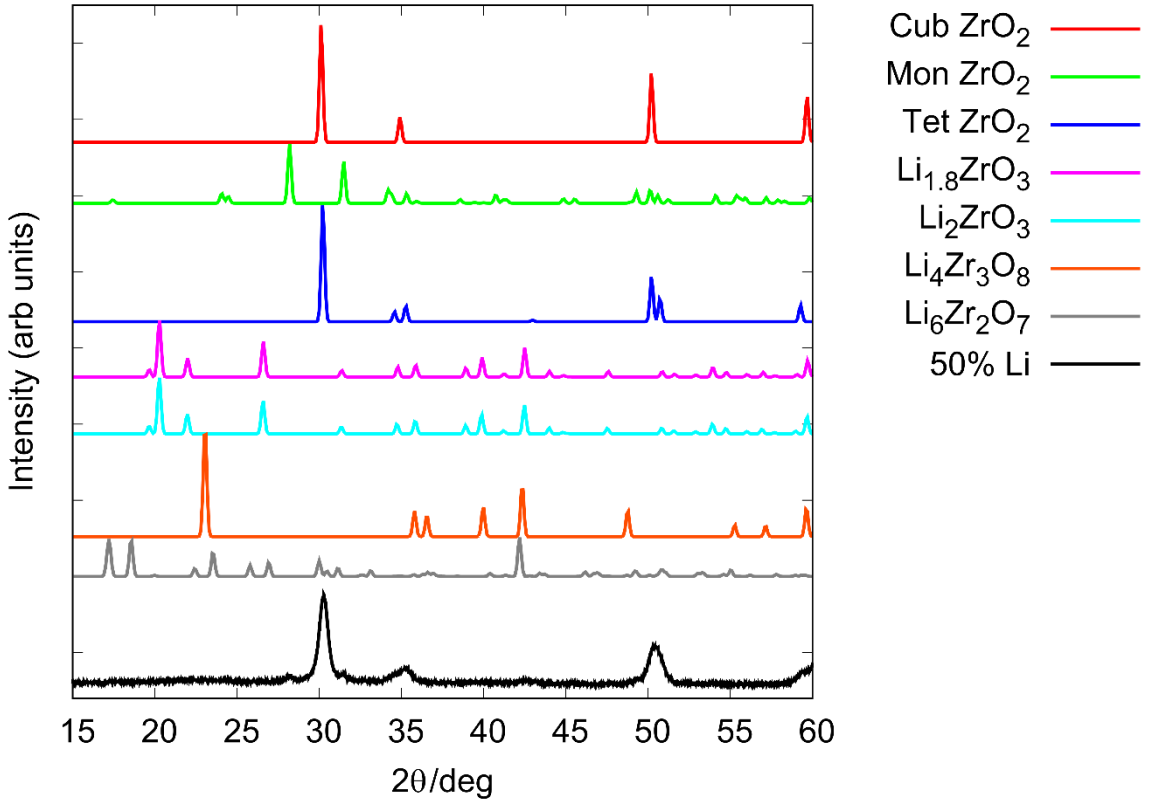

Figure 92 Literature XRD patterns for cubic ZrO_2 [156]*, monoclinic ZrO_2* [154]*, tetragonal ZrO_2* [157]*, and the lithium zirconia structures of $Li_{1.8}ZrO_3$* [158]*, Li_2ZrO_3* [159]*, $Li_4Zr_3O_8$* [160]*, and $Li_6Zr_2O_7$* [161]*. The final black plot to the bottom is the 50% lithium doped ZrO_2 sample heated to 700°C for reference.*

When comparing the 50 mol % Li doped ZrO_2 XRD pattern for the sample that was pre-heated to 700°C with literature values, Figure 92, it was hard to associate any lithiated literature structure with what we produced. However, the cubic, monoclinic and tetragonal literature structures all have a potential to fit our XRD pattern. The highest relative intensity peak that was gained from our sample was at 30° 2θ which aligns with both the cubic and the tetragonal structure. The two smaller peaks either side of the 30 2θ peak is that of the 28° and 31° 2θ peaks which align with the monoclinic literature structure. The main difference in literature XRD patterns between the cubic and tetragonal structures is the presence of doublets in the tetragonal structure at 35° and 50° 2θ. The 50 mol % lithium ZrO_2 sample shows both the doublet associated with the tetragonal structure along with the two 28° and 31° 2θ peaks indicating a presence of monoclinic ZrO_2 within the sample, at a much lower ratio. Comparing the 600°C pre-heated samples, with the exception of the undoped structure, were more aligned with the cubic structure. At the higher temperature of 1000°C, the monoclinic ratio was much higher with a relative intensity that was slightly higher than the tetragonal peak.

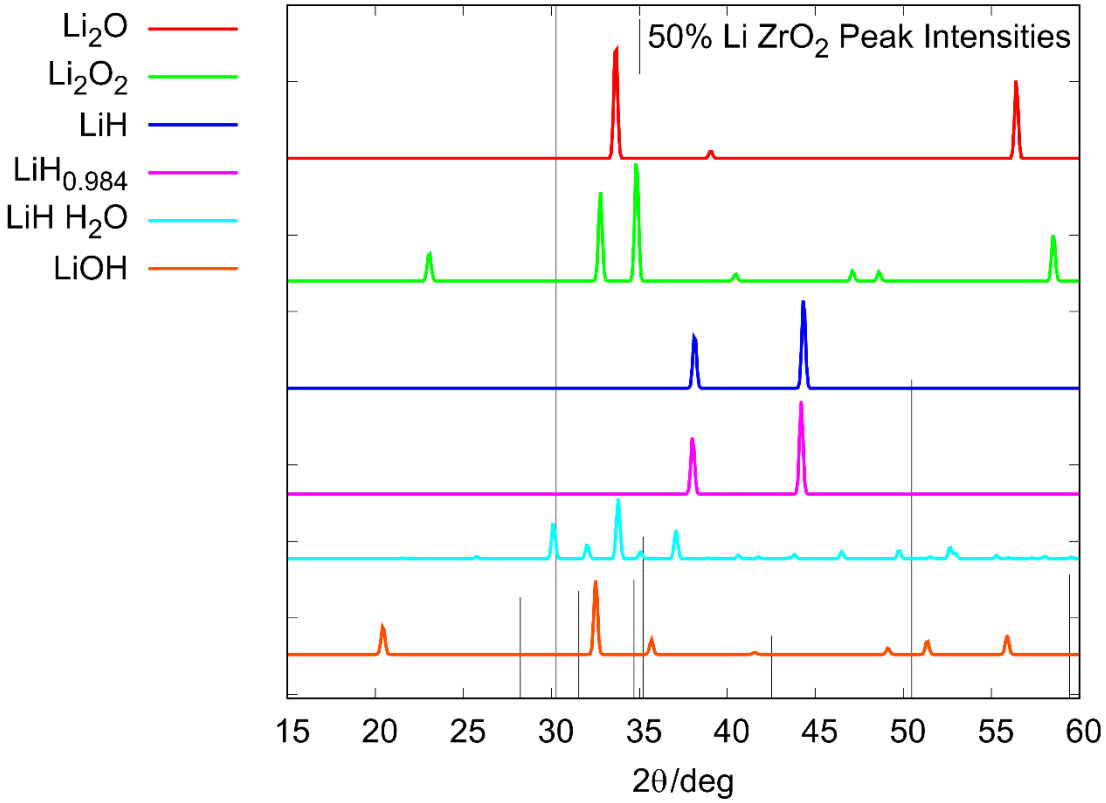

Figure 93 Literature XRD peaks for lithium oxide, hydride and hydroxide [162–166]*.The vertical black lines show the XRD peaks for 50 mol % post STA zirconia sample heated to 700 °C.*

When reviewing the high concentration lithium doped zirconia sample (50 mol %) against literature values for lithium oxide, hydride and hydroxide, Figure 93, the peaks did not match at all. This is not to say that a form of lithium hydroxide is not present, it is just not in a structure that can be identified through XRD.

5.4. Scanning Electron Microscopy with EDX

The first step in identifying the potential grain sizes and lithium location within the grains adopted the scanning electron microscopy with energy dispersive x-ray (SEM with EDX) method. The later, however, would not be possible due to the low energy of characteristic radiation produced from lithium which was placed within the low energy noise region which is not easy to detect and is hence a small limitation of the otherwise effective instrument. The powder was collected by placing carbon tape onto a 12.5 mm SEM stub and then lightly “dipping” the stub into the powder allowing the adhesive to pick up a small amount of the sample. The stub was then given a light brush to ensure that any remaining powder was sufficiently adhered to the stub, preventing any loss during the evacuation of the SEM chamber which could otherwise have the potential to damage the equipment.

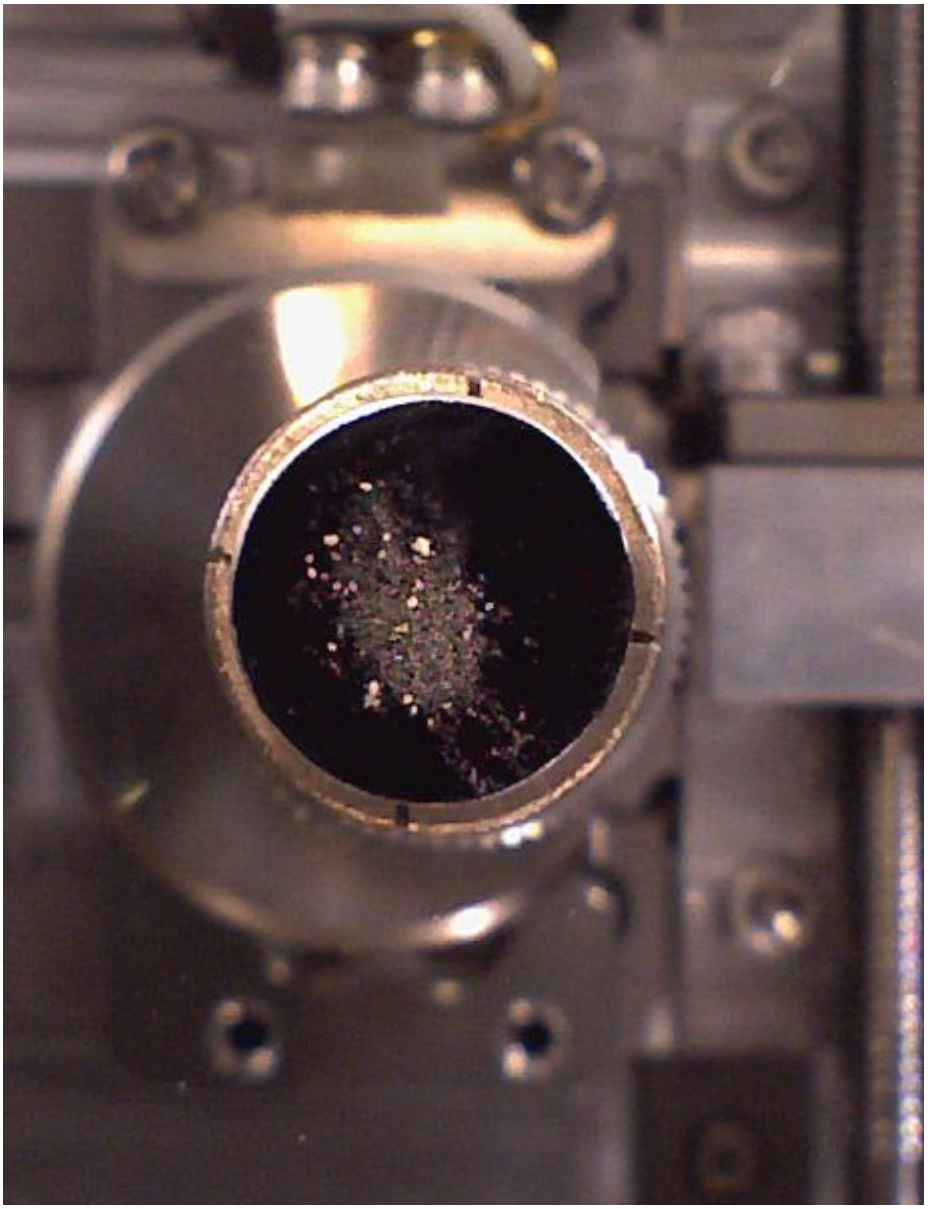

Figure 94 Image of the crystallised 50 mol % Li doped ZrO_2 powder on carbon tape within the SEM.

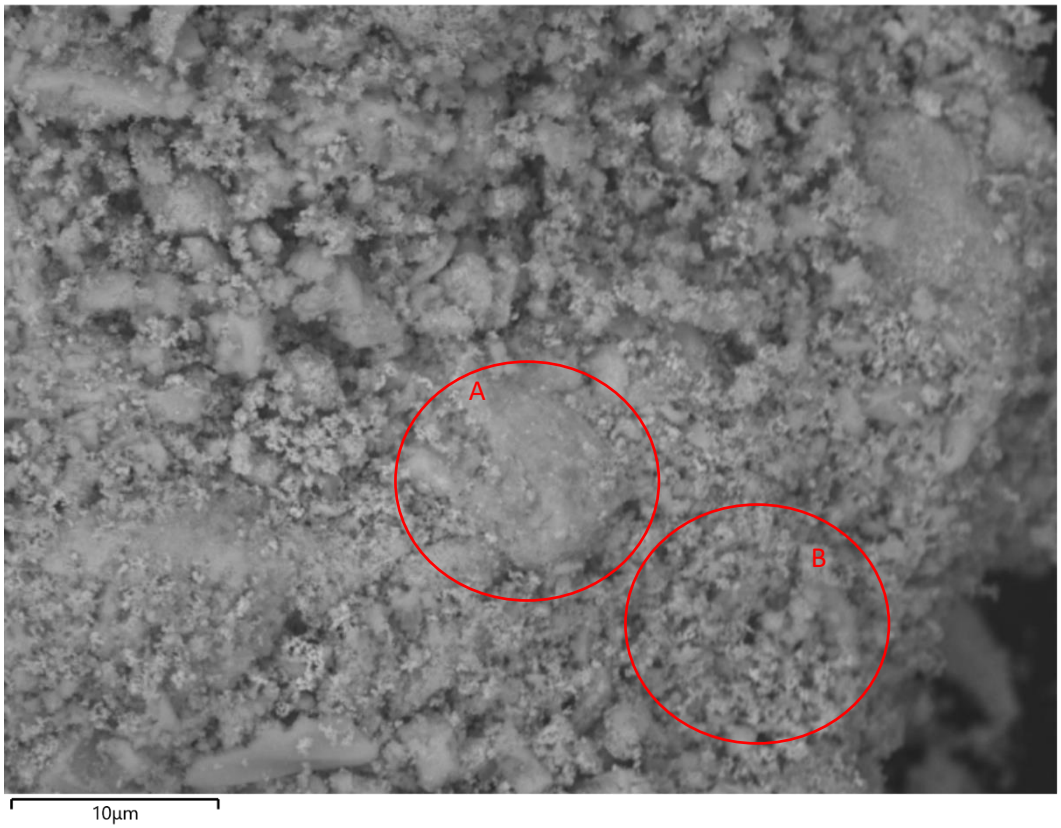

Figure 95 Typical SEM image of 50 mol % Li doped ZrO_2 with a 10-micron scale bar (x 12000 magnification).

When taking the SEM to the maximum zoom with sufficient resolution (*x 12000* magnification), Figure 95, it was difficult to ascertain any specific grains individually. The larger structures (region A) seen were comprised of a cluster of grains that could not be resolved, and this was also the case for the smaller structures (region B) in the SEM image. This provided an indication that the grains would have a size diameter less than a micron and would require a more powerful method to resolve the individual grains. (Figure 94 shows the powder on carbon tape used for the SEM image). There is, however, a story that can be told where the small grains that cannot be resolved effectively clump together. It was later identified through thermal analysis that this clumping occurred during the drying stage of the sol-gel synthesis of amorphous samples where the samples were held at 100 °C for 2 hours. These clumps were likely, initially, held together by trapped water within the clumps themselves. This was later identified where a sample produced with sufficiently large clumps of grains was placed into the thermal analyser. When the thermal ramp-up stage was initiated, a sudden drop in gravimetric data was identified at, just above, 100 °C. This also coincided with an increase of steam produced which was gained through mass spectroscopy, as will be shown in the later sections. The sudden reduction in sample mass was caused by a rapid decompression of one such cluster which also had the unfortunate effect of distributing the light powder throughout the interior of the thermal analyser.

As mentioned, EDX of the sample was restricted in the case of lithium but could still be used to identify the ratio of zirconium and oxygen. Given the uneven topology of the powder sample, gaining a full image in focus proved difficult.

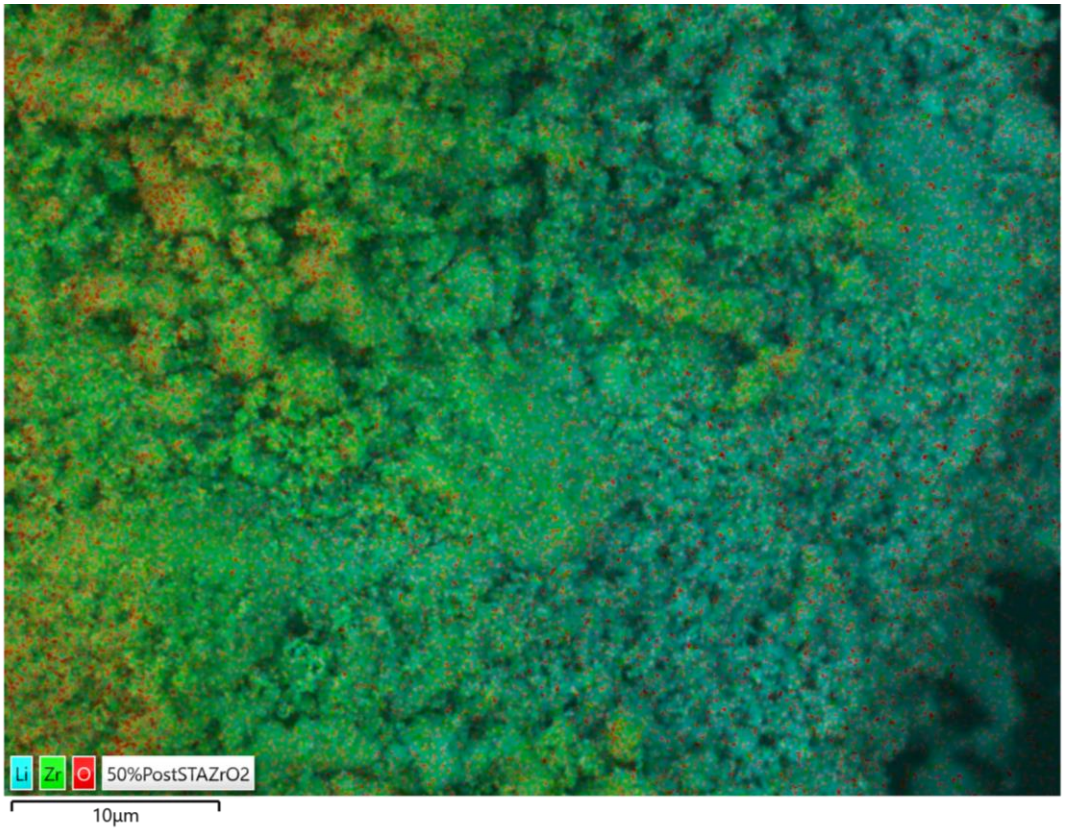

Figure 96 EDX of typical 50 mol % Li doped ZrO_2 sample showing results of Li (blue) Zr (green) and O (red).

The combined lithium, zirconium and oxygen EDX image through the SEM produced an indication of high zirconium (green) and oxygen (red) concentrations to the far left and high concentrations of lithium (blue) to the right, Figure 96. This, however, is not representative of the sample viewed. The far left of the sample is within focus for the EDX and the mid to right regions are out of focus. This is due to the topographical differences in powder height with respect to the point of incidence. Shifting attention to the left region, the zirconium defects seem to be fairly uniform and hold a backdrop of green to the oxygen. The oxygen, however, seems to be held in spot like regions throughout the image overlapping the zirconium. Upon closer inspection, there were areas of yellow which indicate a mix of zirconium and oxygen at relatively equal intensity. The spot like features of oxygen could also be areas containing water. But the low energy of hydrogen, as is the same with lithium, makes it impossible to ascertain through this method. It was possible, however, to split the elements to find the individual relative intensities.

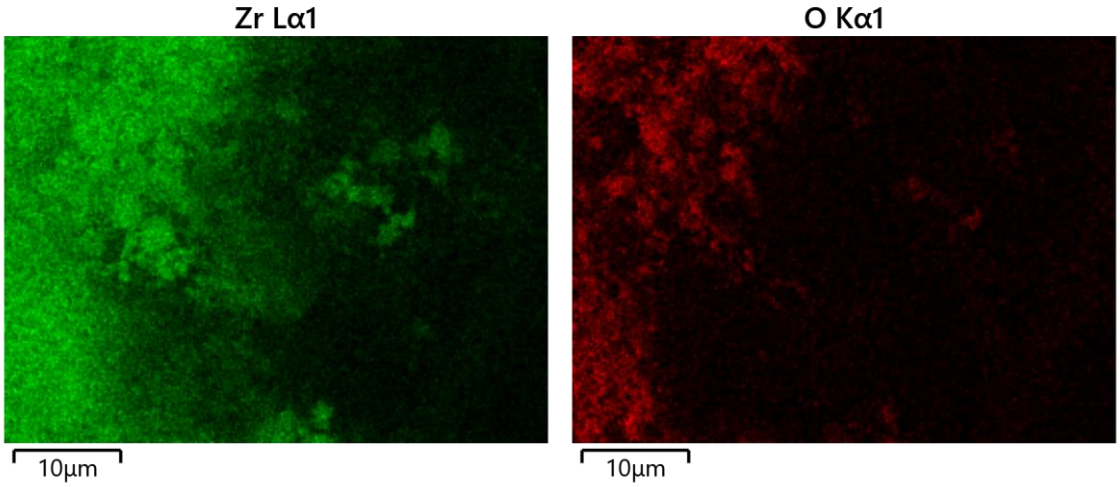

Figure 97 EDX of typical 50 mol % Li doped ZrO_2 sample showing results of Zr (left, green)) and O (right, red).

The zirconium EDX distribution across the image reached through the midpoint of the image in respect to left and right and was fairly unremarkable, Figure 97. The image showing the oxygen distribution was a little misleading in that it showed a much brighter region to the far left and a much greater dark region for most of the right and centre of the image. This, however, was comprised of relative intensity indicating that the far-left region for both images produced a higher intensity result. The oxygen "spots" that were seen in the combined image (Figure 96) were less prevalent here. The oxygen contrast between high intensity to the left of the image was far more striking. As mentioned, this could be the result of water being within the sample which was high in intensity across most of the image, but true ZrO_2 could be found to the far left which increased the relative intensity at those regions when combined with water.

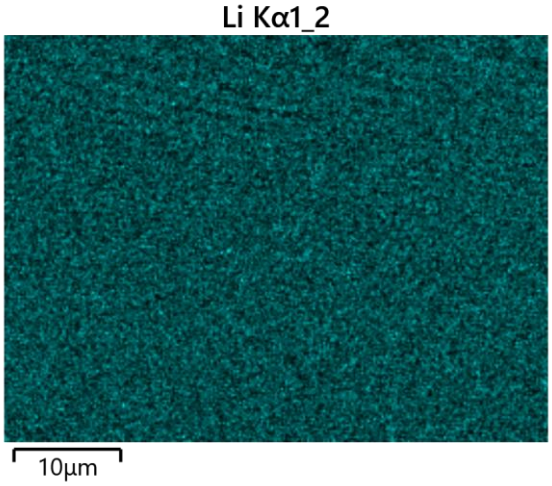

Figure 98 EDX of typical 50 mol % Li doped ZrO_2 sample showing results of Li.

For completion, the EDX for lithium shows a generally uniform distribution across the entire image, Figure 98. Given that the EDX images represent relative intensity of energy dispersion and that the previous Zr and O images show a focused region to the left, this provides evidence of the instrument's limitation in the case of lithium.

Table 9 Elemental distribution of Zr and O for the sample made of 50 mol % Li doped ZrO_2.

Element	Line Type	Weight %	Weight % Sigma	Atomic %
Zr	L series	65.11	0.32	25.42
O	K series	33.26	0.28	74.01
			Total	99.43

The SEM with EDX results for 50 mol % lithium doped ZrO_2 also provide a ratio of atomic percentage, Table 9. Where a 2 to 1 ratio of oxygen is expected for ZrO_2, we find a 3 to 1 ratio of oxygen to zirconium. This is from a sample that has reached temperatures up to 700 °C, which should result in all water being evaporated from the system. The XRD results suggest that the sample is predominantly tetragonal ZrO_2 with small amounts of monoclinic ZrO_2. The XRD, however, does not show the form that the 50 mol % lithium might have taken through thermal treatment. Any indication of lithium is also absent from the XRD results. The EDX results suggest that the lithium may have formed an oxide. With the inability to see hydrogen within the system, it is also possible that the lithium had formed a hydroxide.

Figure 99 Pure amorphous ZrO_2 pellet pressed and viewed through SEM (12000 x magnification)

As a small segway, in the image above, Figure 99, amorphous pure ZrO_2 without lithium was placed in a pellet press up to 5 tonnes for 1 minute and placed into the SEM and provided a fascinating image. The image almost looks to produce grains. However, the clear lines are cracks formed within the pellet. Samples were also placed within the pellet press for all lithium concentrations of amorphous sample and where some were thermally treated. The results were not dissimilar to those gained from samples that remained as powder. Samples that were heated after being pressed

exhibited a volume reduction resulting in the pellets cracking and falling apart. Because this didn't yield any meaningful results to the investigation, this was left as a point of interest.

5.5. Simultaneous Thermal Analysis

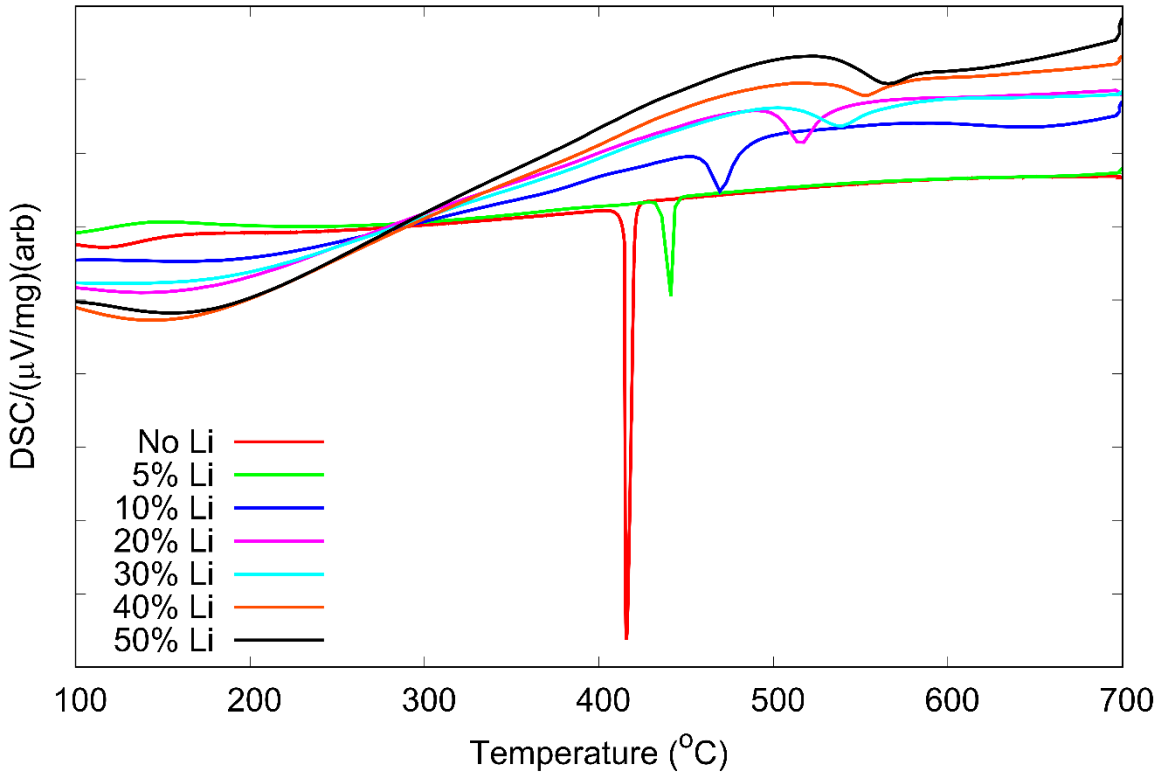

Figure 100 Samples ranging from zero to 50 mol % Li doped amorphous ZrO_2 heat treated through thermal analysis.

Thermal analysis of the amorphous undoped and doped samples produced some spectacular results, Figure 100. The units of differential scanning calorimetry (DSC) highlighted in the given diagram are arbitrary because of the differences produced at low temperatures between 100 and 150°C. This was due to water content within the samples differing which resulted in large changes in DSC at the lowest temperatures which produced a large difference in y scale peaks and troughs at this point (100 to 150°C). When the data was normalised, this produced a trend of increased temperature required to produce a "dip" in DSC at temperatures above 400°C. This dip provides a point in temperature increase where the transfer of heat between the enclosed environment and the sample change. This can be associated with a change in polymorph of the sample. It was clear that the lower vertex of each peak drop in DSC shifts to higher temperatures with increasing lithium concentration, thus providing a potential trend. It was also apparent that peak broadening also incurred with increased lithium concentration. This broadening of peaks is shared with the shallowing of peaks that gives an indication that the transition of polymorph change was prolonged, through temperature increase, due to lithium concentration.

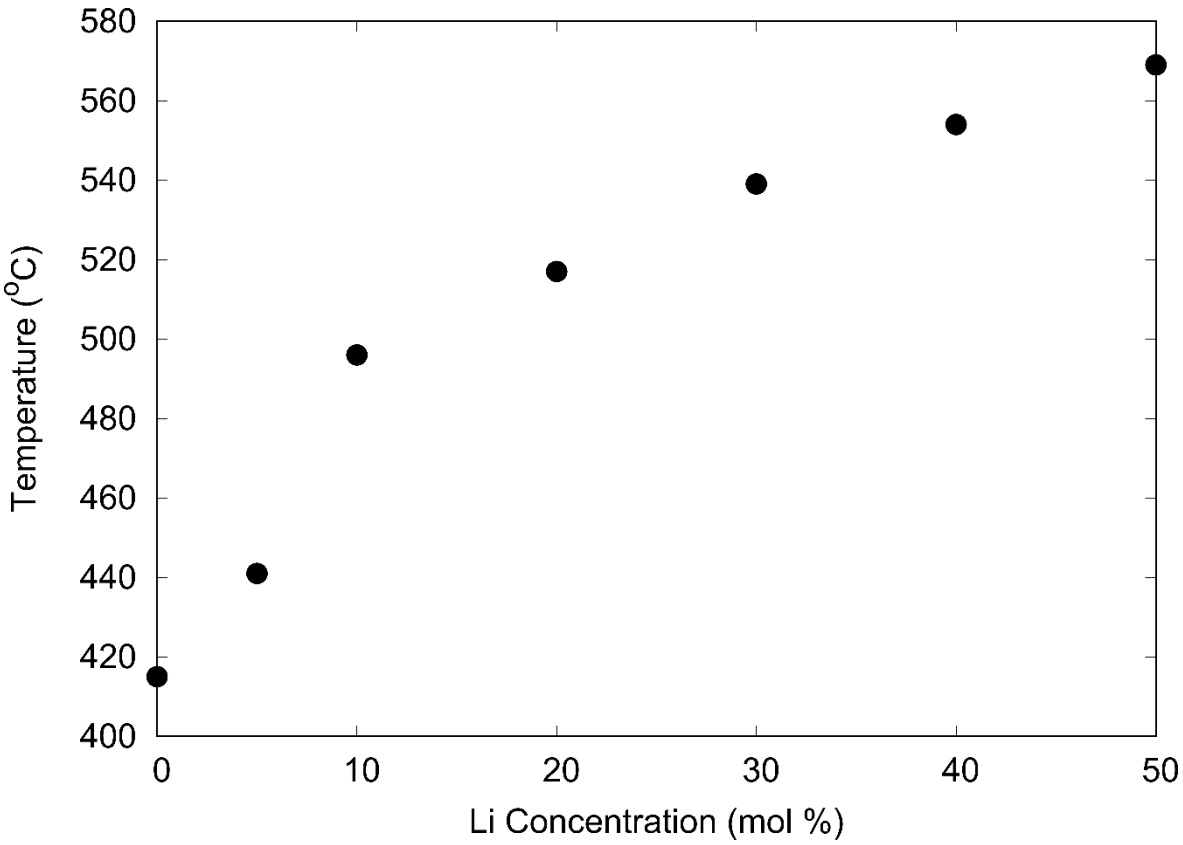

Figure 101 Samples ranging from zero to 50 mol % Li doped amorphous ZrO_2 showing the temperature of polymorph change at the lowest vertex point through thermal analysis.

When the lowest vertex point of each dopant concentration from thermal analysis was plotted, Figure 101, the results were split into two regions. The undoped and 5 mol % Li samples had a polymorph change at much lower temperatures and did not follow the fairly linear trend that could be seen with the higher lithium concentration samples (10 to 50 mol %). There was a clear correlation between lithium concentration and the temperature at which the structure changed polymorph. A higher concentration of lithium resulted in a higher temperature required for a change in polymorph. This provided good evidence that the lithium stabilised the amorphous ZrO_2, however, it could not be seen how this might have occurred.

5.6. Mass spectroscopy and thermogravimetric analysis

Mass spectroscopy provides the ability to monitor molecules that are given from the sample along with the gasses that may be present within the STA environment such as argon. By measuring these molecules, we could determine if lithium is ejected from the system during crystallisation. If no lithium is found, this would provide an indication that the lithium would still be within the sample.

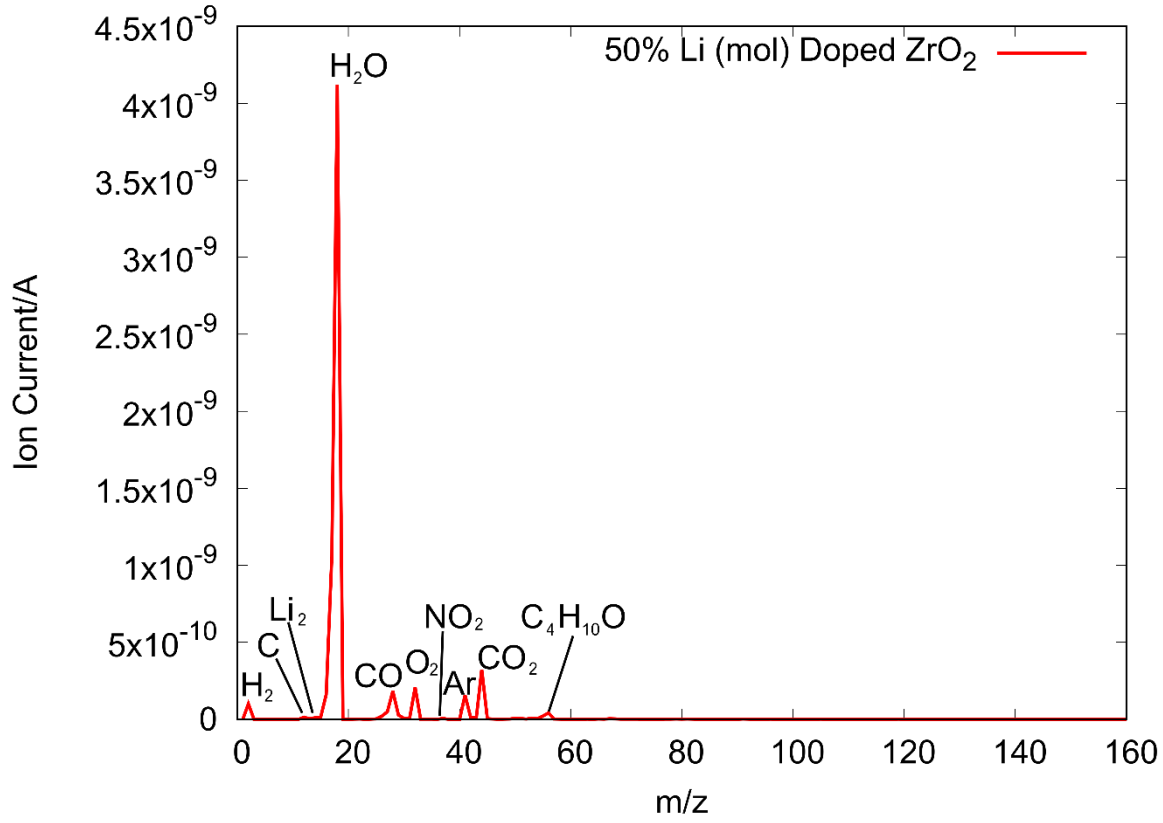

Figure 102 Mass spectroscopy of 50 mol % doped ZrO_2 with maximum values of ion current shown across the full temperature range during thermal analysis.

By taking the maximum ion current values gained through the entirety of the thermal analysis run, Figure 102, we could gain an understanding of any lithium or the molecular form of lithium that may be present. The mass to charge ratio (m/z) for lithium is 7 where molecular Li_2 is 13 and has been marked on the mass spectroscopy plot and neither of which were gained with any relevant ion current. LiOH would produce a value of 24, LiO is 23 and LiH would be 8. None of which are present from the mass spectroscopy results. The results that were gained showed a large amount of H_2O and small amounts of H_2, CO, O_2, NO_2, Ar, and CO_2. There is a small peak at 56 m/z and is likely to be 1-butanol ($C_4H_{10}O$) which was used during the synthesis of the ZrO_2 samples through the sol-gel route. The experiment was performed in an argon environment, so argon was expected to be found from mass spectroscopy. All other atoms and molecules are likely to have originated from the sample itself. The largest peak identified was that of water (steam) which could be investigated further.

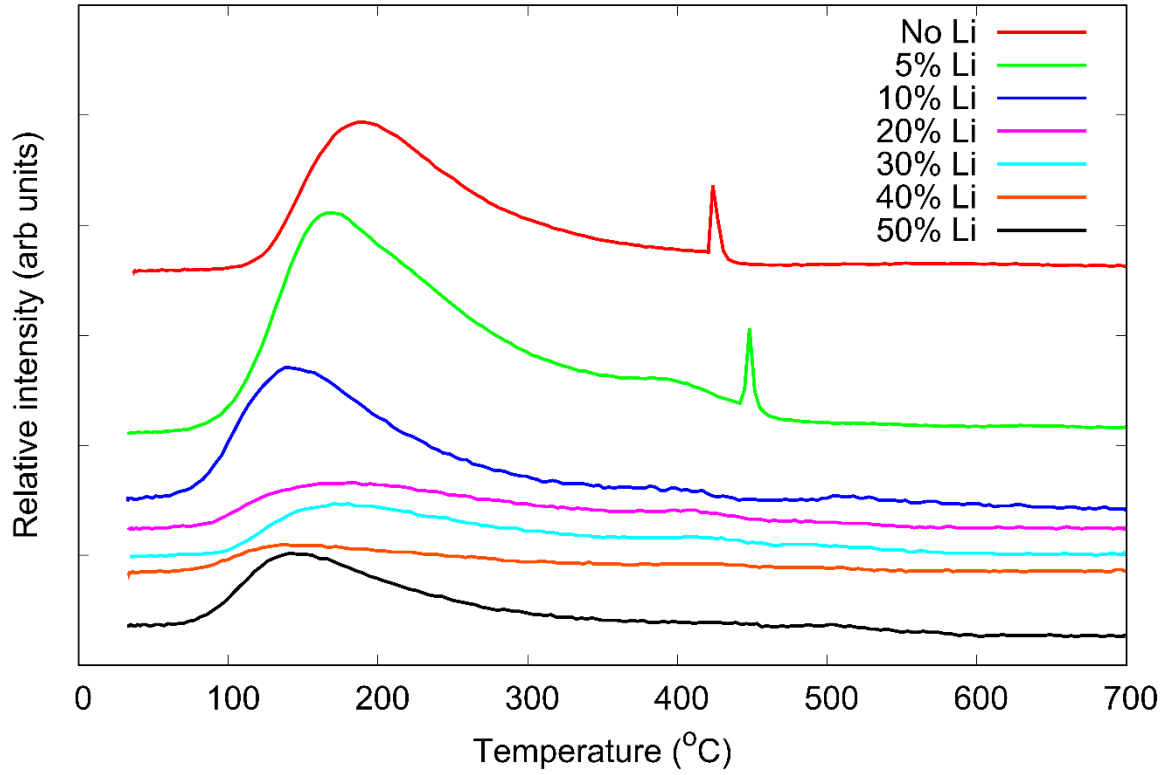

Figure 103 Mass spectroscopy of H_2O gained during thermal analysis of lithium doped samples ranging from zero to 50 mol % Li in ZrO_2 during the heating process up to 700°C.

When viewing the H_2O given from the sample during the heating process up to 700°C, Figure 103, we could identify the expected increase of H_2O (steam) from the sample at 100°C which reduces slowly up to approximately 400°C. The rate of steam release from the samples is related to how dry the samples were at the point of thermal analysis. With samples containing no or 5 mol % Li, we can see that the steam is produced from the sample up to higher temperatures still until a sudden peak occurs between 400 to 450°C. This peak temperature coincides with the polymorph change observed through thermal analysis. What is interesting about this is that the higher lithium concentration samples, 10 to 50 mol %, do not show this peak during the polymorph change. Given that there is no mass spectroscopy evidence of lithium leaving the sample and that higher concentrations of lithium prevent steam from being evacuated during the polymorph change, it provides evidence that the lithium is perhaps combining with the H_2O within the sample preventing steam release. If this is the case, there is potential that a hydroxide such as LiOH, an oxide LiO, or a hydride LiH being formed. But this needed additional tools to identify. For this reason, it was decided to attempt STEM with EELS to help identify the form that the lithium took.

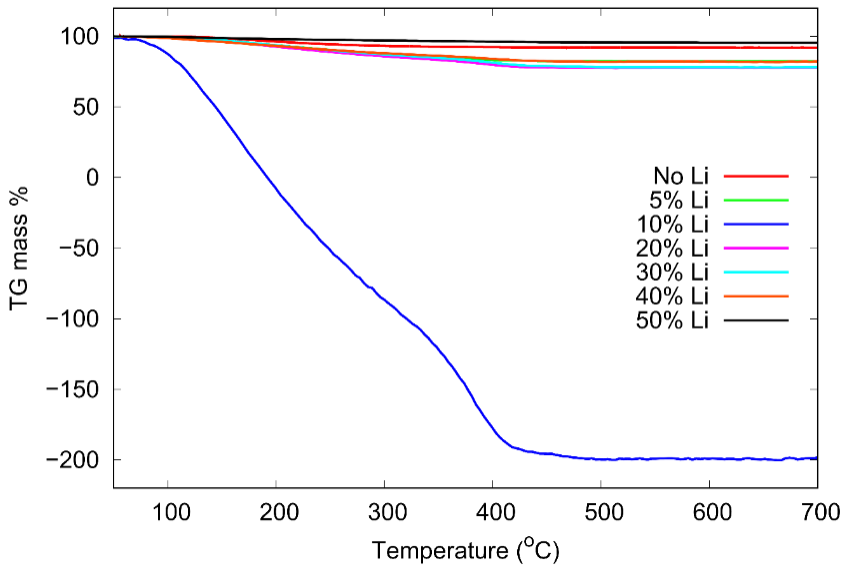

Figure 104 Thermogravimetric data through thermal analysis of lithium doped ZrO_2 ranging from zero to 50 mol % Li-content.

When reviewing the thermogravimetric data gained simultaneously during thermal analysis, Figure 104, it was clear that there was a large loss in the mass percentage of the 10 mol % Li doped sample. This was a result of the sample being much wetter than the other samples. For this reason, the 10 mol % was removed to provide a clearer picture of the other lithium concentration samples.

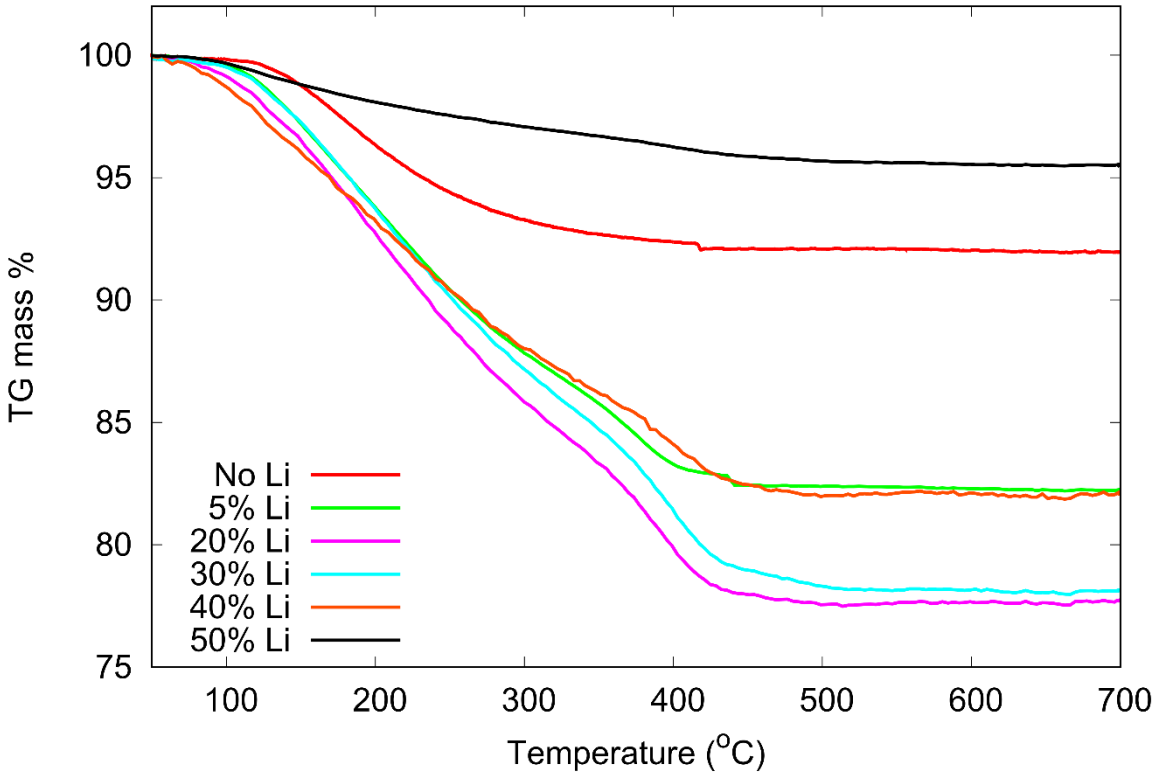

Figure 105 Thermogravimetric data through thermal analysis of lithium doped ZrO_2 ranging from zero Li to 50 mol % with the omission of 10 mol % Li.

The general loss of mass, as seen with the 10 mol % Li sample, was primarily from water removal through steam during the heating process, Figure 105. The mass loss seems fairly unremarkable and consistent for all samples with the exception of zero and 5 mol % Li which both exhibit a small drop in mass between 400 and 450°C. This also coincides with the temperature in which the polymorph changes for these samples and confirms the mass spectroscopy peaks in H_2O observed earlier. This shows that all mass loss is predominantly produced by H_2O gas for all samples.

5.7. Scanning Transmission Electron Microscope with Electron Energy Loss Spectroscopy

To help identify whether the lithium from the samples was incorporated into the bulk or segregated during the polymorph change during thermal analysis experiments, the STEM with EELS equipment was utilised at both Imperial College London and Oxford University. The samples were initially prepared at Imperial College London as mentioned in the method section.

Figure 106 STEM with EELS equipment at the department of materials, Imperial College London.

It was found that the STEM with EELS equipment at Imperial College London utilised a beryllium window, Figure 106. This would mean that any EELS signals gained from lithium would be filtered out. It did, however, produce an indication of crystal size of the samples roughly between 10 and 20 nm.

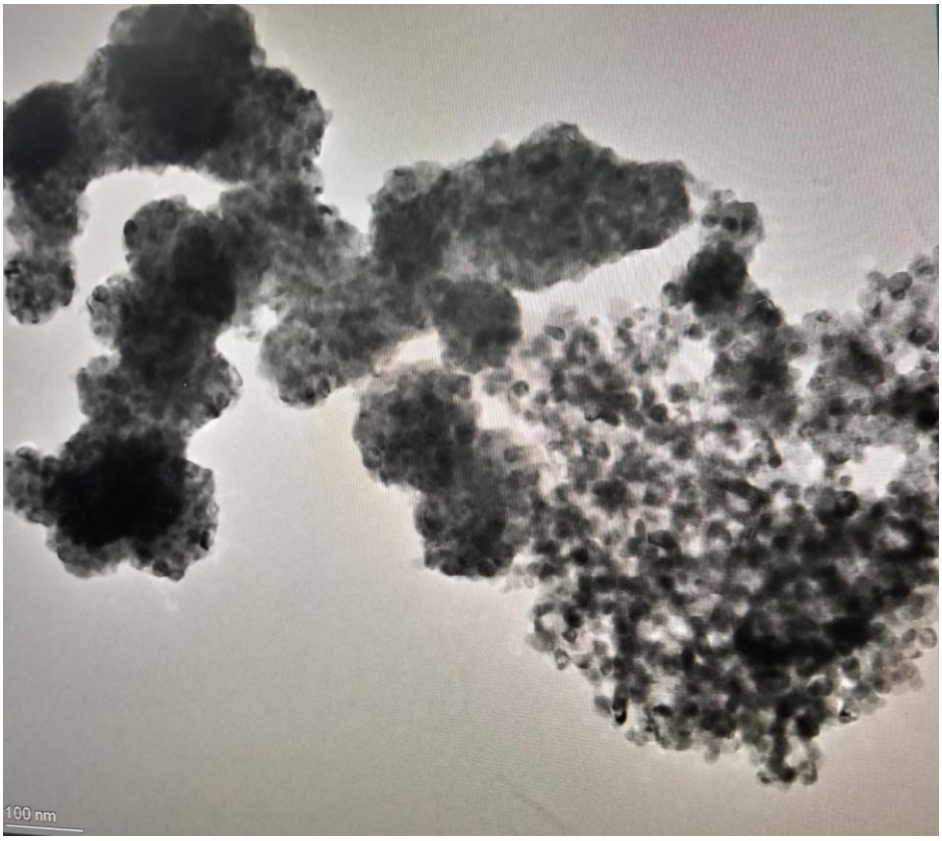

Figure 107. Typical grain size of ZrO_2 samples post thermal analysis with grain sizes averaging between 10 and 20 nm. Pictured are clumps of grains from 100 nm.

Although the images gained from Imperial College were fantastic and provided the first look at the crystals produced through thermal analysis, the STEM with EELS at Oxford University was chosen to continue the work as it had the ability to analyse lithium through EELS, Figure 107. The same samples that were prepared at Imperial College were used. This involved the samples being held in suspension in deionised water and pipetted a couple of drops of the resulting sample onto a copper grating and allowing it to dry before being placed into the STEM. Again, this produced some impressive images.

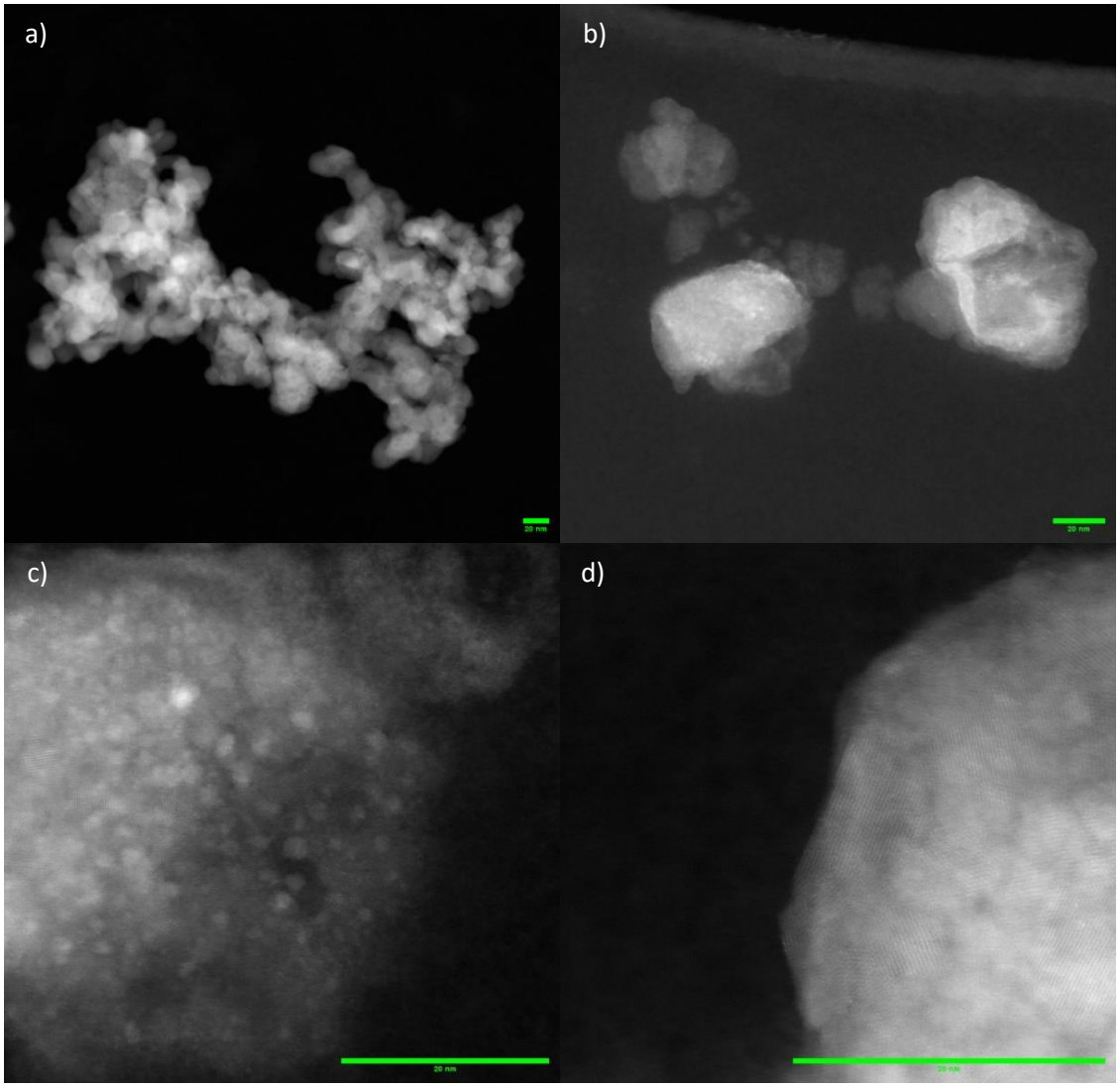

Figure 108 STEM images of post thermal analysis Li doped ZrO_2 increasing focus from a) through to d). The scale bar (green) is 20 nm for all images.

Many of the crystal sizes, as with the previously gained STEM images, are seen to be between 10 and 20 nm, Figure 108. There were, however, very few crystals that were found to be slightly larger. The STEM images show a general image of many crystals (a) and then identified larger crystals that were approximately 40 nm in diameter (b). Focusing into one such crystal (c) showed that there seemed to be possible substructures within the crystals due to changes in shade. This could be seen when further zooming into the sample (d).

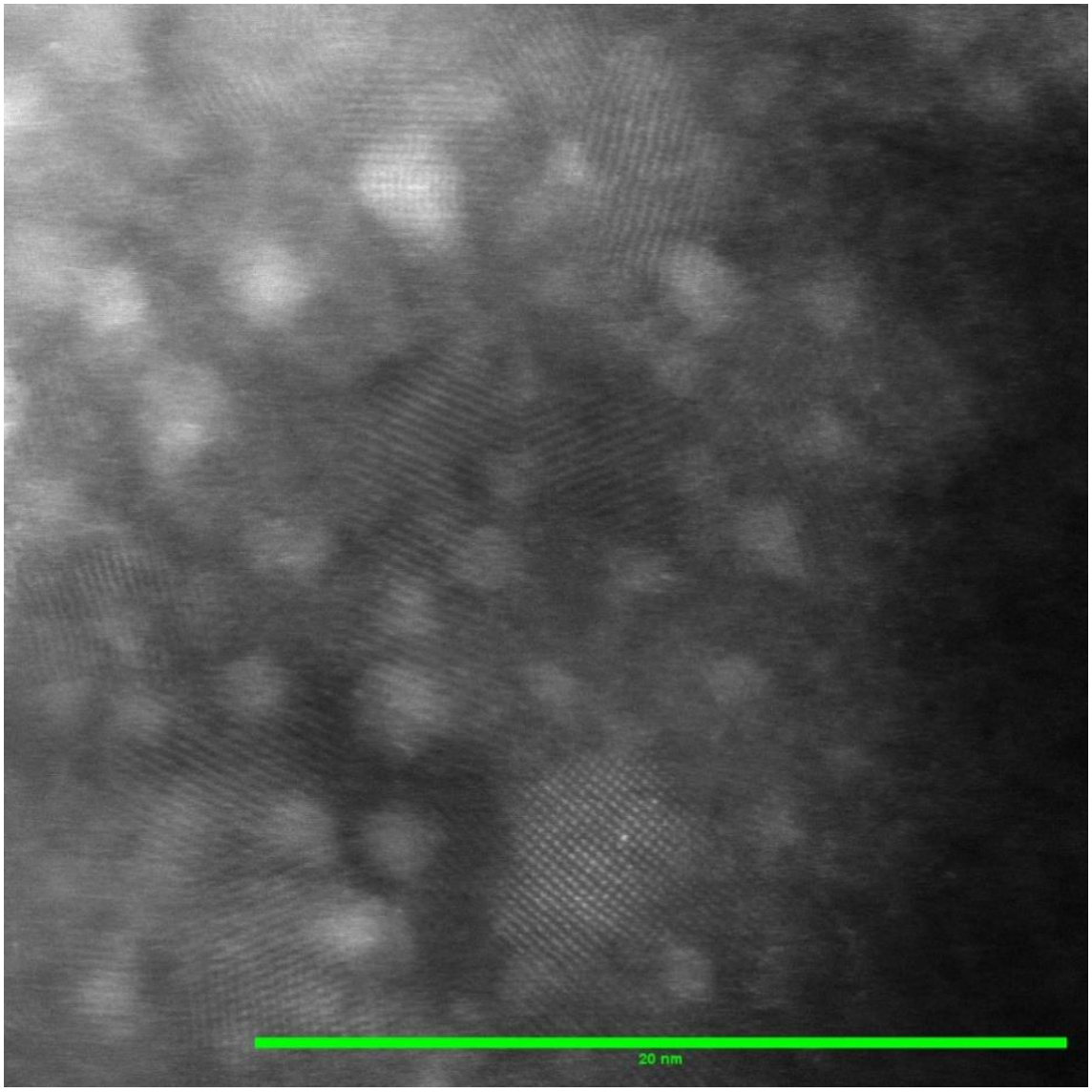

Figure 109 Image gained of 50 mol % Li doped ZrO_2 sample from STEM where the scale bar (green) is set to 20 nm.

The final image gained from STEM provided a spectacular view of the atomic columns within the crystals (bottom centre) Figure 109. This also confirms results gained from literature work [167]. These columns appear to remain consistent in atomic order across the previously assumed substructures indicating that these changes in shade are likely topological in apparent depth changes of the material and not individual crystals within a larger bulk structure.

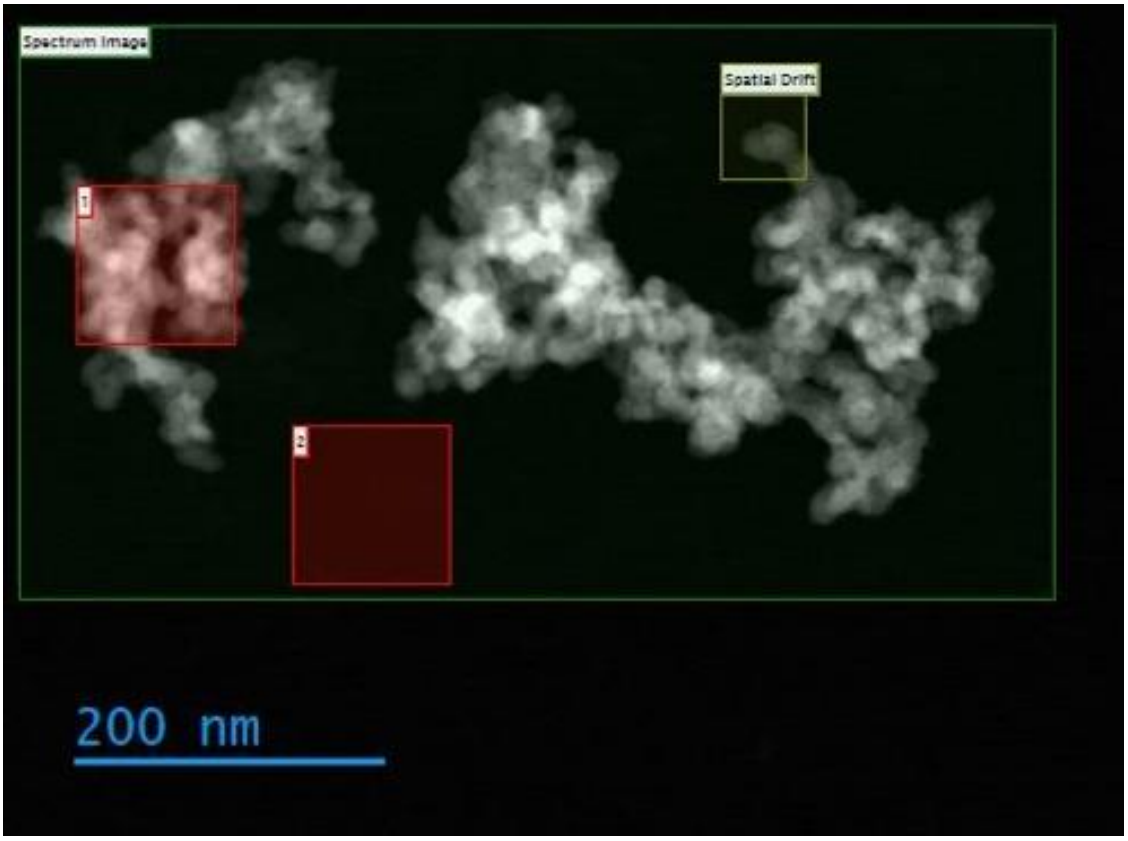

Figure 110 STEM HAADF image containing a cluster of ZrO_2. The green rectangle indicates the location for EELS mapping. The red squares are given as 1, a base sample and 2 the membrane spectra.

To produce the EELS spectra, some background areas were required such as that of the membrane that the sample sat upon, Figure 110. This could then be removed from the final spectra to provide only the sample spectrum without the membrane data.

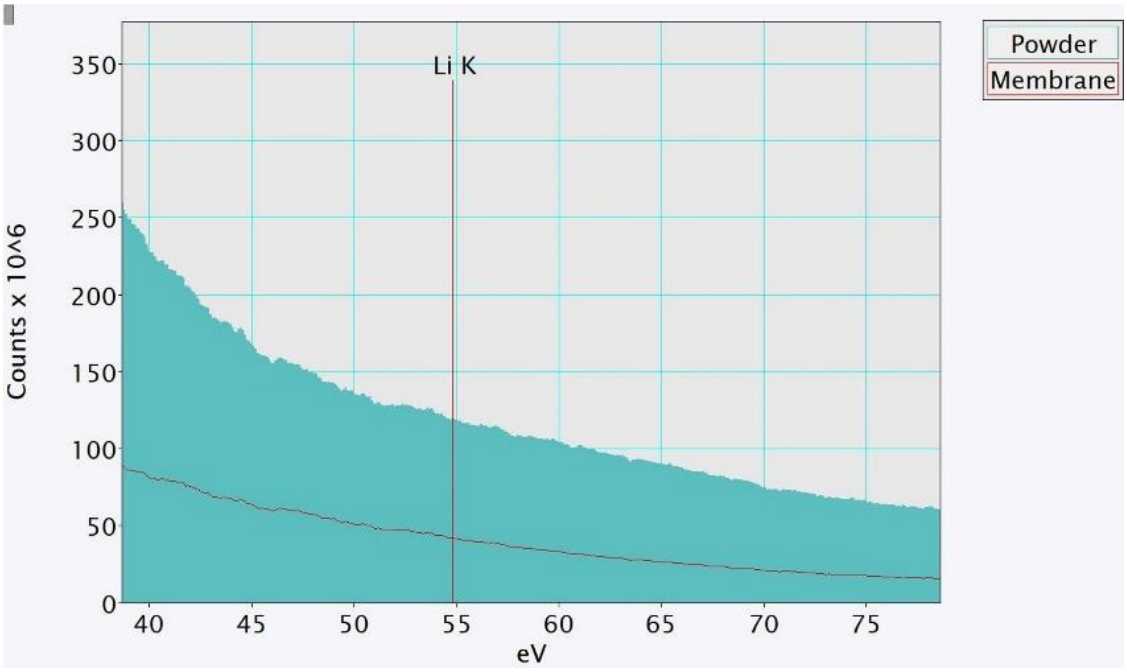

Figure 111 EELS spectra gained from sample with 50 mol % lithium doped ZrO_2 with the expected Li edge indicated.

The response from the sampled region was quite surprising in that no lithium could be identified above normal noise levels, Figure 111. Given that the mass spectroscopy indicated no lithium loss during heating and, conversely, no lithium within the sample using STEM with EELS, this provided a question of whether the lithium was lost in solution in deionised water during the TEM sample preparation. A simple litmus test could provide an indication of base level within the solution which would provide evidence that the lithium was, indeed, present within the deionised water. We had all the evidence needed to indicate that the ZrO_2 had remained in suspension within the water.

Table 10 Litmus test on 50 mol % Li doped ZrO_2 in deionised water and a deionised water control.

Sample	**50 mol % Li doped ZrO_2**	**Deionised Water control**
Sample image		
Litmus test	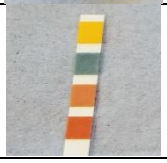	
pH	10	7

The litmus test provided evidence that lithium formed a solution within the deionised water producing an elevated pH of 10, which is above the neutral pH 7 that could be found in deionised water, Table 10. This isn't absolute, as the pH of tetragonal ZrO_2 has been previously found to be between 3 to 14 pH [168]. An alternative method was required to investigate the location of lithium within the samples post thermal analysis. The implications of this lithium solubility could be a means to break down the outer oxide layers through grain boundary degradation.

5.8. Inductively Coupled Plasma Optical Emission Spectroscopy

The inductively coupled plasma optical emission spectroscopy (ICP-OES) method was conducted by the BioComposits department at Bangor University and was divided into 2 parts. The first was to take the solid powder sample and identify the lithium to ZrO_2 ratio. The second would look at the ratio of lithium to ZrO_2 in the sample held in suspension/solution in deionised water. It was hoped that lithium could be identified within both samples to confirm that lithium was within the sample and to validate the mass spectroscopy spectrum which indicated no loss of lithium during thermal analysis. Both experiments were conducted on the 50 mol % lithium doped ZrO_2.

For the solid powder sample, lithium was found at 3.63 mg/g providing a 1:7.2 ratio of lithium to zirconium. For the sample in deionised water, lithium was found at 1.51 mg/L and only 0.29 mg/L of zirconium which produced a 1:0.2 lithium to zirconium ratio. Whilst this proves lithium was within the samples prior to being placed into deionised water, it also provides evidence of lithium forming a solution within the deionised water also. This supports the simulated results gained from both the bulk ZrO_2 solution energy results which predicted that lithium was unlikely to form a solution into monoclinic or tetragonal ZrO_2, but it also confirms that the lithium was within the sample during the amorphous stages too. It also provided evidence that the lithium remained within the sample during thermal analysis which confirmed the results gained through mass spectroscopy.

The remaining samples that had been within deionised water from zero to 50 mol % Li were all dried and placed through the XRD again to ensure no structural changed had taken place and all samples were found to be identical to those that had not been placed in deionised water.

5.9. Summary and Discussion

The experimental methods used to synthesise and characterise lithium doped ZrO_2, with a range of lithium concentrations from 0.001 to 50 mol %, was conducted successfully through the sol-gel route. Though, later, the lowest concentration samples (0.001 to 0.1 mol %) were removed as no meaningful data could be obtained through this route above zero lithium levels. Raman spectroscopy was successfully utilised to confirm an amorphous powder had been produced, however, due to the very small crystal sizes gained through thermal analysis, Raman could not produce distinctly clear peaks that could be analysed with any accuracy. XRD, on the other hand, produced clear results in all cases which provided evidence that the samples were predominantly tetragonal with a small ratio of monoclinic ZrO_2 at 700°C but would also produce similar ratios of tetragonal to monoclinic ZrO_2 when heated to 1000°C. For samples containing 5 mol % and less lithium, very little monoclinic ZrO_2 was evident, higher lithium concentrations (10 to 50 mol %) did produce small monoclinic peaks. This does indicate that there may be some form of stress relief that may be associated with lithium during the change in polymorph from amorphous to crystal structure. Small grain sized zirconia and internal compressive stresses are known to stabilize tetragonal zirconia [169]. During the change of polymorph from amorphous to tetragonal, the lithium was segregated and may have produced a lithium hydroxide or lithium oxide. This process may have destabilized the tetragonal polymorph allowing monoclinic zirconia to form. When reviewing literature XRD peaks for lithium and zirconia (e.g., Li_2ZrO_3), no peaks could be associated with lithiated structures.

SEM with EDX was not able to resolve individual crystals and could not gain data for lithium through EDX due to this being a low energy atom and in a region of noise. It did, however, provide a zirconium and oxygen map which provided much more oxygen than expected with a 3 to 1 ratio of oxygen to zirconium. Whilst XRD showed the samples to be ZrO_2 this additional oxygen could have been part of a lithium oxide or lithium hydroxide which would produce higher oxygen concentrations through EDX. Thermal analysis produced some fascinating results that provided evidence that lithium stabilised the amorphous ZrO_2 structure. An increase in lithium resulted in a higher temperature required to initiate a change in polymorph. Thermogravimetric and mass spectroscopy data associated with thermal analysis indicated that no lithium was lost during the heating process and that steam was the most prevalent ion to be produced from all samples. For zero and 5 mol % lithium samples, it was found that a sudden release of steam was produced at the temperature where the polymorph change was initiated. This was not found in samples containing higher concentrations of lithium (10 to 50 mol % Li) which gives an indication that lithium may have formed an oxide, hydride or hydroxide that prevented similar results. However, without identifying the molecular form which lithium takes post thermal analysis, this is only a hypothesis.

STEM with EELS produced some clear images which provided an indication of typical crystal sizes between 10 to 20 nm in diameter. There were, however, a small number of crystals that were up to 40 nm in diameter. Atomic resolution was obtained showing evidence of structural order within the crystal, but no lithium could be identified through EELS. It transpired that the method in which the samples were prepared, where the Li doped ZrO_2 was placed in deionised water, the lithium formed solution within the water, where the zirconia remained in suspension. This was later confirmed by emission spectroscopy which found lithium to be at a ratio of 1:7.2 to zirconium in the solid sample which was not held in suspension/solution in water, and a ratio of 1:0.2 lithium to zirconium in the

sample that had been in suspension/solution in deionised water. This not only confirmed that the lithium had remained within the sample during thermal analysis, but also confirmed the simulated predictions that found solution to be unlikely in bulk ZrO_2 and was possible in amorphous ZrO_2. Whilst this offers some evidence as to the effects of lithium in ZrO_2, it also poses several questions. Further work, such as in-situ XPS, XAS or EXAFs, could answer questions such as what is the form in which lithium takes when segregated from the crystalising zirconia? If it is possible for lithium to find a path to the metal oxide interface, will this actively discourage the formation of crystals in favour of amorphous structures? If that is the case, could lithium be the reason for equiaxed grain growth over naturally occurring columnar growth that has been observed with samples subjected to lithium accelerated corrosion [170]?

6. Summary and conclusion

The overall goal of this project was to identify the mechanism of how lithium accelerates corrosion of zirconium alloys. Initial research indicated that there were two main hypotheses, with a third for potential extra work, to guide the investigation path. First, the ingress of lithium into the bulk oxide (tetragonal and monoclinic) of the zirconium alloy would cause a change in volume and potentially promote pore formation which would allow oxygen ingress to the metal oxide interface, further increasing oxidation. Secondly, the lithium is accommodated along grain boundaries which further promoted grain boundary phases or formed pores. Lastly, lithium accommodation would induce electro-chemical effects that accelerate the hydrolysis of water. The first hypothesis was largely found to be unlikely, the second, however, provided sufficient results to warrant additional investigation and a plausible route. This largely negated the effort to pursue the third hypothesis in this work as the focus was applied to understand the second hypothesis extensively.

Starting the investigation with the bulk oxide provided two benefits over alternatives when choosing which hypothesis to investigate first. The tetragonal and monoclinic oxide structures were already well defined and thoroughly investigated in the literature so comparison could be consistently maintained ensuring reliable and consistent results. This also allowed for lessons to be learned which could then be carried over when investigating more complex structures subsequently.

Producing relaxed bulk zirconium oxide structures through simulation was successfully conducted gaining a base to which defects, such as those containing lithium, could be applied. The electronic structure of the bulk oxide structures could also be gained and compared to literature and were found to produce reasonable results.

Using the values gained from the bulk oxides of both defect free and defect structures, both formation energy vs bandgap plots and Brouwer diagrams to provide an indication of defect concentration through the oxide layers, could be calculated.

The formation energy vs bandgap plots provided a good indication of which defects to expect where the defects with the lowest formation energies would be more likely to form. A positive charged defect was more likely to form in a negatively charged structure and a negative charged defect was more likely to form in a positive structure.

The Brouwer diagram containing just lithium defects and intrinsic defects showed that two lithium interstitials around a zirconium vacancy $(\mathrm{Li_i}:\mathrm{V_{Zr}})''$ would increase the oxygen vacancy concentration $(\mathrm{V_O^{\bullet\bullet}})$, particularly at the water oxide interface. The lithium concentration, however, needed to be greater than the concentration of intrinsic oxygen vacancy defects to cause this change. This was apparent in both the monoclinic and tetragonal structures. When applying the alloying additions at concentrations expected to be found in Zircaloy-4 which included chromium, iron and tin, the tin had no apparent effect on the intrinsic defect concentrations. Chromium was found to increase the zirconium vacancy defects in the monoclinic structure, but not the tetragonal. Iron, on the other hand, was found to reduce the oxygen vacancy defect concentrations. When all extrinsic defects were combined, the iron defects would suppress the effect of lithium and prevent the increase of oxygen vacancy defects. This provides two main points of interest: in sufficiently high concentrations ($>10^{-10}$ per ZrO_2), lithium would increase the concentration of oxygen vacancy defects. Through this, oxygen may be allowed to “hop” along oxygen vacancy sites and provide a highway for oxygen to pass through the oxide. The second point is that should enough iron be present within the bulk oxide, this would prevent the effect that lithium has and could prevent lithium accelerated corrosion.

When reviewing the possibility of pore growth due to lithium ingress into the bulk oxide, the volume changes resulting from each defect could be reviewed and combined at concentrations gained from the Brouwer diagrams. Despite DFT producing exaggerated volumetric changes when applied to charged defects, the volume change associated was very low in the tetragonal oxide with a volume variation of 3×10^{-4} $Å^3/ZrO_2$. The monoclinic structure was found to produce a slightly higher volume change, but only at the water oxide interface. The change in volume peaked at 1.3 $Å^3/ZrO_2$ but did not proceed to any real depth into the oxide layer. For this reason, the volume change could be considered negligible, and lithium would be unlikely to reduce the volume of the structure sufficiently enough to produce pores as a result.

Finally, the solution energies of the main defects identified in the Brouwer diagrams were reviewed. Whilst a favourable solution energy for tin, iron and chromium defects were calculated, lithium produced a solution energy that was high and positive, indicating that lithium would be unlikely to form solution into either tetragonal or monoclinic zirconia and an unlikely route for lithium accelerated corrosion.

With the solubility of lithium found to be unlikely in the bulk oxide, the attention could turn to the grain boundaries and to address the second hypothesis which would look at the potential for lithium to form solution in the grain boundaries and that this may promote pore growth or promote grain boundary phases. In order to accomplish this, the grain boundary was considered complex and, thus, amorphous.

The techniques used in the bulk structures could also be used in the amorphous structures, however, producing the amorphous structure was more complex. The amorphous structures were produced using molecular dynamics in the first instance and then reduced in size using reverse Monte-Carlo so that they could then be assessed using density functional theory. The resulting structures were reviewed to ensure they remained amorphous using atomic radial distribution and were found to remain amorphous indicating a successful transition in scale.

The formation energy vs bandgap plots produced very similar results to that of the bulk oxide without any real surprises. The main difference between the bulk oxide and amorphous structures is that the Brouwer diagrams in the amorphous zirconia showed fewer defect types in comparison. Chromium and tin did not show on the Brouwer diagrams at all with very low concentrations and only the plus two charged iron interstitial ($Fe_i^{\bullet\bullet}$) had a high enough concentration to appear out of all the alloying additions. As with the bulk oxide, the lithium increased the oxygen vacancy ($V_O^{\bullet\bullet}$) concentration but only when the lithium concentration was higher than that of the intrinsic only level of oxygen vacancy ($>10^{-10}$ per ZrO_2). This does tie into literature experimental work that shows that lithium concentrations are required to be high enough (dependant on temperature) before accelerated corrosion takes place [55]. An increase in oxygen vacancy sites has been shown to increase the likelihood of oxygen to pass from oxygen vacancy site to site [27]. In sufficient quantities, iron showed a potential to mitigate the effect of lithium and reduce the oxygen vacancy concentration. This could prove to be a solution to the lithium accelerated corrosion issue but would require a detailed investigation to identify the physical plausibility.

Combining the volume change of each defect and the associated concentration found in the Brouwer diagram, the volume change was calculated to be between 0.0008 to -0.004 $Å^3/ZrO_2$. Given that the volume change calculated through DFT has been found to exaggerate for charged defects, this provides a good indication that the volume change is insignificant and just as likely to increase the volume as it is to reduce it [135]. This would discount the hypothesis that lithium would generate pores along the grain boundaries.

The solution energy calculated for lithium into the amorphous structure was found to be -0.38 eV with a standard deviation of 1.27 eV. This indicates that solution of lithium is possible along the grain boundaries of the oxide. This was further confirmed experimentally using atom probe where lithium was found to segregate along the grain boundaries [67].

Whilst this does provide an indication of a mechanism by which lithium could promote oxygen transport to the metal oxide interface and, thus, accelerate the corrosion of zirconium alloy. This does not address the second part of hypothesis two which suggested that lithium might promote grain boundary phases. To address this question, the investigation needed to change from simulation to experimental methods.

Amorphous zirconia and lithium doped zirconia were successfully characterised and synthesised through a sol-gel route. From there, the structures were heat treated through simultaneous thermal analysis and it was found that lithium stabilised the amorphous structure where higher temperatures were required to change the polymorph with higher lithium concentrations. Through XRD, the resulting structures were found to be tetragonal for samples containing no lithium and tetragonal/cubic for 5 mol % lithium. For samples containing more than 5 mol % lithium, the resulting structures were found to be predominantly tetragonal with a small ratio of monoclinic zirconia. During thermal analysis, no lithium was found to have been ejected from the samples when analysing the gases produced through mass spectroscopy. Steam, however, was found to be produced at the point of structure change for the 0 and 5 mol % lithium samples but not the samples containing a higher concentration of lithium. This indicated that the lithium prevented hydroxide species from being ejected from the samples and that it may have produced a lithium hydroxide of some form.

When attempting to identify the location of the lithium post heat treatment, STEM with EELS could not identify lithium but could identify the zirconium crystals which were approximately 20 nm in diameter. The method used to prepare the samples for STEM was to place the samples in suspension in deionised water and pipette the samples onto the sample grating. It was later found that because the lithium was segregated from the zirconia during crystallisation, the lithium was able to form solution into the water where the zirconia crystals were in suspension. The lithium was later identified in the deionised water through inductively coupled plasma optical emission spectroscopy. The small size in crystals provided a reason as to why Raman spectroscopy was unable to effectively provide substantial peaks for analysis.

The experimental results produced evidence that supports the second part of hypothesis two in that lithium promotes grain boundary phases. This is evident when considering the stabilisation of the amorphous structure during heat treatment.

The segregation of lithium along grain boundaries and the unlikely solution of lithium into the bulk oxide identified through simulations were also confirmed. The evidence for this was provided through STEM with EELS which could only identify the zirconium crystals and the ICP-OES which found that lithium would form solution in water where the zirconia remained in crystal form when placed in deionised water. Given that lithium has been previously identified as segregating along grain boundaries [67] and that lithium is highly soluble in water when segregated, this could have potential to break down grain boundaries and cause grains to peel away when the zirconium alloy is in an aqueous environment.

Whilst this does offer a good indication to explain how lithium might accelerate the corrosion of zirconium alloys, there are a number of verifications that are required to form a solid conclusion. In addition to this, there are a plethora of routes that might be taken to identify ways to mitigate the accelerated corrosion in the future.

7. Future Work

Whilst the segregation of lithium from the bulk oxide and into the grain boundaries has been identified through both simulation and experiment, the form in which lithium takes once there is a polymorph change from amorphous to bulk is yet to be known. The experimental work has shown that lithium prevents stream from being ejected at the point of crystallisation which only suggests that a form of lithium hydroxide might be created. However, this would need to be verified. A potential method to verify this would be through in-situ x-ray photoelectron spectroscopy. This method could monitor the produced molecules whilst undergoing heat treatment during the polymorph change.

Evidence to show that lithium stabilises the amorphous structure has been provided in this work, but the detrimental effects that this may have on grain growth has not. Identifying if lithium is able to reach the metal oxide interface is required, first, to ascertain this potential. At the time of writing, the author has been notified that this work will be taking place in the near future by Jacobs PLC. Should lithium be found at the metal oxide interface, and that lithium stabilises the grain boundary phases under these conditions, it is likely that the grain growth will be reduced and that more grain boundaries are promoted. This would be seen as small equiaxial grains which should be smaller than what was seen in normal conditions with an absence of lithium.

The simulation work has indicated that lithium would increase the oxygen vacancy defect concentration through the oxide layer, particularly at the water oxide interface. This has yet to be verified experimentally. Again, identifying if lithium is able to reach the metal oxide interface, this has the potential to increase the oxygen vacancy defect concentration all the way to the metal surface and provide a highway, of sorts, for oxygen to penetrate the metal surface and increase the rate of oxidation.

The simulation work has provided an indication that an increase in iron concentration might hinder or mitigate the increase of oxygen vacancy defects caused by lithium ingress. Should this be the case, a simple increase of iron as an alloying addition may prevent lithium accelerated corrosion. Whilst this does need further experimental verification, this would also couple with an enhanced investigation to identify the in-reactor implications that could be apparent as a result of an increase in iron in the alloy.

Other alternatives to lithium, alkaline coolant additives have been suggested in the past as a potential route to prevent lithium accelerated corrosion, including sodium and potassium. The methodology presented within this work would provide a good starting point to assess if these are viable candidates, in the first instance.

Finally, whilst not entirely associated with lithium accelerated corrosion, previous work has identified that a decrease in electron transport results in greater rates of hydrogen pickup [11]. Hydrogen pickup is associated with hydrogen embrittlement of the zirconium based cladding material. The simulations produced in this work would be able to give an indication of bandgap changes associated with dopants. If this is the case, identifying defects which effectively increase the bandgap could result in a reduction of hydrogen ingress and possibly mitigate hydrogen embrittlement. A small probing study into this may provide a solid foundation for a much larger investigative project.

References

[1] J. Yang, M. Youssef, B. Yildiz, Electro-chemo-mechanical effects of lithium incorporation in zirconium oxide, Phys Rev Mater 2 (2018). https://doi.org/10.1103/PhysRevMaterials.2.075405.

[2] File:Pilling-Bedworth-Verhältnis.svg - Wikipedia, (n.d.). https://en.m.wikipedia.org/wiki/File:Pilling-Bedworth-Verh%C3%A4ltnis.svg (accessed April 22, 2024).

[3] P.R. Cantwell, M. Tang, S.J. Dillon, J. Luo, G.S. Rohrer, M.P. Harmer, Grain boundary complexions, Acta Mater 62 (2014) 1–48. https://doi.org/10.1016/j.actamat.2013.07.037.

[4] S.J. Dillon, M.P. Harmer, Relating grain-boundary complexion to grain-boundary kinetics II: Silica-doped alumina, Journal of the American Ceramic Society 91 (2008) 2314–2320. https://doi.org/10.1111/j.1551-2916.2008.02432.x.

[5] J.W. Jewett, R.A. Serway, Physics for scientists and engineers with modern physics, Cengage Learning EMEA, 2008.

[6] V.I. Kopeikin, L.A. Mikaelyan, V. V. Sinev, Reactor as a source of antineutrinos: Thermal fission energy, Physics of Atomic Nuclei 67 (2004) 1892–1899. https://doi.org/10.1134/1.1811196.

[7] Nuclear Fission Fragments, (n.d.). http://www.hsc.edu.kw/student/materials/Physics/website/hyperphysics%20modified/hbase/nucene/fisfrag.html (accessed April 22, 2024).

[8] S.J. Zinkle, G.S. Was, Materials challenges in nuclear energy, Acta Mater (2013). https://doi.org/10.1016/j.actamat.2012.11.004.

[9] L. Hallstadius, S. Johnson, E. Lahoda, Cladding for high performance fuel, Progress in Nuclear Energy 57 (2012) 71–76. https://doi.org/10.1016/j.pnucene.2011.10.008.

[10] P. Properties, C. Resistance, R. Effects, M.I.I. Str, Zirconium Cladding, (1950).

[11] A.T. Motta, A. Couet, R.J. Comstock, Corrosion of Zirconium Alloys Used for Nuclear Fuel Cladding, Annu Rev Mater Res 45 (2015) 311–343. https://doi.org/10.1146/annurev-matsci-070214-020951.

[12] P.P. Sanchez, A. dos Santos, Prediction of the Power Peaking Factor in a Boron-Free Small Modular Reactor Based on a Support Vector Regression Model and Control Rod Bank Positions, Nuclear Science and Engineering 195 (2021) 555–562. https://doi.org/10.1080/00295639.2020.1854541.

[13] Y.A. Hassan, S. Osturk, S. Lee, Rheological characterization of buffered boric acid aqueous solutions in light water reactors, Progress in Nuclear Energy 85 (2015) 239–253. https://doi.org/10.1016/j.pnucene.2015.06.025.

[14] T. Wellock, CRUD: Another Acronym Bites the Dust, 2015. https://www.nrc.gov/docs/ML2018/ML20182A653.pdf (accessed October 16, 2023).

[15] J. Blok, S. Chauffiriat, P. Frattini, Modeling the axial offset anomaly in PWRs, Proceedings of International Conference on Water Chemistry of Nuclear Reactor Systems–Operation Optimisation and New Developments (2002) 1–9.

[16] P.L. Frattini, J. Blok, S. Chauffriat, J. Sawicki, J. Riddle, Axial offset anomaly: Coupling PWR primary chemistry with core design, Nuclear Energy 40 (2001) 123–135.

[17] F. Nordmann, PWR and BWR chemistry optimization, Nuclear Engineering International 56 (2011) 24. https://www.neimagazine.com/features/featurepwr-and-bwr-chemistry-optimization/.

[18] J. Mart, A. Klein, A. Soldatov, Feasibility study of a soluble boron-free small modular integral pressurized water reactor, Nucl Technol 188 (2014) 8–19. https://doi.org/10.13182/NT13-135.

[19] H. Hulme, A. Panteli, F. Baxter, M. Gass, A. Cole-Baker, P. Binks, M. Fenwick, M. Waters, J. Smith, Investigating the Corrosion Behaviour of Zircaloy-4 in LiOH under a Thermal Gradient and Two Phase Flow Regime., Awaiting Publication (2019).

[20] A.T. Motta, A. Yilmazbayhan, R.J. Comstock, J. Partezana, G.P. Sabol, B. Lai, Z. Cai, Microstructure and Growth Mechanism of Oxide Layers Formed on Zr Alloys Studied with Micro-Beam Synchrotron Radiation, J ASTM Int 2 (2005). www.astm.org.

[21] Y.H. Jeong, K.H. Kim, J.H. Baek, Cation incorporation into zirconium oxide in LiOH, NaOH, and KOH solutions, Journal of Nuclear Materials 275 (1999) 221–224. https://doi.org/10.1016/S0022-3115(99)00148-8.

[22] I.L. Bramwell, P.D. Parsons, D.R. Tice, Corrosion of Zircaloy-4 PWR fuel cladding in lithiated and borated water environments, (1991). http://inis.iaea.org/Search/search.aspx?orig_q=RN:23052627.

[23] F. Garzarolli, J. Pohlmeyer, S. Trap-Pretsching, H.G. Weidinger, Fundamental Aspects Of Corrosion On Zirconium Base Alloys In Water Reactor Environments Proceedings Of A Technical Committee Meeting Organized By The International Atomic Energy Agency, IAEA Technical Committee Meeting Proceedings (1990) 65–72.

[24] D. Pêcheur, J. Godlewski, P. Billot, J. Thomazet, Microstructure of Oxide Films Formed during the Waterside Corrosion of the Zircaloy-4 Cladding in Lithiated Environment, in: Zirconium in the Nuclear Industry: Eleventh International Symposium, 2009. https://doi.org/10.1520/stp16169s.

[25] N. Ramasubramanian, N. Precoanin, V. Ling, Lithium Uptake and the Accelerated Corrosion of Zirconium Alloys, Zirconium in the Nuclear Industry: Eighth International Symposium (2008) 187-187–15. https://doi.org/10.1520/stp18865s.

[26] D. Pêcheur, J. Godlewski, J. Peybernès, L. Fayette, M. Noé, A. Frichet, O. Kerrec, Contribution to the understanding of the effect of the water chemistry on the oxidation kinetics of Zircaloy-4 cladding, in: ASTM Special Technical Publication, 2000. https://doi.org/10.1520/stp14328s.

[27] M.W. Owen, M.J.D. Rushton, L.J. Evitts, A. Claisse, M. Puide, W.E. Lee, S.C. Middleburgh, Diffusion in doped and undoped amorphous zirconia, Journal of Nuclear Materials 555 (2021) 153108. https://doi.org/10.1016/j.jnucmat.2021.153108.

[28] B. Cox, Corrosion And Hydriding Of Zircaloy Fuel Cladding-The Inside (And Outside) Story, 1999. https://inis.iaea.org/search/search.aspx?orig_q=RN:33026637 (accessed October 18, 2023).

[29] K. R, M.K. Asundi, Zirconium alloys in nuclear technology, Indian Acad Sci 4 (1980) 41–56. https://doi.org/10.1007/BF01118114.

[30] C.L. Withmarsh, Review of Zircaloy-2 and Zircaloy-4 Properties Relevant to N.S. Savannah Reactor Design, (No. ORNL-3281). Oak Ridge National Lab., Tenn.. 4500 (1962) 70. https://doi.org/Report No. ORNL-3281, UC-80-Reactor Technology, TID-4500 (17th ed.).

[31] A.T. Motta, A. Couet, R.J. Comstock, Corrosion of Zirconium Alloys Used for Nuclear Fuel Cladding, Annu Rev Mater Res 45 (2015) 311–343. https://doi.org/10.1146/annurev-matsci-070214-020951.

[32] S. Müller, L. Lanzani, Corrosion of zirconium alloys in concentrated lithium hydroxide solutions, in: Journal of Nuclear Materials, 2013: pp. 251–257. https://doi.org/10.1016/j.jnucmat.2012.07.030.

[33] A.S.M. International, A.S.M.International.H. Committee, A.S.M.International.A.P.D. Committee, Metals Handbook: Properties and selection, ASM International, 1990.

[34] ATI Metals, Zircaloy-4 Annealed - Technical Data Sheet, 1 (2015) 2014–2016.

[35] S.C. Lumley, S.T. Murphy, P.A. Burr, R.W. Grimes, P.R. Chard-Tuckey, M.R. Wenman, The stability of alloying additions in Zirconium, Journal of Nuclear Materials 437 (2013) 122–129. https://doi.org/10.1016/j.jnucmat.2013.01.335.

[36] C. Kittel, Introduction to Solid State Physics, 8th edition, Wiley & Sons, New York, NY (2004).

[37] S.C. Lumley, S.T. Murphy, P.A. Burr, R.W. Grimes, P.R. Chard-Tuckey, M.R. Wenman, The stability of alloying additions in Zirconium, Journal of Nuclear Materials 437 (2013) 122–129. https://doi.org/10.1016/j.jnucmat.2013.01.335.

[38] L. Atom, S. Group, H.S. Group, I. Compound, T. Ele-, B.S. Murty, Laves Phase Learn more about Laves Phase Intermetallics , Interstitial Compounds and Metallic Glasses in High-Entropy Alloys, 2 (2014).

[39] K. Annand, M. Nord, I. MacLaren, M. Gass, The corrosion of Zr(Fe, Cr)2 and Zr2Fe secondary phase particles in Zircaloy-4 under 350 °C pressurised water conditions, Corros Sci 128 (2017) 213–223. https://doi.org/10.1016/j.corsci.2017.09.014.

[40] W. Xiao, C. Ma, Study on the precipitates in Zircaloy-4 by Mössbauer spectroscopy, Journal of Nuclear Materials (1998). https://doi.org/10.1016/S0022-3115(98)00032-4.

[41] R.A. Holt, The beta to alpha phase transformation in zircaloy-4, Journal of Nuclear Materials (1970). https://doi.org/10.1016/0022-3115(70)90216-3.

[42] N.G. Park, J.K. Park, J.I. Kim, K.L. Jeon, PWR fuel debris filtering performance measurement method and its application, Nuclear Engineering and Design 281 (2015) 96–102. https://doi.org/10.1016/j.nucengdes.2014.11.024.

[43] K.T. Kim, The study on grid-to-rod fretting wear models for PWR fuel, Nuclear Engineering and Design 239 (2009) 2820–2824. https://doi.org/10.1016/j.nucengdes.2009.08.018.

[44] J.B. Bai, C. Prioul, D. François, Hydride embrittlement in ZIRCALOY-4 plate: Part I. Influence of microstructure on the hydride embrittlement in ZIRCALOY-4 at 20 °C and 350 °C, Metallurgical and Materials Transactions A 25 (1994) 1185–1197. https://doi.org/10.1007/BF02652293.

[45] J. Deshon, D. Hussey, B. Kendrick, J. McGurk, J. Secker, M. Short, Pressurized water reactor fuel crud and corrosion modeling, Jom 63 (2011) 64–72. https://doi.org/10.1007/s11837-011-0141-z.

[46] V.K. Milinchuk, E.R. Klinshpont, V.I. Belozerov, A. V. Zagorodnyaya, Hydrozirconium reaction in heterogeneous compositions, Izvestiya Wysshikh Uchebnykh Zawedeniy, Yadernaya Energetika 3 (2016) 23–30. https://doi.org/10.26583/npe.2016.4.03.

[47] D.J. Park, J.Y. Park, Y.H. Jeong, Microstructural analysis and XPS investigation of nodular oxides formed on Zircaloy-4, Journal of Nuclear Materials (2011). https://doi.org/10.1016/j.jnucmat.2011.03.010.

[48] A.T. Motta, A. Couet, R.J. Comstock, Corrosion of Zirconium Alloys Used for Nuclear Fuel Cladding, Annu Rev Mater Res 45 (2015) 311–343. https://doi.org/10.1146/annurev-matsci-070214-020951.

[49] M. Gass, M. Fenwick, H. Hulme, M. Waters, P. Binks, A. Panteli, M. Chatterton, V. Allen, A. Cole-Baker, Corrosion of Zircaloys: Relating the microstructural observations to the corrosion kinetics, Journal of Nuclear Materials 509 (2018) 343–354. https://doi.org/10.1016/j.jnucmat.2018.07.017.

[50] H. Swan, M.S. Blackmur, J.M. Hyde, A. Laferrere, S.R. Ortner, P.D. Styman, C. Staines, M. Gass, H. Hulme, A. Cole-Baker, P. Frankel, The measurement of stress and phase fraction distributions in pre and post-transition Zircaloy oxides using nano-beam synchrotron X-ray diffraction, Journal of Nuclear Materials 479 (2016) 559–575. https://doi.org/10.1016/J.JNUCMAT.2016.07.024.

[51] Z. Wang, B. Zhou, B. Wang, M. Yao, Q. Li, J. Huang, The initial oxidation of Zircaloy-4 in lithiated water under autoclave conditions as examined by TEM, Corros Sci (2016). https://doi.org/10.1016/j.corsci.2016.01.011.

[52] A. Yilmazbayhan, A.T. Motta, R.J. Comstock, G.P. Sabol, B. Lai, Z. Cai, Structure of zirconium alloy oxides formed in pure water studied with synchrotron radiation and optical microscopy: Relation to corrosion rate, Journal of Nuclear Materials 324 (2004) 6–22. https://doi.org/10.1016/j.jnucmat.2003.08.038.

[53] K. Li, T. Aarholt, J. Liu, H. Hulme, A. Garner, M. Preuss, S. Lozano-Perez, C. Grovenor, 3D-characterization of deuterium distributions in zirconium oxide scale using high-resolution SIMS, Appl Surf Sci 464 (2019) 311–320. https://doi.org/10.1016/j.apsusc.2018.09.101.

[54] A. Garner, P. Frankel, J. Partezana, M. Preuss, The effect of substrate texture and oxidation temperature on oxide texture development in zirconium alloys, Journal of Nuclear Materials 484 (2017) 347–356. https://doi.org/10.1016/j.jnucmat.2016.10.037.

[55] H. Hulme, A. Panteli, F. Pickering, M. Gass, A. Cole-Baker, P. Binks, M. Fenwick, M. Waters, J. Smith, Investigating the Corrosion Behaviour of Zircaloy-4 in LiOH under a Thermal Gradient and Two-Phase Flow Regime, Zirconium in the Nuclear Industry: 19th International Symposium (2021) 537–563. https://doi.org/10.1520/stp162220190008.

[56] R.B. Adamson, F. Garzarolli, B. Cox, A. Strasser, P. Rudling, ZIRAT 12 Special Topic Report 2007 - Corrosion mechanisms in zirconium alloys, (2007) 45.

[57] L. Kurpaska, I. Jozwik, J. Jagielski, Study of sub-oxide phases at the metal-oxide interface in oxidized pure zirconium and Zr-1.0% Nb alloy by using SEM/FIB/EBSD and EDS techniques, Journal of Nuclear Materials 476 (2016) 56–62. https://doi.org/10.1016/j.jnucmat.2016.04.038.

[58] M. Youssef, M. Yang, B. Yildiz, Doping in the Valley of Hydrogen Solubility: A Route to Designing Hydrogen-Resistant Zirconium Alloys, Phys Rev Appl 5 (2016). https://doi.org/10.1103/PhysRevApplied.5.014008.

[59] X. Iltis, F. Lefebvre, C. Lemaignan, Microstructural study of oxide layers formed on Zircaloy-4 in autoclave and in reactor part II: Impact of the chemical evolution of intermetallic precipitates on their zirconia environment, Journal of Nuclear Materials (1995). https://doi.org/10.1016/0022-3115(95)00069-0.

[60] X. Iltis, F. Lefebvre, C. Lemaignan, Microstructural study of oxide layers formed on Zircaloy-4 in autoclave and in reactor Part I: Impact of irradiation on the microstructure of the zirconia layer, Journal of Nuclear Materials (1995). https://doi.org/10.1016/0022-3115(95)00070-4.

[61] L. Kurpaska, M. Frelek-Kozak, J.L. Grosseau-Poussard, I. Jozwik, L. Lahoche, J. Favergeon, J. Jagielski, Identification of the Zirconia Phases by Means of Raman Spectroscopy for Specimens Prepared by FIB Lift-Out Technique, Oxidation of Metals 88 (2017) 521–530. https://doi.org/10.1007/s11085-016-9675-3.

[62] M. Griffiths, R.W. Gilbert, V. Fidleris, Zirconium in the nuclear industry: Eighth International Symposium, ASTM STP 1023, in: American Society for Testing and Materials, 1989: pp. 658–677.

[63] A.M. Garde, E.R. Bradley, Zirconium in the nuclear industry: tenth international symposium, in: ASTM, 1994.

[64] G.R. Kilp, D.R. Thornburg, R.J. Comstock, IAEA Technical Committee Meeting on Fundamental Aspects of Corrosion on Zirconium Base Alloys in Water Reactor Environments, IAEA IWGFPT/34, Portland, OR, USA (1990) 145.

[65] E. Hillner, Corrosion of zirconium-base alloys—an overview, Zirconium in the Nuclear Industry, ASTM STP 633 (1977): 211-235. (1997) 211–235.

[66] W. Gong, H. Zhang, Y. Qiao, H. Tian, X. Ni, Z. Li, X. Wang, Grain morphology and crystal structure of pre-transition oxides formed on Zircaloy-4, Corros Sci (2013). https://doi.org/10.1016/j.corsci.2013.05.007.

[67] A. Garner, C. Gillen, G. Stephens, P. Styman, S. Armson, J. Robinson, J. Liu, A. Carruthers, F. Pickering, S. Sherry, C. Chan, M. Fenwick, H. Hulme, S. Ortner, C. Riley, C. Grovenor, P. Frankel, S.C. Middleburgh, A. Cole-Baker, Understanding the Mechanistic Role of Lithium in Accelerated Corrosion of Zirconium Alloys Using Advanced Characterization and Atomistic Simulation, in: Zirconium in the Nuclear Industry: 20th International Symposium, ASTM International100 Barr Harbor Drive, PO Box C700, West Conshohocken, PA 19428-2959, 2023: pp. 356–386. https://doi.org/10.1520/STP164520220054.

[68] R.B. Adamson, F. Garzarolli, B. Cox, A. Strasser, P. Rudling, ZIRAT 12 Special Topic Report 2007 - Corrosion mechanisms in zirconium alloys, (2007) 45.

[69] B. De Gabory, A.T. Motta, K. Wang, Transmission electron microscopy characterization of Zircaloy-4 and ZIRLO™ oxide layers, Journal of Nuclear Materials (2015). https://doi.org/10.1016/j.jnucmat.2014.09.073.

[70] H. Hulme, F. Baxter, R.P. Babu, M.A. Denecke, M. Gass, A. Steuwer, K. Norén, S. Carlson, M. Preuss, An X-ray absorption near-edge structure (XANES) study of the Sn L_3 edge in zirconium alloy oxide films formed during autoclave corrosion, Corros Sci 105 (2016) 202–208. https://doi.org/10.1016/j.corsci.2016.01.018.

[71] J. Lin, H. Li, J.A. Szpunar, R. Bordoni, A.M. Olmedo, M. Villegas, A.J.G. Maroto, Analysis of zirconium oxide formed during oxidation at 623 K on Zr-2.5Nb and Zircaloy-4, Materials Science and Engineering A (2004). https://doi.org/10.1016/j.msea.2004.04.019.

[72] W. Harlow, H. Ghassemi, M.L. Taheri, Determination of the initial oxidation behavior of Zircaloy-4 by in-situ TEM, Journal of Nuclear Materials (2016). https://doi.org/10.1016/j.jnucmat.2016.03.009.

[73] H.H. Kim, J.H. Kim, J.Y. Moon, H.S. Lee, J.J. Kim, Y.S. Chai, High-temperature oxidation behavior of Zircaloy-4 and Zirlo in steam ambient, J Mater Sci Technol (2010). https://doi.org/10.1016/S1005-0302(10)60132-6.

[74] M. Steinbrück, J. Birchley, A. V. Boldyrev, A. V. Goryachev, M. Grosse, T.J. Haste, Z. Hózer, A.E. Kisselev, V.I. Nalivaev, V.P. Semishkin, L. Sepold, J. Stuckert, N. Vér, M.S. Veshchunov, High-temperature oxidation and quench behaviour of Zircaloy-4 and E110 cladding alloys, Progress in Nuclear Energy (2010). https://doi.org/10.1016/j.pnucene.2009.07.012.

[75] P. Platt, V. Allen, M. Fenwick, M. Gass, M. Preuss, Observation of the effect of surface roughness on the oxidation of Zircaloy-4, Corros Sci (2015). https://doi.org/10.1016/j.corsci.2015.05.013.

[76] J.H. Kim, M.H. Lee, B.K. Choi, Y.H. Jeong, Failure behavior of Zircaloy-4 cladding after oxidation and water quench, Journal of Nuclear Materials (2007). https://doi.org/10.1016/j.jnucmat.2006.10.026.

[77] H.G. Kim, I.H. Kim, J.Y. Park, S.J. Yoo, J.G. Kim, In situ heating TEM analysis of oxide layer formed on Zr-1.5Nb alloy, Journal of Nuclear Materials (2014). https://doi.org/10.1016/j.jnucmat.2014.03.050.

[78] S. Xie, B. Zhou, X. Liang, W. Liu, H. Li, Q. Li, M. Yao, J. Zhang, A novel mechanism for nodular corrosion of Zircaloy-4 corroded in 773 K superheated steam, Corros Sci (2017). https://doi.org/10.1016/j.corsci.2017.06.007.

[79] A.I.A. Almarshad, A.C. Klein, A model for waterside oxidation of Zircaloy fuel cladding in pressurized water reactors, Journal of Nuclear Materials (1991). https://doi.org/10.1016/0022-3115(91)90487-R.

[80] J. Han, G. Xomeritakis, Y.S. Lin, Oxygen permeation through thin zirconia/yttria membranes prepared by EVD, Solid State Ion 93 (1997) 263–272. https://doi.org/10.1016/s0167-2738(96)00528-0.

[81] P.A.J. Bagot, A.J. Wilkinson, C.R.M. Grovenor, J. Hu, B. Setiadinata, T. Aarholt, A. Garner, A. Vilalta-Clemente, J. Partezana, P. Frankel, P. Bagot, S. Lozano-Perez, A. Wilkinson, M. Preuss, M. Moody, C. Grovenor, Understanding Corrosion and Hydrogen Pickup of Zirconium Fuel Cladding Alloys: the Role of Oxide Microstructure III-V semiconductors, (2017) 1–27.

[82] M. Oskarsson, E. Ahlberg, K. Pettersson, Oxidation of Zircaloy-2 and Zircaloy-4 in water and lithiated water at 360°C, Journal of Nuclear Materials (2001). https://doi.org/10.1016/S0022-3115(01)00480-9.

[83] M. Oskarsson, E. Ahlberg, K. Pettersson, Phase transformation of stabilised zirconia in water and 1.0 M LiOH, Journal of Nuclear Materials 295 (2001) 126–130. https://doi.org/10.1016/S0022-3115(01)00482-2.

[84] H. Sun, X. Wu, E.H. Han, Y. Wei, Effects of pH and dissolved oxygen on electrochemical behavior and oxide films of 304SS in borated and lithiated high temperature water, Corros Sci (2012). https://doi.org/10.1016/j.corsci.2012.03.022.

[85] X. Liu, E.H. Han, X. Wu, Effects of pH value on characteristics of oxide films on 316L stainless steel in Zn-injected borated and lithiated high temperature water, Corros Sci (2014). https://doi.org/10.1016/j.corsci.2013.09.017.

[86] D. Pecheur, J. Godlewski, P. Billot, J. Thomazet, Microstructure of oxide films formed during the waterside corrosion of the zircaloy-4 cladding in lithiated environment, (1996) 94–113.

[87] B. Cox, Is zirconium oxide morphology on fuel cladding largely determined by lithium hydroxide concentration effects?, Journal of Nuclear Materials (1997). https://doi.org/10.1016/S0022-3115(97)00192-X.

[88] A.M. Garde, E.R. Bradley, Zirconium in the nuclear industry: tenth international symposium, in: ASTM, 1994.

[89] I. Nuclear, The concentration of the coolant 7 Li in Kozloduy Nuclear Power Plant operating with potassium hydroxide as an alkalizing reagent (possible impact on the occurrence of axial offset anomaly), (n.d.).

[90] P.L. Frattini, J. Blok, S. Chauffriat, J. Sawicki, J. Riddle, Axial offset anomaly: Coupling PWR primary chemistry with core design, Nuclear Energy 40 (2001) 123–135. https://doi.org/10.1680/nuen.40.2.123.39952.

[91] M.F. L'Annunziata, Radioactivity and Our Well-Being, in: Radioactivity, Elsevier, 2016: pp. 1–66. https://doi.org/10.1016/B978-0-444-63489-4.00001-0.

[92] Y.H. Jeong, K.H. Kim, J.H. Baek, Cation incorporation into zirconium oxide in LiOH, NaOH, and KOH solutions, Journal of Nuclear Materials 275 (1999) 221–224. https://doi.org/10.1016/S0022-3115(99)00148-8.

[93] J. Yang, M. Youssef, B. Yildiz, Oxygen self-diffusion mechanisms in monoclinic ZrO_2 revealed and quantified by density functional theory, random walk analysis, and kinetic Monte Carlo calculations, Phys Rev B 97 (2018). https://doi.org/10.1103/PhysRevB.97.024114.

[94] R.E. Voskoboinikov, Y.N. Osetsky, D.J. Bacon, Statistics of primary damage creation in high-energy displacement cascades in copper and zirconium, Nucl Instrum Methods Phys Res B 242 (2006) 68–70. https://doi.org/10.1016/j.nimb.2005.08.166.

[95] A. Skokan, PHASE STABILITY INVESTIGATIONS IN THE CERAMIC BREEDER SYSTEMS Li2O-Al2O3 and Li2O-ZrO2, Fusion Technology 1990 (1991) 772–776. https://doi.org/10.1016/b978-0-444-88508-1.50139-0.

[96] G.P. Wyers, E.H.P. Cordfunke, PHASE RELATIONS IN THE SYSIEM Li2O-ZrO2, Nuclear Materials 168 (1989) 24–30.

[97] L.C. Martel, R.S. Roth, System $Li_2O(Li_2CO_3)$-ZrO_2, Am. Ceram. Soc. Bull 60 (1981) 376.

[98] S.C. Middleburgh, S. Dumbill, A. Qaisar, I. Vatter, M. Owen, S. Vallely, D. Goddard, D. Eaves, M. Puide, M. Limbäck, W.E. Lee, Enrichment of Chromium at Grain Boundaries in Chromia Doped UO_2, Journal of Nuclear Materials 575 (2023) 154250. https://doi.org/10.1016/j.jnucmat.2023.154250.

[99] G. Bergerhoff, I.D. Brown, F.H. Allen, Crystallographic Databases, International Union of Crystallography (1987).

[100] D. Zagorac, H. Müller, S. Ruehl, J. Zagorac, S. Rehme, Recent developments in the Inorganic Crystal Structure Database: theoretical crystal structure data and related features, J Appl Crystallogr 52 (2019) 918–925. https://doi.org/10.1107/S160057671900997X.

[101] H. Behrens, P. Luksch, A bibliometric study in crystallography, Acta Crystallogr B 62 (2006) 993–1001. https://doi.org/10.1107/S0108768106030278.

[102] A. Belsky, M. Hellenbrandt, V.L. Karen, P. Luksch, New developments in the Inorganic Crystal Structure Database (ICSD): accessibility in support of materials research and design, Acta Crystallogr B 58 (2002) 364–369. https://doi.org/10.1107/S0108768102006948.

[103] M. Yashima, T. Hirose, S. Katano, Y. Suzuki, M. Kakihana, M. Yoshimura, Structural changes of ZrO_2-CeO_2 solid solutions around the monoclinic-tetragonal phase boundary, Phys Rev B 51 (1995) 8018–8025. https://doi.org/10.1103/PhysRevB.51.8018.

[104] B. Bondars, G. Heidemane, J. Grabis, K. Laschke, H. Boysen, J. Schneider, F. Frey, Powder diffraction investigations of plasma sprayed zirconia, J Mater Sci 30 (1995) 1621–1625. https://doi.org/10.1007/BF00375275.

[105] A.P. Thompson, H.M. Aktulga, R. Berger, D.S. Bolintineanu, W.M. Brown, P.S. Crozier, P.J. in 't Veld, A. Kohlmeyer, S.G. Moore, T.D. Nguyen, R. Shan, M.J. Stevens, J. Tranchida, C. Trott, S.J. Plimpton, LAMMPS - a flexible simulation tool for particle-based materials modeling at the atomic, meso, and continuum scales, Comput Phys Commun 271 (2022) 108171. https://doi.org/10.1016/j.cpc.2021.108171.

[106] M.W.D. Cooper, M.J.D. Rushton, R.W. Grimes, A many-body potential approach to modelling the thermomechanical properties of actinide oxides, Journal of Physics Condensed Matter 26 (2014). https://doi.org/10.1088/0953-8984/26/10/105401.

[107] D.G. Frost, C.O.T. Galvin, M.W.D. Cooper, E.G. Obbard, P.A. Burr, Thermophysical properties of urania-zirconia $(U,Zr)O_2$ mixed oxides by molecular dynamics, Journal of Nuclear Materials 528 (2020). https://doi.org/10.1016/J.JNUCMAT.2019.151876.

[108] M.J.D. Rushton, A. Chroneos, Impact of uniaxial strain and doping on oxygen diffusion in CeO2, Sci Rep 4 (2014) 2–7. https://doi.org/10.1038/srep06068.

[109] M.J.D. Rushton, I. Ipatova, L.J. Evitts, W.E. Lee, S.C. Middleburgh, Stoichiometry deviation in amorphous zirconium dioxide, RSC Adv 9 (2019) 16320–16327. https://doi.org/10.1039/c9ra01865d.

[110] S. Chib, E. Greenberg, Understanding the Metropolis-Hastings Algorithm, 1995.

[111] C. Freysoldt, B. Grabowski, T. Hickel, J. Neugebauer, G. Kresse, A. Janotti, C.G. Van De Walle, First-principles calculations for point defects in solids, Rev Mod Phys 86 (2014) 253–305. https://doi.org/10.1103/RevModPhys.86.253.

[112] G. Kresse, J. Furthmüller, J. Hafner, Theory of the crystal structures of selenium and tellurium: The effect of generalized-gradient corrections to the local-density approximation, Phys Rev B 50 (1994) 13181–13185. https://doi.org/10.1103/PhysRevB.50.13181.

[113] G. Kresse, J. Furthmüller, Efficiency of ab-initio total energy calculations for metals and semiconductors using a plane-wave basis set, Comput Mater Sci 6 (1996) 15–50. https://doi.org/10.1016/0927-0256(96)00008-0.

[114] G. Kresse, J. Furthmüller, Efficient iterative schemes for ab initio total-energy calculations using a plane-wave basis set, Phys Rev B Condens Matter Mater Phys 54 (1996) 11169–11186. https://doi.org/10.1103/PhysRevB.54.11169.

[115] D.S. Sholl, J.A. Steckel, DENSITY FUNCTIONAL THEORY A Practical Introduction, 1st ed., John Wiley & Sons, 2022.

[116] J.P. Perdew, K. Burke, M. Ernzerhof, Generalized Gradient Approximation Made Simple, 1996.

[117] U. Guth, Kröger-Vinks Notation of Point Defects, in: Encyclopedia of Applied Electrochemistry, 2014. https://doi.org/10.1007/978-1-4419-6996-5_310.

[118] K. Pathmanathan, P. Iyngaran, N. Kuganathan, Structural, defect, transport, and solution properties of Li2GeO3, AIP Adv 13 (2023). https://doi.org/10.1063/5.0153486.

[119] S.T. Murphy, N.D.M. Hine, Point defects and non-stoichiometry in Li_2TiO_3, Chemistry of Materials 26 (2014) 1629–1638. https://doi.org/10.1021/cm4038473.

[120] S.T. Murphy, N.D.M. Hine, Anisotropic charge screening and supercell size convergence of defect formation energies, (2013). http://wrap.warwick.ac.uk/78152.

[121] M. Youssef, B. Yildiz, Intrinsic point-defect equilibria in tetragonal ZrO_2: Density functional theory analysis with finite-temperature effects, Phys Rev B Condens Matter Mater Phys 86 (2012). https://doi.org/10.1103/PhysRevB.86.144109.

[122] K. Singh, J. Nowotny, V. Thangadurai, Amphoteric oxide semiconductors for energy conversion devices: a tutorial review, Chem. Soc. Rev 42 (2013). https://doi.org/10.1039/c2cs35393h.

[123] B.D.C. Bell, S.T. Murphy, P.A. Burr, R.W. Grimes, M.R. Wenman, Accommodation of tin in tetragonal ZrO_2, J Appl Phys 117 (2015). https://doi.org/10.1063/1.4909505.

[124] X.S. Yin, S.P. Li, Q.H. Zhang, J.G. Yu, Synthesis and CO2 adsorption characteristics of lithium zirconates with high lithia content, Journal of the American Ceramic Society 93 (2010) 2837–2842. https://doi.org/10.1111/j.1551-2916.2010.03769.x.

[125] W. Gong, H. Zhang, Y. Qiao, H. Tian, X. Ni, Z. Li, X. Wang, Grain morphology and crystal structure of pre-transition oxides formed on Zircaloy-4, Corros Sci (2013). https://doi.org/10.1016/j.corsci.2013.05.007.

[126] X-Ray Diffraction (XRD) | Braggs Equation & Applications of XRD, (n.d.). https://letstalkacademy.com/x-ray-diffraction/ (accessed October 19, 2023).

[127] Scanning Electron Microscopy - SEM - Advancing Materials, (n.d.). https://www.thermofisher.com/blog/materials/what-is-sem-scanning-electron-microscopy-explained/ (accessed October 19, 2023).

[128] Netzsh Simultaneous thermal analyser, (n.d.). https://analyzing-testing.netzsch.com/en/products/simultaneous-thermogravimetry-differential-scanning-calorimetry-sta-tg-dsc (accessed October 19, 2023).

[129] G.F. Stephens, Y.R. Than, W. Neilson, L.J. Evitts, M.R. Wenman, S.T. Murphy, R.W. Grimes, A. Cole-Baker, S. Ortner, N. Gotham, M.J.D. Rushton, W.E. Lee, S.C. Middleburgh, The accommodation of lithium in bulk ZrO2, Solid State Ion 373 (2021) 115813. https://doi.org/10.1016/j.ssi.2021.115813.

[130] G.F. Stephens, L.J. Evetts, M.J. Rushton, W.E. Lee, S.C. Middleburgh, Y.N. Than, A. Cole-Baker, W. Neilson, S.T. Murphy, M.R. Wenman, R.W. Grimes, N. Gotham, S.R. Ortner, Lithium Accommodation in ZrO_2, in: European Nuclear Society - Top Fuel, Santandar, 2021. https://www.euronuclear.org/scientific-resources/conference-proceedings/#1559592636459-42447d8c-0fcc (accessed October 18, 2023).

[131] M. Gass, M. Fenwick, H. Hulme, M. Waters, P. Binks, A. Panteli, M. Chatterton, V. Allen, A. Cole-Baker, Corrosion of Zircaloys: Relating the microstructural observations to the corrosion kinetics, Journal of Nuclear Materials 509 (2018) 343–354. https://doi.org/10.1016/j.jnucmat.2018.07.017.

[132] J. Chevalier, L. Gremillard, A. V. Virkar, D.R. Clarke, The tetragonal-monoclinic transformation in zirconia: Lessons learned and future trends, Journal of the American Ceramic Society 92 (2009) 1901–1920. https://doi.org/10.1111/j.1551-2916.2009.03278.x.

[133] J. Yang, M. Youssef, B. Yildiz, Electro-chemo-mechanical effects of lithium incorporation in zirconium oxide, Phys Rev Mater 2 (2018). https://doi.org/10.1103/PhysRevMaterials.2.075405.

[134] R.D. Shannon, C.T. Prewitt, IUCr, Effective ionic radii in oxides and fluorides, Urn:Issn:0567-7408 25 (1969) 925–946. https://doi.org/10.1107/S0567740869003220.

[135] A. Goyal, K. Mathew, R.G. Hennig, A. Chernatynskiy, C.R. Stanek, S.T. Murphy, D.A. Andersson, S.R. Phillpot, B.P. Uberuaga, The Conundrum of Relaxation Volumes in First-Principles Calculations of Charged Defects in UO_2, Applied Sciences 9 (2019) 5276. https://doi.org/10.3390/app9245276.

[136] G.F. Stephens, M.W. Owen, E.M. Ghardi, A. Fraile, S. Ortner, M.J.D. Rushton, W.E. Lee, A. Cole-Baker, S.C. Middleburgh, Assessing Li accommodation at amorphous ZrO2 grain boundaries, Journal of Nuclear Materials 588 (2024) 154780. https://doi.org/10.1016/j.jnucmat.2023.154780.

[137] M.W. Owen, M.J.D. Rushton, L.J. Evitts, A. Claisse, M. Puide, W.E. Lee, S.C. Middleburgh, Diffusion in doped and undoped amorphous zirconia, Journal of Nuclear Materials 555 (2021) 153108. https://doi.org/10.1016/j.jnucmat.2021.153108.

[138] V. Gritsenko, D. Gritsenko, S. Shaimeev, V. Aliev, K. Nasyrov, S. Erenburg, V. Tapilin, H. Wong, M.C. Poon, J.H. Lee, J.W. Lee, C.W. Kim, Atomic and electronic structures of amorphous ZrO2 and HfO 2 films, in: Microelectron Eng, 2005: pp. 524–529. https://doi.org/10.1016/j.mee.2005.03.056.

[139] S.M. Chang, R.A. Doong, Interband transitions in sol-gel-derived ZrO2 films under different calcination conditions, Chemistry of Materials 19 (2007) 4804–4810. https://doi.org/10.1021/cm070606n.

[140] T. Ito, M. Maeda, K. Nakamura, H. Kato, Y. Ohki, Similarities in photoluminescence in hafnia and zirconia induced by ultraviolet photons, J Appl Phys 97 (2005). https://doi.org/10.1063/1.1856220.

[141] D. Ciuparu, A. Ensuque, G. Shafeev, F. Bozon-Verduraz, Synthesis and apparent bandgap of nanophase zirconia, J Mater Sci Lett 19 (2000) 931–933. https://doi.org/10.1023/A:1006799701474.

[142] G.F. Stephens, M.W. Owen, E.M. Ghardi, A. Fraile, S. Ortner, M.J.D. Rushton, W.E. Lee, A. Cole-Baker, S.C. Middleburgh, Assessing Li accommodation at amorphous ZrO_2 grain boundaries, (In Press) (2023).

[143] A. Garner, C. Gillen, G. Stephens, P. Styman, S. Armson, J. Robinson, J. Liu, A. Carruthers, F. Pickering, S. Sherry, C. Chan, M. Fenwick, H. Hulme, S. Ortner, C. Riley, C. Grovenor, P. Frankel, S.C. Middleburgh, A. Cole-Baker, Mechanistically Understanding the Role of Lithium in Accelerated Corrosion of Zirconium Alloys Using Advanced Characterisation and Atomistic Simulation, (In Press) (2022).

[144] B. V. Cockeram, P.D. Edmondson, K.J. Leonard, B.F. Kammenzind, J.L. Hollenbeck, Atom probe examinations of Zircaloy irradiated at nominally 358 °C, Nuclear Materials and Energy 19 (2019) 416–432. https://doi.org/10.1016/j.nme.2019.03.023.

[145] Y. Dong, A.T. Motta, E.A. Marquis, Atom probe tomography study of alloying element distributions in Zr alloys and their oxides, Journal of Nuclear Materials 442 (2013) 270–281. https://doi.org/10.1016/j.jnucmat.2013.08.055.

[146] F.L. Garcia, V.G. de Resende, E. De Grave, A. Peigney, A. Barnabé, C. Laurent, Iron-stabilized nanocrystalline ZrO2 solid solutions: Synthesis by combustion and thermal stability, Mater Res Bull 44 (2009) 1301–1311. https://doi.org/10.1016/J.MATERRESBULL.2008.12.014.

[147] B.D.C. Bell, S.T. Murphy, P.A. Burr, R.W. Grimes, M.R. Wenman, Accommodation of tin in tetragonal ZrO2, J Appl Phys 117 (2015). https://doi.org/10.1063/1.4909505.

[148] P. Erhart, K. Albe, A. Klein, First-principles study of intrinsic point defects in ZnO: Role of band structure, volume relaxation, and finite-size effects, (n.d.). https://doi.org/10.1103/PhysRevB.73.205203.

[149] G.F. Stephens, J.A. Wilson, S.F. Curling, G. He, P.J. Thomas, D.W. Williams, S. Ortner, C. Grovenor, M.J.D. Rushton, A.C.- Baker, S.C. Middleburgh, Lithium stabilization of amorphous

ZrO2, Progress in Nuclear Energy 171 (2024) 105165. https://doi.org/10.1016/j.pnucene.2024.105165.

[150] X. Zhao, D. Vanderbilt, Phonons and lattice dielectric properties of zirconia, Phys Rev B Condens Matter Mater Phys 65 (2002) 1–10. https://doi.org/10.1103/PhysRevB.65.075105.

[151] C. Carlone, Raman spectrum of zirconia-hafnia mixed crystals, n.d.

[152] M.J.D. Rushton, I. Ipatova, L.J. Evitts, W.E. Lee, S.C. Middleburgh, Stoichiometry deviation in amorphous zirconium dioxide, RSC Adv 9 (2019) 16320–16327. https://doi.org/10.1039/c9ra01865d.

[153] J. Huang, W. Wang, D. Li, S. Xu, Q. Liu, X. Chen, Z. Fei, Z. Zhang, M. Cui, J. Tang, X. Qiao, Facile construction of non-crystalline ZrO2 as an active yet durable catalyst for methane oxychlorination, J Solgel Sci Technol 92 (2019) 163–172. https://doi.org/10.1007/s10971-019-05089-x.

[154] D.K. Smith, H.W. Newkirk, The Crystal Structure of Baddeleyite (Monoclinic ZrO_2) and its Relation to the Polymorphism of ZrO_2, 1965.

[155] B. Bondars, G. Heidemane, J. Grabis, K. Laschke, H. Boysen, J. Schneider, F. Frey, Powder diffraction investigations of plasma sprayed zirconia, J Mater Sci 30 (1995) 1621–1625. https://doi.org/10.1007/BF00375275.

[156] D. Wang, Y. Guo, K. Liang, K. Tao, Crystal structure of zirconia by Rietveld refinement, Sci China Ser A Math 42 (1999) 80–86. https://doi.org/10.1007/BF02872053.

[157] B. Bondars, G. Heidemane, J. Grabis, K. Laschke, H. Boysen, J. Schneider, F. Frey, Powder diffraction investigations of plasma sprayed zirconia, J Mater Sci 30 (1995) 1621–1625. https://doi.org/10.1007/BF00375275.

[158] E.A. Sherstobitova, A.F. Gubkin, I.A. Bobrikov, A. V. Kalashnova, M.I. Pantyukhina, Bottle-necked ionic transport in Li_2ZrO_3: high temperature neutron diffraction and impedance spectroscopy, Electrochim Acta 209 (2016) 574–581. https://doi.org/10.1016/j.electacta.2016.05.113.

[159] G. Dittrich, R. Hoppe, Die Kristallstruktur von Li_2ZrO_3 und Li_2HfO_3, Z Anorg Allg Chem 371 (1969) 306–317. https://doi.org/10.1002/zaac.19693710513.

[160] P. Quintana, J. Leal, R.A. Howie, A.R. West, Li_2ZrO_3: A new polymorph with the α-$LiFeO_2$ structure, Mater Res Bull 24 (1989) 1385–1389. https://doi.org/10.1016/0025-5408(89)90144-X.

[161] R. Czekalla, W. Jeitschko, Preparation and crystal structure of $Li_6Zr_2O_7$ and $Li_6Hf_2O_7$, Z Anorg Allg Chem 619 (1993) 2038–2042. https://doi.org/10.1002/zaac.19936191212.

[162] T.W.D. Farleytq, W. Hayest, S. Hull, M.T. Hutchingsf, M. Vrtisg, Investigation of thermally induced Li+ ion disorder in LizO using neutron diffraction, 1991.

[163] F. Fehér, I. Von Wilucki, G. Dost, Beiträge zur Kenntnis des Wasserstoffperoxyds und seiner Derivate, VII. Mitteil.: Über die Kristallstruktur des Lithiumperoxyds, Li_2O_2, Chem Ber 86 (1953) 1429–1437. https://doi.org/10.1002/cber.19530861111.

[164] E. Wigner, Zeitschrift fur physikalische chemie-abteilung b-chemie der elementarprozesse, Aufbau Der Materie 19 (1932) 203–216.

[165] M. Atoji, M. Kikuchi, Crystal Structure of LiH0.984C0.016, J Chem Phys 52 (1970) 6434–6436. https://doi.org/10.1063/1.1672968.

[166] N.W. Alcock, Refinement of the crystal structure of lithium hydroxide monohydrate, Acta Crystallogr B 27 (1971) 1682–1683. https://doi.org/10.1107/S056774087100459X.

[167] S. Dey, J.W. Drazin, Y. Wang, J.A. Valdez, T.G. Holesinger, B.P. Uberuaga, R.H.R. Castro, Radiation Tolerance of Nanocrystalline Ceramics: Insights from Yttria Stabilized Zirconia, (2015). https://doi.org/10.1038/srep07746.

[168] B.H. Davis, Effect of pH on Crystal Phase of ZrO_2 Precipitated from Solution and Calcined at 600°C, Journal of the American Ceramic Society 67 (1984) C-168-C–168. https://doi.org/10.1111/j.1151-2916.1984.tb19185.x.

[169] B. Benali, M.H. Ghysel, I. Gallet, A.M. Huntz, M. Andrieux, Stress driven phase transformation in ZrO 2 film, (2006). https://doi.org/10.1016/j.apsusc.2006.01.060.

[170] P. Styman, A. Garner, J. Robinson, A. Cole-Baker, S. Ortner, Characterising The Effect Of Li On Zircaloy Corrosion, (In Press) Fontevraud 10 (2022).

Appendix

A.1. Cr Doped Tetragonal ZrO_2

In the case of chromium, the defects that were well within the bandgap calculations were numerous, so most had the potential to feature on the Brouwer diagrams. Various charged defects from chromium interstitials, substitutions and small clusters including $(\mathrm{Cr_i})$, $(\mathrm{Cr_{Zr}})$, $(\mathrm{Cr_{Zr}}{:}\,\mathrm{V_O})$ and $(2\mathrm{Cr_{Zr}}{:}\,\mathrm{V_O})$. Unlike the lithium defects, due to the high number of potential chromium defects, the formation energy vs Fermi energy plots have been split between defect species.

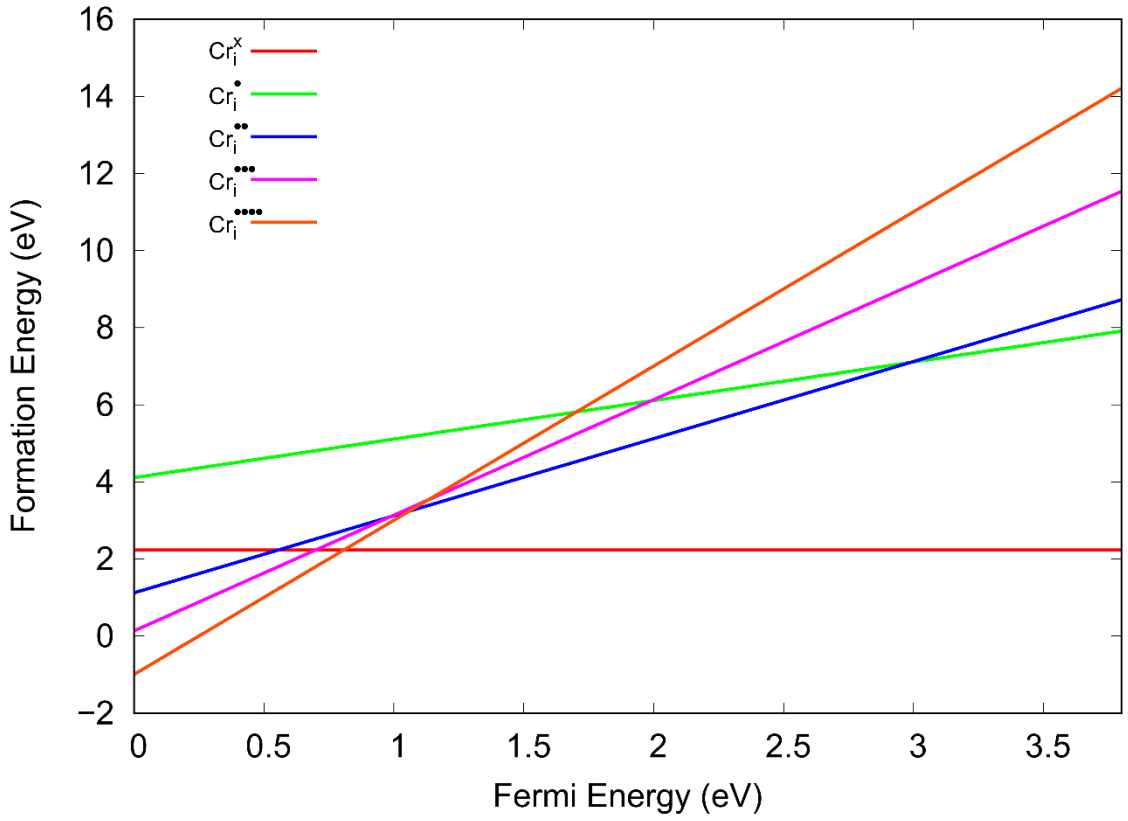

Figure 112 Formation energy of chromium interstitial defects with a range of charges across the Fermi energy of the bandgap of tetragonal ZrO_2.

For chromium interstitials, Figure 112, the positive 4 charged $(\mathrm{Cr_i^{\bullet\bullet\bullet\bullet}})$ occupies a small region towards the valence band at the bottom of the bandgap but is the only defect to have a negative formation energy. The remainder of the bandgap is dominated by the neutral charged interstitial $(\mathrm{Cr_i^{\times}})$.

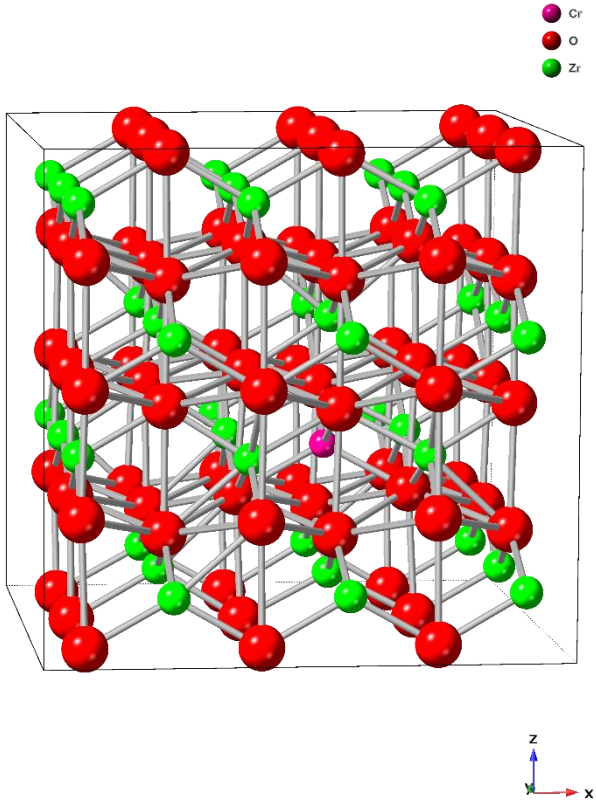

Figure 113 Tetragonal ZrO_2 structure with chromium interstitial (purple) centre (Different orientation to aid in visual).

The chromium interstitial structure (Figure 113) seems, visually, to be relatively unchanged when relaxed in tetragonal ZrO_2.

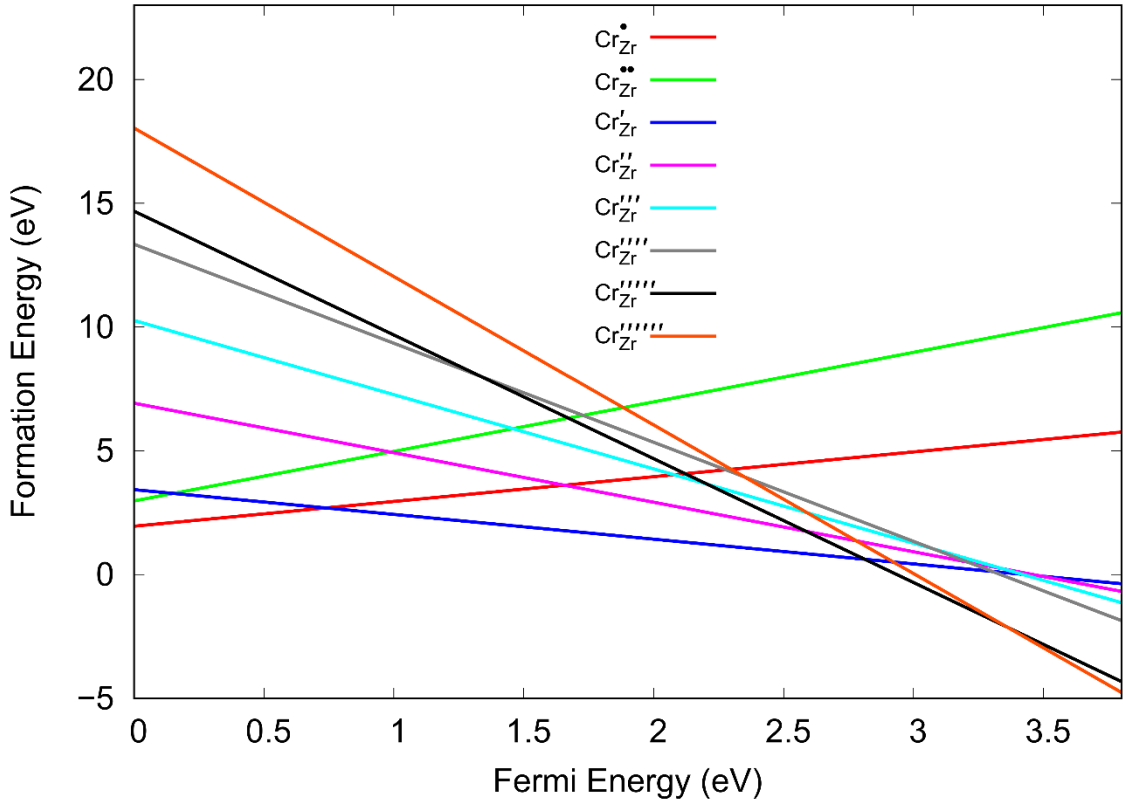

Figure 114 Formation energy of chromium substitutions on zirconium site defects with a range of charges across the Fermi energy of the bandgap of tetragonal ZrO_2.

For chromium substitutions on zirconium sites, Figure 114, the positive one charged $(Cr_{Zr}^{\bullet})$ shows at the bottom of the band gap to the left which is replaced by the negative one charged defect $(Cr_{Zr}^{\prime})$ towards the top of the bandgap. At the very top of the bandgap to the right, which is first negative five charged $(Cr_{Zr}^{\prime\prime\prime\prime\prime})$ but is eventually replaced by the negative six charged defect $(Cr_{Zr}^{\prime\prime\prime\prime\prime\prime})$.

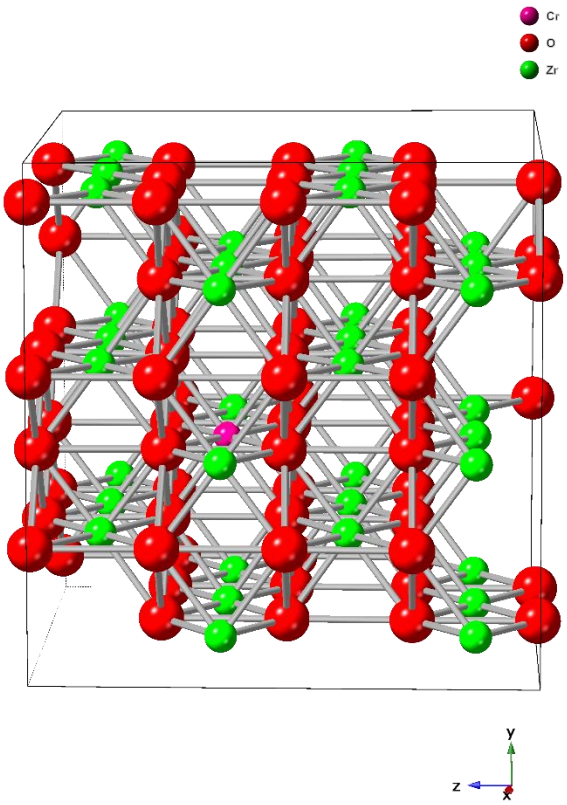

Figure 115 Tetragonal ZrO_2 structure with chromium substitution (purple) on a zirconium site (green). The orientation is changed for defect clarity.

As with the chromium interstitial defect in tetragonal ZrO_2, the chromium substitution on a zirconium site (Figure 115) shows little change in atomic positions when relaxed with a small movement of oxygen to the right of the chromium substitution closer to the defect.

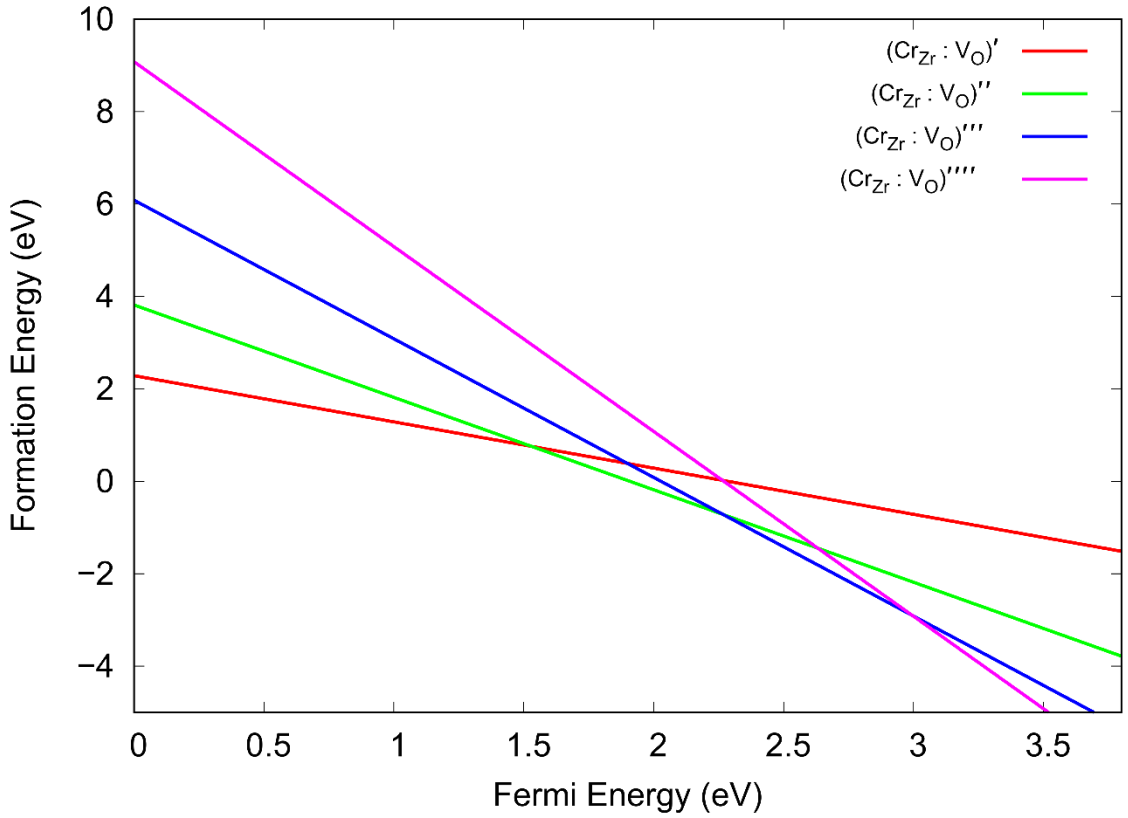

Figure 116 Formation energy of chromium substitutions on zirconium sites with an oxygen vacancy defect with a range of charges across the Fermi energy of the bandgap of tetragonal ZrO_2.

The small cluster defect of a chromium substitution on a zirconium site and an oxygen vacancy, Figure 116, the negative one charged defect $(\mathrm{Cr_{Zr}}:\mathrm{V_O})'$ has the lowest formation energy to the left at the bottom of the bandgap. This is briefly replaced by the negative two defect, followed by the negative three and then the negative four defect at the top of the bandgap.

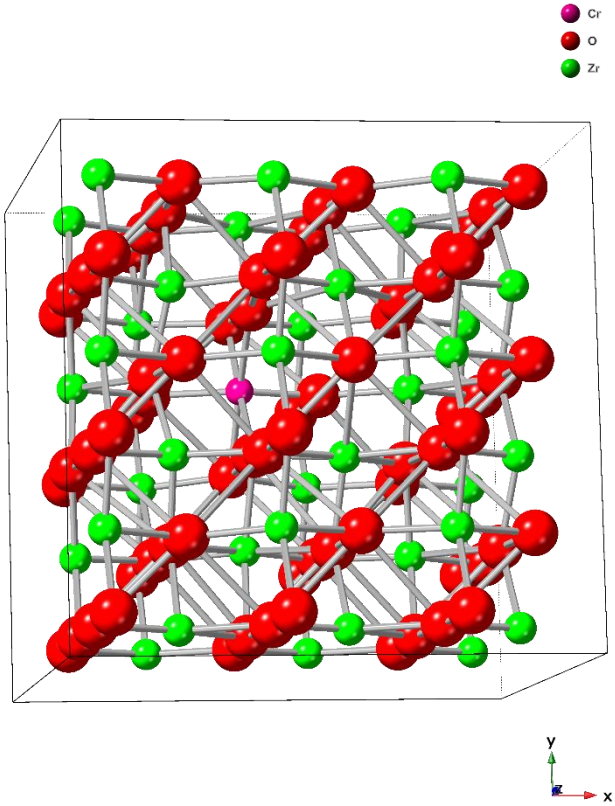

Figure 117 Tetragonal ZrO_2 structure with a chromium substitution on a zirconium site and a oxygen vacancy.

The tetragonal structure of ZrO_2 with a chromium substitution and an oxygen vacancy (Figure 117) shows little change of atomic position when relaxed.

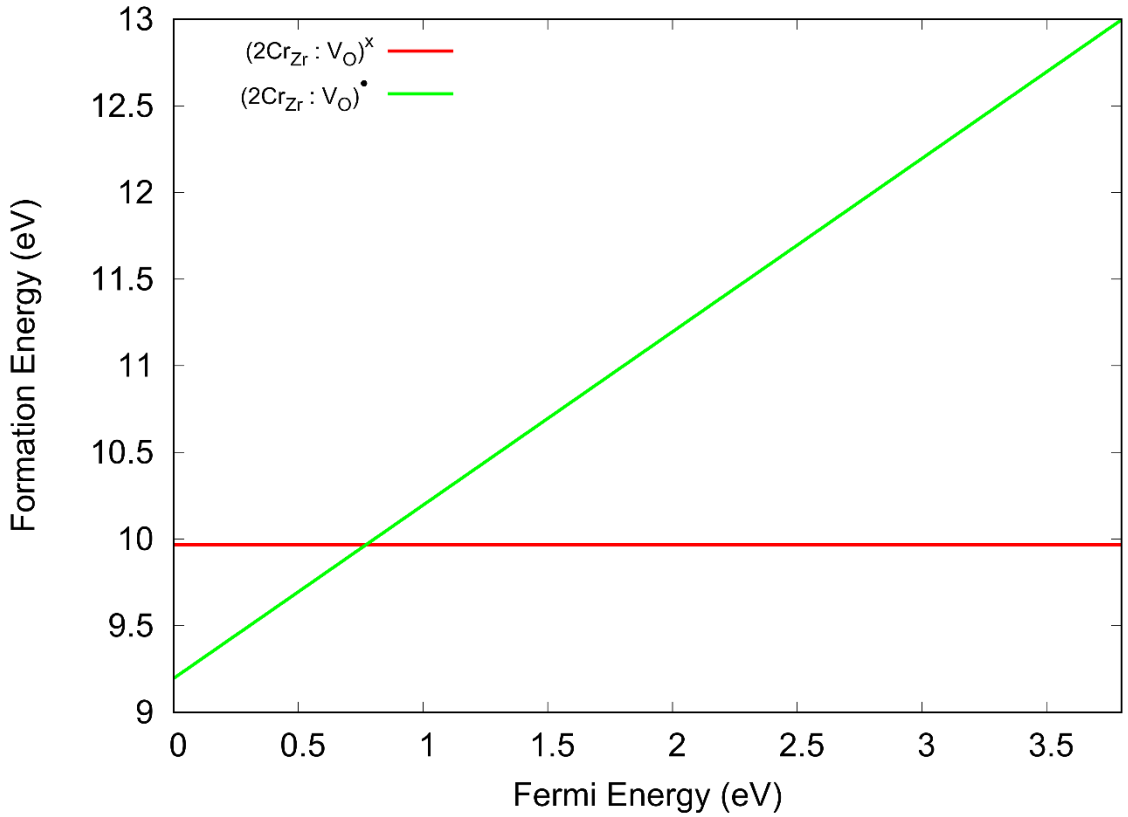

Figure 118 Formation energy of two chromium substitutions on a zirconium site with an oxygen vacancy defect with a range of charges across the Fermi energy of the bandgap of tetragonal ZrO_2.

The $(2\mathrm{Cr}_{\mathrm{Zr}}{:}\,\mathrm{V}_{\mathrm{O}})$ defect has a very high formation energy so would be unlikely to feature in the Brouwer diagram, Figure 118. The positive one charged defect is prevalent at the bottom of the bandgap to the left but is replaced by the neutral charged defect covering the remained of the bandgap.

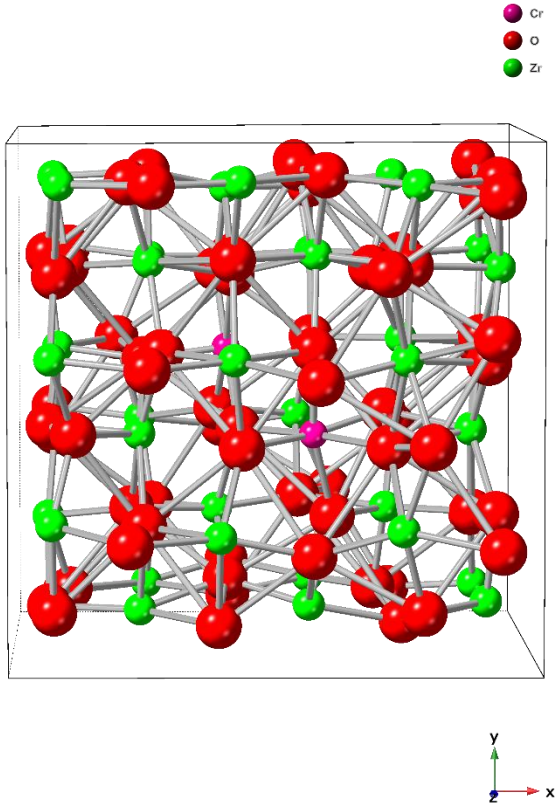

Figure 119 Tetragonal ZrO_2 structure with two chromium substitutions on zirconium sites and an oxygen vacancy.

When looking at the tetragonal ZrO_2 structure with two chromium substitutions on zirconium sites along with an oxygen vacancy (Figure 119), the cluster of defects caused much larger variations in atomic positions.

Given the number of defects that hold low formation energies containing chromium, this provided an indication that the produced Brouwer diagram would be very busy. For this reason, the higher Cr concentration of 10^{-3} is placed individually before placing the plots of all the concentrations together in a single figure, as was the case for the Li defects. Once the main features of the high concentration Brouwer diagram could be identified, all of the concentration plots are added together for comparison.

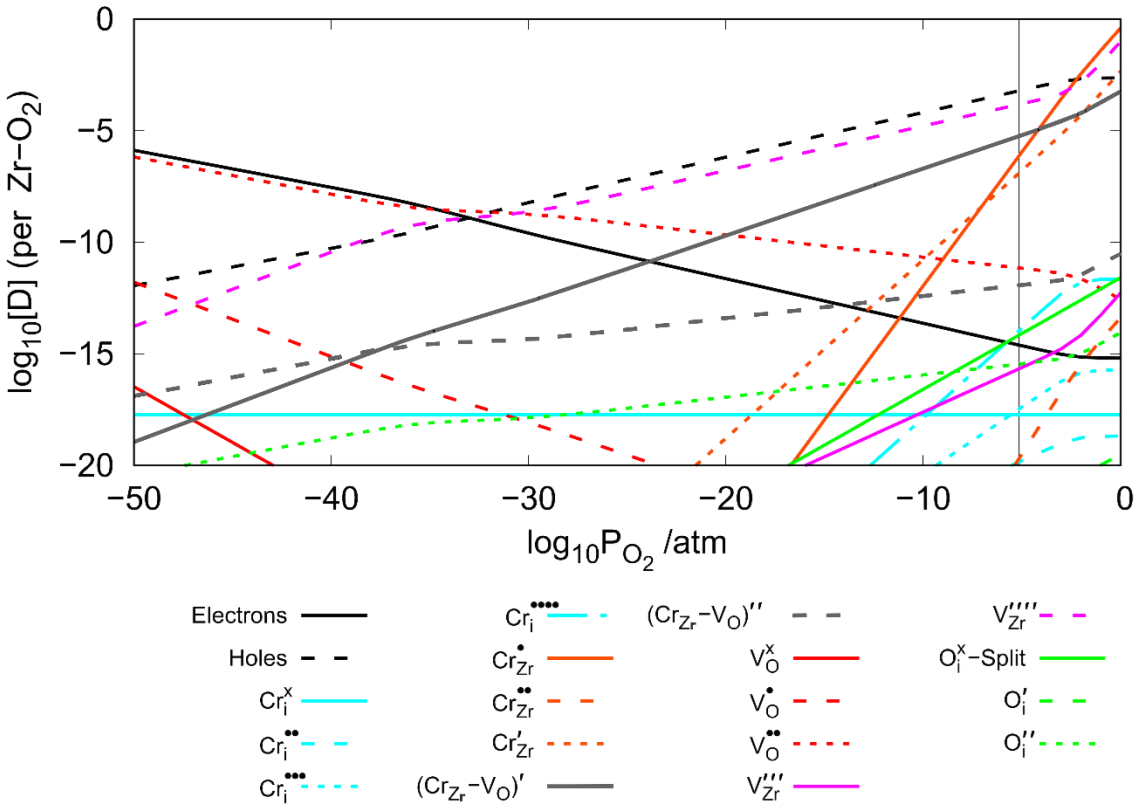

Figure 120 Brouwer diagram at 635 K with no fixed concentration of Cr and intrinsic defects in tetragonal ZrO_2.

For the Cr doped tetragonal ZrO_2 Brouwer diagram, Figure 120, the chromium interstitials have a low concentration throughout the oxide with small increases in concentration at higher partial pressures of charged interstitials. These appear to accommodate an increase of the negative two charged oxygen interstitial concentration (O_i''). The $(Cr_{Zr}:V_O)'$ follows the (V_{Zr}'''') defect in following the concentration of holes with an overall lower concentration. However, the (V_{Zr}'''') defect has an increased in concentration at the highest partial pressure when intersecting $(Cr_{Zr}^{\bullet})$ which coincides with a decrease of $(V_O^{\bullet\bullet})$ at the same partial pressure. The $(O_i^{\times} - \text{split})$ and the (V_{Zr}''') defects have no real change from intrinsic levels with the exception of a slight increase in (V_{Zr}''') at the highest partial pressure. The key difference from that of lithium defects here is that there is no fixed concentration for chromium. At high partial pressures, the $(Cr_{Zr}:V_O)'$ defect is found to be at 10^{-3} per ZrO_2. However, further into the oxide, this level drops off to ~10^{-19}. This would indicate that the chromium defects would be more likely to be found at the water oxide interface.

To visualise how the intrinsic defect concentrations change as a result of Cr, viewing the Brouwer diagram with the extrinsic defects hidden would allow for easier identification of intrinsic defect changes.

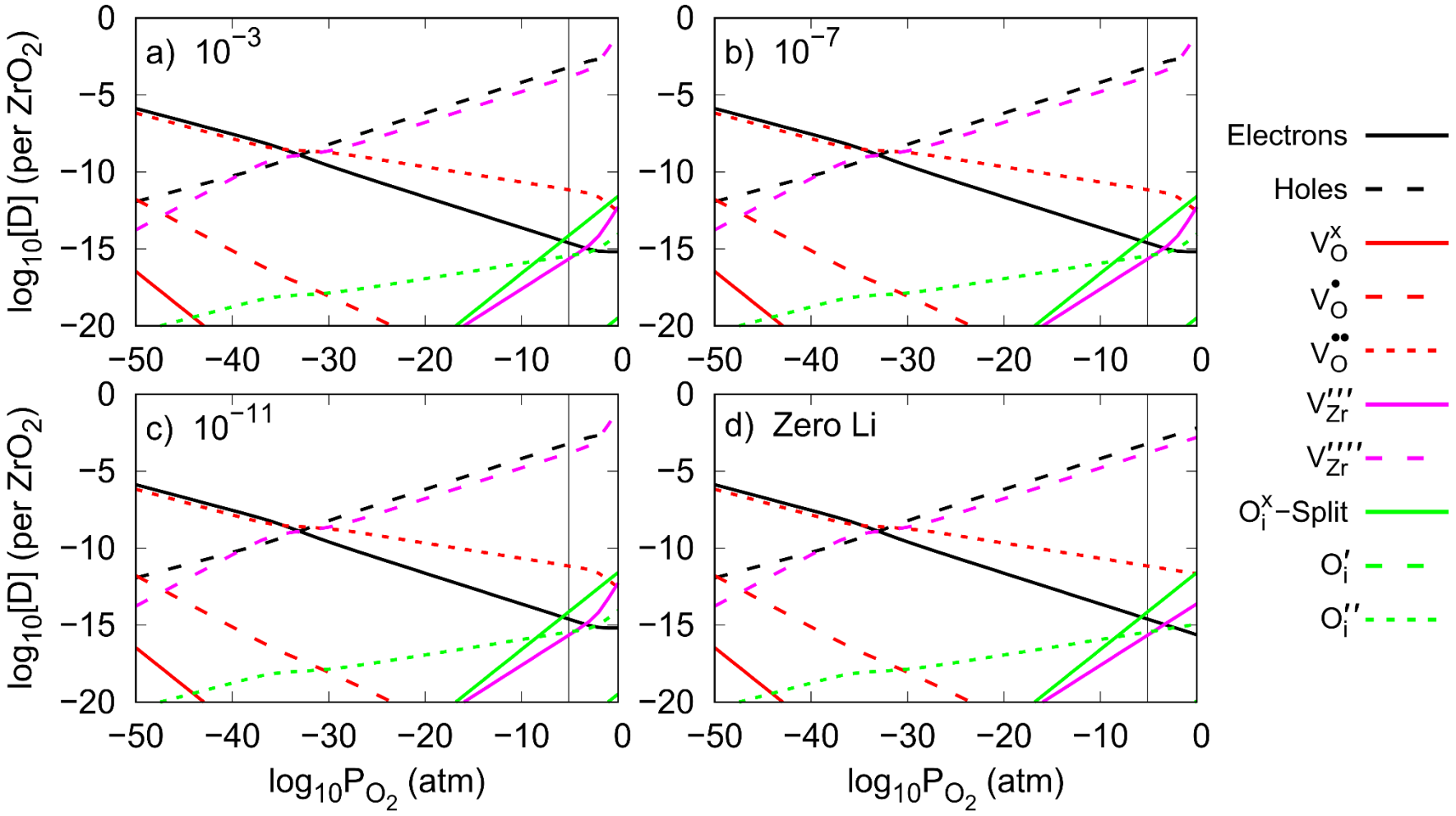

Figure 121 Cr doped tetragonal ZrO_2 Brouwer diagrams showing only intrinsic defects as a result of hidden Cr concentrations of a) 10^{-3} b) 10^{-7} c) 10^{-11} and d) with intrinsic defects only.

When the extrinsic defects are hidden from the Brouwer diagrams at 10^{-3}, 10^{-7} and 10^{-11}, it is clear that chromium defects have very little effect on the tetragonal structure with the exception of small changes at high partial pressures, Figure 121. This is due to very high chromium concentrations in this region, Figure 120. The minimal change in intrinsic defect concentrations is consistent across all Cr concentrations.

A.2. Fe Doped Tetragonal ZrO_2

Iron defects have been split into defect species due to the high number of defects that may feature in the Brouwer diagrams. Like the chromium defects, we have iron interstitials $(\mathrm{Fe_i})$, iron substitutions on zirconium sites $(\mathrm{Fe_{Zr}})$, the small cluster of an iron substitution on a zirconium site along with an oxygen vacancy $(\mathrm{Fe_{Zr}{:}\,V_O})$ and another small cluster of two iron substitutions on two zirconium sites along with a oxygen vacancy $(2\mathrm{Fe_{zr}{:}\,V_O})$. All formation energy diagrams across the bandgap show the defect species with a variation of charge. The first formation energy diagram shows the iron interstitials.

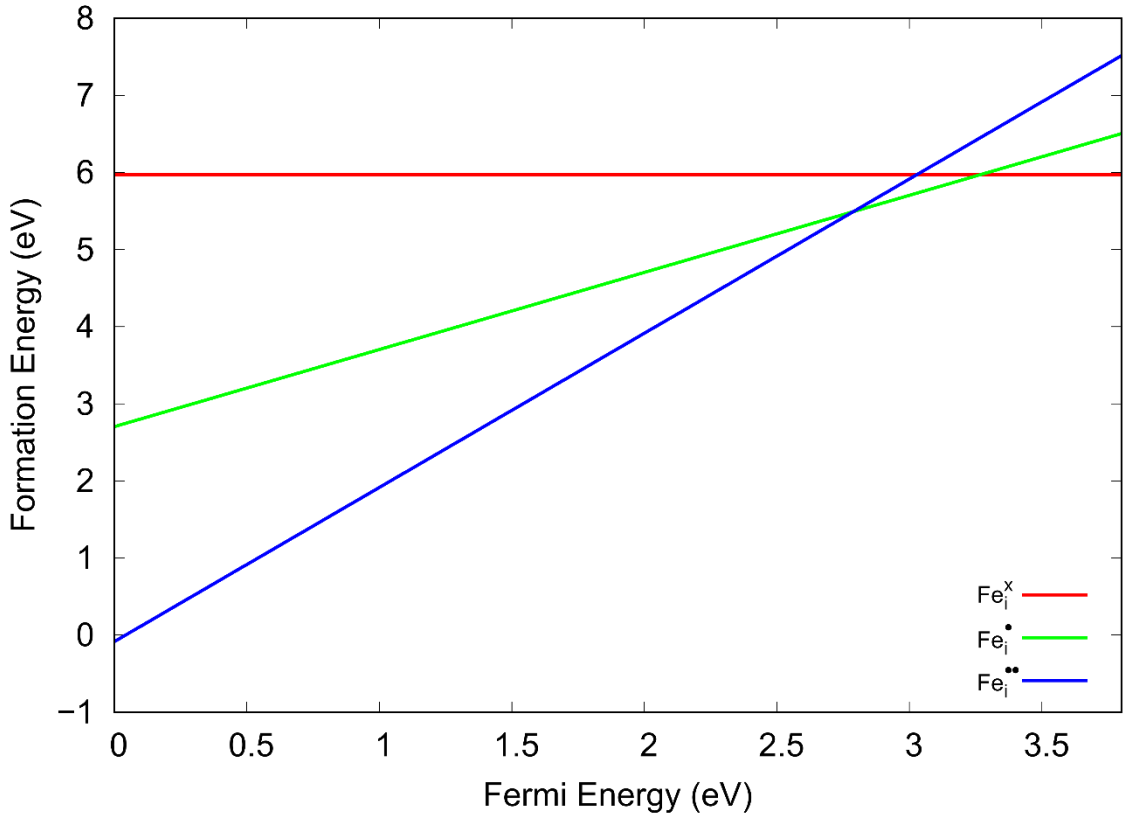

Figure 122 Formation energy of iron interstitial defects with a range of charges across the Fermi energy of the bandgap of tetragonal ZrO_2.

All the defect formation energies for the iron interstitials are well above zero with the exception of the positive two charged $(\mathrm{Fe_i^{\bullet\bullet}})$ which has a very small region at the top of the valence band to the left, Figure 122. Whilst it is not unheard of for defects to feature within the Brouwer diagram with positive formation energy values, the overall charge of the combined defects and formation energies need to be favourable for such a defect to be present.

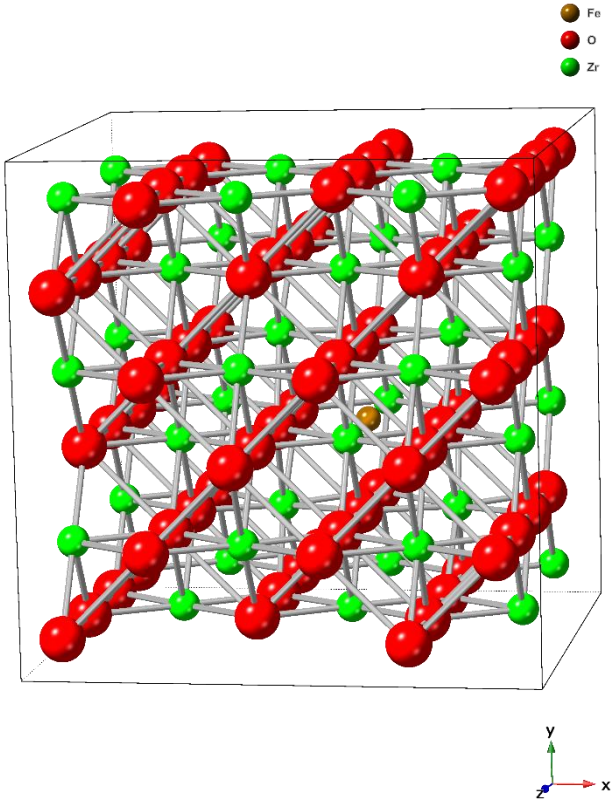

Figure 123 Tetragonal ZrO_2 structure with iron interstitial (gold) centre.

The iron interstitial defect in the tetragonal ZrO_2 structure (Figure 123) shows very little change in surrounding atomic positions when relaxed.

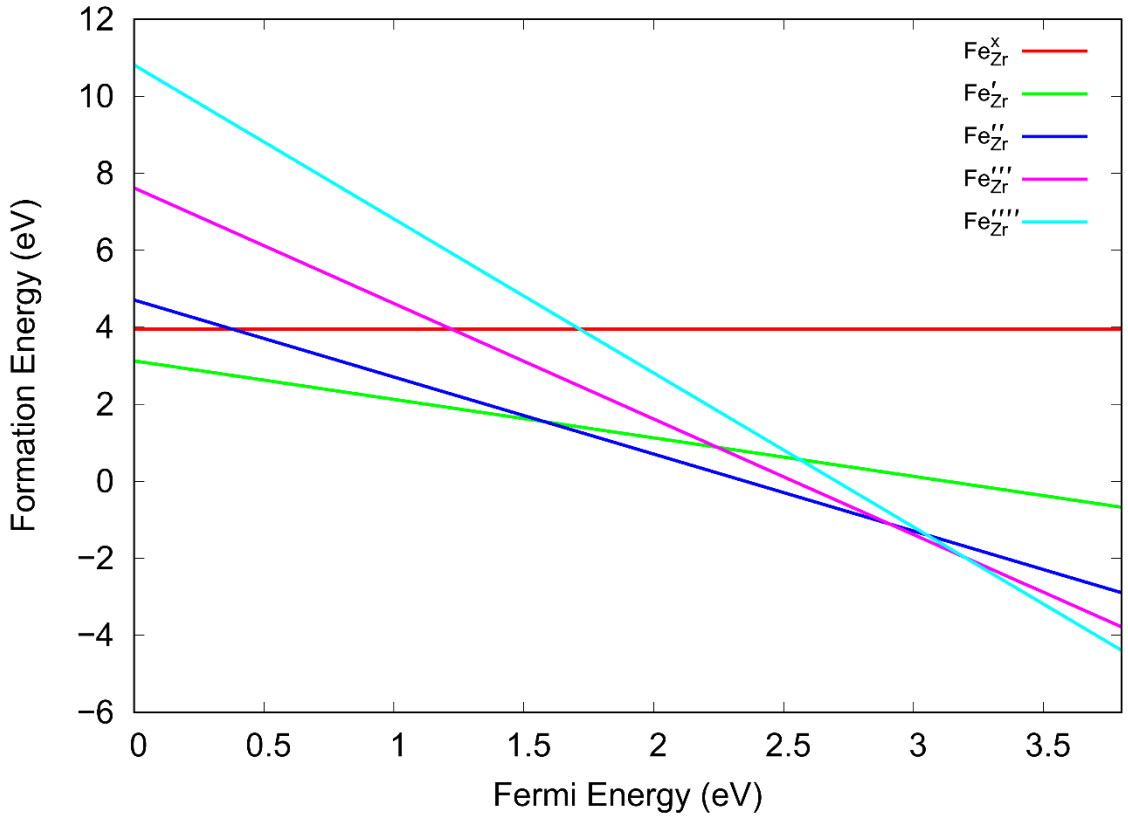

Figure 124 Formation energy of iron substitutions of zirconium defects with a range of charges across the Fermi energy of the bandgap of tetragonal ZrO_2.

Each of the Fe substitution on Zr site defects, with the exception of the neutral charged (Fe_{Zr}^{x}), holds a position of lowest formation energy across the bandgap, Figure 124. The (Fe_{Zr}^{x}) is also the only defect to consistently hold a positive formation energy at 4 eV. The remaining defects show a lower formation energy from the top of the valence band to the left with (Fe_{Zr}') and then moving to the bottom of the conduction band to the right we have (Fe_{Zr}''), then (Fe_{Zr}''') and finally (Fe_{Zr}''''). These defects all hold a negative formation energy towards the conduction band and a positive formation energy towards the valence band. Where the Fermi energy is below 2 eV, all substitution defects have a positive formation energy.

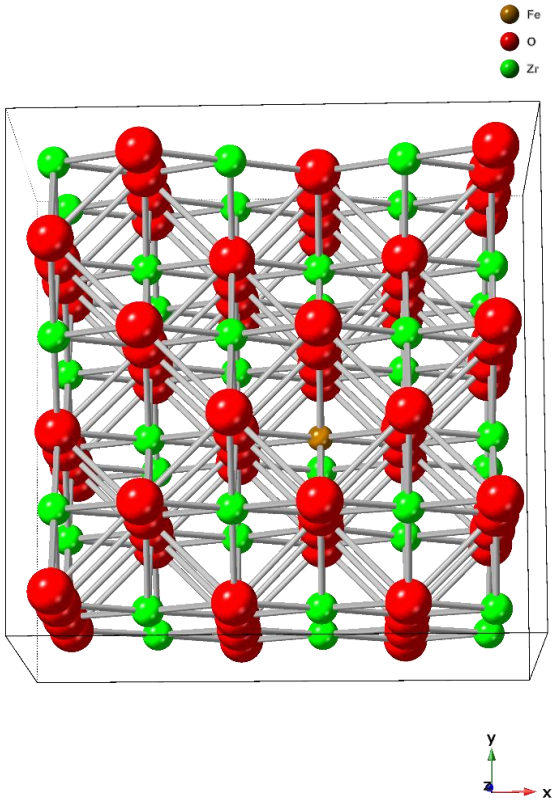

Figure 125 Tetragonal ZrO_2 structure with an iron interstitial on a zirconium site (gold) centre.

Much like the iron interstitial defect in the tetragonal ZrO_2 structure, the iron substitution on a zirconium site (Figure 125) also causes very little variation in intrinsic atomic position when relaxed. There does appear to be a small attraction of nearest neighbour oxygen atoms around the iron substitution but is minimal. This is likely due to ionic bonding of the closest surrounding oxygen atoms to the iron atom.

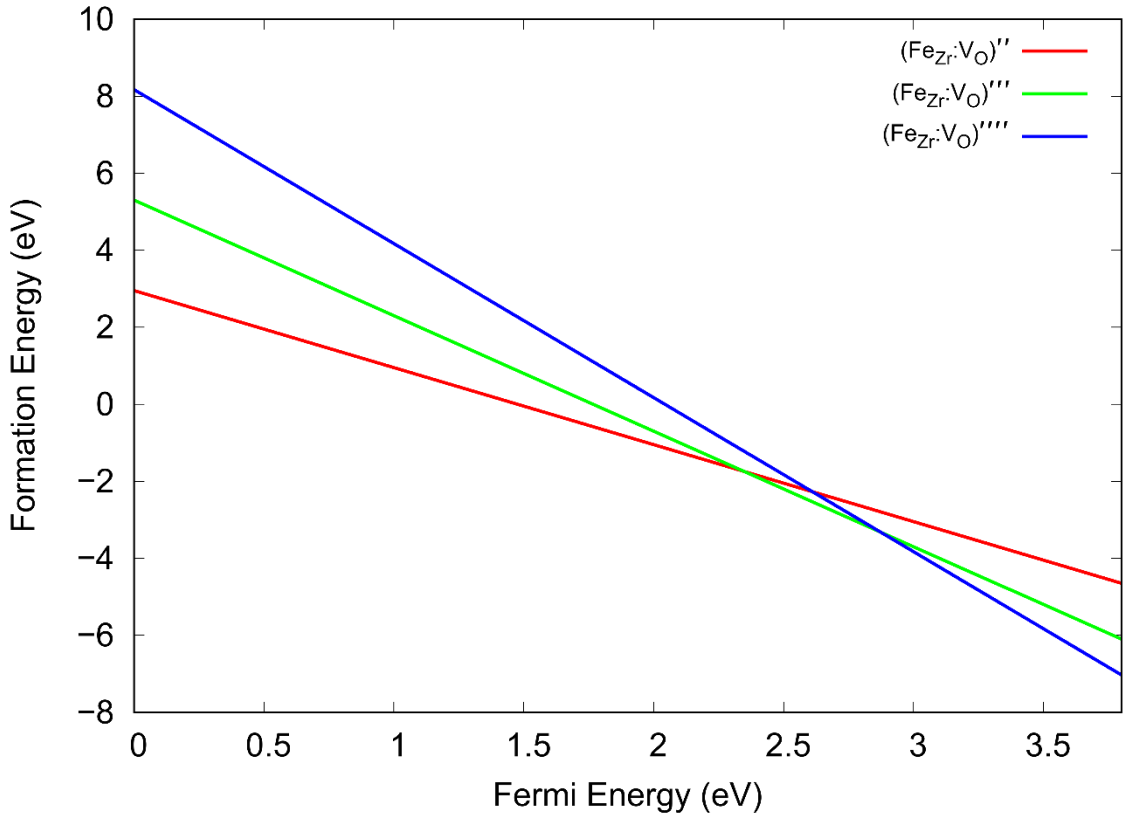

Figure 126 Formation energy of iron substitutions on zirconium sites with an oxygen vacancy defect with a range of charges across the Fermi energy of the bandgap of tetragonal ZrO_2.

For the small cluster of an Fe substitution on a Zr site and an oxygen vacancy, Figure 126, the neutral and negative one charged clusters had an energy which placed these defects outside of the bandgap and were no longer considered. To the left at the top of the valence band, all defects hold a positive formation energy. Above 2 eV, all defects have a negative formation energy, and all have a lower formation energy than the other defects for the remainder of the Fermi energy. First, the $(\mathrm{Fe_{Zr}}:\mathrm{V_O})''$ holds the lowest formation energy from the top of the valence band to the left. This is then replaced by the $(\mathrm{Fe_{Zr}}:\mathrm{V_O})'''$ briefly at around 2.5 eV. This is finally replaced by the $(\mathrm{Fe_{Zr}}:\mathrm{V_O})''''$ for the remainder of the bandgap towards the bottom of the conduction band to the right.

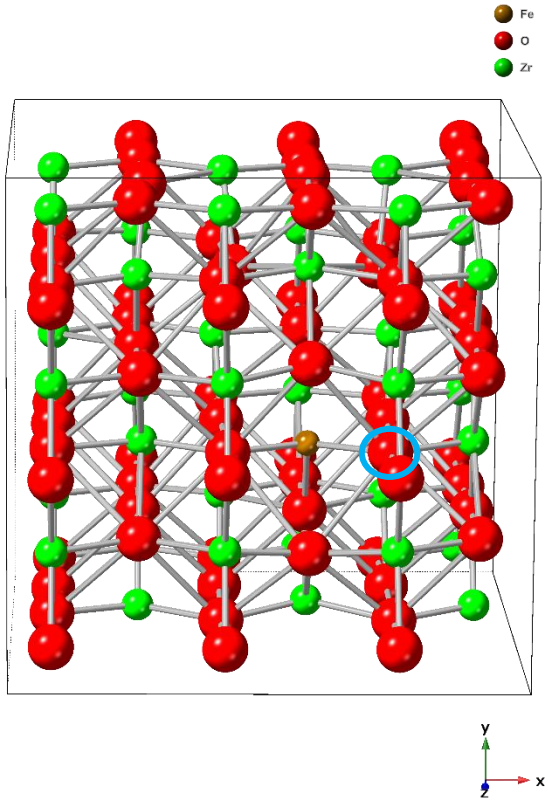

Figure 127 Tetragonal ZrO_2 structure with an iron substitution on a zirconium site and an oxygen vacancy.

The iron substitution on a zirconium site with an oxygen vacancy (Figure 127) shows little intrinsic atomic position changes around the substitution. The oxygen atoms surrounding the oxygen vacancy site, however, have shown slight position changes (Circled in blue).

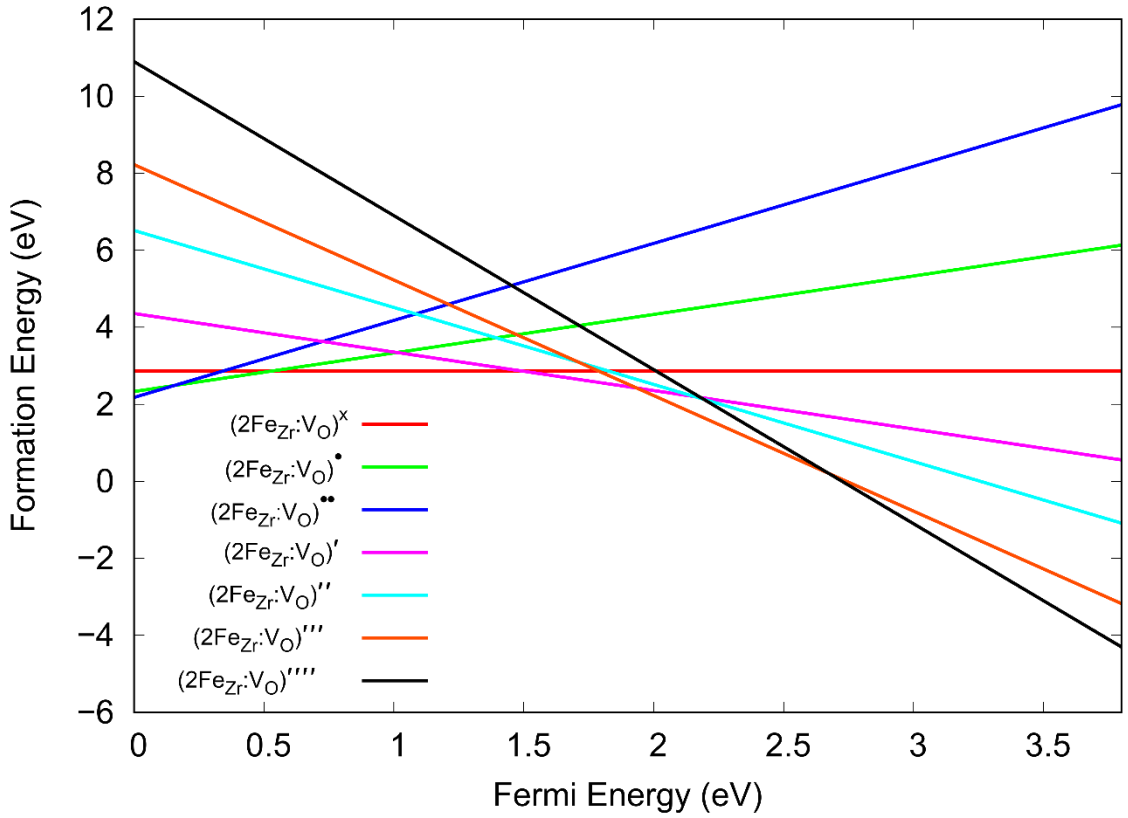

Figure 128 Formation energy of two iron substitutions on a zirconium site with an oxygen vacancy defect with a range of charges across the Fermi energy of the bandgap of tetragonal ZrO_2

Finally, the small cluster of two substitute Fe on two Zr sites with an oxygen vacancy $(2\mathrm{Fe_{Zr}}:\mathrm{V_O})$, Figure 128. Here, all charged defects were within the bandgap during the calculation, and not only this, but each defect at one point has the lowest formation energy with only the exception of the negative two charged $(2\mathrm{Fe_{Zr}}:\mathrm{V_O})''$. However, only three charges (minus two, three and four) have a negative formation energy, all of which are above 2.5 eV in the Fermi energy towards the bottom of the conduction band to the right. Starting from the top of the valence band to the left, the plus two charged defect $(2\mathrm{Fe_{Zr}}:\mathrm{V_O})^{\bullet\bullet}$ has the lowest formation energy but is quickly replaced by the plus one charged $(2\mathrm{Fe_{Zr}}:\mathrm{V_O})^{\bullet}$ for a short time, again, before being replaced by the neutral charged $(2\mathrm{Fe_{Zr}}:\mathrm{V_O})^{\times}$. The negative one charged defect $(2\mathrm{Fe_{Zr}}:\mathrm{V_O})'$ has the lowest formation energy at about 1.5 eV, but this defect, along with all already mentioned, do not have a negative formation energy. From here, just below 2 eV, the negative three defect has the lowest formation energy until just below 2.5 eV where the negative four $(2\mathrm{Fe_{Zr}}:\mathrm{V_O})''''$ has the lowest formation energy for the remainder of the bandgap.

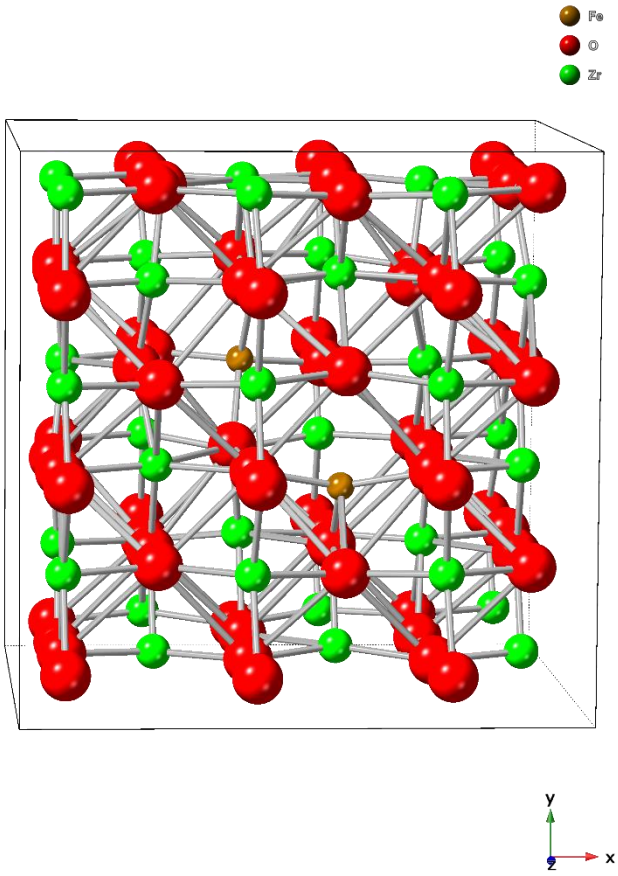

Figure 129 Tetragonal ZrO_2 structure with two iron substitutions to zirconium sites and an oxygen vacancy.

The two iron substitutions on zirconium sites with an oxygen vacancy cluster defect (Figure 129) is surprising in how little the intrinsic atomic positions change when comparing this to the single iron substation with an oxygen vacancy structure when relaxed. Whilst there are small atomic position movements, they are not as severe as those found in the later.

When calculating the Brouwer diagram from the introduced iron defects, there were a number of surprises when considering the formation energy trends in relation to Fermi energy.

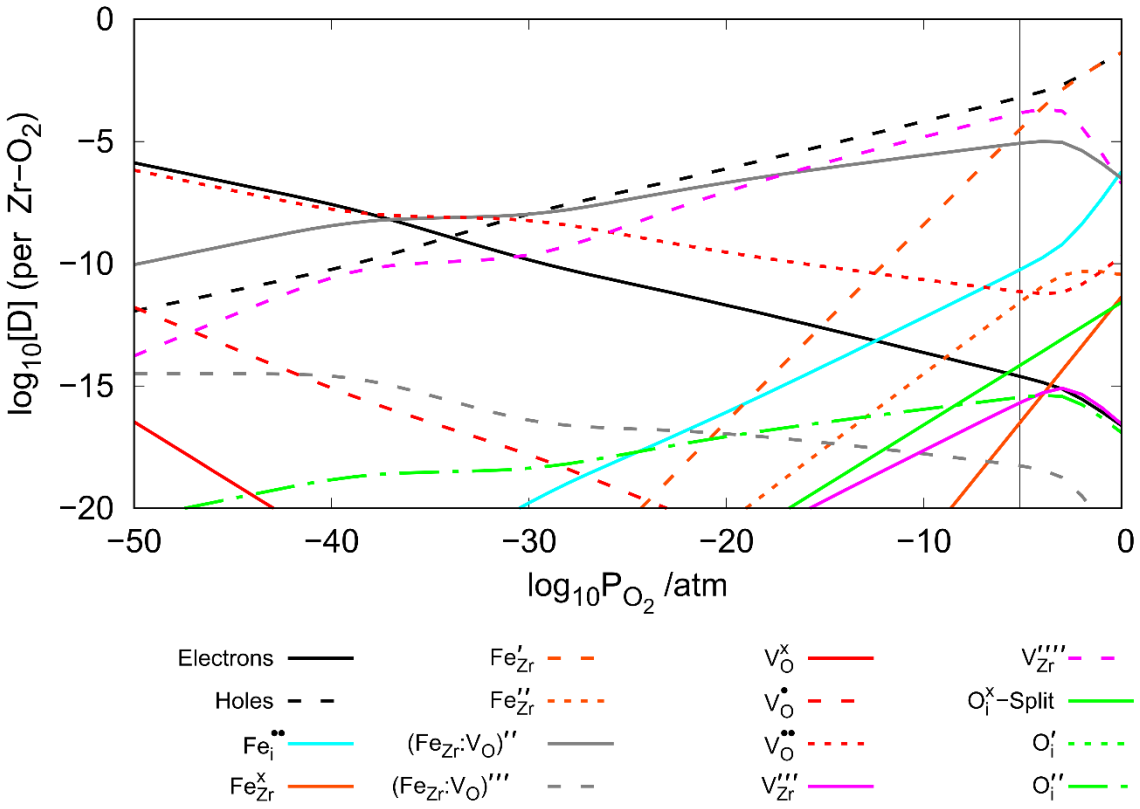

Figure 130 Brouwer diagram at 635 K with no fixed concentration of Fe and intrinsic defects in tetragonal ZrO_2.

A stipulated Fe defect concentration was not held throughout the partial pressure range where there was a drop in overall iron concentration with a reduction in the partial pressure of oxygen, Figure 130. The Fe defects have minimal impact on the intrinsic defects for most of the partial pressures of oxygen with large changes in intrinsic defects only at the highest partial pressure of oxygen to the right. What is more surprising is that a number of defects that were expected to be present due to negative formation energies are not present such as all of the $(2\mathrm{Fe_{Zr}}\mathrm{:V_O})$ defects. Other defects that were not present that all held a negative formation energy towards the conduction band were $(\mathrm{Fe_{Zr}}\mathrm{:V_O})''''$, $(\mathrm{Fe'''_{Zr}})$ and $(\mathrm{Fe''''_{Zr}})$. A defect that was present in the Brouwer diagram that was not expected due to a positive formation energy had a lower formation energy towards the valence band which was $(\mathrm{Fe'_{Zr}})$. The neutral charged $(\mathrm{Fe^{\times}_{Zr}})$ shows at the highest partial pressure of oxygen to the right of the Brouwer diagram in small concentrations. However, the formation energy across the Fermi energy maintained a positive 4 eV without having the lowest formation energy of the species at any point. The $(\mathrm{Fe_{Zr}}\mathrm{:V_O})''$ small cluster has the highest concentration of the Fe defects shown in the Brouwer diagram which has a negative formation energy towards the mid Fermi energy but has a positive formation energy towards the valence band. The next two higher concentration Fe defects also follow this trend in formation energy and are shown at higher partial pressures to the right and are the $(\mathrm{Fe^{\bullet\bullet}_i})$ and the $(\mathrm{Fe''_{Zr}})$ defects. Finally, at lower concentration of the Brouwer diagram, the defect $(\mathrm{Fe_{Zr}}\mathrm{:V_O})'''$ has higher concentrations towards the lower partial pressures to the left but lowers at higher partial pressures to the right. This defect holds a negative formation energy towards the conduction band.

As with the Cr Brouwer diagram, it can be difficult to see the effects of Fe on intrinsic defects due to the number of defects present which can obscure changes. For the same reason, the Fe defects in the following diagram are hidden.

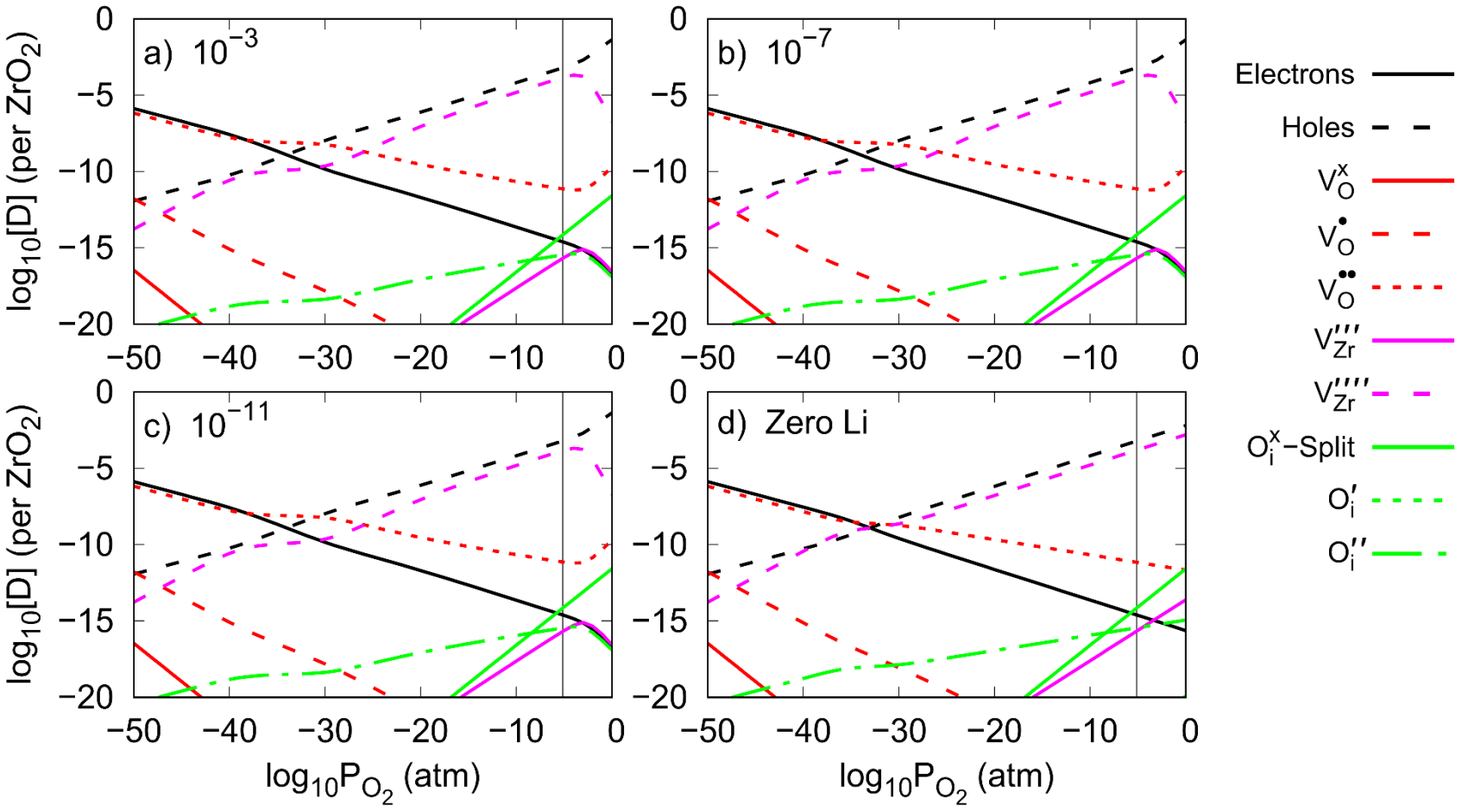

Figure 131 Fe doped tetragonal ZrO_2 Brouwer diagrams showing only intrinsic defects as a result of Fe concentrations of a) 10^{-3} b) 10^{-7} c) 10^{-11} and d) with hidden Fe defects showing intrinsic defects only. The vertical black line represents the water oxide interface.

As with the Cr defect Brouwer diagram, the Fe defects show minimal changes to intrinsic defects within the oxide, Figure 131. Most changes occur at partial pressures greater than that of the calculated water oxide interface. However, there is a small deviation in concentrations for electrons, $(V_O^{\bullet\bullet})$ and $(V_{Zr}^{''''})$ at the partial pressure of oxygen of around -30 on the diagram. This shows a small region with a slight increase in $(V_O^{\bullet\bullet})$ and a slight decrease of electrons and $(V_{Zr}^{''''})$ concentrations. These changes can all be attributed to the $(Fe_{Zr}:V_O)''$ defect that converges with these defects at the point of deviation. The $(Fe_{Zr}:V_O)''$ defect increases the $(V_O^{\bullet\bullet})$ due to an increase in negative charge increase associated with the $(Fe_{Zr}:V_O)''$. This, in turn, causes a decrease in the negatively charged electrons and $(V_{Zr}^{''''})$. Once the $(Fe_{Zr}:V_O)''$ defect converges with the hole concentration, the $(V_O^{\bullet\bullet})$ coupling with the $(Fe_{Zr}:V_O)''$ is released and the intrinsic defects resume to normal concentrations.

A.3. Sn Doped Tetragonal ZrO_2

The last defect to be reviewed in Zircaloy-4 is tin. Similarly, to Li, Cr, and Fe, the reviewed defects were interstitials (Sn_i), tin substitutions on zirconium sites (Sn_{Zr}), the small cluster of tin on a zirconium site substitution with a oxygen vacancy $(Sn_{Zr}:V_O)$, and finally the two tin substitutions on two zirconium sites with a oxygen vacancy $(2Sn_{Zr}:V_O)$. The later, however, did not produce formation energies within the bandgap during the calculations and were omitted from further calculations when producing the Brouwer diagrams.

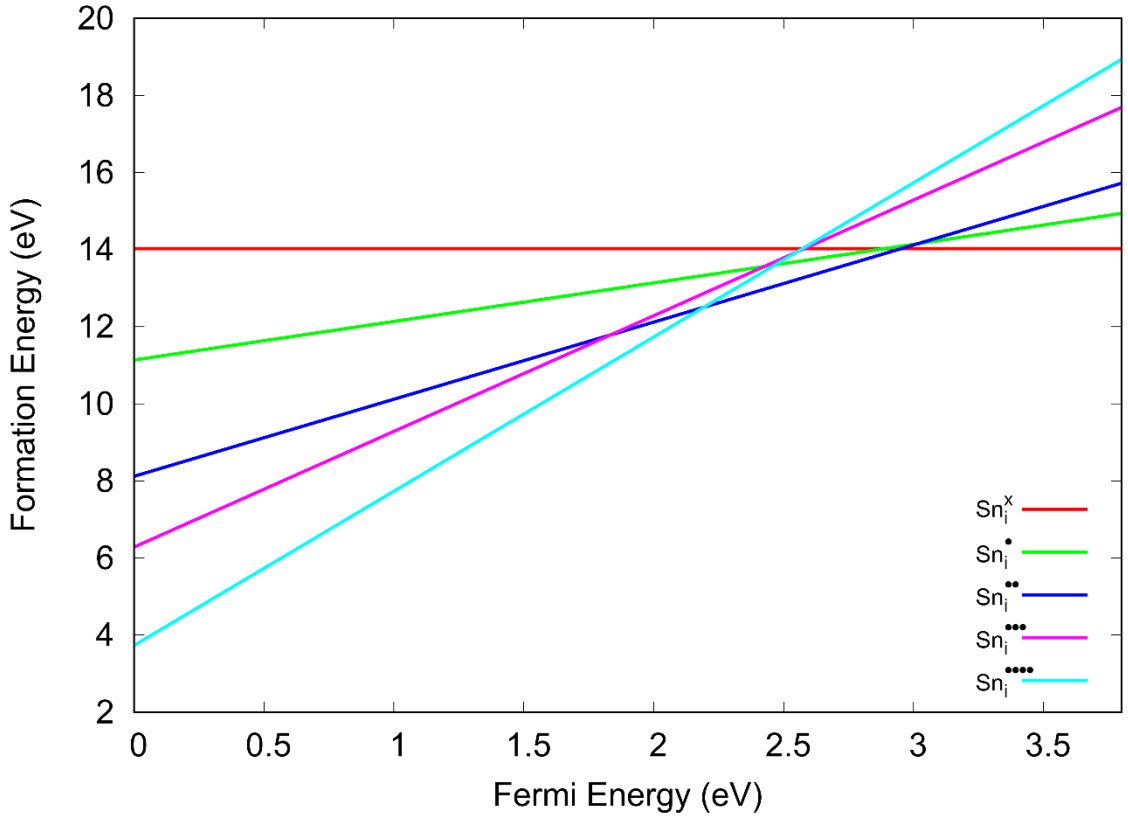

Figure 132 Formation energy of tin interstitial defects with a range of charges across the Fermi energy of the bandgap of tetragonal ZrO_2.

For the tin interstitials, Figure 132, there were no defects with a negative formation energy. The lowest formation energy came from the plus 4 charged interstitial $(Sn_{Zr}^{\bullet\bullet\bullet\bullet})$ from the top of the valence band up to, just above, 2 eV. Between 2 and 3 eV, the plus two charged $(Sn_{Zr}^{\bullet\bullet})$ has the lowest formation energy and, finally, the neutral charged $(Sn_{Zr}^{\times})$ has the lowest formation energy

towards the bottom of the conduction band. The formation energies are very high, particularly for the neutral charged $(Sn_{Zr}^{\times})$ which maintains a 14 eV formation energy across the bandgap.

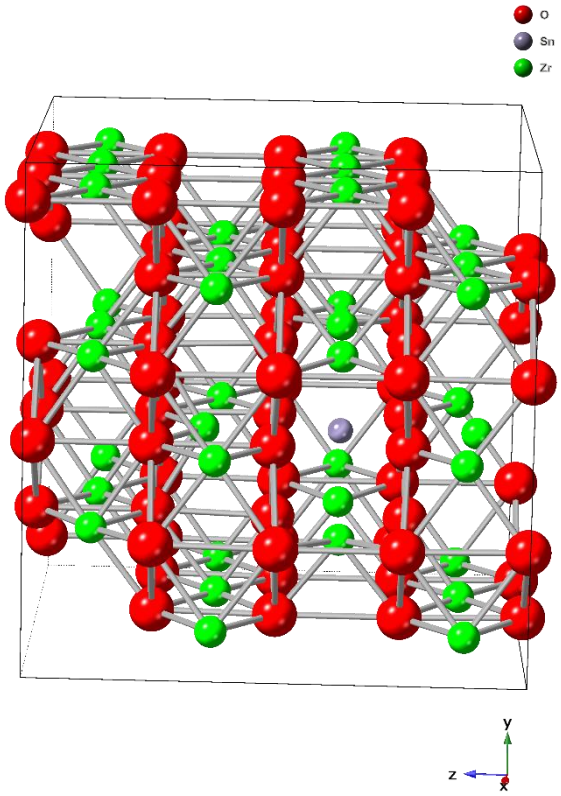

Figure 133 Tetragonal ZrO_2 structure with a tin interstitial (purple) centre.

When viewing the tin interstitial in a tetragonal ZrO_2 structure (Figure 133), there are small variations in surrounding oxygen atoms. What makes tin unique in the defects reviewed is that all nearest neighbour zirconium atoms show a position repulsion to the tin, unlike the lithium, chromium and iron interstitials.

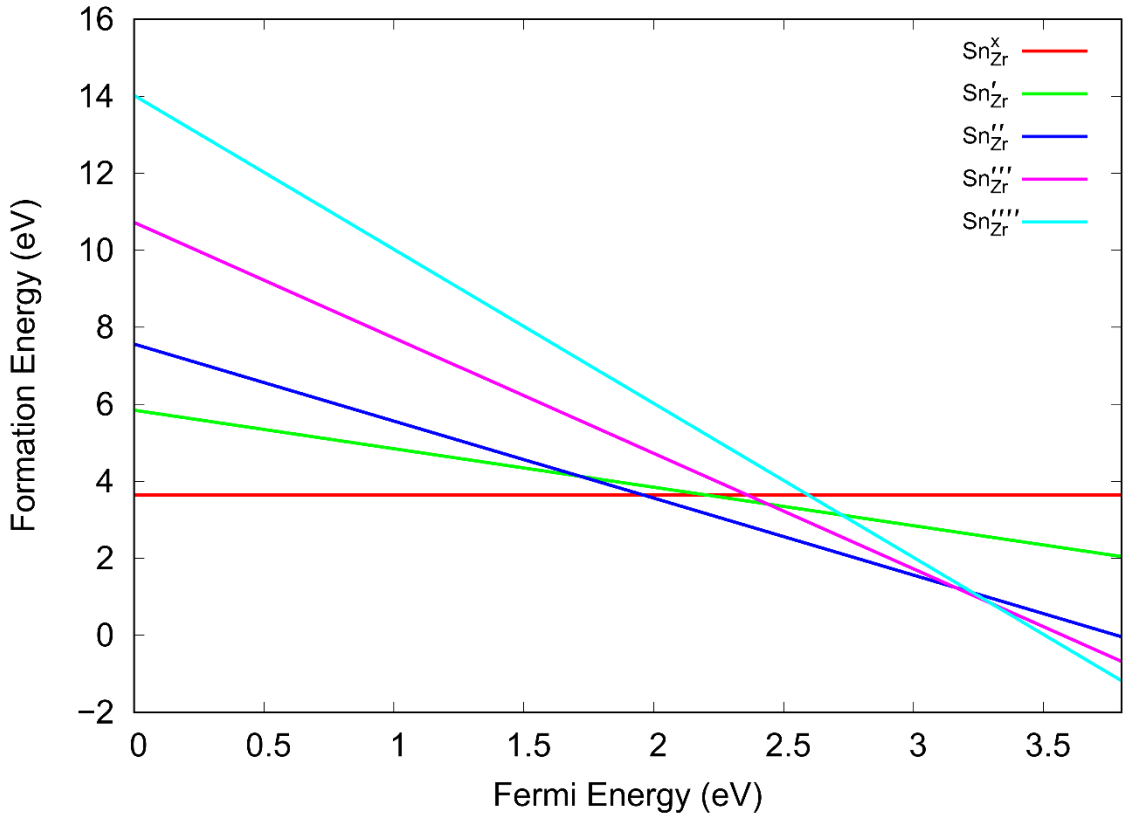

Figure 134 Formation energy of tin substitutions of zirconium defects with a range of charges across the Fermi energy of the bandgap of tetragonal ZrO_2.

For the tin substitution on a zirconium site (Sn_{Zr}) defect, *Figure 134*, the natural charged defect $(Sn_{Zr})^{\times}$ has the lowest formation energy towards the top of the valence band to the left and holds a consistent energy below 4 eV for the entirety of the bandgap. The negative one charged defect $(Sn_{Zr})'$ does not have the lowest formation energy at any point. At around 2 eV Fermi level, the negative two charged defect has the lowest formation energy at the middle of the bandgap. For a very brief Fermi energy between 3 and 3.5 eV, the negative three charged defect has the lowest formation energy but is quickly replaced by the negative four charged $(Sn_{Zr})''''$ defect towards the bottom of the conduction band to the right. Only the negative three and four defects have a negative formation energy towards the bottom of the conduction band to the right.

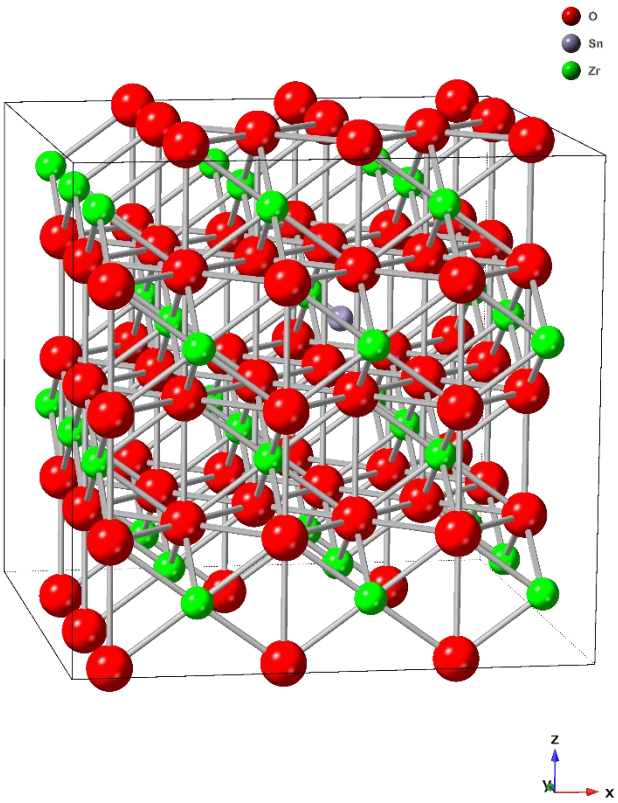

Figure 135 Tetragonal ZrO_2 structure with a tin substitution on a zirconium site.

The tin substitution on a zirconium site (Figure 135) shows very little change in surrounding atomic location when relaxed.

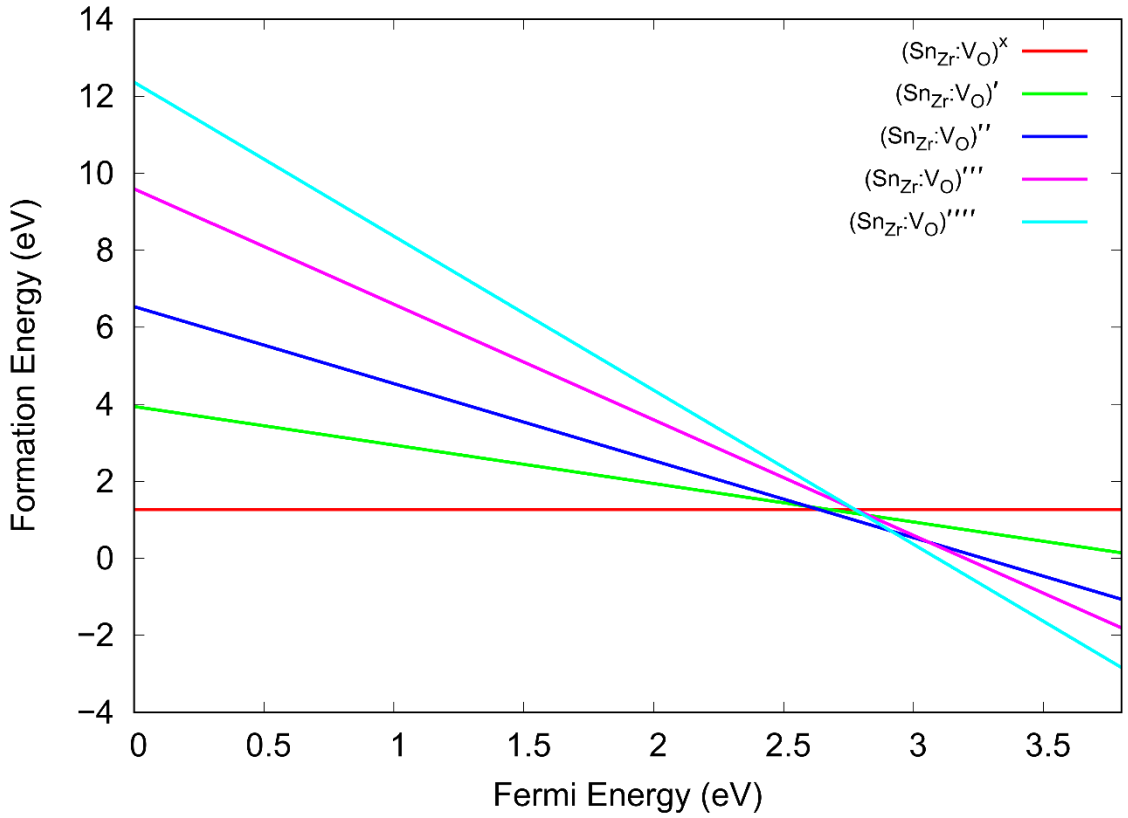

Figure 136 Formation energy of tin substitutions on zirconium sites with an oxygen vacancy defect with a range of charges across the Fermi energy of the bandgap of tetragonal ZrO_2.

The formation energies for the small cluster of a tin substitute to a zirconium atom combined with an oxygen vacancy $(\mathrm{Sn_{Zr}}:\mathrm{V_O})$ shows more promise with relatively lower formation energies than that of the other tin defects reviewed previously, Figure 136. At the top of the valence band to the left, the neutral charged cluster $(\mathrm{Sn_{Zr}}:\mathrm{V_O})^{\times}$ has the lowest formation energy but remains in positive values. Just above 2.5 eV Fermi energy has the negative two cluster $(\mathrm{Sn_{Zr}}:\mathrm{V_O})''$ which is quickly replaced by the negative four $(\mathrm{Sn_{Zr}}:\mathrm{V_O})''''$ cluster to the bottom of the conduction band to the right. Only the negative two, three and four charged defect clusters show a negative formation energy, all of which are towards the bottom of the conduction band to the right.

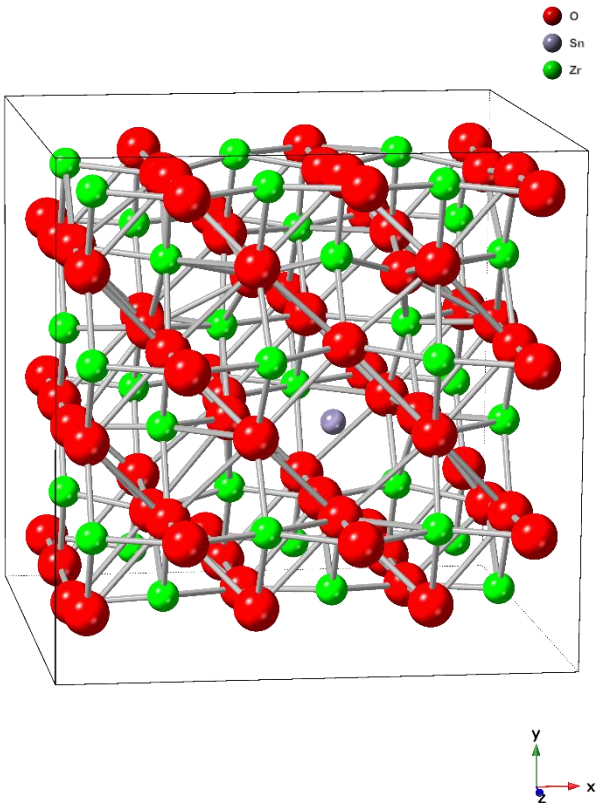

Figure 137 Tetragonal ZrO_2 structure with a tin substitution on a zirconium site with a oxygen vacancy.

When viewing the defect within the relaxed structure (Figure 137), again, the tin interstitial shows little change in intrinsic atom position. There are, however, changes in oxygen position as a result of the oxygen vacancy association with the defect cluster.

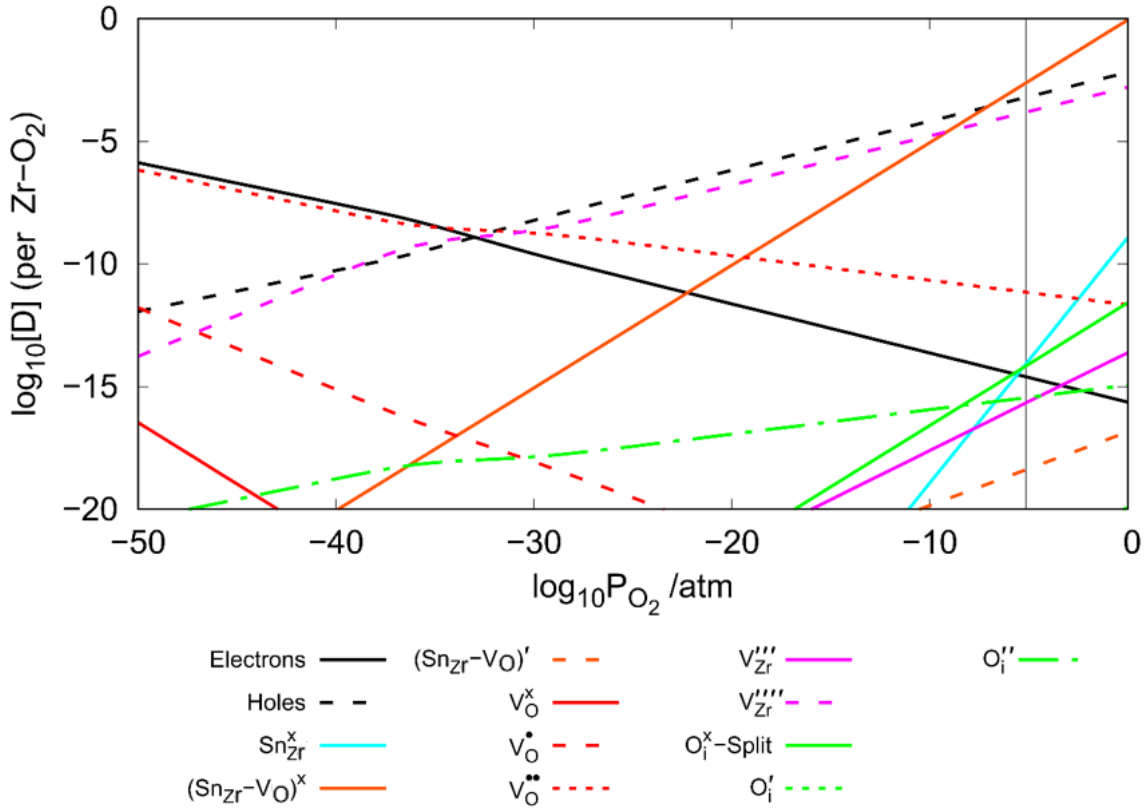

Figure 138 Brouwer diagram at 635 K without a fixed concentration of Sn and intrinsic defects in tetragonal ZrO_2.

The Brouwer diagram of 10^{-3} concentration tin defects in zirconium oxide at 635 K shows only three defects, Figure 138. These defects are the neutral charged tin substitute ($\mathrm{Sn}_{\mathrm{Zr}}^{\times}$), the neutral charged small cluster $(\mathrm{Sn}_{\mathrm{Zr}}{:}\,\mathrm{V}_{\mathrm{O}})^{\times}$ and the negative one charged small cluster $(\mathrm{Sn}_{\mathrm{Zr}}{:}\,\mathrm{V}_{\mathrm{O}})'$. Unsurprisingly, the neutral charged defects do not affect the intrinsic defects a great deal in respect to charge neutrality and the negative charged cluster $(\mathrm{Sn}_{\mathrm{Zr}}{:}\,\mathrm{V}_{\mathrm{O}})'$ is at very low concentrations and at high partial pressures of oxygen to the right. The tin defect with the highest concentration is the neutral charged cluster $(\mathrm{Sn}_{\mathrm{Zr}}{:}\,\mathrm{V}_{\mathrm{O}})^{\times}$. Again, like iron and chromium, the tin concentration was not stipulated. As such, the dopant concentration was allowed to reach both the highest and the lowest concentrations visible on the plot (0 to 10^{-20}). This does give an indication that tin is unlikely to have any effect on the intrinsic defects within ZrO_2.

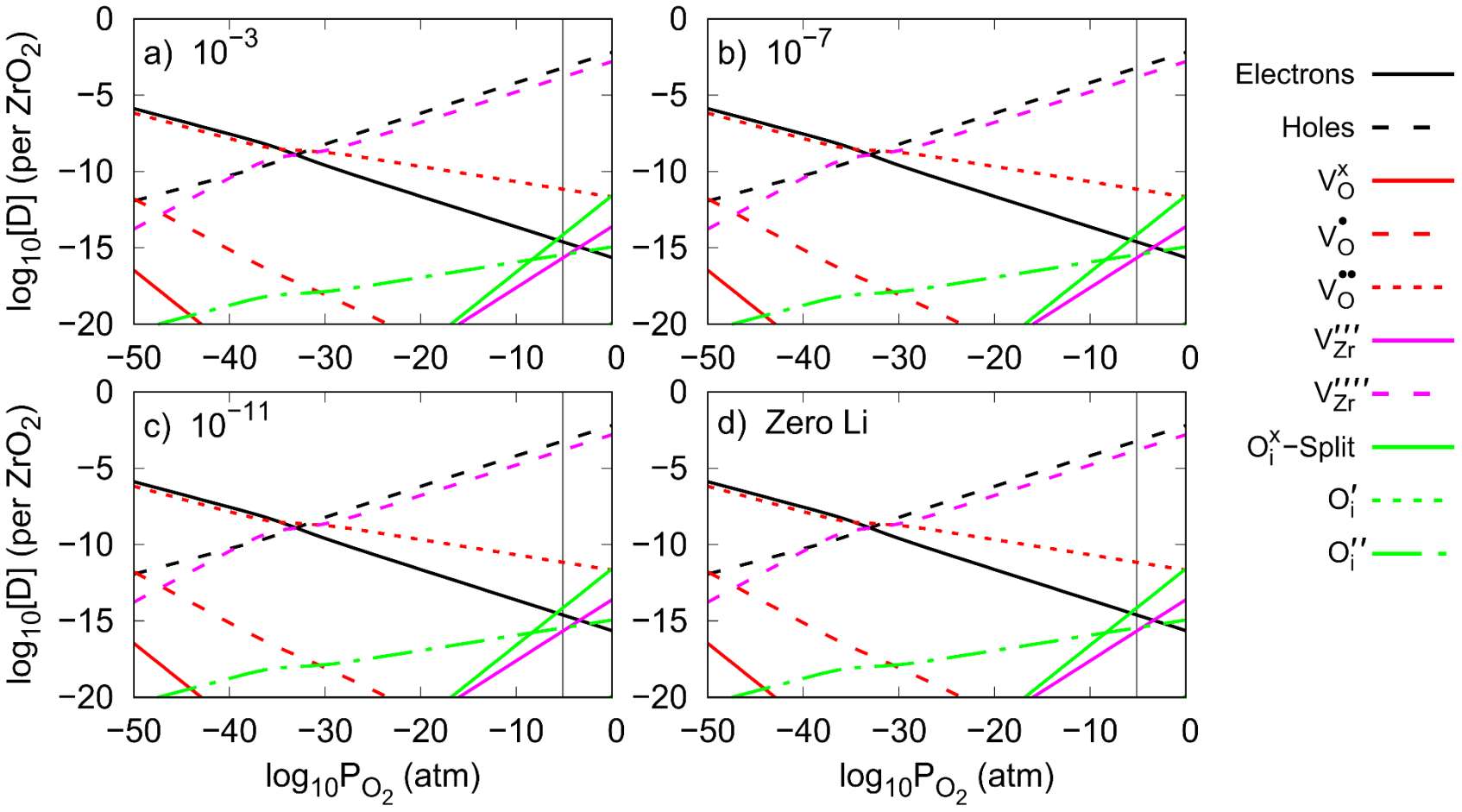

Figure 139 Sn doped tetragonal ZrO_2 Brouwer diagrams showing only intrinsic defects as a result of Sn concentrations of a) 10^{-3} b) 10^{-7} c) 10^{-11} and d) with intrinsic defects only. The vertical black line represents the water oxide interface.

For the sake of completion, the Brouwer diagrams of tin defects at the concentrations of 10^{-3}, 10^{-7}, 10^{-11} and intrinsic defects only is given with the tin defects hidden so that any affect from tin might be more readily observed, Figure 139. It is, however, clear that no changes in intrinsic defect concentration can be seen as a result of tin.

A.4. Combined Dopant Tetragonal ZrO_2

Plotting all expected defects in one Brouwer diagram may offer a more accurate indication of possible defect concentrations. In particular, for our investigation, we are interested in the concentration of oxygen as we try to understand the mechanisms of corrosion. Understandably, combining all defects will result in a very difficult to read Brouwer diagram. It is required, however, to show such a complicated Brouwer diagram to highlight changes in intrinsic defect concentrations. The complexity may then be peeled away to gain an idea of where the change of lithium concentration may influence the intrinsic defect concentrations whilst also effected by alloying additions.

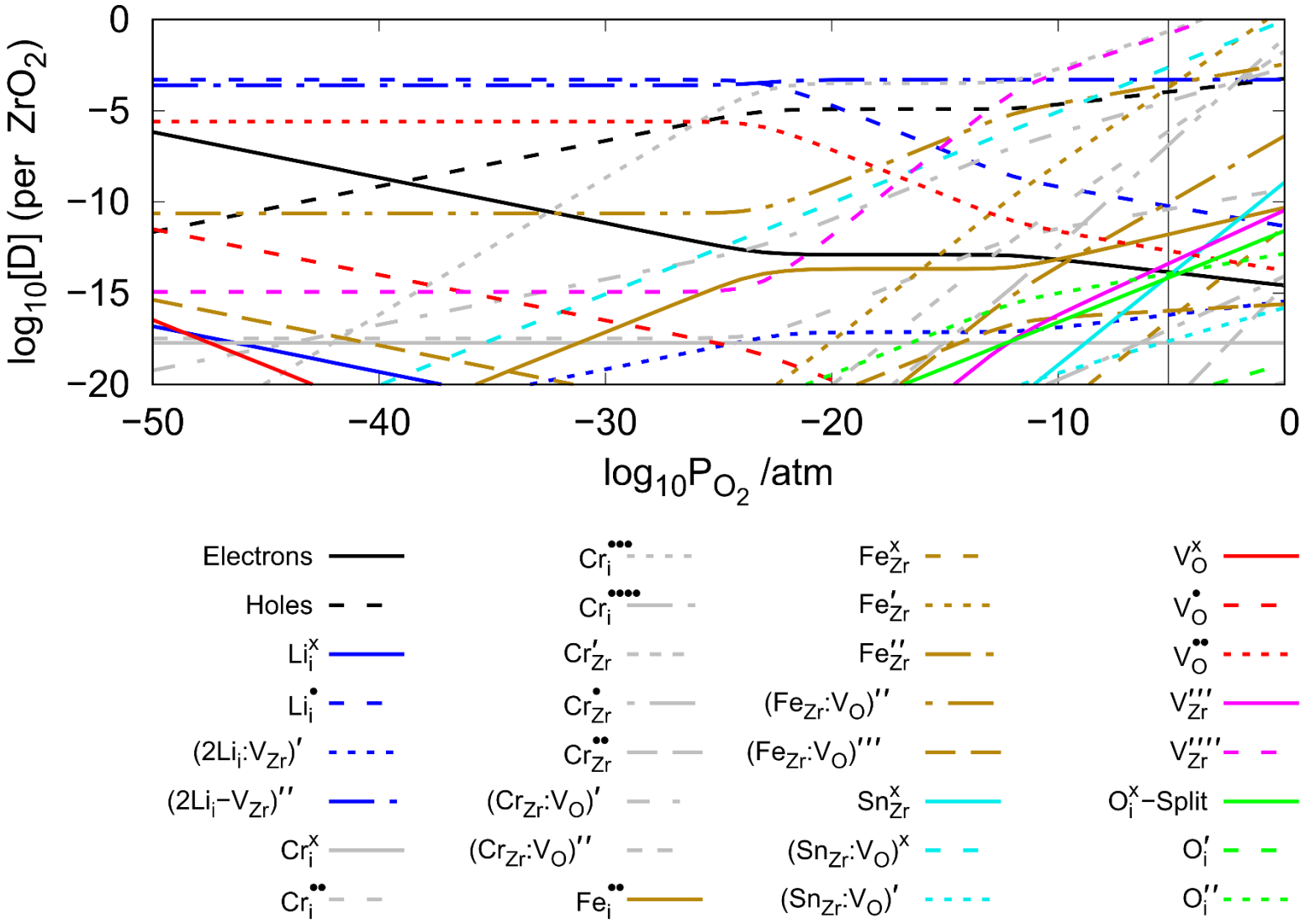

Figure 140 Brouwer diagram with defects with a defect concentration of 10-3 Li, 5.7 x 10^{-4} Cr, 1.47 x 10^{-3} Fe, 15.62 x 10^{-3} Sn at 635 K

The chromium, iron and tin defect concentrations in Zircaloy-4 are given as 1.2 wt% Sn, 0.2 wt% Fe and 0.1 wt% Cr [178], Figure 140. These correspond to 0.01562 Sn, 0.00147 Fe and 0.00057 Cr atoms per ZrO_2. The lithium defects are given as 0.001 (10^{-3}) per ZrO_2 and will be the only dopant concentration that will be changed for the remainder of the chapter. Because Sn has provided little change to intrinsic defects previously, this was the first defect that we looked at. The Sn substitution to a Zr site and the negative one charged cluster $(\mathrm{Sn_{Zr}}:\mathrm{V_O})'$ have low concentrations at high partial pressure to the right and have very little impact on other defect concentrations. The neutral cluster $(\mathrm{Sn_{Zr}}:\mathrm{V_O})^{\times}$ is has low concentrations at low partial pressures and increases to very high concentrations at high partial pressure. This defect, however, shows no change in any other defect and shows a linear increase in concentration from -40 to 0 partial pressures. The Sn defects could, subsequently, be hidden to gain a little more clarity on the other defects.

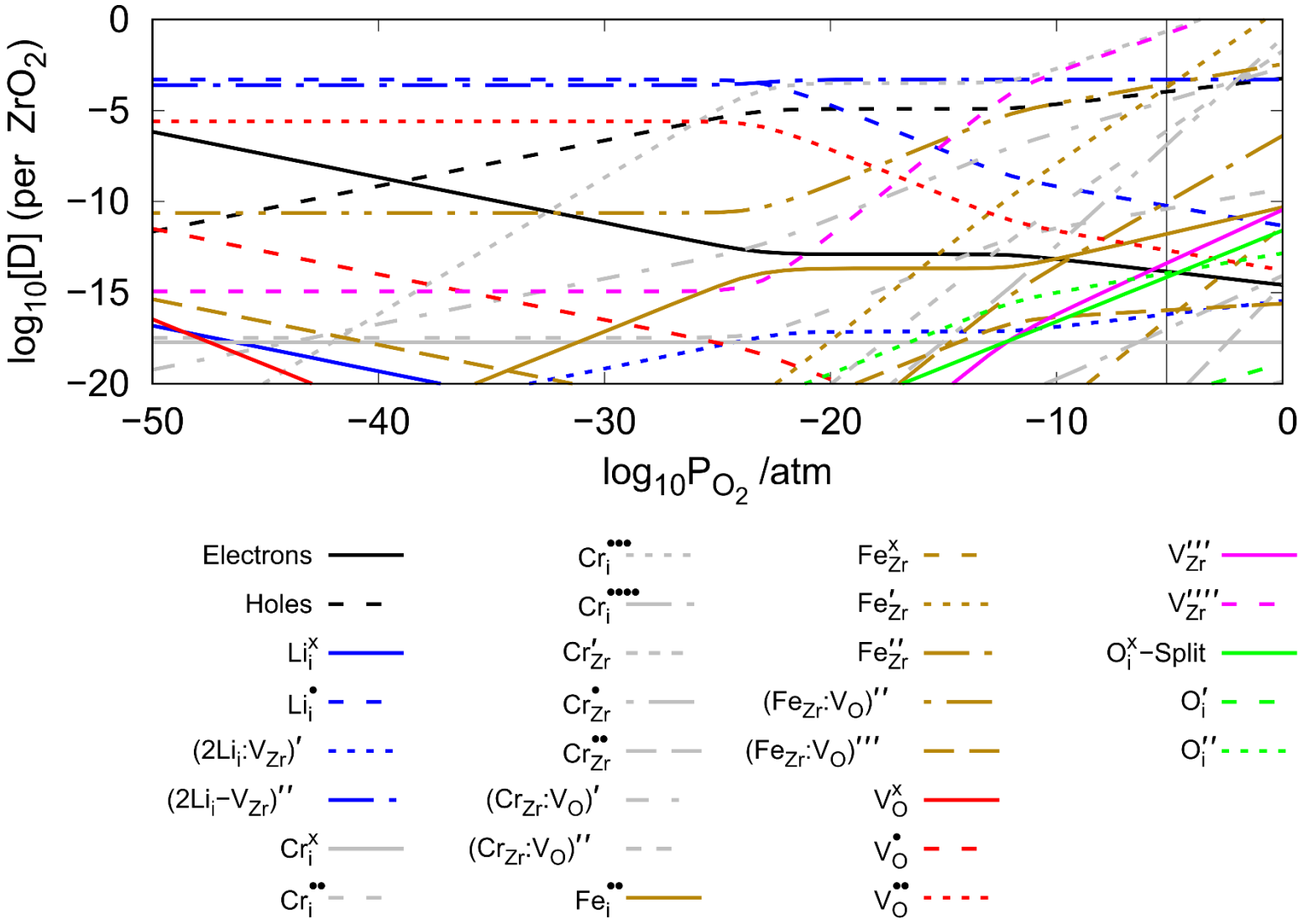

Figure 141 Brouwer diagram with defects with a defect concentration of 10^{-3} Li, 5.7 x 10^{-4} Cr, 1.47 x 10^{-3} Fe, 15.62 x 10^{-3} Sn at 635 K. The Sn defects are hidden.

The chromium defects show a mix of interaction with some showing interactions with other defect concentrations and others showing no caused change, Figure 141. The neutral charged Cr interstitial ($\mathrm{Cr_i^{\times}}$) shows unchanging, low, concentrations with no interaction with any other defect. Other defects show at high partial pressures but do not interact with any other defect including ($\mathrm{Cr_{Zr}^{\bullet\bullet}}$), ($\mathrm{Cr_i^{\bullet\bullet\bullet\bullet}}$), ($\mathrm{Cr_{Zr}^{\bullet}}$), and ($\mathrm{Cr_{Zr}^{\prime}}$) from high partial pressure to low, respectively. The ($\mathrm{Cr_i^{\bullet\bullet}}$) is not visible on the Brouwer diagram due to very low concentrations. The highest concentration Cr defect is the plus three charged ($\mathrm{Cr_i^{\bullet\bullet\bullet}}$) which shows little interaction at lower partial pressure. As partial pressure increases so too does the concentration of the ($\mathrm{Cr_i^{\bullet\bullet\bullet}}$) until it reaches the concentration of the small Li cluster $(\mathrm{2Li_i : V_{Zr}})^{\prime\prime}$. This also coincides with a decrease in ($\mathrm{V_O^{\bullet\bullet}}$) and holes. The ($\mathrm{Cr_i^{\bullet\bullet\bullet}}$) follows the $(\mathrm{2Li_i : V_{Zr}})^{\prime\prime}$ until it intercepts the negative four zirconium vacancy $(\mathrm{V_{Zr}})^{\prime\prime\prime\prime}$. At that point, the ($\mathrm{Cr_i^{\bullet\bullet\bullet}}$) follows the $(\mathrm{V_{Zr}})^{\prime\prime\prime\prime}$ with increasing concentrations with higher partial pressures. The concentration crosses the point with a 1:1 ratio of defect per ZrO_2, which would certainly seem implausible in the case of zirconium vacancy. The next chromium defect with higher concentrations is the cluster $(\mathrm{Cr_{Zr} : V_O})^{\prime}$ which has very low concentrations at low partial pressure and increases with higher partial pressure. This defect, however, does not show any interaction with any other defect. Finally, the $(\mathrm{Cr_{Zr} : V_O})^{\prime\prime}$ defect has a consistently low concentration towards lower partial pressures and begins to increase in concentration when it intercepts the ($\mathrm{V_O^{\bullet}}$) and the Li cluster $(\mathrm{2Li_i : V_{Zr}})^{\prime}$. The concentration increases towards higher partial pressures until it intercepts the ($\mathrm{V_O^{\bullet\bullet}}$) defect, where the increase is reduced. This also coincides with a reduction in decrease of ($\mathrm{V_O^{\bullet\bullet}}$) concentrations towards the highest partial pressures which indicates a mutual interaction. From this, the chromium defects could then be hidden to evaluate the iron defects.

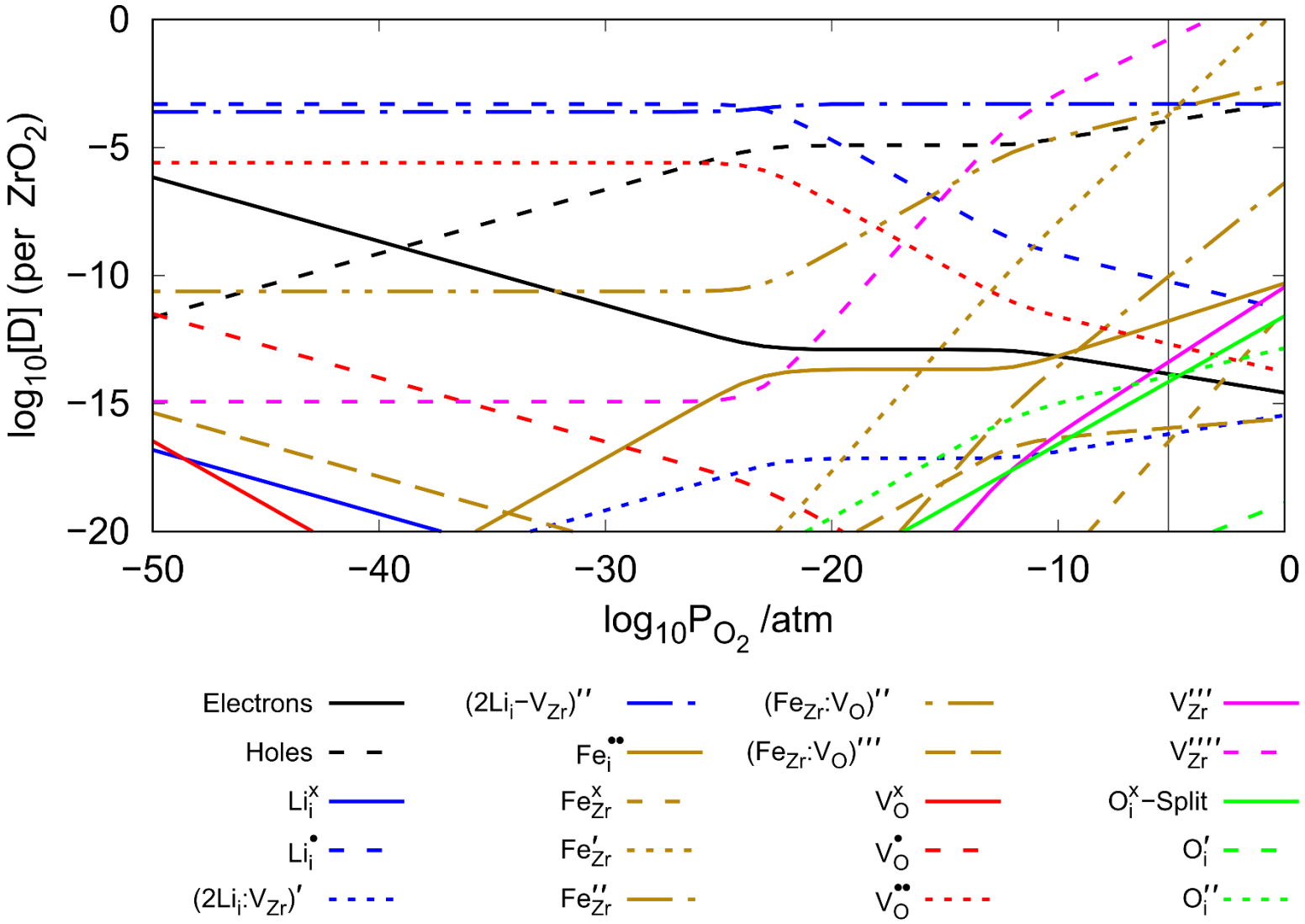

Figure 142 Brouwer diagram with defects with a defect concentration of 10^{-3} Li, 5.7 x 10^{-4} Cr, 1.47 x 10^{-3} Fe, 15.62 x 10^{-3} Sn at 635 K. The Sn and Cr defects are hidden.

Turning to the iron defects, again, there are a number of defects to the lower right at the higher partial pressures which have no clear interaction with any other defect to cause changes in concentration, Figure 142. These include, from lowest to highest concentration, $(\mathrm{Fe}_{\mathrm{Zr}}^{\times})$, $(\mathrm{Fe}_{\mathrm{Zr}}^{''})$, and $(\mathrm{Fe}_{\mathrm{Zr}}^{'})$. At the lowest partial pressure to the left, there is also the cluster $(\mathrm{Fe}_{\mathrm{Zr}}:\mathrm{V}_{\mathrm{O}})'''$ which does not show any interaction with other defects. In the medium range of partial pressure, there are a few interactions that seem to stem from the iron defects. At lower concentrations, the plus two charged interstitial $(\mathrm{Fe}_{\mathrm{i}}^{\bullet\bullet})$ increases with an increase in partial pressure which is reduced by an interaction with electrons and the zirconium vacancy $(\mathrm{V}_{\mathrm{Zr}}^{''''})$. This causes an increase in $(\mathrm{V}_{\mathrm{Zr}}^{''''})$ and a coupled plateau in electron and $(\mathrm{V}_{\mathrm{Zr}}^{''''})$ concentrations. This also coincides with a decrease in $(\mathrm{V}_{\mathrm{O}}^{\bullet\bullet})$ and hole concentrations which was earlier associated with $(\mathrm{Cr}_{\mathrm{i}}^{\bullet\bullet\bullet})$, but also an increase in $(\mathrm{Fe}_{\mathrm{Zr}}:\mathrm{V}_{\mathrm{O}})''$. The increase in $(\mathrm{Fe}_{\mathrm{Zr}}:\mathrm{V}_{\mathrm{O}})''$ is reduced when it intersects the hole concentration which is also increase at this point. This is also coupled with an increase in $(\mathrm{Fe}_{\mathrm{i}}^{\bullet\bullet})$ concentrations towards higher partial pressures. At higher partial pressures, the cluster $(\mathrm{Fe}_{\mathrm{Zr}}:\mathrm{V}_{\mathrm{O}})'''$ shows low concentrations which has an interaction with the negative one charged Li cluster $(2\mathrm{Li}_{\mathrm{i}}:\mathrm{V}_{\mathrm{Zr}})'$ which reduces the concentration of $(\mathrm{Fe}_{\mathrm{Zr}}:\mathrm{V}_{\mathrm{O}})'''$ and an increase in $(2\mathrm{Li}_{\mathrm{i}}:\mathrm{V}_{\mathrm{Zr}})'$. The Fe defects may now be hidden for just intrinsic defects along with lithium.

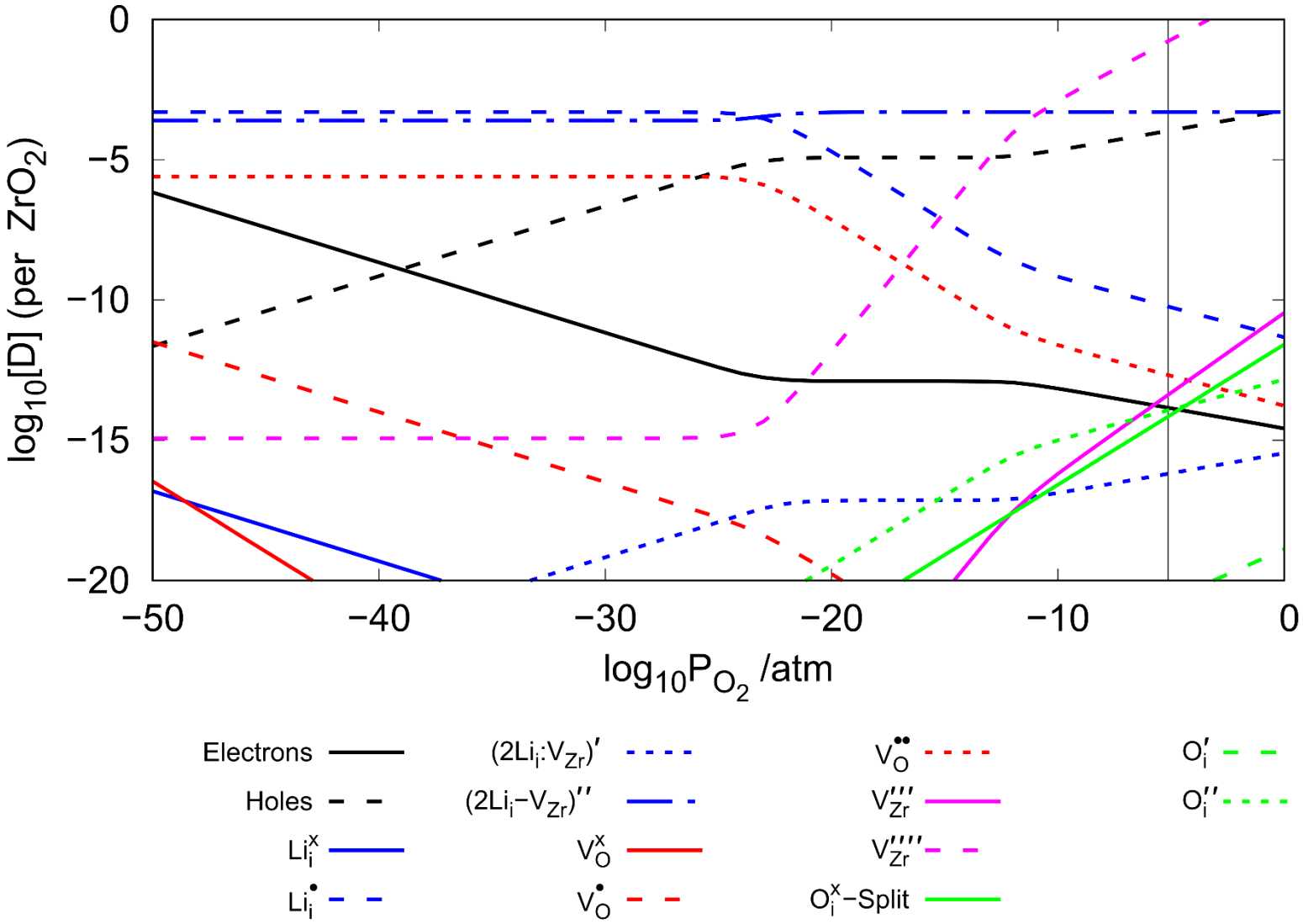

Figure 143 Brouwer diagram with defects with a defect concentration of 10^{-3} Li, 5.7 x 10^{-4} Cr, 1.47 x 10^{-3} Fe, 15.62 x 10^{-3} Sn at 635 K. The Sn, Cr and Fe defects are hidden.

When considering the just the Li and intrinsic defects shown earlier, there is a large difference with respect to oxygen vacancy and zirconium vacancy defect concentrations. Where we saw lithium increased the concentrations of oxygen vacancy before all the way up to the water oxide interface, here there is a substantial reduction in oxygen vacancy, Figure 143. Conversely, the zirconium vacancy concentrations are hugely increased towards the water oxide interface. The plateau of both electron and hole concentrations caused by previous defects is also apparent. Although the plateau is found on the Li/intrinsic defect Brouwer diagram, these occur at higher partial pressures which also coincides with the point at which zirconium vacancy increases.

All defects need to be applied together whilst evaluating the effects of the change in Li concentration, Figure 144. For this reason, all defects will be placed together with a change in Li defect concentration. Then, the Sn, Cr, and Fe concentrations will be hidden so that just the Li and intrinsic defects will be visible for clarity, Figure 145.

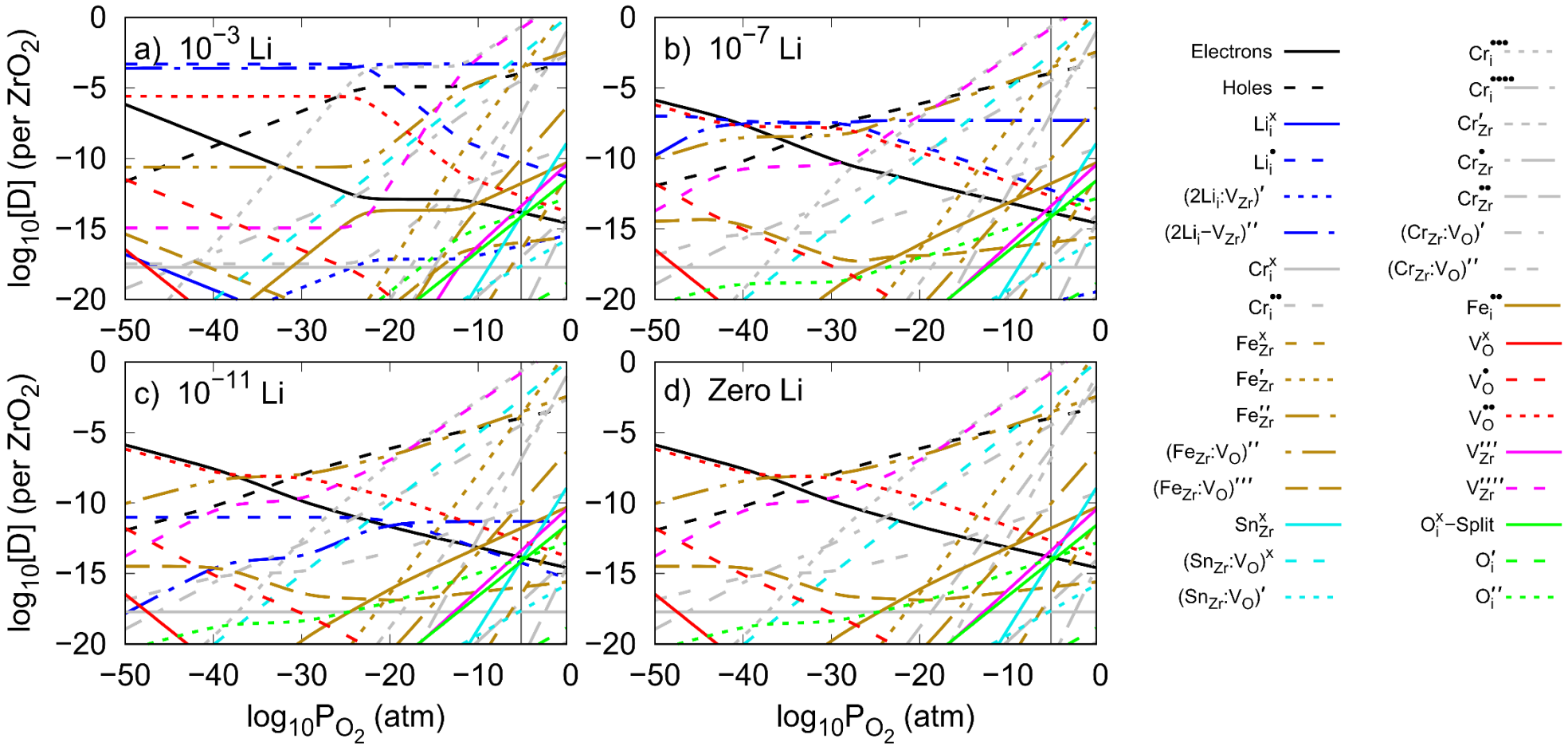

Figure 144 Tetragonal ZrO_2 Brouwer diagram with defects with a defect concentration of 5.7 x 10^{-4} Cr, 1.47 x 10^{-3} Fe, 15.62 x 10^{-3} Sn at 635 K with Li concentrations of a) 10^{-3} b) 10^{-7} c) 10^{-11} and d) zero Li

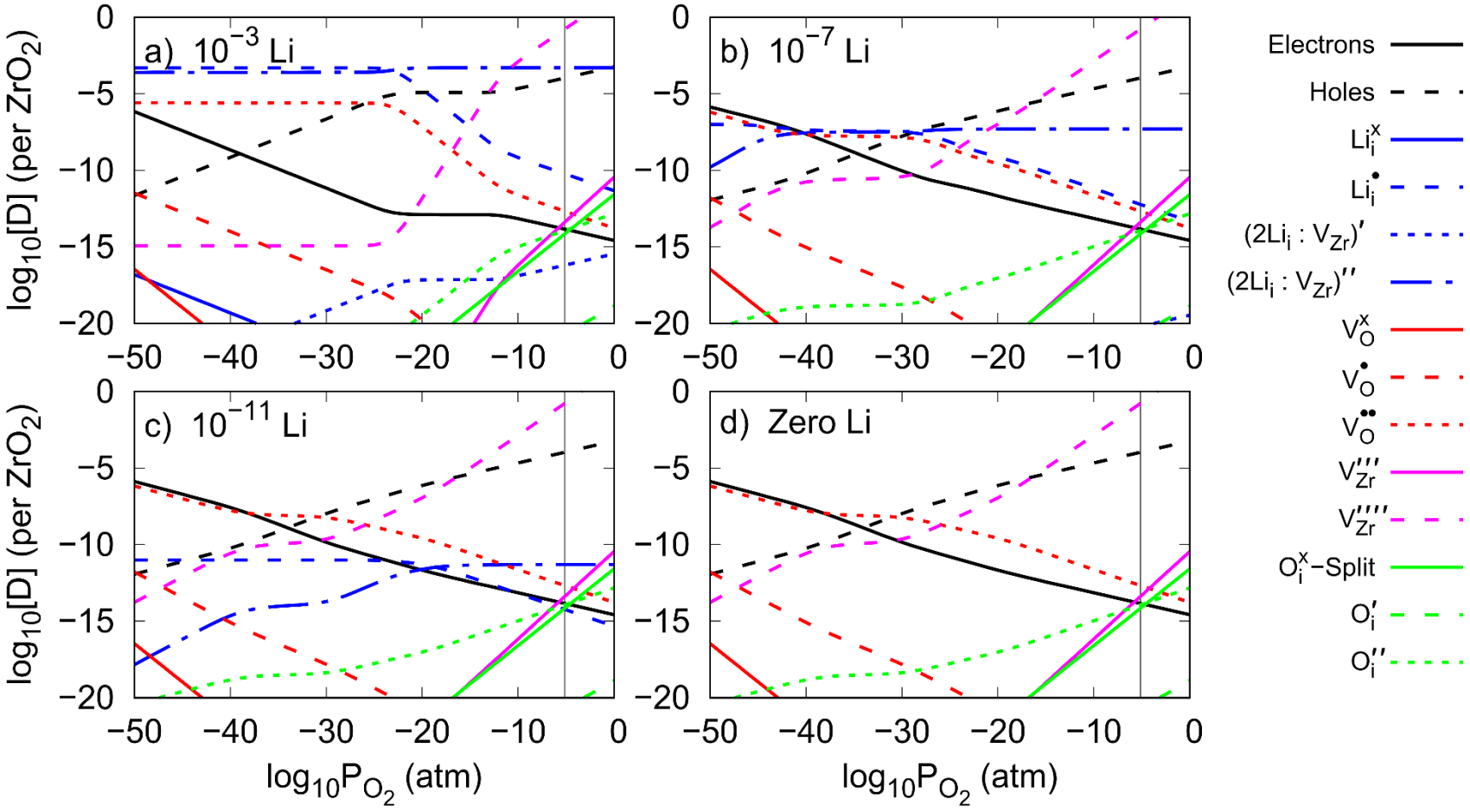

Figure 145 Tetragonal ZrO2 Brouwer diagram with defects with a defect concentration of 5.7 x 10^{-4} Cr, 1.47 x 10^{-3} Fe, 15.62 x 10^{-3} Sn at 635 K with Li concentrations of a) 10^{-3} b) 10^{-7} c) 10^{-11} and d) zero Li. The Cr, Fe and Sn defects are hidden for clarity.

When viewing the final Brouwer diagram including Cr, Fe and Sn defects (which are hidden for clarity), Figure 145, we can see that changes associated with lithium only occurs with the highest 10^{-3} concentration. For 10^{-7}, 10^{-11} and no Li defects, these all show the same concentration trends for all intrinsic defects. In the case of 10^{-3} Li concentration, we can see changes associated with this this which include $(V_O^{\bullet\bullet})$, $(V_{Zr}^{''''})$, $(V_{Zr}^{'''})$, $(O_i^{''})$, electrons and holes. The $(V_O^{\bullet\bullet})$ shows higher concentrations at lower partial pressures which reduce back to normal levels when it intersects hole concentrations. Without the addition of Cr, Fe and Sn defects, Li was found to increase the $(V_O^{\bullet\bullet})$ concentrations all the way up to the water oxide interface. Whilst we have an indication of combined defect concentrations within the tetragonal oxide layer, this does not give an indication of plausibility. This will be reviewed later where the solution energies will be calculated to provide an indication of whether these defects may be found within the oxide layer.

A.5. Cr Doped Monoclinic ZrO_2

The attention now turns to the chromium defects within the monoclinic structure. The defects that were found to be within the bandgap during calculations included (Cr_i), (Cr_{Zr}), $(Cr_{Zr}{:}V_O)$ and $(2Cr_{Zr}{:}V_O)$. The associated charged for each defect, which could be taken further into the investigation, were numerous which meant that, unlike the lithium defects, each defect species would need to be separated into individual formation energy diagrams. These start with the chromium interstitial defect.

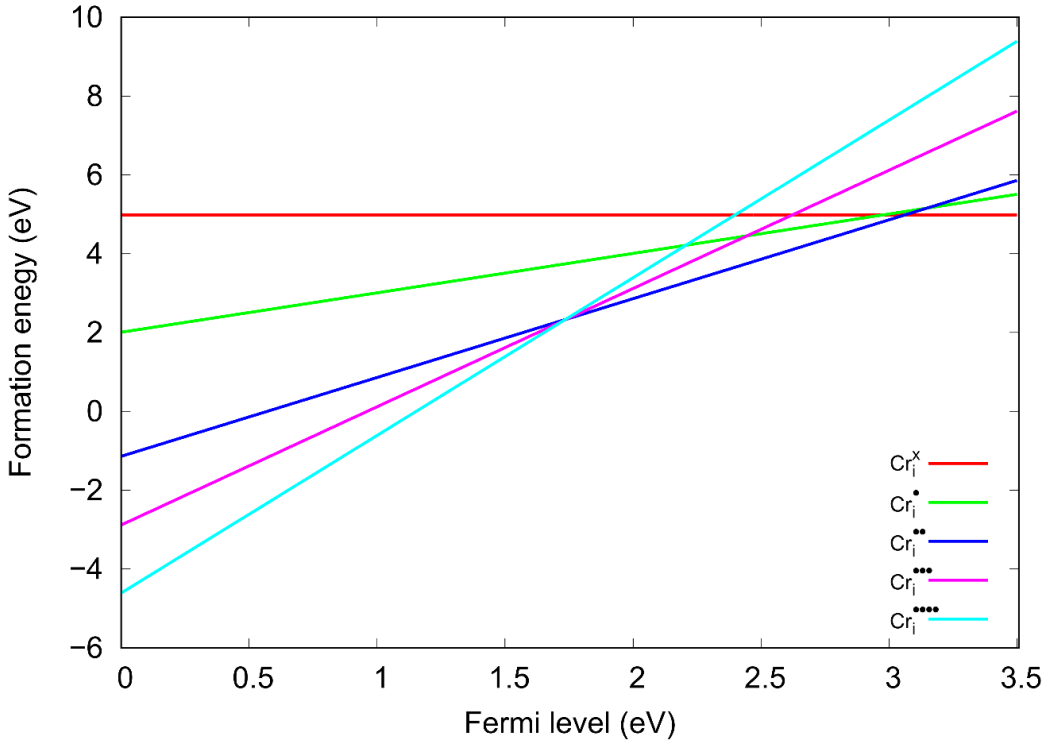

Figure 146 Formation energy of chromium interstitial defects with a range of charges across the Fermi energy of the bandgap in monoclinic ZrO_2.

Towards the top of the valence band to the left, the positive four charged chromium interstitial shows the lowest formation energy, of which it maintains until the middle of the bandgap at roughly 1.7 eV, Figure 146. From here, the positive two interstitial has the lowest formation energy moving towards the bottom of the conduction band to the right. At the very bottom of the conduction band to the far right, the neutral charged interstitial has the lowest formation energy. The defects with a

negative formation energy are all towards the top of the valence band to the right and include the plus four, three and two interstitial defects. All of which show a positive formation energy above 1.2 eV in the bandgap. All defects above 1.2 eV Fermi energy show a positive formation energy, which would only be favoured within a Brouwer diagram if the conditions favoured a positive charged defect towards the bottom of the conduction band.

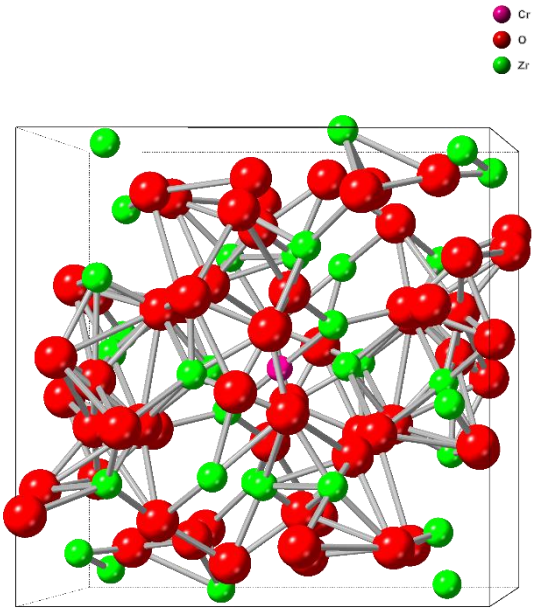

Figure 147 Monoclinic ZrO_2 structure with a chromium interstitial (purple) centre. Additional deformation of the structure could take place in unfavourable positions.

The structure given in Figure 150 is a worst-case scenario of the monoclinic ZrO_2 with a chromium interstitial. Any order has been lost and the structure might as well be amorphous. This would result in prolonged DFT calculations for completion and irregular associated energies. Whilst this would provide evidence that the order was lost, it highlighted the need to check structures visually. The position in which the chromium interstitial was placed was found to be the cause of this irregularity. The standard chromium interstitial structure was found to show very little change in atomic position from the perfect, relaxed, structure.

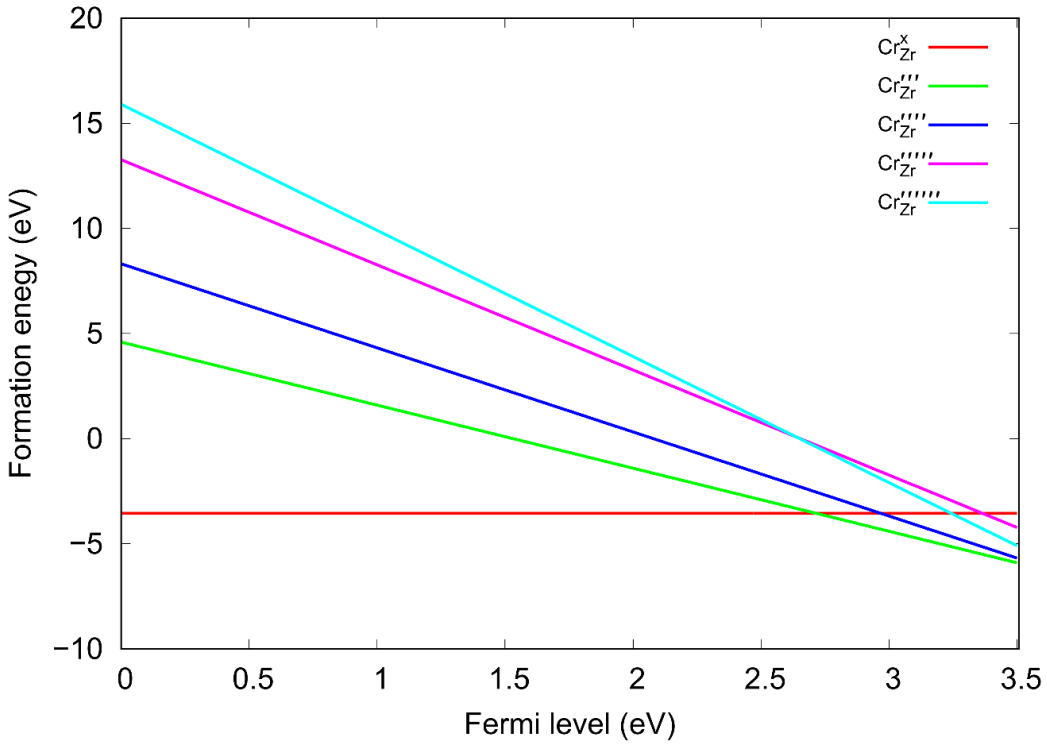

Figure 148 Formation energy of chromium substitution on a zirconium site defect with a range of charges across the Fermi energy of the bandgap in monoclinic ZrO_2.

In the case of the chromium substitution to a zirconium site, Figure 148, the negative one and two defects were calculated outside of the bandgap, so are not present in the formation energy calculations. The neutral charged substitution shows the lowest formation energy across most of the bandgap from zero up to roughly 2.7 eV. It is also the only defect to show a negative formation towards the top of the valence band to the left. The negative three charged substitution shows a negative formation energy above 1.5 eV but only has the lowest formation energy above 2.7 eV and up to the bottom of the conduction band to the far right. The remaining defects, including negative four, five and six, all have a negative formation energy above 2.7 eV and up to the bottom of the conduction band, but do not show as having the lowest formation energy at any point. The neutral charged defect is the only defect which shows a consistent negative formation energy across the bandgap, where all other negative charged defects show a positive formation energy towards the top of the valence band.

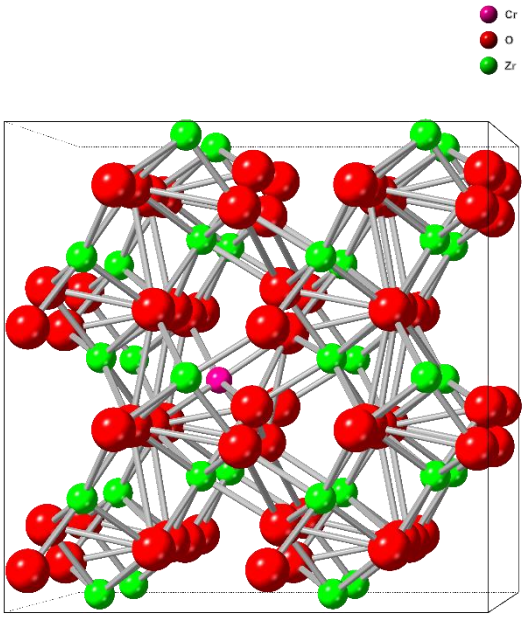

Figure 149 Monoclinic ZrO_2 structure with a chromium substitution on a zirconium site.

The monoclinic ZrO_2 structure with a chromium substitution on a zirconium site (Figure 152) shows very little change in position for the oxygen and zirconium atoms from the relaxed perfect structure.

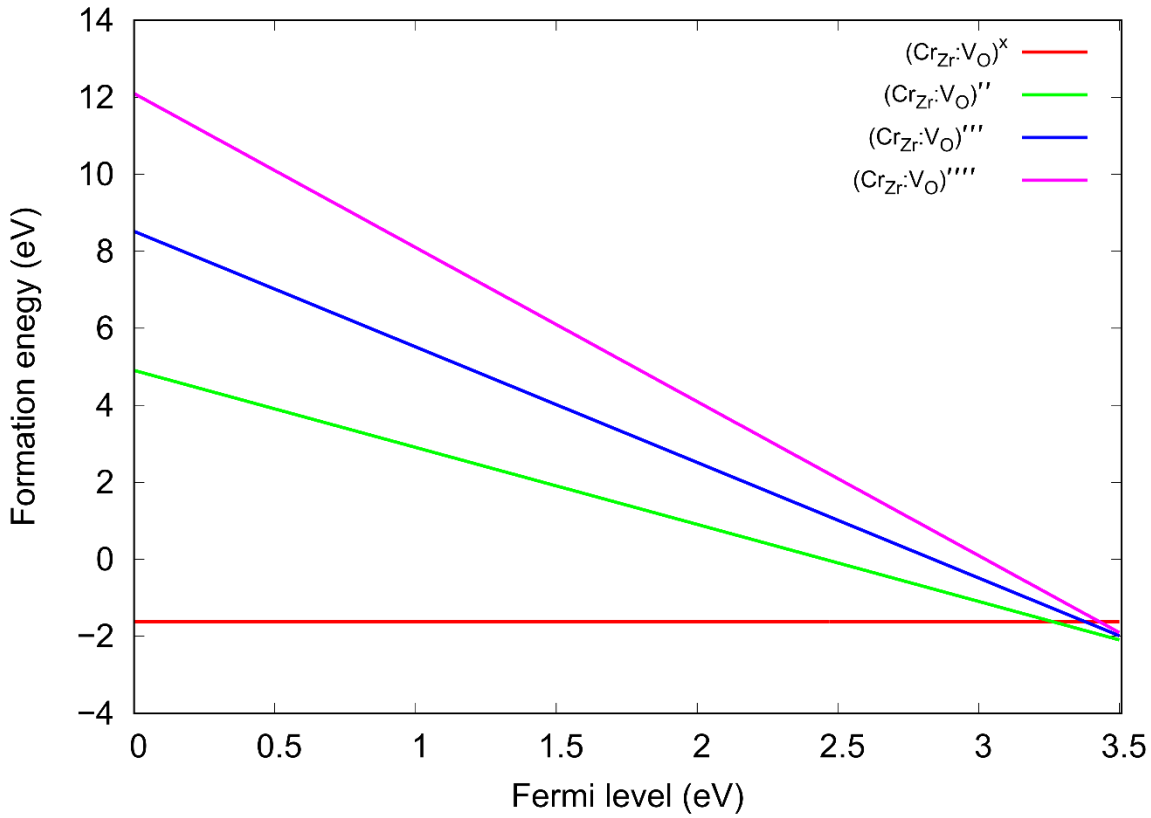

Figure 150 Formation energy of chromium substitution on a zirconium site and an oxygen vacancy cluster defect with a range of charges across the Fermi energy of the bandgap in monoclinic ZrO_2.

For the small cluster containing a chromium substitution on a zirconium site and an oxygen vacancy, Figure 150, the negative one defect was calculated outside of the bandgap. There are a lot of parallels with the chromium substitution formation energy plot. The neutral charged cluster shows a consistent negative formation energy, and all negative charged defects show a positive formation energy towards the top of the valence band but a negative formation energy from between 2.5 eV and the bottom of the conduction band to the right. In this formation energy plot, however, the negative two defect shows the lowest formation energy towards the bottom of the conduction band to the right.

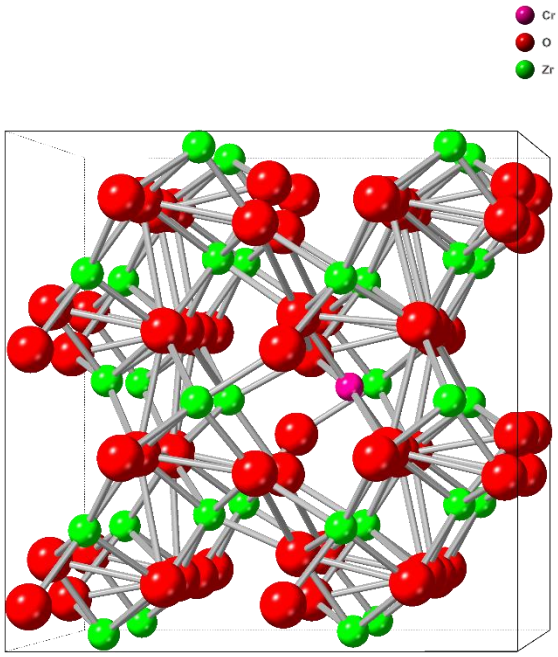

Figure 151 Monoclinic ZrO_2 structure with a chromium substitution on a zirconium site and a oxygen vacancy.

The chromium substitution on a zirconium site with an oxygen vacancy cluster (Figure 154) shows no remarkable changes in zirconium or oxygen positions once relaxed.

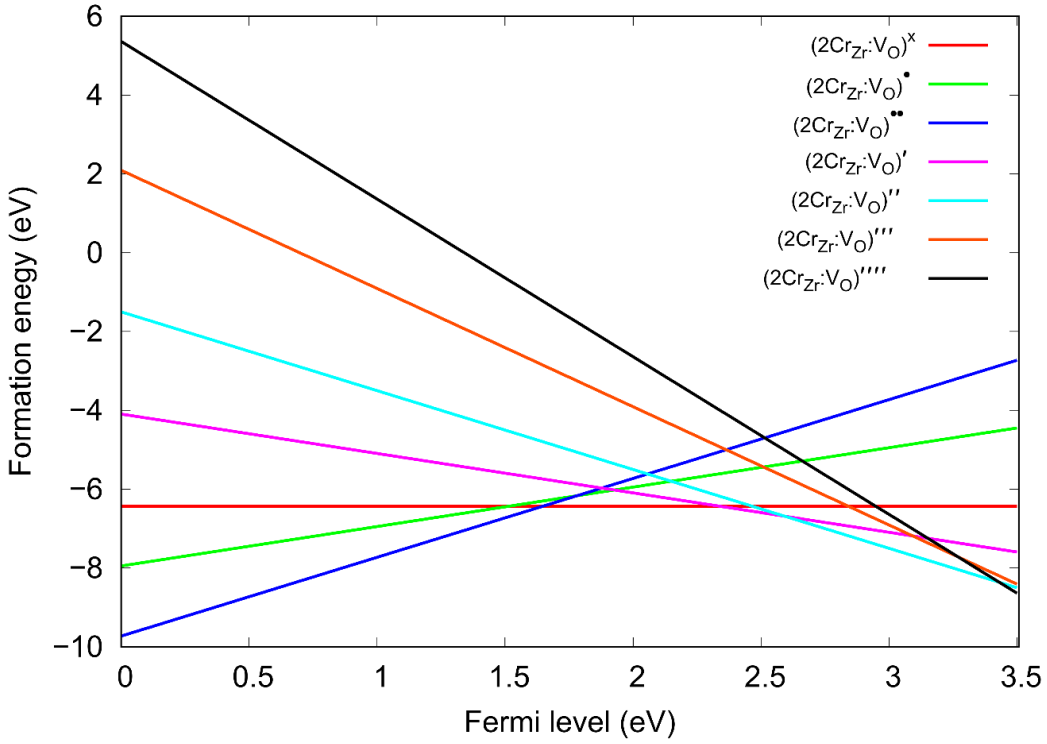

Figure 152 Formation energy of two chromium substitution defects on two zirconium sites and an oxygen vacancy with a range of charges across the Fermi energy of the bandgap in monoclinic ZrO_2.

Finally, the small cluster of two chromium substitutions on two zirconium sites with an oxygen vacancy, Figure 152, shows all attempted defects up to a negative 4 charge. All of the defects present a negative formation energy where only the negative three and four defects showing a positive formation energy towards the top of the valence band to the left. Starting from the left at the top of the valence band, the lowest formation energy is that of the plus two charged defect. This holds the lowest formation energy up to approximately 1.6 eV where the neutral charged defect has the lowest formation energy up to approximately 2.4 eV. From there up to approximately 2.6 eV, the negative one defect has the lowest formation energy. The negative two charged defect then has the lowest formation energy up to approximately 3.4 eV before finally being replaced by the negative four defect which holds the lowest formation energy up to the bottom of the conduction band to the right.

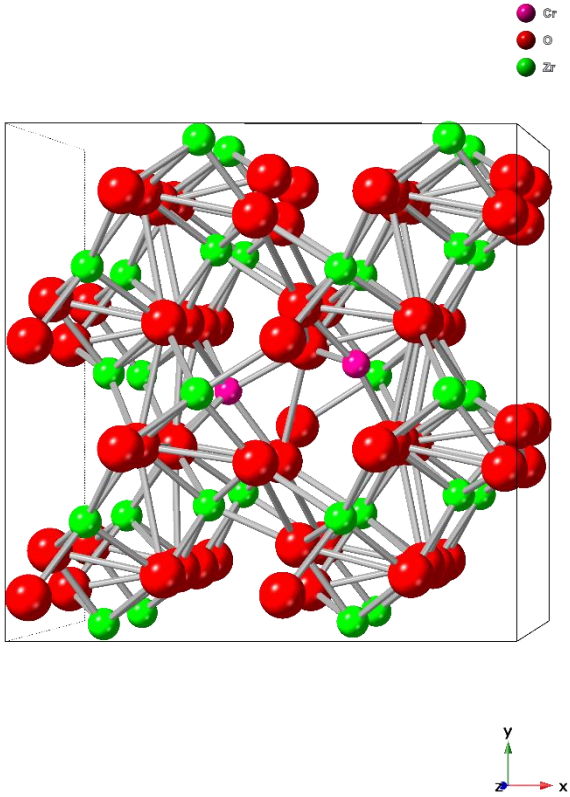

Figure 153 Monoclinic ZrO_2 structure with two chromium substitutions on zirconium sites and a oxygen vacancy.

As with most of the chromium defects, there is little change in atomic position (Figure 156) from two chromium substitutions on zirconium sites with an oxygen vacancy cluster.

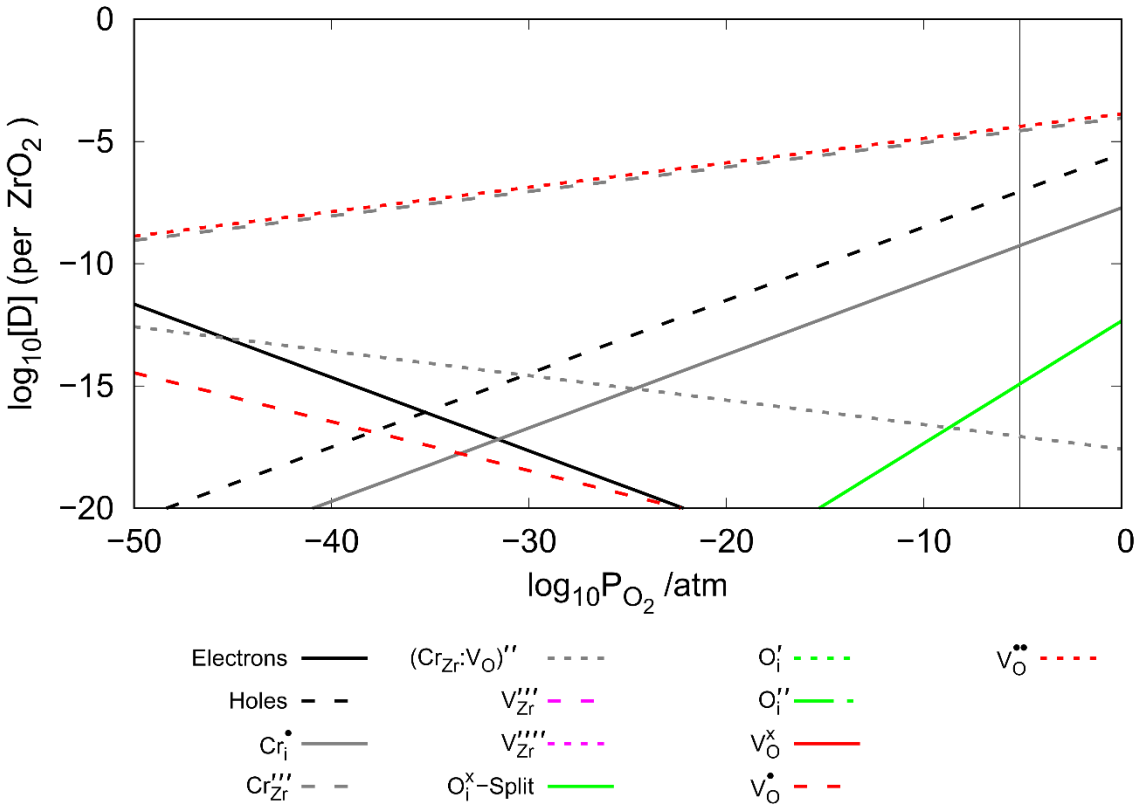

Figure 154 Brouwer diagram at 635 K with no fixed concentration of Cr and intrinsic defects in monoclinic ZrO_2.

When viewing the chromium doped Brouwer diagram of monoclinic zirconia with no fixed chromium concentration, Figure 154, there is a clear increase in plus two charged oxygen vacancy defects as a result of negative three chromium substitution on a zirconium site. There is a coupled increase in both the chromium substitution and oxygen vacancy concentrations towards higher partial pressures of oxygen to the right. There is also an absence of zirconium vacancy defects that we would expect to see with intrinsic defects only. There are lower concentrations of plus one chromium interstitials, which loosely follow hole concentrations with lower concentrations at lower partial pressures and higher concentrations at higher partial pressures. The small cluster of a chromium substitute at a zirconium site and an oxygen vacancy with a negative two charge has higher concentrations towards lower partial pressures to the left and decreases with higher partial pressures to the right.

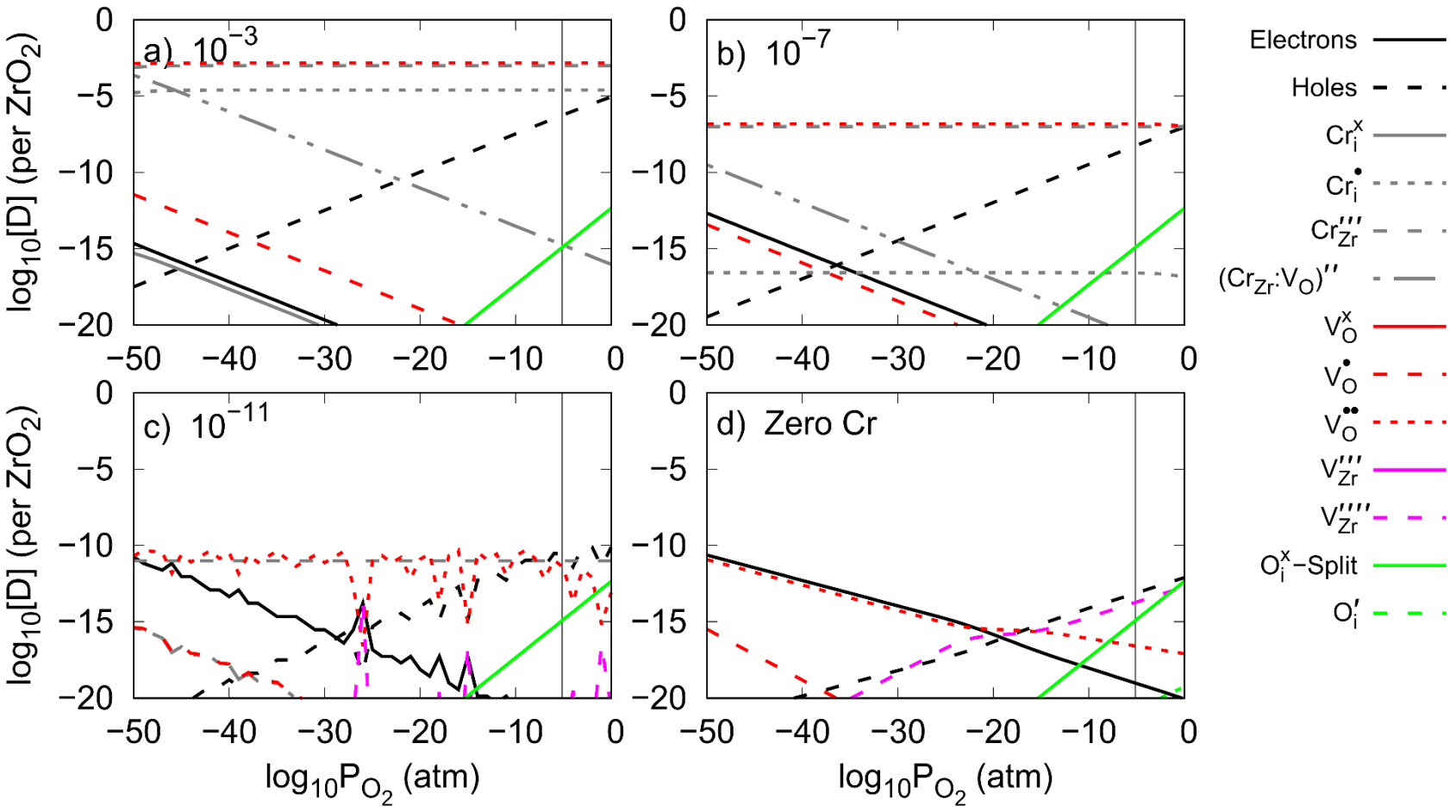

Figure 155 Cr doped monoclinic ZrO_2 Brouwer diagrams with the Cr concentrations of a) 10^{-3} b) 10^{-7} c) 10^{-11} and d) with intrinsic defects only.

When altering the stipulated concentration of chromium in the ZrO_2 structure, *Figure 155*, we can see some clear differences. With a chromium concentration of 10^{-3} (a), the plus two charged oxygen vacancy follows the negative three charged chromium substitution defect with consistent concentrations across the partial pressure range. Just beneath this is the plus one chromium interstitial. The negative two charged cluster of a chromium substitution on a zirconium site with a oxygen vacancy shows high concentrations at lower partial pressures to the left and reduces towards higher partial pressures to the right. The last chromium defect to feature on the Brouwer diagram is the neutral charged chromium interstitial which shows low concentration at lower partial pressures to the right. There is an absence of zirconium vacancy defects and the point of convergence between the electron and holes has been pushed to lower partial pressures to the far left. The plus one oxygen vacancy concentration has also increased towards lower partial pressures. When the chromium concentration is reduced to 10^{-7} (b), the plus two charged oxygen vacancy follows this change in concentration indicating a coupling effect. The plus one chromium defect, however, is reduced significantly as a result. All three of these defects maintain the constant concentration throughout the partial pressure range. The concentration of the small cluster of chromium substitution on a zirconium site with a oxygen vacancy is also reduced and remains higher towards lower partial pressures. The neutral charged chromium interstitial has been removed as the concentration is now below the given range. The plus one oxygen vacancy defect concentration is slightly reduced, and the electron and hole convergence point is shifted slightly towards higher partial pressures in respect to the 10^{-3} chromium defect Brouwer diagram. When the chromium concentration was decreased to 10^{-11} (c), a clear limit had been reached in the Brouwer diagram software calculations, which is almost void of defined trends. It is, However, possible to pick out the general trends. The plus two charged oxygen vacancy defect, again, follows the concentration of the negative three charged chromium substation. The plus one oxygen vacancy follows the reduced negative two charged small cluster. We see the introduction of the zirconium vacancy defect at the lowest concentrations. Finally, the electron and hole point of convergence is shifted towards higher partial pressures. When comparing the intrinsic defects alone (d), the electron hole concentration is further towards higher partial pressures and the plus two oxygen vacancy defect follows the electron concentration. The negative four zirconium vacancy defect follows the hole concentration which increases with higher partial pressure. The plus one oxygen vacancy is relatively unchanged compared to that of the 10^{-11} chromium Brouwer diagram.

A.6. Fe Doped Monoclinic ZrO_2

The iron doped Brower diagram considered similar defects that have been reviewed previously including iron interstitials $(\mathrm{Fe\_i})$, iron substitutions on a zirconium site $(\mathrm{Fe_{Zr}})$, the small cluster of and iron substitution on a zirconium site with a oxygen vacancy $(\mathrm{Fe_{Zr}:V_O})$, and the small cluster of two iron substitutions on two zirconium sites with a oxygen vacancy $(\mathrm{2Fe_{Zr}:V_O})$. Due to the large number of defects that could be considered, the defect species were split into individual formation energy plots with the associated charges that could be calculated within the bandgap energy. Defects omitted were a result of being calculated outside of the Fermi energy.

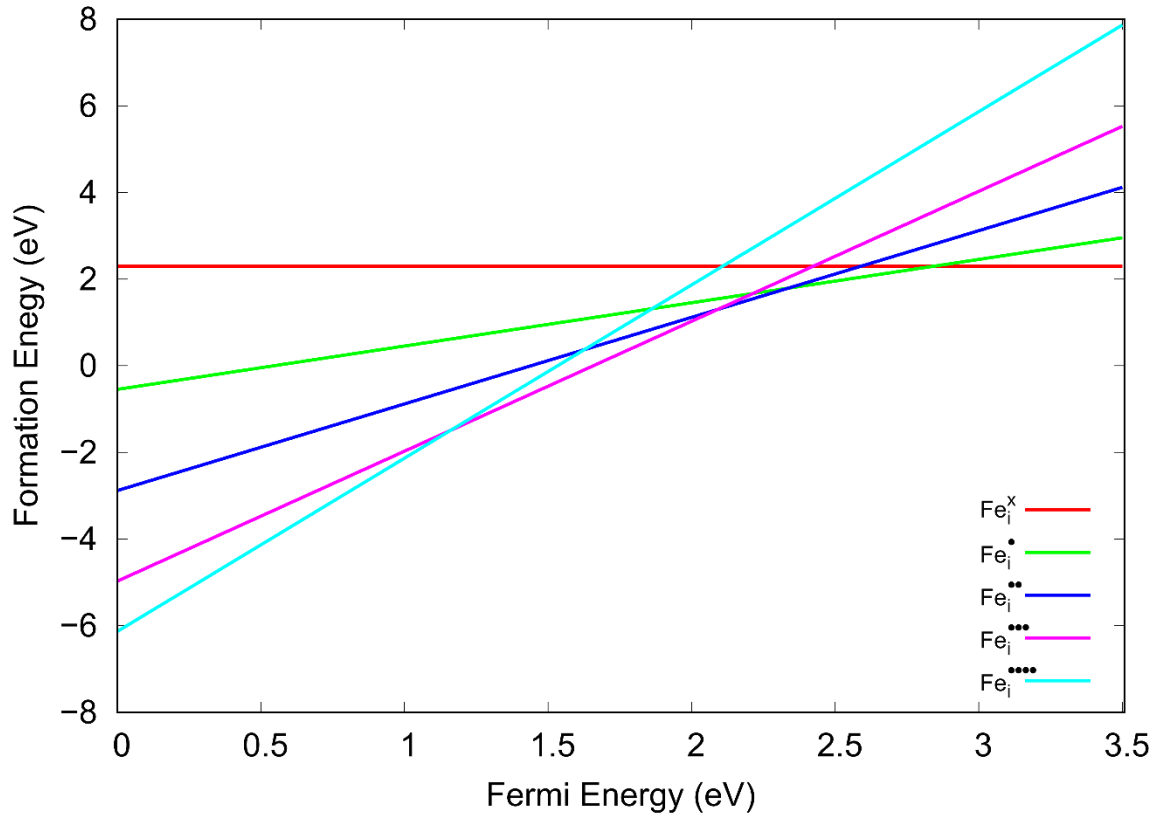

Figure 156 Formation energy of iron interstitial defects with a range of charges across the Fermi energy of the bandgap in monoclinic ZrO_2.

For iron interstitials, the positive four defect has the lowest formation energy at the top of the valence band to the left, Figure 156. This continues up to roughly 1.2 eV where the positive three interstitial has the lowest formation energy. The positive three interstitial crosses from a negative formation energy into a positive formation energy at 2 eV and is replaced by the positive two interstitial for a brief Fermi energy before the positive one interstitial has the lowest formation energy from approximately 2.4 eV. Finally, the neutrally charged interstitial has the lowest formation energy from 2.8 eV and maintains the lowest formation energy up to the bottom of the conduction band to the right. The neutral charged interstitial is the only defect to maintain a positive formation energy throughout the bandgap. All other defects have a negative formation energy towards the top of the conduction band and a positive formation energy towards the bottom of the conduction band.

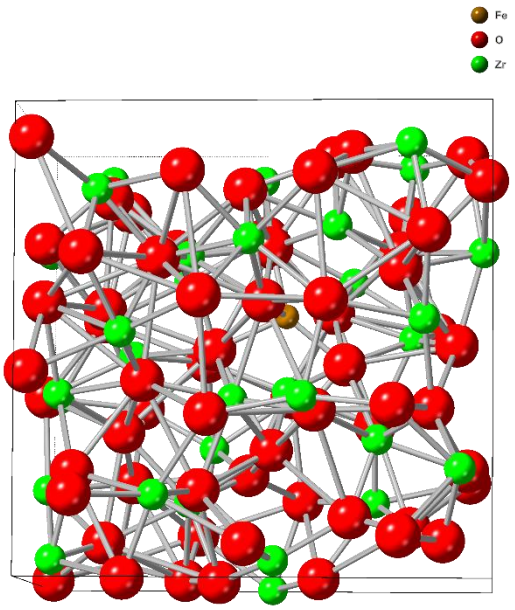

Figure 157 Monoclinic ZrO_2 structure with an iron interstitial (gold) centre. The iron interstitial location has the potential to disform the monoclinic structure depending on location (as highlighted)

As was found with the chromium interstitials, the iron interstitials could result in a loss of order within the structure if in an unfavourable position (Figure 160). Most intrinsic positions, however, resulted in generally unremarkable changes in intrinsic atom positions.

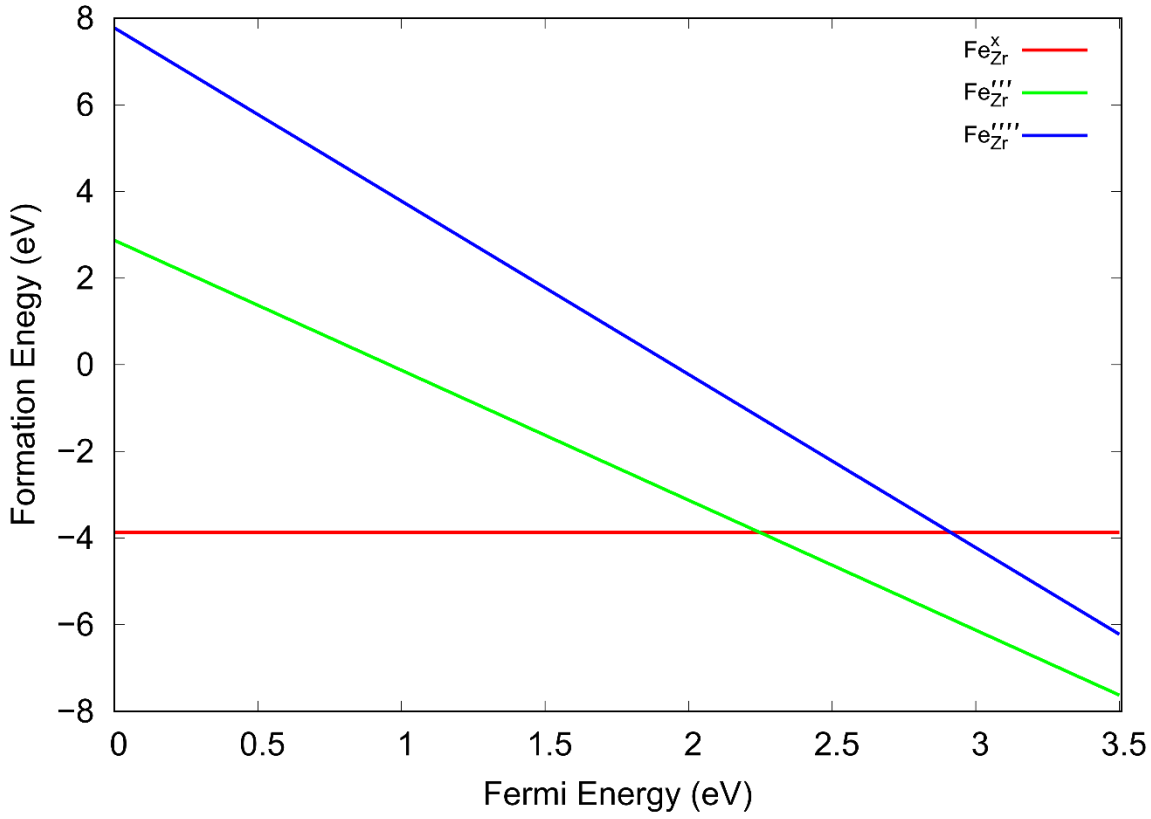

Figure 158 Formation energy of iron substitution defects on zirconium sites with a range of charges across the Fermi energy of the bandgap in monoclinic ZrO_2.

The iron substitutions on zirconium sites are surprisingly few in number when compared to other defects, Figure 158. All of the defects that were calculated within the Fermi energy held a negative formation energy from 0.9 eV and towards the bottom of the conduction band to the right. At the top of the valence band to the left, the neutral charged substitution holds the lowest formation energy up to approximately 2.2 eV. From there, the negative three substitution has the lowest formation energy up to the bottom of the conduction band to the right. The negative four defect does not hold the lowest formation energy at any point across the bandgap.

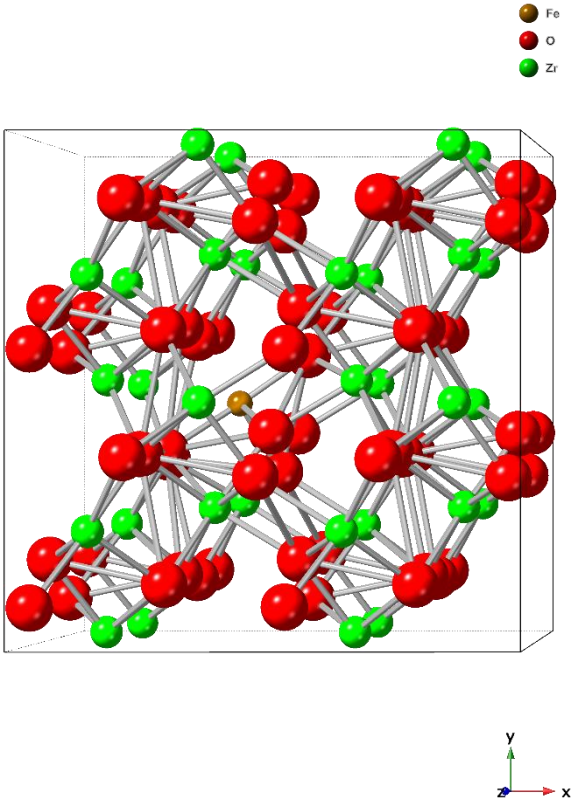

Figure 159 Monoclinic ZrO_2 structure with an iron substitution on a zirconium site.

The iron substitution on a zirconium site produced little change in zirconium positions and caused very small changes in neighbouring oxygen atomic position (Figure 162).

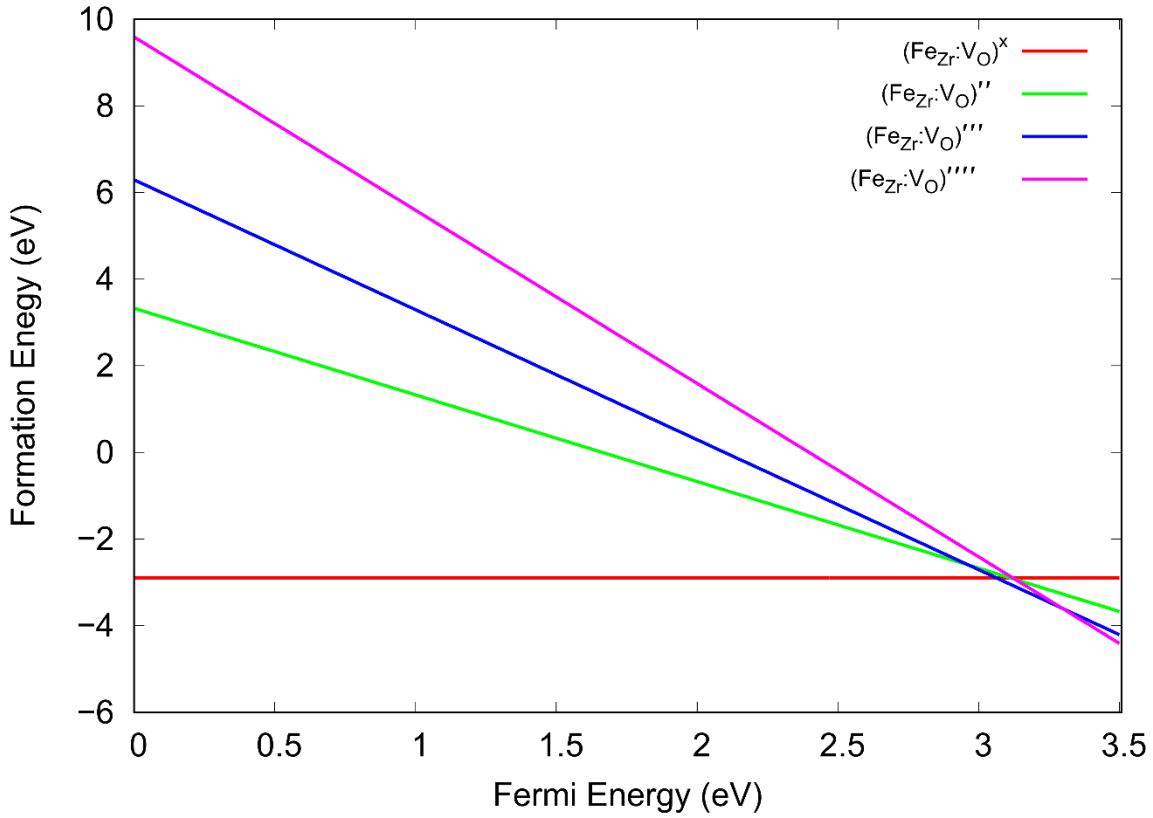

Figure 160 Formation energy of the small defect cluster of an iron substitution on a zirconium site with a oxygen vacancy with a range of charges across the Fermi energy of the bandgap in monoclinic ZrO_2

In the case of the small cluster of an iron substitution on a zirconium site with an oxygen vacancy, all defects hold a negative formation energy towards the bottom of the conduction band to the right, *Figure 160*. At the top of the valence band to the left, only the neutral charged cluster shows a negative formation energy. The neutral charged defect holds the lowest formation energy up to 3.1 eV before the negative three charged cluster briefly has the lowest formation energy. The negative four charged cluster has the lowest formation energy for the remainder of the bandgap up to the bottom of the conduction band. The negative two charged defect does not hold the lowest formation energy at any point across the bandgap.

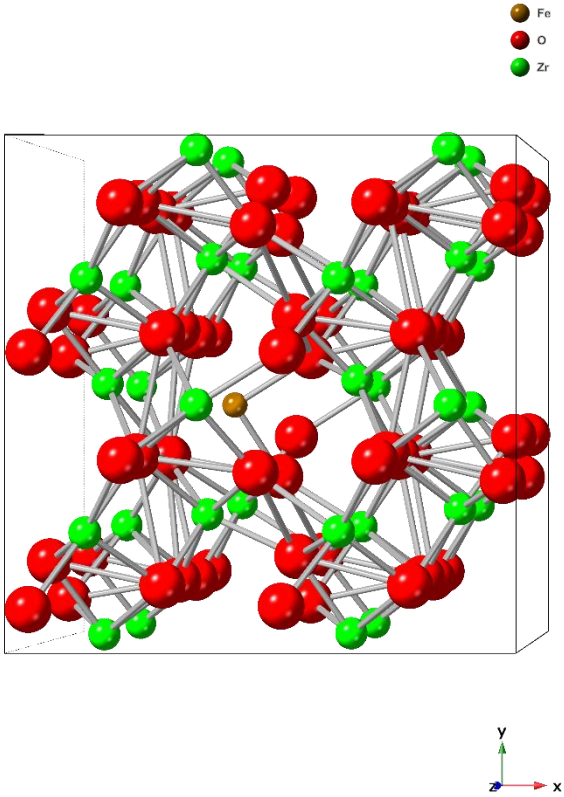

Figure 161 Monoclinic ZrO_2 structure with a iron substitution on a zirconium site and a oxygen vacancy.

The iron substitution on a zirconium site with an oxygen vacancy in the monoclinic ZrO_2 structure (Figure 164) shows no remarkable changes in intrinsic atom position.

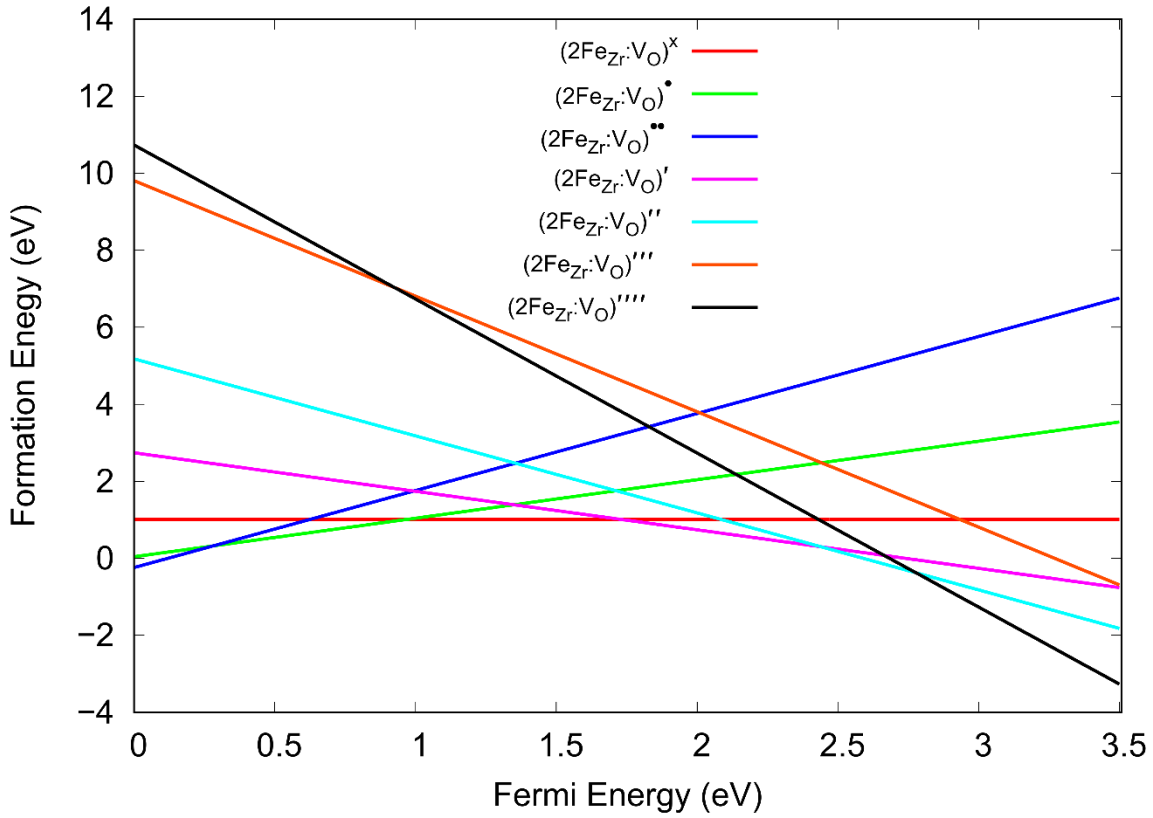

Figure 162 Formation energy of the small defect cluster of two iron substitutions on two zirconium sites with a oxygen vacancy with a range of charges across the Fermi energy of the bandgap in monoclinic ZrO_2

Finally, we have the small cluster of two iron substitutions two zirconium sites with an oxygen vacancy, *Figure 162*. Two of the charged defects do not hold a negative formation energy across the bandgap and neutral charged clusters. The negative one and three have a negative formation energy in a small region towards the bottom of the conduction band to the right. Almost all of the clusters share the lowest formation energy at some point across the bandgap with the exception of the negative three charged cluster. Starting from the top of the valence band to the left, the lowest formation energy defect is the plus two charged cluster which crosses from a negative to positive formation energy. This is replaced by the plus one charged cluster at around 0.3 eV. From 1 eV, the neutral charged defect has the lowest formation energy up to 1.7 eV. From there, the negative one charged cluster has the lowest formation energy up to 2.4 eV. The negative two cluster takes over with the lowest formation energy and also crosses from a positive formation energy and returns to a negative formation energy. This cluster has the lowest formation energy up to approximately 2.7 eV where the negative four cluster has the lowest formation for the remainder of the bandgap up to the bottom of the conduction band to the right.

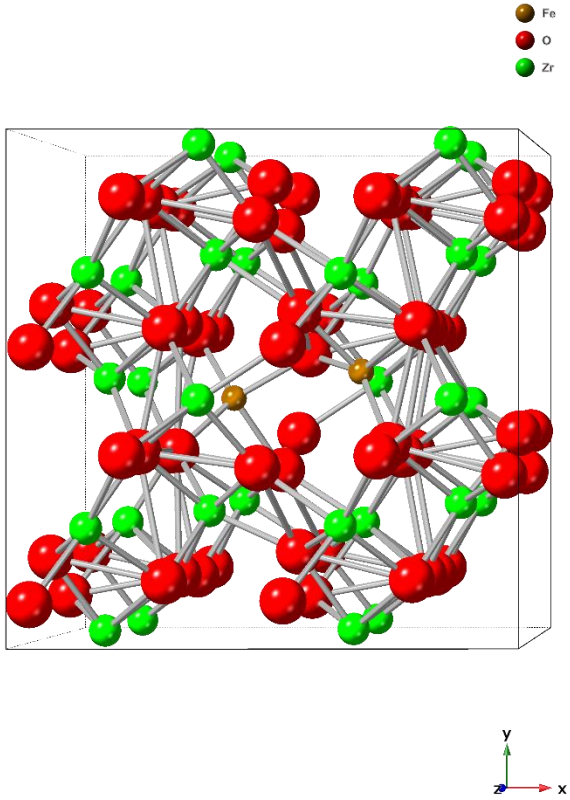

Figure 163 Monoclinic ZrO_2 structure with two iron substitutions on zirconium sites and a oxygen vacancy.

The two iron substitutions on zirconium sites with an oxygen vacancy in the monoclinic ZrO_2 structure (Figure 166) shows marginal oxygen position changes and very little change in zirconium positions.

This completes the potential iron defects and the iron doped monoclinic ZrO_2 Brouwer diagrams could then be calculated.

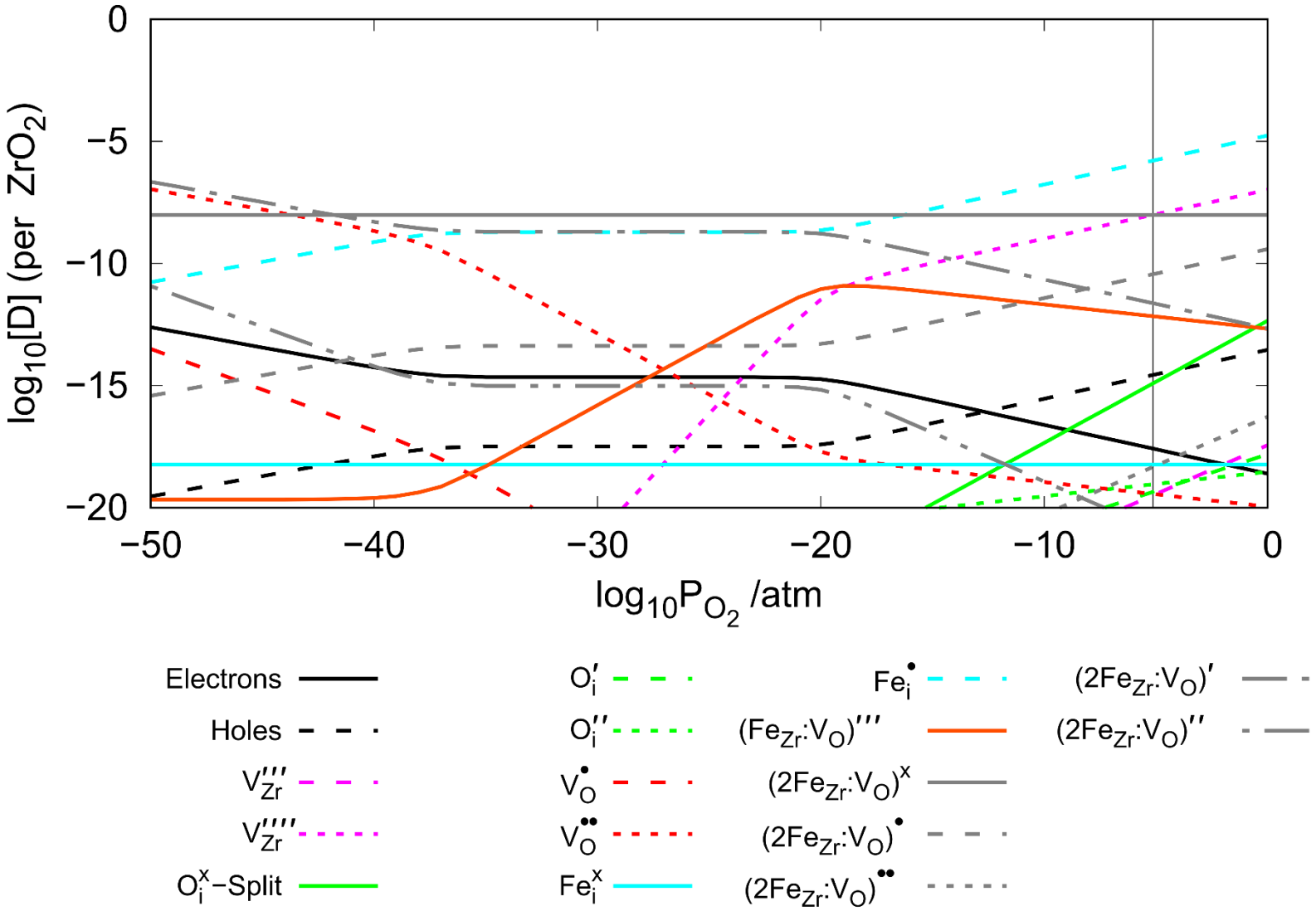

Figure 164 Brouwer diagram at 635 K with no fixed concentration of Fe and intrinsic defects in monoclinic ZrO_2.

The Brouwer diagram produced with intrinsic defects doped with an unstipulated concentration of iron, *Figure 164*, has proved to be quite complex. At the lowest partial pressures to the left, the negative one charged cluster of one iron substitutions to two zirconium sites $(2\mathrm{Fe}_{\mathrm{Zr}}:\mathrm{V}_{\mathrm{O}})'$ has the highest concentration but is quickly replaced by the neutral charged cluster $(2\mathrm{Fe}_{\mathrm{Zr}}:\mathrm{V}_{\mathrm{O}})^{\times}$ through the mid region of partial pressures. At the higher partial pressures to the right, the plus one charged iron interstitial $(\mathrm{Fe}_{\mathrm{i}}^{\bullet})$ has the higher concentration. When considering the interactions from these three defects, the negative one cluster $(2\mathrm{Fe}_{\mathrm{Zr}}:\mathrm{V}_{\mathrm{O}})'$ is followed by the plus two charged oxygen vacancy $(\mathrm{V}_{\mathrm{O}}^{\bullet\bullet})$ up until this is met by the plus one interstitial $(\mathrm{Fe}_{\mathrm{i}}^{\bullet})$. The interstitial then couples with the interstitial until the negative four zirconium vacancy $(\mathrm{V}_{\mathrm{Zr}}^{\prime\prime\prime\prime})$ concentration increases. When the $(\mathrm{V}_{\mathrm{Zr}}^{\prime\prime\prime\prime})$ intersects the negative three charged cluster $(\mathrm{Fe}_{\mathrm{Zr}}:\mathrm{V}_{\mathrm{O}})'''$, it appears that this is coupled with both a reduction in zirconium vacancy $(\mathrm{V}_{\mathrm{Zr}}^{\prime\prime\prime\prime})$ and the $(2\mathrm{Fe}_{\mathrm{Zr}}:\mathrm{V}_{\mathrm{O}})'$. This also shows an increase in both the interstitial $(\mathrm{Fe}_{\mathrm{i}}^{\bullet})$ and the plus one charged defect $(2\mathrm{Fe}_{\mathrm{Zr}}:\mathrm{V}_{\mathrm{O}})^{\bullet}$. At lower concentrations, the negative two cluster $(2\mathrm{Fe}_{\mathrm{Zr}}:\mathrm{V}_{\mathrm{O}})''$ shows a reduction in concentration from the lower partial pressures but is levelled off when the cluster couples with the electron concentration causing them both to plateau. This plateau also has the knock-on effect of pushing the intersect of electrons and holes to higher partial pressures than what can be seen with just intrinsic defects alone and also causes an overall decrease in the plus two charged oxygen vacancy $(\mathrm{V}_{\mathrm{O}}^{\bullet\bullet})$. There is also an overall increase in negative four zirconium vacancy $(\mathrm{V}_{\mathrm{Zr}}^{\prime\prime\prime\prime})$ concentrations at higher partial pressures. At the lowest concentration, the neutral iron interstitial can be seen which maintains a constant concentration across the range of partial pressures without any seemingly obvious interaction.

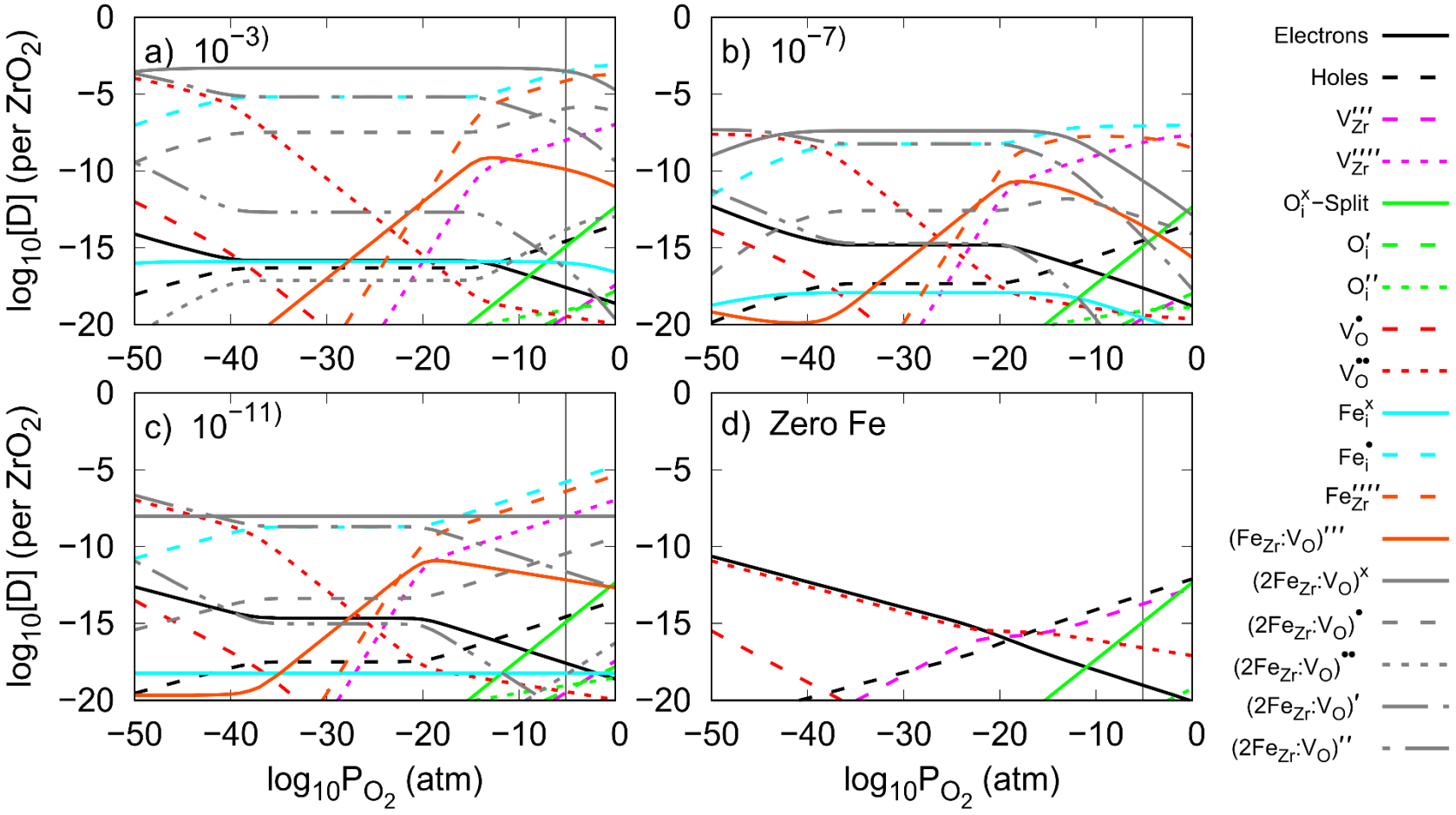

Figure 165 Fe doped monoclinic ZrO_2 Brouwer diagrams with the Fe concentrations of a) 10^{-3} b) 10^{-7} c) 10^{-11} and d) with intrinsic defects only.

When the iron defect concentrations are stipulated, *Figure 165*, it changes the dynamic of the intrinsic defect concentrations. When the iron concentrations are increased to 10^{-3} per ZrO_2 (a), the overall concentration of the plus two oxygen vacancy defect $(V_O^{\bullet\bullet})$ is vastly increased at lower partial pressures to the left and reduced at higher partial pressures. The negative four zirconium vacancy $(V_{Zr}^{''''})$ has a very high concentration towards higher partial pressures to the right when comparing this to the intrinsic defects (d). the overall trends and effects caused by each defect is similar to that found in the Brouwer diagram containing no stipulated concentration of iron. The 10^{-7} per ZrO_2 concentration Brouwer diagram (b) is extremely similar to that of the Brouwer diagram containing no stipulated iron concentrations with the exception of the neutral charged cluster $(2Fe_{Zr}:V_O)^{\times}$. Which has a reduction in concentration towards both the lowest and highest partial pressures. This is also true for the neutral charged interstitial $(Fe_i^{\times})$ at overall lower concentrations. The lower iron concentration of 10^{-11} per ZrO_2 (c) is virtually identical to the Brouwer diagram with no stipulated iron concentration. This, however, produced much higher iron concentrations than 10^{-11} per ZrO_2. This is the result of a maximum allowed deviation of 3 eV in the dopant chemical potential which can result in an overall adjustment of the dopant concentration if the stipulated concentration cannot be met. One defect, however, is present in the stipulated concentration Brouwer diagrams that was not present in the non-stipulated diagram which was the negative four iron substitution on a zirconium site $(Fe_{Zr}^{''''})$. Through the different defect concentrations, this defect increases in concentration from the mid partial pressures to the higher partial pressures. When the substitution concentration reaches the plus one interstitial $(Fe_i^{\bullet})$, the substitution $(Fe_{Zr}^{''''})$ couples with the interstitial and follows the rate of increase that the interstitial takes. There is no indication that the substitution has any effect on any other defect.

A.7. Sn Doped Monoclinic ZrO_2

The final defect to consider in the monoclinic structure is tin. Again, the defects under consideration are the tin interstitials (Sn_i), tin substitutions on zirconium sites (Sn_{Zr}), the small cluster of a tin interstitial on a zirconium site with an oxygen vacancy $(Sn_{Zr}:V_O)$, and two tin substitutions on two zirconium sites with a oxygen vacancy $(2Sn_{Zr}:V_O)$. Each defect species is accompanied by a range of charges that were calculated within the bandgap.

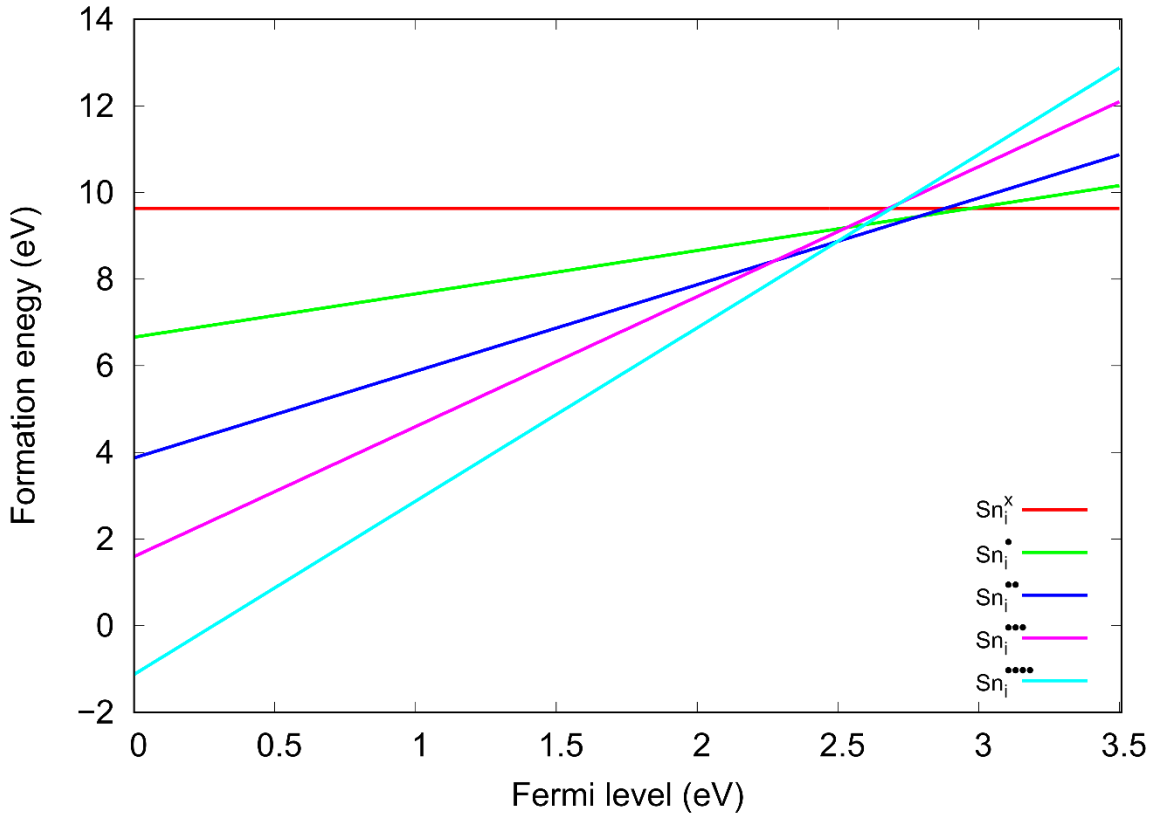

Figure 166 Formation energy of tin interstitial defects with a range of charges across the Fermi energy of the bandgap in monoclinic ZrO_2.

The tin interstitials have a predominantly positive formation energy across the bandgap, *Figure 166*, with the exception of a small region at the top of the valence band to the left where the positive four interstitial has a negative formation energy up to 0.3 eV. The defects through the remainder of the bandgap all have a positive formation energy. From the top of the valence band, the $(Sn_i^{\bullet\bullet\bullet\bullet})$ holds the lowest formation energy up to approximately 2.5 eV. From there the plus two interstitial $(Sn_i^{\bullet\bullet})$ has the lowest formation energy up to roughly 2.8 eV where the plus one interstitial $(Sn_i^{\bullet})$ has the lowest formation energy up to 3 eV. The remainder of the bandgap has the neutral interstitial $(Sn_i^{\times})$ with the lowest formation energy up to the bottom of the conduction band. The plus three interstitial $(Sn_i^{\bullet\bullet\bullet})$ does not have the lowest formation energy at any point across the bandgap.

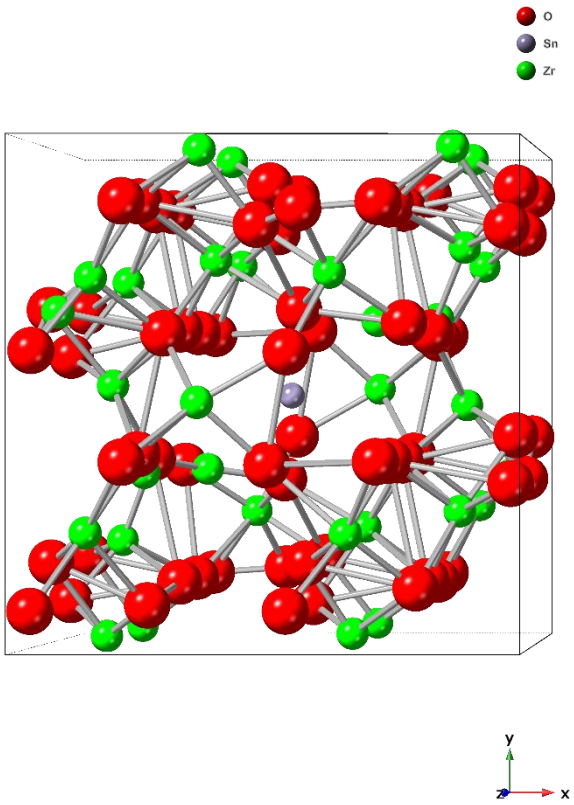

Figure 167 Monoclinic ZrO_2 structure with a tin interstitial (purple) centre.

As what was found with the chromium and iron interstitials, the tin interstitial location within the monoclinic ZrO_2 structure had the potential to cause relatively large movements of individual atoms (Figure 170). Whilst this is an example of a worst-case scenario of tin interstitial, as seen before, it provides evidence for the need to check structures visually once relaxed. In the given example, the two nearest neighbour zirconium atoms have been pushed into locations of the next nearest neighbour zirconium sites. This has had a knock-on effect of bushing the next nearest neighbour zirconium atoms further still. The nearest oxygen defects have been pushed towards their next nearest oxygen neighbour sites causing two oxygen clusters in the plus and minus y direction from the original location. The only interstitial defect that seemed to have the least effect on surrounding intrinsic atomic locations was the lithium interstitial.

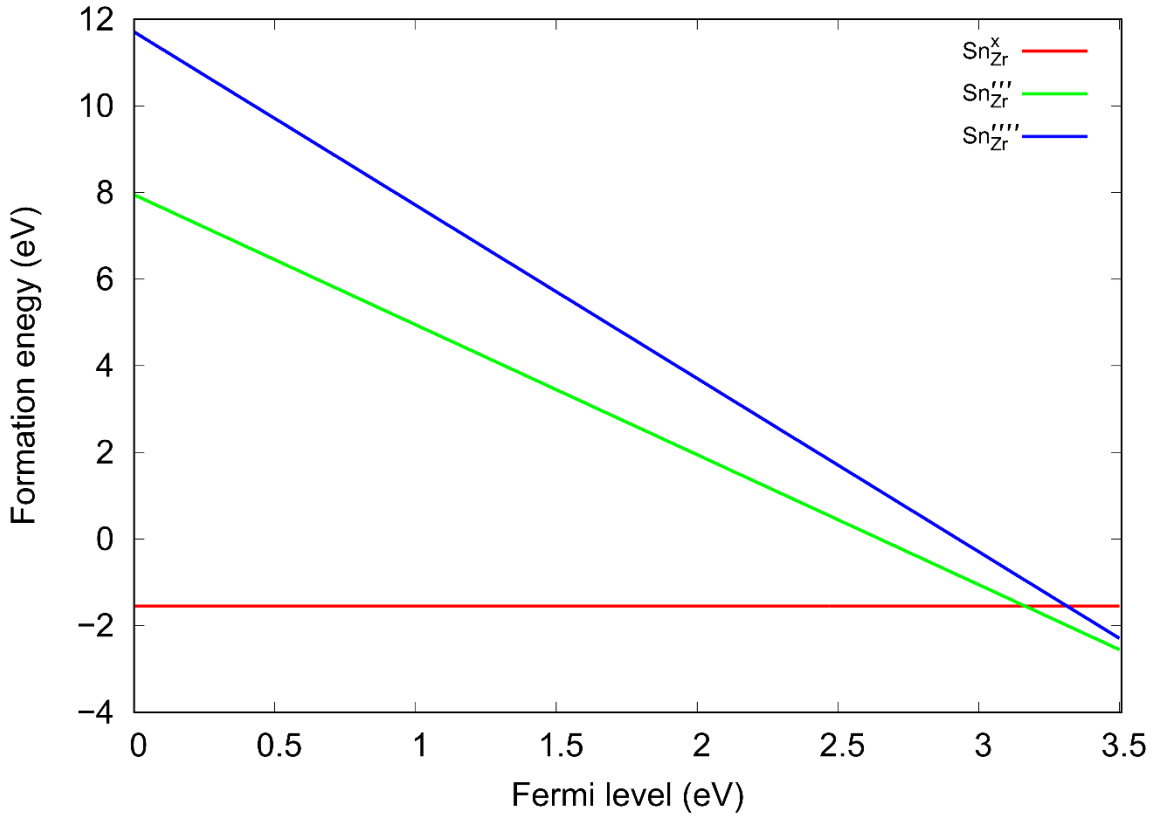

Figure 168 Formation energy of tin substitution defects on zirconium sites with a range of charges across the Fermi energy of the bandgap in monoclinic ZrO_2.

Similar to the iron substitution defects, the tin substation defects on zirconium sites have a neutral, negative three and negative four charge, Figure 168. The neutral charged defect (Sn_{Zr}^{x}) has a consistent negative formation energy across the bandgap and has the lowest formation energy from the top of the valence band up to 3.2 eV. From there, the remainder of the bandgap has the negative three charged substitution (Sn_{Zr}''') with the lowest formation energy to the bottom of the conduction band. The negative four substitution (Sn_{Zr}'''') does not have the lowest formation energy across the entirety of the bandgap. All the defects have a negative formation energy at the bottom of the conduction band to the right. Below 2.6 eV, the negative three and four substitutions have a positive formation energy.

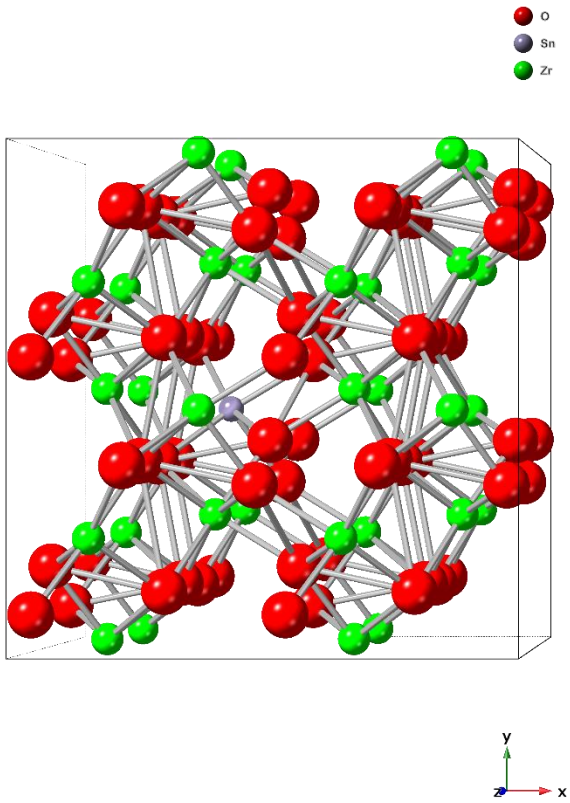

Figure 169 Monoclinic ZrO_2 structure with a tin substitution on a zirconium site.

The tin substitution on a zirconium site in the monoclinic ZrO_2 structure (Figure 172) shows very little change in intrinsic atomic position.

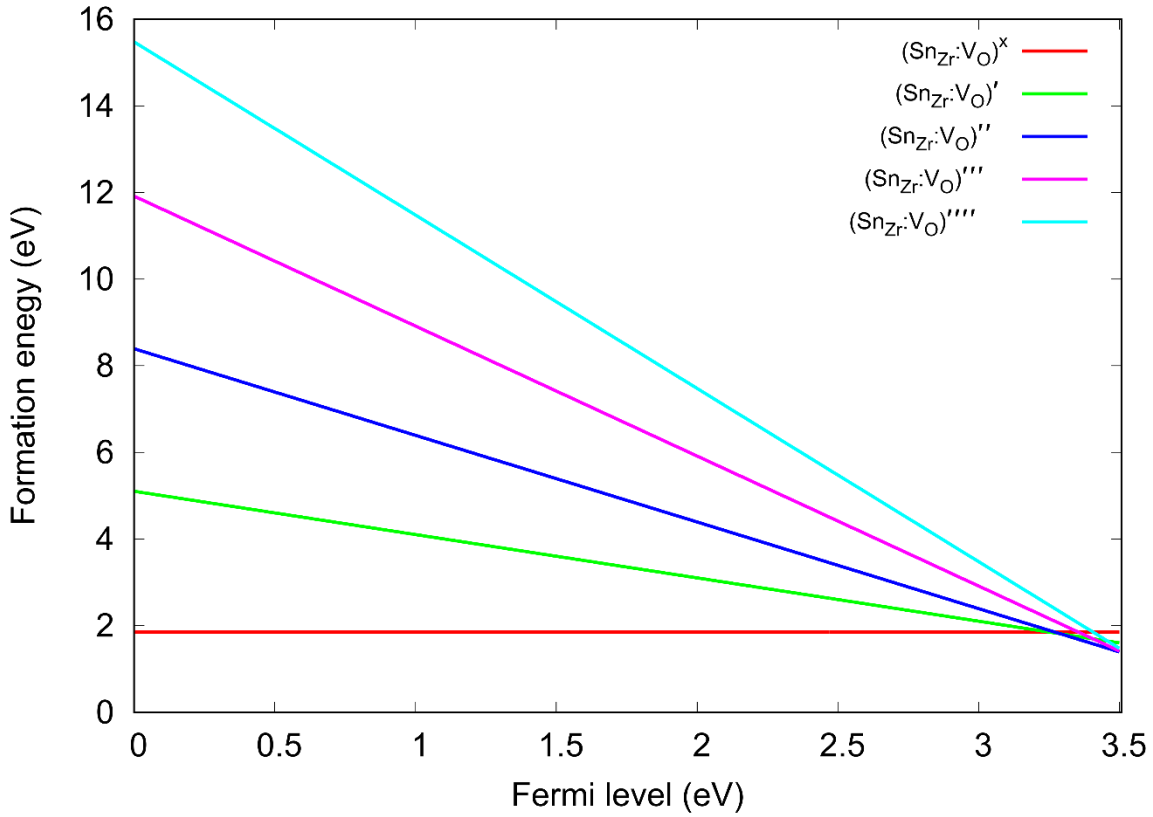

Figure 170 Formation energy of the small defect cluster of a tin substitution on a zirconium site with a oxygen vacancy with a range of charges across the Fermi energy of the bandgap in monoclinic ZrO_2

The small cluster of a tin substitution on a zirconium vacancy site with an oxygen vacancy defect, *Figure 170*, does not show a negative formation energy with any charge across the bandgap. The lowest formation energy for most of the bandgap is held by the neutral charged cluster $(\mathrm{Sn_{Zr}}{:}\,\mathrm{V_O})^{\times}$ from the top of the valence band to the left and up to 3.3 eV. The remainder of the bandgap up to the bottom of the conduction band is the negative two charged $(\mathrm{Sn_{Zr}}{:}\,\mathrm{V_O})''$ which has the lowest formation energy of all the defects. The remaining negative one, three and four charged defects do not hold the lowest formation energy at any point across the bandgap.

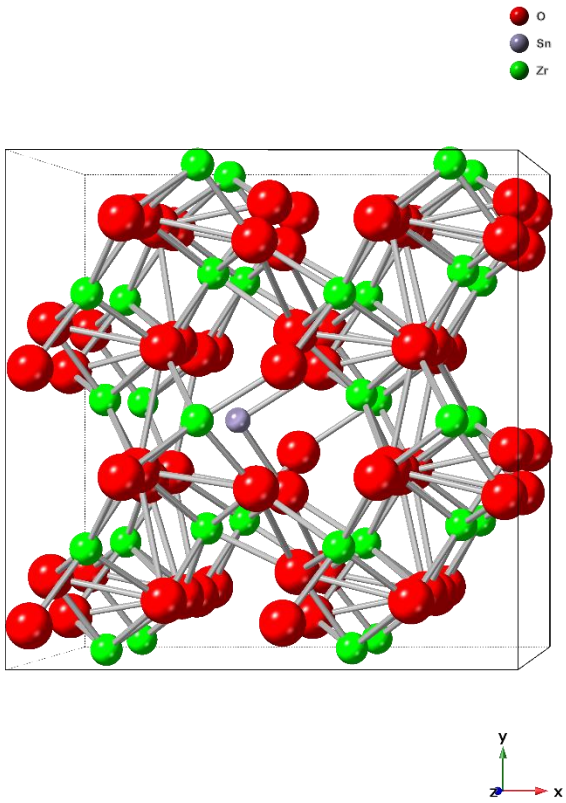

Figure 171 Monoclinic ZrO_2 structure with a tin substitution on a zirconium site with a oxygen vacancy.

The cluster of a tin substitution on a zirconium site and a oxygen vacancy defect in the monoclinic ZrO_2 structure (Figure 174) shows little change in positions of surrounding atoms.

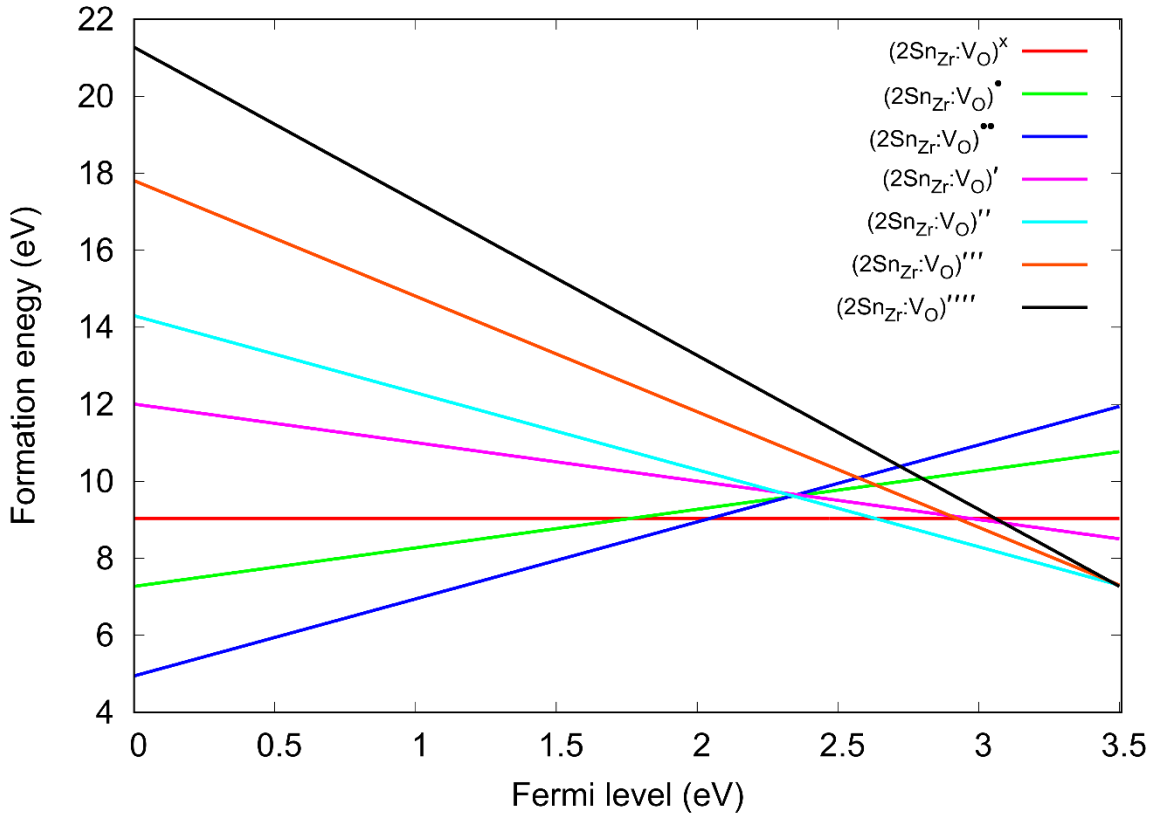

Figure 172 Formation energy of the small defect cluster of two tin substitutions on two zirconium sites with a oxygen vacancy with a range of charges across the Fermi energy of the bandgap in monoclinic ZrO_2

The last defect species to be investigated in the monoclinic structure is the small cluster of two tin substitutions to two zirconium sites with a oxygen vacancy, *Figure 172*. Again, none of these charged defects hold a negative formation energy at any point across the bandgap. At the top of the valence band to the left, the plus two charged cluster $(2\mathrm{Sn_{Zr}}:\mathrm{V_O})^{\bullet\bullet}$ has the lowest formation energy. This plus two cluster holds the lowest formation energy up to 2.1 eV where the neutral charged cluster $(2\mathrm{Sn_{Zr}}:\mathrm{V_O})^{\times}$ then has the lowest formation energy up to 2.6 eV. From there, the negative two charged defect cluster $(\mathrm{Sn_{Zr}}:\mathrm{V_O})''$ holds the lowest formation energy up to the bottom of the conduction band to the far right. The plus one, negative one, three and four all do not hold the lowest formation energy across the whole bandgap.

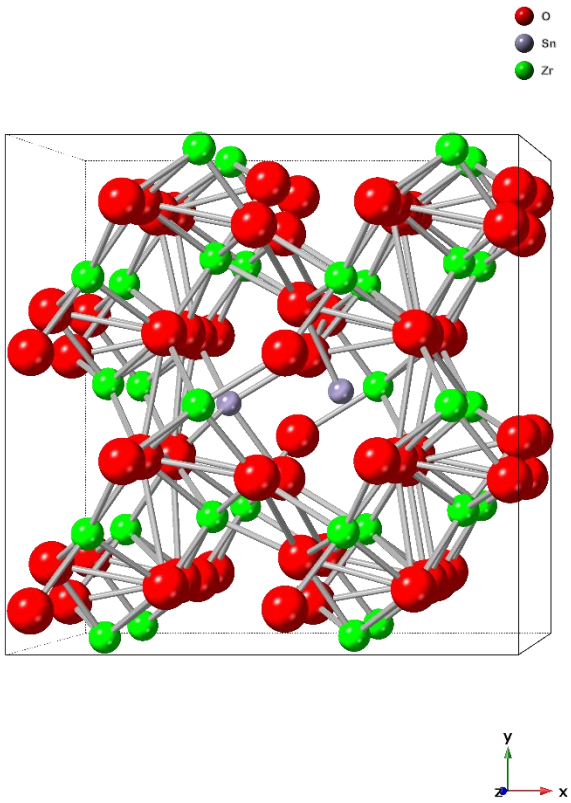

Figure 173 Monoclinic ZrO_2 structure with two tin substitutions on zirconium sites and a oxygen vacancy.

The two tin substitutions and an oxygen vacancy cluster in ZrO_2 (Figure 176) shows a small change in position of the nearest neighbour oxygen atoms when relaxed compared to the perfect monoclinic structure.

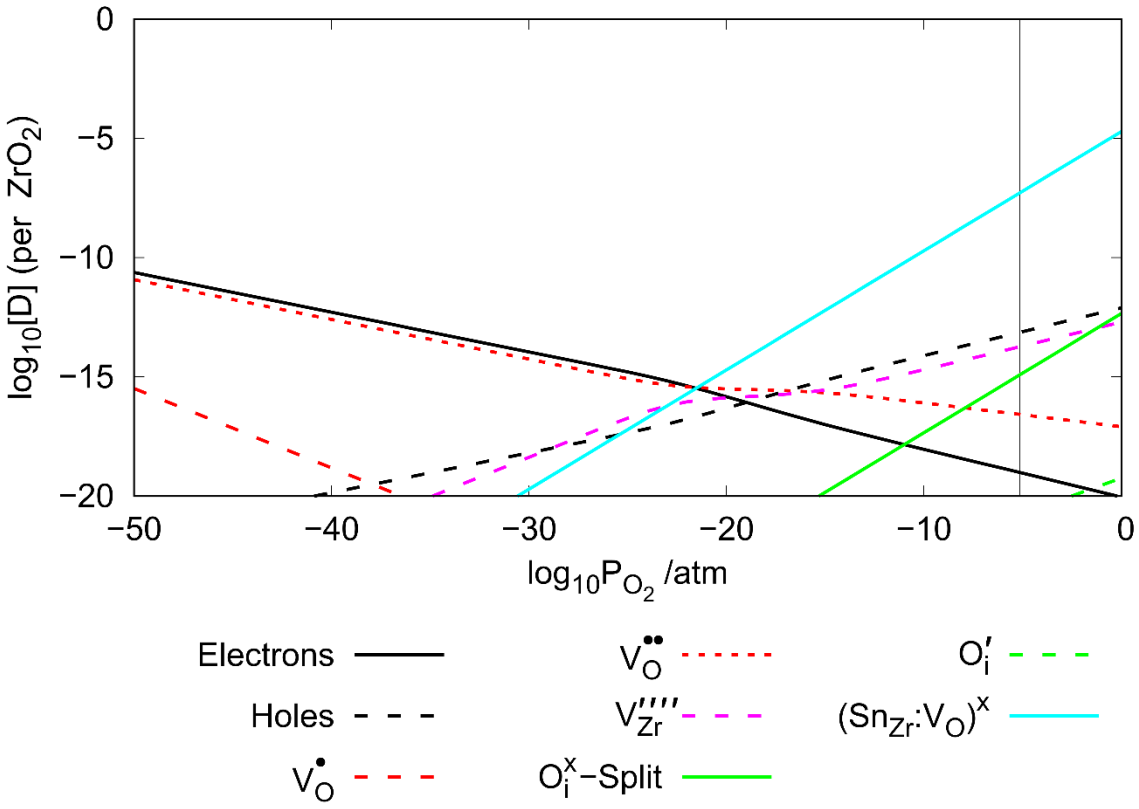

Figure 174 Brouwer diagram at 635 K with no fixed concentration of Sn and intrinsic defects in monoclinic ZrO_2.

The tin doped ZrO_2 Brouwer diagram with no fixed tin concentration, *Figure 174*, is relatively unremarkable. The only tin defect to make an appearance is the small neutral charged cluster of a tin substation on a zirconium site with a oxygen vacancy. This defect, however, does not have any bearing on any intrinsic defects which makes this difficult to discuss further. It is surprising that the only defect present is one that holds a neutral charge with a positive formation energy. Other defects that were expected were the positive four charged interstitial ($\mathrm{Sn}_{\mathrm{i}}^{\bullet\bullet\bullet\bullet}$) and the neutral charged tin substitution ($\mathrm{Sn}_{\mathrm{Zr}}^{\times}$) due to the negative formation energy of each defect.

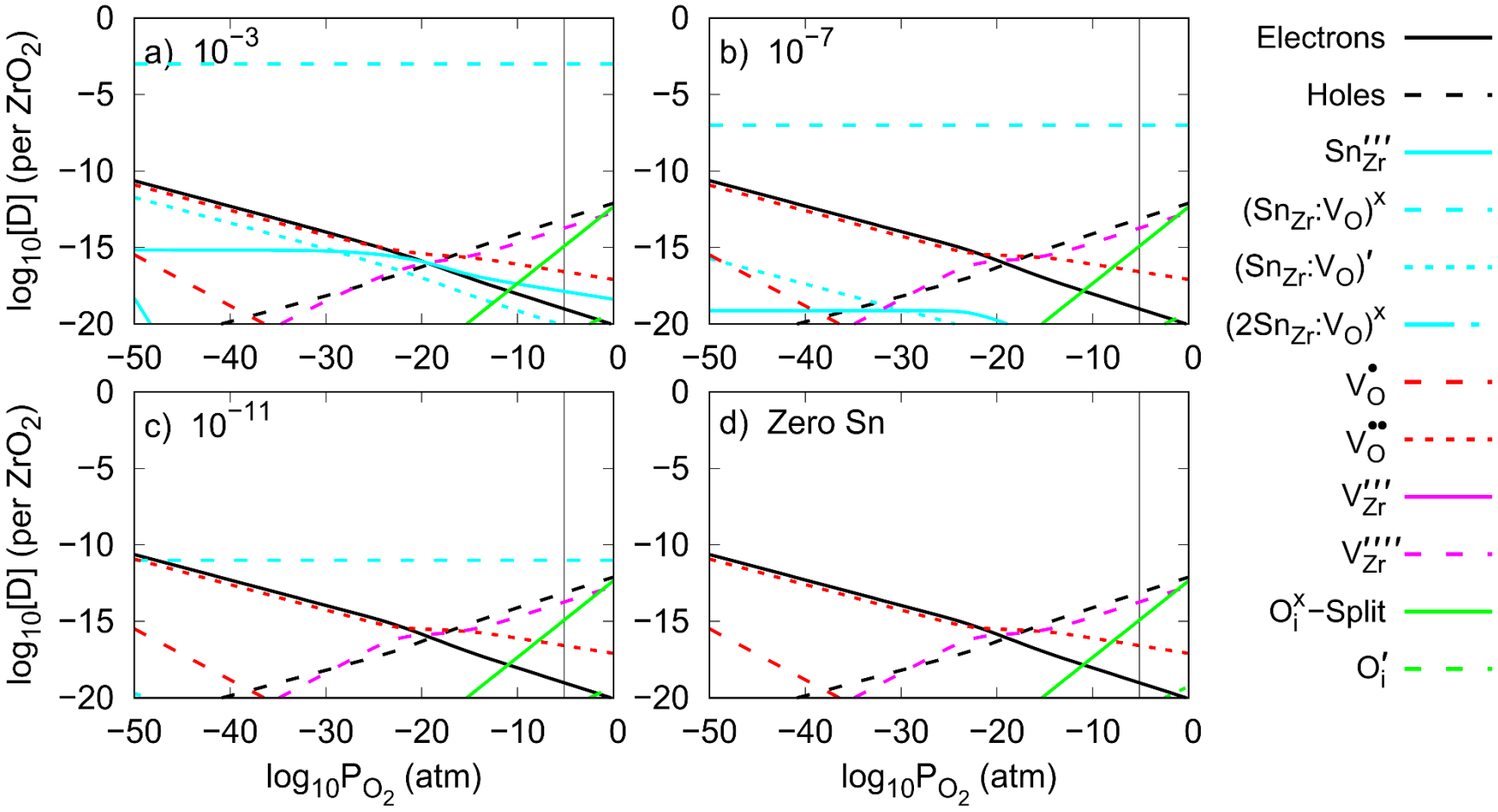

Figure 175 Sn doped monoclinic ZrO_2 Brouwer diagrams with the Sn concentrations of a) 10^{-3} b) 10^{-7} c) 10^{-11} and d) with intrinsic defects only.

The tin Brouwer diagram, *Figure 175*, containing concentrations of 10^{-3}, 10^{-7} and 10^{-11} tin per ZrO_2 indicates that tin has no effect on intrinsic defect concentrations regardless of tin content. This does provide a slightly anticlimactic end for individual dopant Brouwer diagrams, but it does offer a little more information towards a final conclusion. The tin concentrations behaved very well and met the stipulated concentration perfectly. The highest concentration tin defect in all diagrams was the small neutral charged $(\mathrm{Sn_{Zr}}:\mathrm{V_O})^{\times}$ without any competition. Further down the concentration axis, the negative one charged small cluster $(\mathrm{Sn_{Zr}}:\mathrm{V_O})'$ follows the plus two charged oxygen vacancy $(\mathrm{V_O^{\bullet\bullet}})$ and the electron concentration at lower partial pressures to the left. In the mid partial pressures, the oxygen vacancy defect $(\mathrm{V_O^{\bullet\bullet}})$ increases in concentration over the electrons. The negative one cluster $(\mathrm{Sn_{Zr}}:\mathrm{V_O})'$, however, continues to follow the electron concentration. The neutral charged small cluster $(2\mathrm{Sn_{Zr}}:\mathrm{V_O})^{\times}$ does make a very small appearance at the lowest concentration and lowest partial pressure to the far right in the 10^{-3} Brouwer diagram only (a). The last tin defect to appear is the negative three substitution $(\mathrm{Sn_{Zr}'''})$ which has a linear concentration at low partial pressures. At mid partial pressure, where this defect intersects with the electrons, the concentration begins to drop towards higher partial pressures to the right. Because the tin defects have remarkably no effect on the intrinsic defects, these trends of intrinsic defects remain the same with the exception of concentration from 10^{-3} (a), 10^{-7} (b), and 10^{-11} (c). The final diagram containing intrinsic defects only (d) is useful in order to see how little tin effects these intrinsic defects.

A.8. Combined Dopant Monoclinic ZrO_2

As with the tetragonal structure, it is helpful to find how individual species of defects may alter the intrinsic defect concentrations within the structure. Only by combining all the defects, however, can a full picture be gained of what may be potentially occurring more accurately. Though, the number of defects does certainly make the Brouwer diagram extremely complex and difficult to interpret. In an attempt to pick through the complexity, each defect element will be reviewed and then hidden before reviewing the next defect element. Because we are attempting to look at the effect of lithium on the intrinsic defects, we will finally review just the lithium defect along with the intrinsic defects with all the chromium, iron and tin defects hidden. Again, due to the investigation focusing on corrosion, the oxygen concentration is the focus of the work.

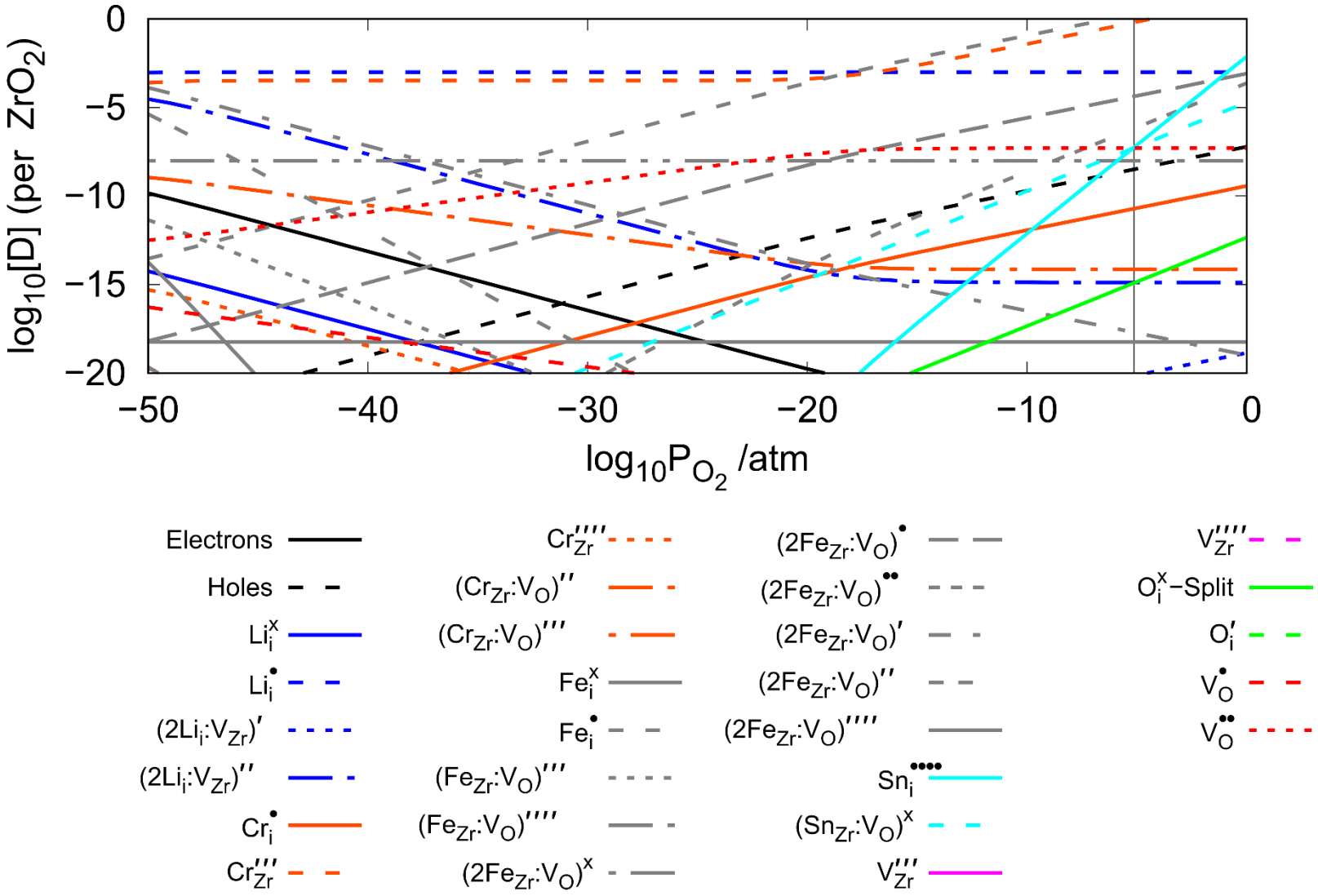

Figure 176 Monoclinic ZrO_2 Brouwer diagram with all defects with a defect concentration of 5.7 x 10^{-4} Cr, 1.47 x 10^{-3} Fe, 15.62 x 10^{-3} Sn at 635 K with Li concentrations of 10^{-3}.

The monoclinic Brouwer diagram containing all reviewed defects, *Figure 176*, contains more defects than that of the tetragonal. As with the tetragonal structure, the lithium concentration is 0.001, chromium is 0.00057, iron is 0.00147 and tin is 0.01562 per ZrO_2. There are, however, important differences such as the absence of the zirconium vacancy defects. There are also fewer chromium defects in the monoclinic structure than that of the tetragonal such as the absence of $(\mathrm{Cr}_\mathrm{i}^{\times})$, $(\mathrm{Cr}_\mathrm{i}^{\bullet\bullet})$, $(\mathrm{Cr}_\mathrm{i}^{\bullet\bullet\bullet})$, $(\mathrm{Cr}_\mathrm{i}^{\bullet\bullet\bullet\bullet})$, $(\mathrm{Cr}'_{\mathrm{Zr}})$, $(\mathrm{Cr}^{\bullet}_{\mathrm{Zr}})$, $(\mathrm{Cr}^{\bullet\bullet}_{\mathrm{Zr}})$ and $(\mathrm{Cr}_{\mathrm{Zr}}:\mathrm{V}_\mathrm{O})'$. There are, however, chromium defects in the monoclinic structure that do not appear in the tetragonal structure including $(\mathrm{Cr}_\mathrm{i}^{\bullet})$, $(\mathrm{Cr}'''_{\mathrm{Zr}})$, $(\mathrm{Cr}''''_{\mathrm{Zr}})$, and $(\mathrm{Cr}_{\mathrm{Zr}}:\mathrm{V}_\mathrm{O})'''$. The highest concentration chromium defect is the $(\mathrm{Cr}'''_{\mathrm{Zr}})$ which holds a 10^{-4} concentration at lower partial pressures up to just above 10^{-20} atm where it intercepts the iron cluster $(2\mathrm{Fe}_{\mathrm{Zr}}:\mathrm{V}_\mathrm{O})''$ and increases in concentration up to the highest partial pressure. The concentration that is reached is much higher than the stipulated concentration and is unlikely to be physically expected in real terms. This defect does not seem to have any effect on any intrinsic defects. The next higher defect concentrations are the negative two cluster $(\mathrm{Cr}_{\mathrm{Zr}}:\mathrm{V}_\mathrm{O})''$ at lower partial pressures to the left and the plus one interstitial $(\mathrm{Cr}_\mathrm{i}^{\bullet})$ at higher partial pressures to the right. The interstitial follows the hole concentration and seems relatively unchanged in concentration by the intrinsic defects other than a slight dip in the linear concentration increase from mid to high partial pressures which coincides with a point where the $(2\mathrm{Li}_\mathrm{i}:\mathrm{V}_{\mathrm{Zr}})''$, $(\mathrm{Cr}_{\mathrm{Zr}}:\mathrm{V}_\mathrm{O})''$, $(2\mathrm{Fe}_{\mathrm{Zr}}:\mathrm{V}_\mathrm{O})'$, $(2\mathrm{Fe}_{\mathrm{Zr}}:\mathrm{V}_\mathrm{O})^{\bullet\bullet}$, and $(\mathrm{Sn}_{\mathrm{Zr}}:\mathrm{V}_\mathrm{O})^{\times}$ defects all intersect. It also causes a plateauing of both the $(2\mathrm{Li}_\mathrm{i}:\mathrm{V}_{\mathrm{Zr}})''$ and the $(\mathrm{Cr}_{\mathrm{Zr}}:\mathrm{V}_\mathrm{O})''$ defects that were on a reducing concentration trajectory from lower to higher partial pressures. The small negative three cluster $(\mathrm{Cr}_{\mathrm{Zr}}:\mathrm{V}_\mathrm{O})'''$ is not present in the 10^{-3} Li Brouwer diagram but will make an appearance at lower Li concentrations. This leaves the negative three chromium substitution $(\mathrm{Cr}''''_{\mathrm{Zr}})$ which has a low concentration at lower partial pressures to the far left and seems to have little interaction with any other defect.

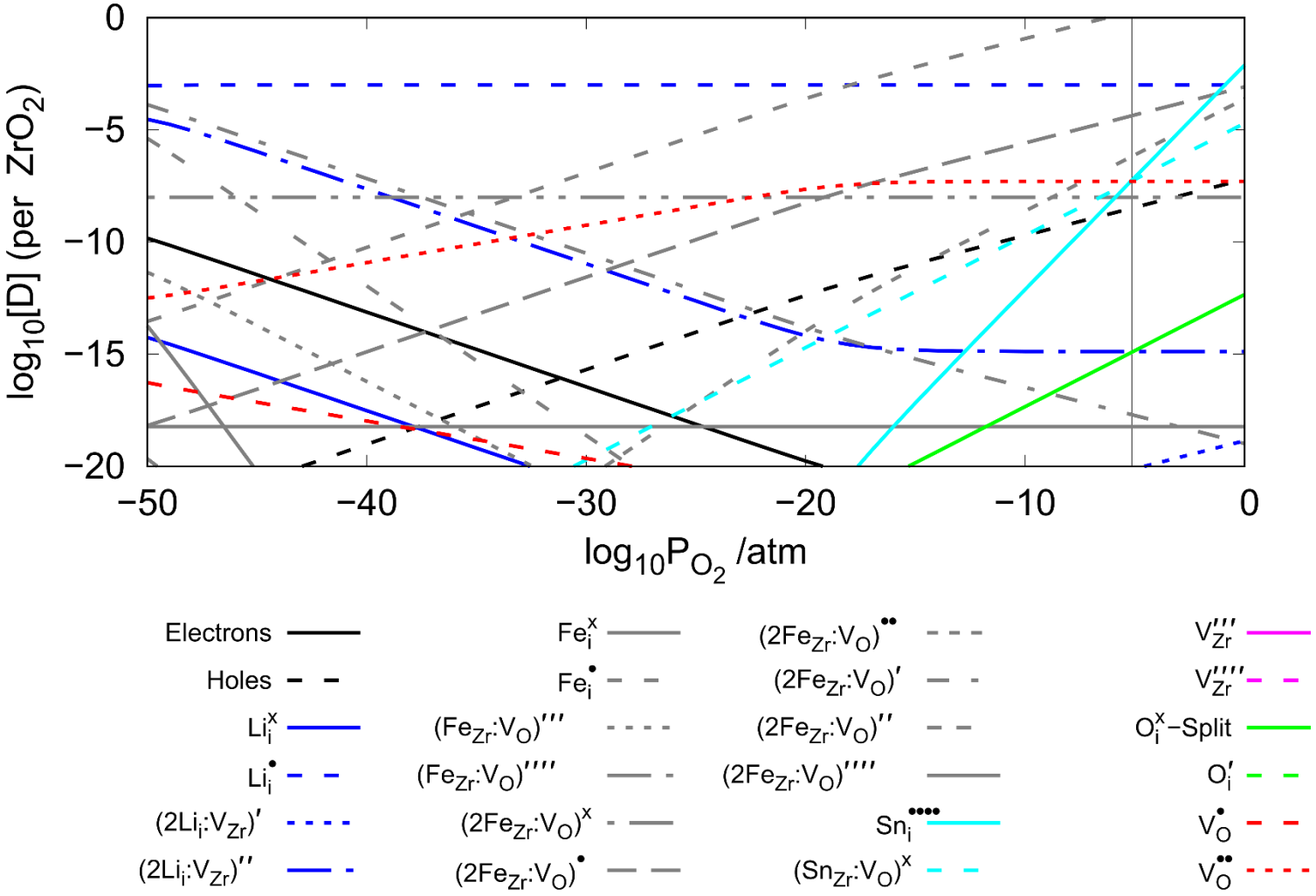

Figure 177 Monoclinic ZrO_2 Brouwer diagram showing defects with a defect concentration of 5.7 x 10^{-4} Cr, 1.47 x 10^{-3} Fe, 15.62 x 10^{-3} Sn at 635 K with Li concentrations of 10^{-3} where the Cr defects are hidden.

As with the chrome defects, the iron defects show differences between the tetragonal and monoclinic structure. The iron defects that are absent in the monoclinic structure that were in the tetragonal structure are $(\mathrm{Fe}_{\mathrm{i}}^{\bullet\bullet})$, $(\mathrm{Fe}_{\mathrm{Zr}}^{\times})$, $(\mathrm{Fe}_{\mathrm{Zr}}^{\prime})$, $(\mathrm{Fe}_{\mathrm{Zr}}^{\prime\prime})$ and $(\mathrm{Fe}_{\mathrm{Zr}}:\mathrm{V}_{\mathrm{O}})''$. There are, however, many defects in the monoclinic structure, *Figure 177*, that are not in the tetragonal and these are $(\mathrm{Fe}_{\mathrm{i}}^{\times})$, $(\mathrm{Fe}_{\mathrm{i}}^{\bullet})$, $(\mathrm{Fe}_{\mathrm{Zr}}:\mathrm{V}_{\mathrm{O}})''''$, $(2\mathrm{Fe}_{\mathrm{Zr}}:\mathrm{V}_{\mathrm{O}})^{\times}$, $(2\mathrm{Fe}_{\mathrm{Zr}}:\mathrm{V}_{\mathrm{O}})^{\bullet}$, $(2\mathrm{Fe}_{\mathrm{Zr}}:\mathrm{V}_{\mathrm{O}})^{\bullet\bullet}$, $(2\mathrm{Fe}_{\mathrm{Zr}}:\mathrm{V}_{\mathrm{O}})'$, $(2\mathrm{Fe}_{\mathrm{Zr}}:\mathrm{V}_{\mathrm{O}})''$, $(2\mathrm{Fe}_{\mathrm{Zr}}:\mathrm{V}_{\mathrm{O}})''''$. The highest concentration defect is that of the plus two cluster $(2Fe_{Zr}:V_O)^{\bullet\bullet}$ which far exceeds the stipulated concentration at higher partial pressures and is unlikely to occur in reality. The concentration of this defect does drop towards lower partial pressures to the left and does not seem to interact with any other defect other than the previously stated chromium defect. At the lowest partial pressure, the cluster $(\mathrm{Fe}_{\mathrm{Zr}}:\mathrm{V}_{\mathrm{O}})''''$ has the highest concentration but reduces moving to higher partial pressures with a trend similar to that of the electrons which hold lower concentrations. The lithium defect cluster $(2\mathrm{Li}_{\mathrm{i}}:\mathrm{V}_{\mathrm{Zr}})''$ couples with the $(\mathrm{Fe}_{\mathrm{Zr}}:\mathrm{V}_{\mathrm{O}})''''$ defect until the lithium defect intersects the plus two $(2\mathrm{Fe}_{\mathrm{Zr}}:\mathrm{V}_{\mathrm{O}})^{\bullet\bullet}$ defect and the lithium defect concentration plateaus. This does coincide with an intercept of the tin cluster $(\mathrm{Sn}_{\mathrm{Zr}}:\mathrm{V}_{\mathrm{O}})^{\times}$, however, it is unlikely that the tin defect causes any change in any other defect. The iron defect $(2\mathrm{Fe}_{\mathrm{Zr}}:\mathrm{V}_{\mathrm{O}})^{\times}$ shows linear concentration across the partial pressure range with a concentration of roughly 10^{-7} per ZrO_2. This defect interacts with the oxygen vacancy defect $(\mathrm{V}_{\mathrm{O}}^{\bullet\bullet})$ which, at lower partial pressures, increases in concentration until it intercepts the iron cluster $(2\mathrm{Fe}_{\mathrm{Zr}}:\mathrm{V}_{\mathrm{O}})^{\times}$ where it plateaus. The oxygen vacancy defect then maintains the linear concentration with the iron cluster through to the higher partial pressures to the right. The next defect is the plus one charged cluster $(2\mathrm{Fe}_{\mathrm{Zr}}:\mathrm{V}_{\mathrm{O}})^{\bullet}$ which has a very low concentration at low partial pressures but increases to roughly 10^{-3} concentration at the highest partial pressure. This defect, however, does not appear to affect any other defect. The remaining iron defects do not appear to have any impact on the remaining defects and are predominantly concentrated at lower partial pressures to the left and include, in order of concentration high to low, $(2\mathrm{Fe}_{\mathrm{Zr}}:\mathrm{V}_{\mathrm{O}})''$, $(\mathrm{Fe}_{\mathrm{Zr}}:\mathrm{V}_{\mathrm{O}})'''$, and $(2\mathrm{Fe}_{\mathrm{Zr}}:\mathrm{V}_{\mathrm{O}})''''$. The neutral $(\mathrm{Fe}_{\mathrm{i}}^{\times})$ holds a very low concentration across the whole partial pressure range and does not interact with any other defect.

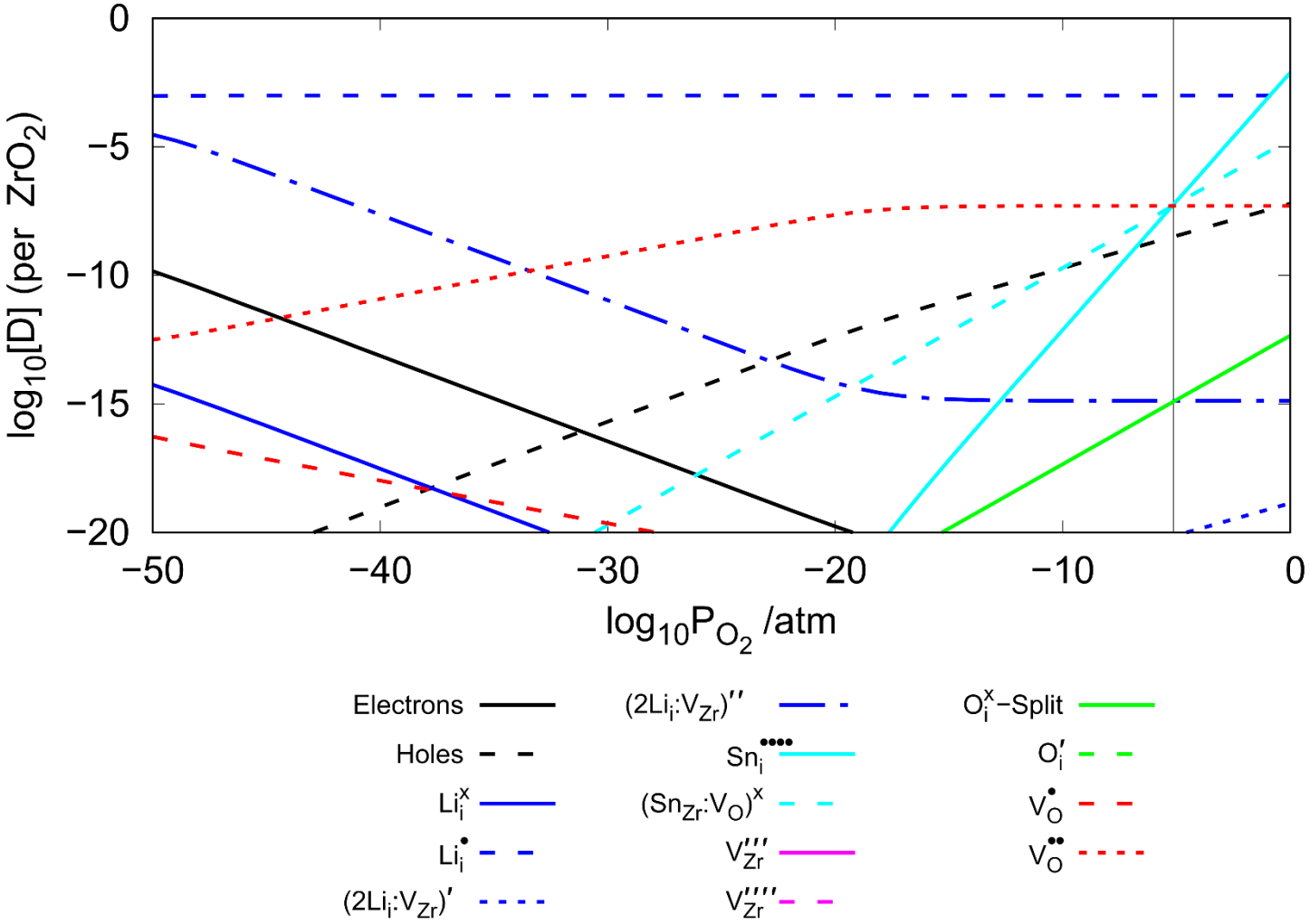

Figure 178 Monoclinic ZrO_2 Brouwer diagram showing tin defects with a defect concentration of 5.7 x 10^{-4} Cr, 1.47 x 10^{-3} Fe, 15.62 x 10^{-3} Sn at 635 K with Li concentrations of 10^{-3} where the Cr and Fe defects are hidden.

There is not a lot that can be said for tin defects in the monoclinic, *Figure 178*, or tetragonal structures as, in both structures, there are no apparent interactions that can be gained through Brouwer diagram calculations. Much like chromium and iron, there are differences of tin defects that are present between the monoclinic and tetragonal structures which may tell its own story. The tin defects that are present in the tetragonal structure that cannot be found in the monoclinic are the $(\mathrm{Sn}_{\mathrm{Zr}}^{\times})$ and the negative one cluster $(\mathrm{Sn}_{\mathrm{Zr}}{:}\,\mathrm{V}_{\mathrm{O}})'$. The monoclinic structure shows the plus four interstitial $(\mathrm{Sn}_{\mathrm{i}}^{\bullet\bullet\bullet\bullet})$ where the tetragonal structure does not. The tin defect that is common to both the monoclinic and tetragonal structures is the neutral charged $(\mathrm{Sn}_{\mathrm{Zr}}{:}\,\mathrm{V}_{\mathrm{O}})^{\times}$. The tin defect concentration trend is the same for both monoclinic and tetragonal where all tin defects show higher concentrations at higher partial pressures.

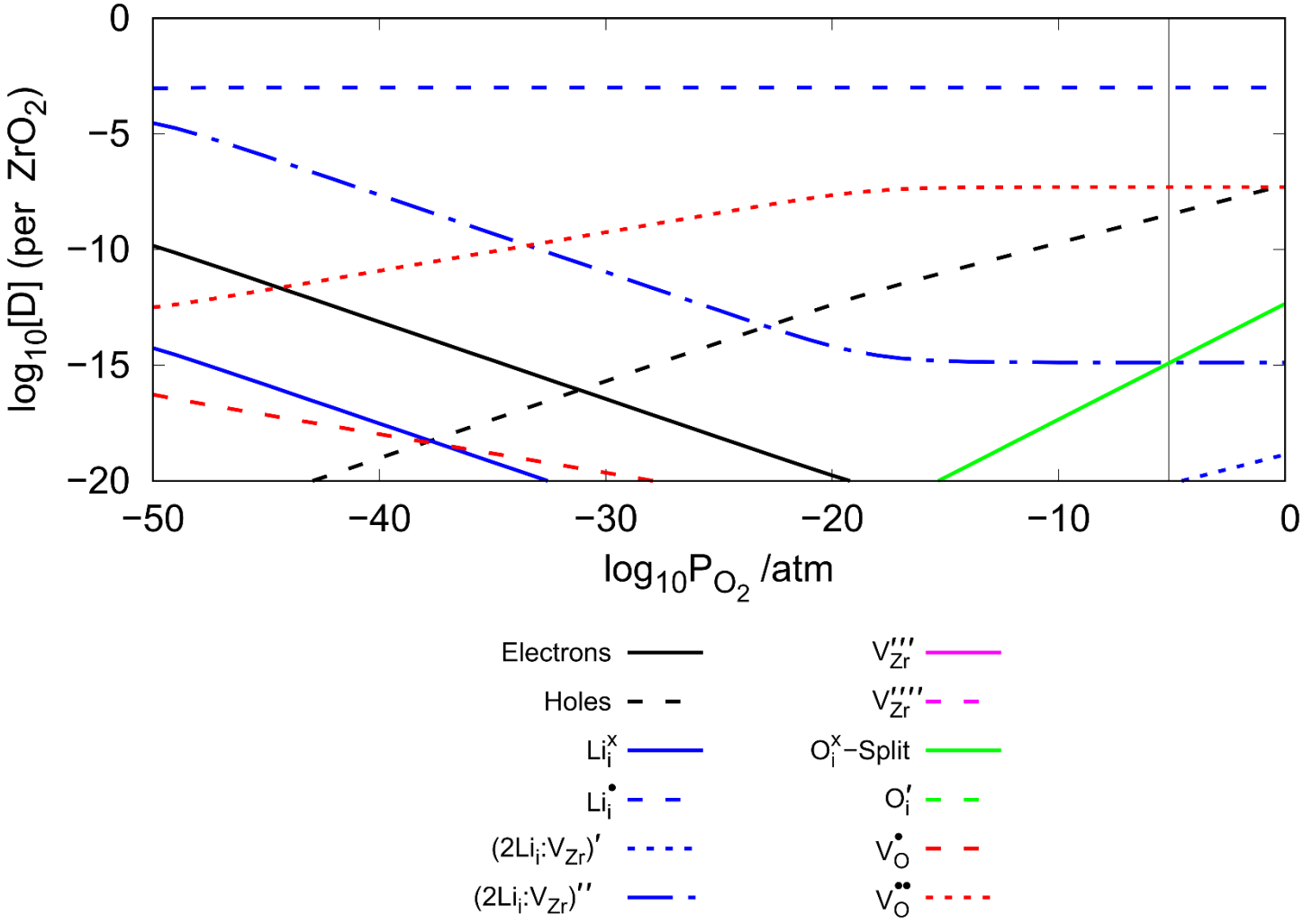

Figure 179 Monoclinic ZrO_2 Brouwer diagram showing lithium defects with a defect concentration of 5.7 x 10^{-4} Cr, 1.47 x 10^{-3} Fe, 15.62 x 10^{-3} Sn at 635 K with Li concentrations of 10^{-3} where the Cr, Fe and Sn defects are hidden.

Finally, the lithium and intrinsic defects, *Figure 179*, are left and there are some large differences between the tetragonal and monoclinic concentrations. As mentioned already, the zirconium vacancy defects are absent in the monoclinic structure. Unlike the chromium, iron and tin defects, the lithium defect species are the same between the monoclinic and the tetragonal structures. The main difference is that in the monoclinic structure, the plus one $(\mathrm{Li}_i^{\bullet})$ defect has the higher 10^{-3} per ZrO_2 concentration, the tetragonal structure has the cluster $(2\mathrm{Li}_i : \mathrm{V}_{Zr})''$ has the higher defect concentration. With the Brouwer diagram simplified through hidden Cr, Fe and Sn defects, it is clear to see that the oxygen vacancy defects $(\mathrm{V}_O^{\bullet\bullet})$ are very much higher concentrations at higher partial pressures. When compared to the tetragonal structure, the neutral $(\mathrm{Li}_i^{\times})$ at lower partial pressures have higher concentrations in the monoclinic structure and, at higher partial pressures, the cluster $(2\mathrm{Li}_i : \mathrm{V}_{Zr})'$ has a much lower concentration in the monoclinic structure. In addition to this, the plus one oxygen vacancy $(\mathrm{V}_O^{\bullet})$ has a much lower concentration than that of the tetragonal structure and the neutral oxygen vacancy defect $(\mathrm{V}_O^{\times})$ is not present at all in the monoclinic structure.

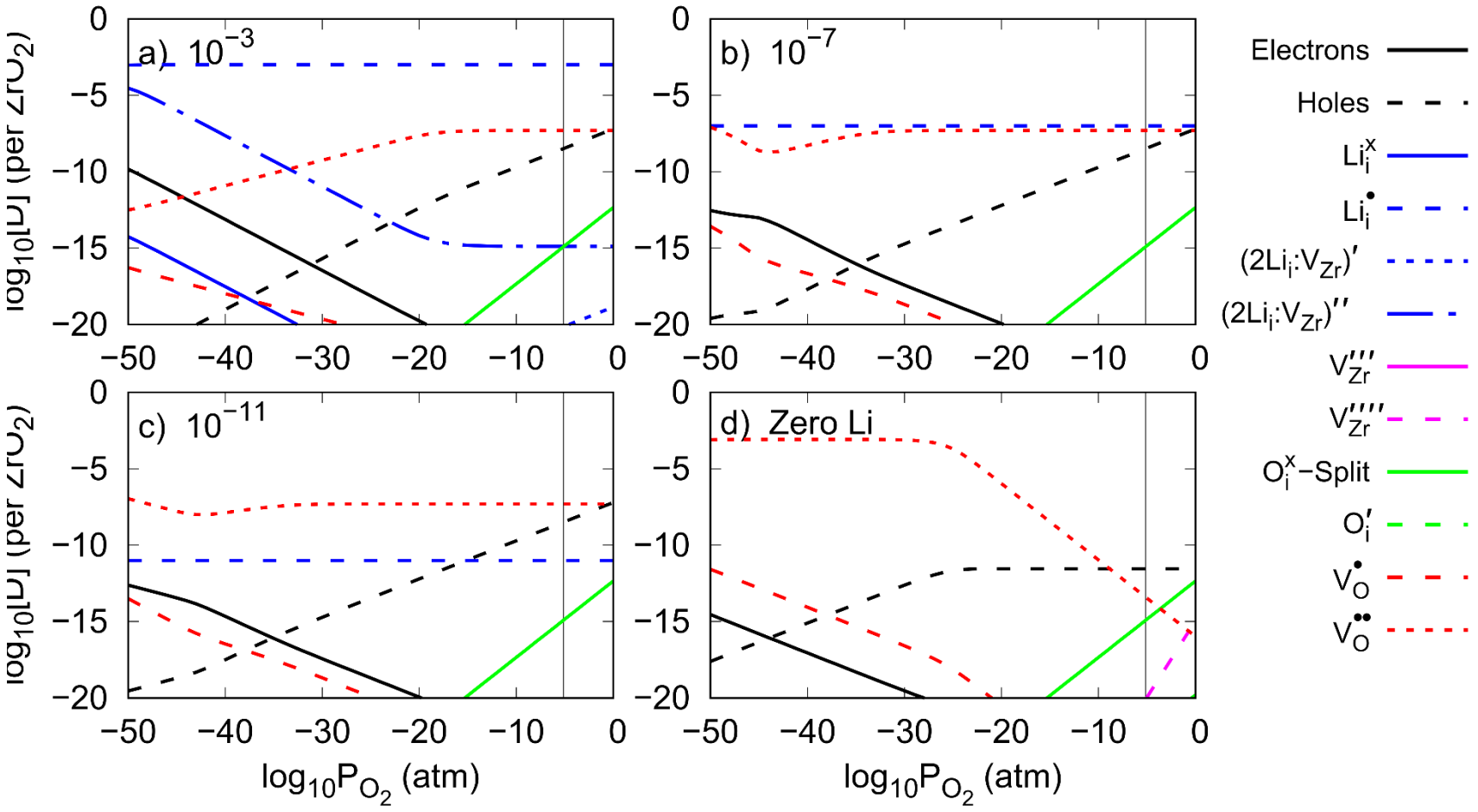

Figure 180 Monoclinic ZrO_2 Brouwer diagram with defects with a defect concentration of 5.7 x 10^{-4} Cr, 1.47 x 10^{-3} Fe, 15.62 x 10^{-3} Sn at 635 K with Li concentrations of a) 10^{-3} b) 10^{-7} c) 10^{-11} and d) zero Li. The Cr, Fe and Sn defects are hidden for clarity.

The monoclinic Brouwer diagram, *Figure 180*, showing the change in lithium concentrations whilst hiding the chromium, iron and tin defects really does show very large changes in the plus two oxygen vacancy ($V_O^{\bullet\bullet}$) concentrations. The difference between 10^{-3} per ZrO_2 lithium (a) and no lithium (d) is quite remarkable and almost mirror one another. At higher lithium concentrations, the ($V_O^{\bullet\bullet}$) defects have high concentrations at high partial pressures. With no lithium, the ($V_O^{\bullet\bullet}$) have low concentrations at high partial pressures. The reverse of this is true at low partial pressures. The zirconium vacancy defect ($V_{Zr}^{''''}$) makes an appearance when there is no lithium within the structure, all be it, with small concentrations at the highest partial pressure to the right. At slightly lower lithium concentrations, 10^{-7} and 10^{-11} per ZrO_2, the oxygen vacancy concentration becomes almost linear in concentration across the partial pressure range. There is, however, a small trough in concentration at around the 10^{-45} atm which would be caused by another, hidden, defect. In the case of the 10^{-7} per ZrO_2 diagram (b), the oxygen vacancy ($V_O^{\bullet\bullet}$) follows the lithium interstitial ($Li_i^{\bullet}$) quite closely, but at the lower lithium concentration of 10^{-11} per ZrO_2, the oxygen vacancy concentration is higher than that of lithium. The electron and hole intersect point is at a higher partial pressure with higher lithium concentrations from 10^{-30} atm (a) and shifts through each change of lithium concentration until it reaches 10^{-45} atm in the diagram with no lithium (d).